Innovative analytical methodologies to characterize original and weathered materials of extraterrestrial origin and terrestrial analogues to meteorites

Leticia Gómez Nubla

2015

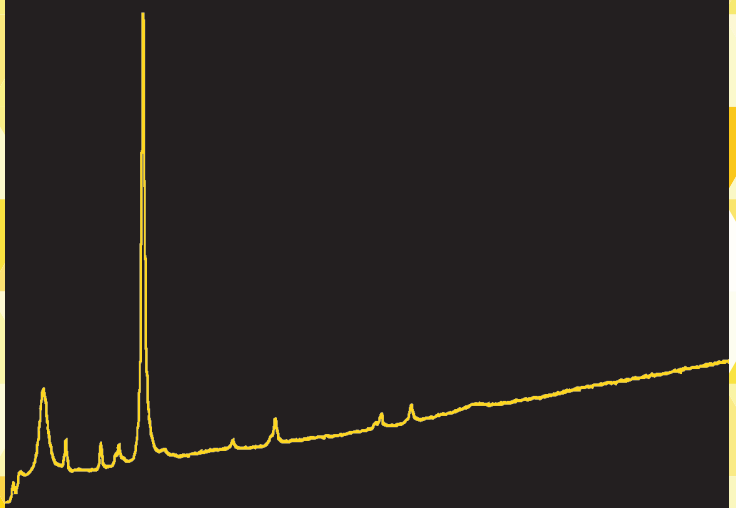

eman ta zabal zazu

Universidad del País Vasco

Euskal Herriko Unibertsitatea

Universidad del País Vasco
Euskal Herriko Unibertsitatea

Department of Analytical Chemistry

Innovative analytical methodologies to characterize original and weathered materials of extraterrestrial origin and terrestrial analogues to meteorites

Report to compete for the International PhD degree

Leticia Gómez Nubla

July 2015

ACKNOWLEDGEMENTS

Leticia Gómez is grateful to the Vice Rectorate for Research of the University of the Basque Country (UPV/EHU) for her predoctoral fellowship (2011-2015).

Moreover, this PhD work has been developed thanks to the funding of various projects;

1.- Soil Health and Chemical Pollution: Development and Application of Technologies for Identification, Diagnosis and Therapy (BERRILUR III) (BERRILUR III, Dpto. de Industria, Comercio y Turismo del Gobierno Vasco, Programa ETORTEK, ref. IE09-242).

2.- Study of material associated with meteorite impact (Acciones Especiales UPV/EHU, ref. AE11/26).

3.- Meteorite and impact products: common processes in the Solar System (Acciones Especiales UPV/EHU, ref. AE13/28).

4.- Research and Innovation in physic and urban environment, natural resources and health (Consolidated Group type A, EJ-GV). Basque Government, ref. IT-742-13).

I would like to acknowledge also Xabier Murelaga (Department of Stratigraphy and Palaeontology, Faculty of Science and Technology (UPV/EHU)), Ainhoa Alonso, Mª Cruz Zuluaga and Luis Angel Ortega (Department of Mineralogy and Petrology, Faculty of Science and Technology

(UPV/EHU)) for the sampling pretreatments, measurements and human support provided.

Furthermore, we would like to acknowledge to the Applied Physics Institute of Johannes Kepler University (JKU), (Linz, Austria) especially to Prof. Johannes Pedarnig for welcoming us in their laboratories in order to acquire knowledge about one of the techniques in this PhD work.

Finally, the technical and human support provided by: the Singular Coupled Multispectroscopy Laboratory (LASPEA) (SGIker), X-Ray Service of Rocks and Minerals Unit from the Research General Services of the UPV/EHU (SGIker), the General Service X-Ray of the University of the Basque Country and SCAB from SGIker of UPV/EHU (UPV/EHU, MINECO, GV/EJ, ERDF and ESF, (SGIker)) is gratefully acknowledged.

Además, me gustaría dar las gracias a mis directores de tesis, Juanma y Silvia, por el apoyo que me han dado siempre, sus consejos, el trabajo y el tiempo que le han dedicado a esta tesis. Juanma, muchas gracias por darme la oportunidad de entrar en este "mundillo", de realizar esta tesis que ha ido enganchándome cada vez más y por confiar en mí. Silvia, muchas gracias por el esfuerzo, dedicación y el haber sabido guiarme en los momentos en los que no veía las cosas demasiado claras. Gracias a los dos por todo lo que he aprendido y haber hecho esto posible.

También me gustaría agradecer a toda la gente del departamento que está en Leioa, profesores, doctores y futuros doctores, la ayuda que me han brindado siempre que lo he necesitado, especialmente gracias a Josean, Arantza, Ainara, Azibar, Julen, Oskar, Mireia y Naiara por vuestra ayuda y los buenos momentos que me habéis hecho pasar en el labo, viajes, cenas, etc.

No me puede faltar dar las gracias a toda la gente de Zamudio, con los que he pasado tantas horas "extraordinarias", de risas y también de desesperación.

Julene a ti en especial, muchísimas gracias por estar ahí siempre, tanto en lo personal como en lo profesional desde el momento en que empezamos. Creo que no me podía haber tocado una mejor compañera. Olivia, gracias por tu ayuda siempre, por esas charlas terapéuticas que hacían que los momentos estresantes que hemos llevado en paralelo fueran más llevaderos. A y gracias a las dos por acompañarme al Cubo, que cualquiera no se planta delante de una cámara jajjja. Nikole, Ane, Marco, Arri y Nagore muchas gracias por vuestra ayuda, apoyo, risas y consejos en estos cuatro años. Sin todos vosotros esto no hubiera sido lo mismo.

Fuera de éste ámbito, muchas gracias a mis amigas de toda la vida, especialmente en este último periodo a Lara, Naiara y Eli por vuestro apoyo, palabras de ánimo, momentos "run for fun" y por la súper portada de tesis que te has currado Eli, supongo que con ayuda de Sandro ;).

Finalmente agradecer a mi familia, sobre todo a mis padres el apoyo incondicional y los buenos y positivos consejos que me habéis dado, a Guiller, Paula y Niko por vuestras palabras de ánimo y toques de humor referentes a la tesis cuando era necesario, y a Mikel, gracias por todo tu apoyo, la santa paciencia, tu comprensión y tus palabras de ánimo, creo que tu también te doctoras conmigo.

¡Muchas gracias a todos!

"Sólo una cosa vuelve un sueño imposible: el miedo a fracasar"
Paulo Coelho

INDEX

Preface **1**

1 Impact Glasses 4

2 Terrestrial analogs 5

3 Development of Analytical Procedures 7

4 The Experimental and Ethical aspects 8

Chapter 1: Introduction **11**

1.1 Libyan Desert Glass (LDG) 15

1.2 Darwin Glass (DG) 22

1.3 Steel Slag 26

Chapter 2: Objectives **35**

Chapter 3: Materials and methods **39**

3.1 Samples and sampling procedure 39

3.1.1 Libyan Desert Glasses (LDG) 39

3.1.2 Darwin Glasses (DG) 40

3.1.3 Steel slag collected in steel factories and in civil constructions 40

3.1.4 Steel slag collected in forest tracks 42

3.2 Pretreatment of the samples 43

3.2.1 Thick and thin sections preparations 43

3.2.2 Grinding and weighing of samples 44

3.3 Qualitative and quantitative analysis 45

3.3.1 Microscopic and elemental characterization 45

3.3.2 Molecular characterization 49

3.3.3 Elemental quantification by Laser-Induced Breakdown Spectroscopy (LIBS) 56

3.3.4 Terrestrial weathering analysis by leaching tests 57

3.3.5 Characterization of organic compounds 63

3.4 Chemometrics and statistics 66

3.5 Chemical and thermodynamic modeling 66

Chapter 4: Elemental and molecular characterization of the materials **69**

A. *Characterization of Libyan Desert Glass (LDG)* 71

A.1. External Characterization 71

1. Elemental Results 72

1.1 Micro-Energy Dispersive X-Ray Fluorescence Spectroscopy (μ-EDXRF) 72

2. Molecular Results 74

2.1 Raman Spectroscopy 74

2.2 X-Ray Diffraction (XRD) 86

3. Discussion 86

A.2. Internal Characterization 87

1. Inner matrix of the LDGs 89

2. Dark and brownish glassy inclusions in the inner part of the LDG 96

3. Cavities and Embedded bubbles 107

4. Pyrolysis - Gas Chromatography Mass Spectrometry (Py-GC-MS) 112

5. Discussion 114

B. *Characterization of Darwin Glasses (DG)* 117

1. Elemental Results 118

1.1 Energy Dispersive X-Ray Fluorescence Spectroscopy (EDXRF) 118

1.2 Scanning Electron Microscopy/Energy Dispersive X-Ray Spectroscopy (SEM-EDX) 119

1.3 Electron Probe Micro Analysis (EPMA) 121

2. Molecular Results 122

2.1 Raman Spectroscopy 122

2.2 X-Ray Diffraction (XRD) 127

3. Pyrolysis - Gas Chromatography Mass Spectrometry (Py-GC-MS) 127

4. Discussion 131

C. *Characterisation of Electric Arc Furnace (EAF) steel slag* 132

1. Elemental Results 135

1.1 Micro-Energy Dispersive X-Ray Fluorescence Spectroscopy (μ-EDXRF) 135
1.2 X-Ray Photoelectron Spectroscopy (XPS) 138
2. Molecular Results 139
2.1 Raman Spectroscopy 139
2.2 X-Ray Diffraction (XRD) 149
2.3 Structural and Chemical Analyser (SCA) 150
3. Pyrolysis - Gas Chromatography Mass Spectrometry (PY-GC-MS) 155
4. Discussion 155
D. *Black and White steel slag used as filler in forest tracks about 30 years ago* 157
1. Elemental Results 158
1.1 Energy Dispersive X-Ray Fluorescence Spectroscopy (μ-EDXRF) 158
1.1 Scanning Electron Microscopy/Energy Dispersive X-Ray Spectroscopy (SEM-EDX) 159
2. Molecular Results 161
2.1 Raman Spectroscopy 161
2.2 X-Ray Diffraction (XRD) 163
2.3 Scanning Electron Microscopy/Energy Dispersive X-Ray Spectroscopy (SEM-EDX) 164
3. Pyrolysis - Gas Chromatography - Mass Spectrometry (Py-GC-MS) 166
4. Discussion 166
Chapter 5: Laser-Induced Breakdown Spectroscopy (LIBS) application 169
1. Results 175
1.1 Powder pellets 175
1.2 Homogeneity of the powder pellets 176
1.2.1 Scanning Electron Microscopy-Energy Dispersive X-ray Spectroscopy (SEM-EDX) 177

1.2.2 Raman spectroscopy 178
1.3 LIBS analysis of the powder pellets 179
1.4 Analysis of the samples 193
2. Discussion 195
Chapter 6: Weathering processes of the studied materials exposed to the terrestrial atmosphere 199
A. *Electric Arc Furnace (EAF) steel slag* 204
1. Spectroscopic Techniques Results 206
2. Leaching Tests Results 208
2.1. Comparison of leaching tests 210
2.2 Milli-Q water as extractant 211
2.3 Acetic acid as extractant 216
2.4 Nitric-hydrochloric acid as extractant 217
3. Statistical Analysis 218
3. 1 Correlation Analysis (CA) 218
3. 2 Principal Component Analysis (PCA) 221
4. Simulation processes through Chemical Modelling 223
5. Discussion 227
B. *Black and White steel slag used as filler in forest tracks about 18-34 years ago* 230
1. Spectroscopic Techniques Results 231
2. Leaching Tests Results 233
2.1 Milli-Q water as extractant 233
2.2 Acetic acid as extractant 235
2.3 Nitric-hydrochloric acid as extractant 237
3. Rain Water Samples Results 240
4. Statistical Analysis 240
4. 1 Correlation Analysis (CA) 240
5. Discussion 244
C. *Libyan Desert Glass (LDG)* 246
1. Spectroscopic Techniques Results 248
2. Leaching Test Results: Milli-Q water 248

3. Gas Chromatography Mass Spectrometry (SPME-GC-MS and HS-GC-MS) 254
4. Simulation processes through Chemical Modelling 255
5. Discussion 256
D. *Darwin Glasses (DG)* 258
1. Spectroscopic Techniques Results 259
2. Leaching Test Results: Milli-Q water 260
3. Gas Chromatography Mass Spectrometry (SPME-GC-MS and HS-GC-MS) 265
4. Simulation processes through Chemical Modelling 266
5. Discussion 268
Chapter 7: Integrated discussion and conclusions **271**
Chapter 8: Appendices **285**
APPENDIX I. Future works 286
APPENDIX II. Glossary and list of abbreviations 287
APPENDIX III. Tables with concentrations values obtained from the leaching tests 292
APPENDIX IV. Scientific publications 302

PREFACE

In 2001, the US National Research Council, at the request of NASA, initiated a broad review of the current state of solar system exploration, including recommendations for the next decade (http://www.aas.org/~dps/decadal/). This was conducted by constituting formal panels of National Academy members and other prominent scientists. One of such panels was on Terrestrial Analogues to Mars. It is well recognized that interpretations of Mars must begin with the Earth as a reference[1].

One of the conclusions from that panel of experts stated that, "[…] over the next decade, a new phase of Mars study must be started as the era of reconnaissance global mapping is ending and we begin to focus on detailed analysis at the regional to outcrop level". In that sense, recommendations from the Terrestrial Analogues to Mars community panel included: process studies at analog sites, field workshops, instrument and operations tests, and laboratory measurements.

Prediction of capabilities and interpretation of data from future instruments was also considered a critical need[1], optimizing the choice of instruments and their operating parameters through tests in analogue environments on Earth.

The suite of recommended instruments included, among others, high resolution stereo imagers from orbit, lander or microscope, high resolution topography, hyperspectral visible and Near-Infrared imaging, as well as Scanning electron microscopy with Energy Dispersive X-ray spectroscopy (SEM-EDX) together with Infrared (IR), Raman, Mössbauer and Laser-Induced Breakdown Spectroscopy (LIBS).

[1] T.G. Farr, Terrestrial analogs to Mars: the NCR community decadal report, Planetary and Space Science 52 (2004) 3-10.

Laboratory studies were recommended to be focused on spectroscopic measurements and determination of the physical and chemical properties of Mars analogue materials, but also including Mars meteorites. Moreover, such rock and mineral analogues were considered useful for instrument tests as well.

The study of meteorites must take into account the alterations suffered by the different minerals present. There are three levels of alteration on meteorites: (a) alterations due to the high pressures (shock) attained when an asteroid impacted the surface of a body (Mars for example) and dispersed material (meteorites) to the space, (b) alterations due to the thermal (and pressure) impact attained when the meteorite entered through the atmosphere of Earth (formation of fusion crusts) before arriving to the land, and (c) alterations due to the weathering processes when standing in the surface of the Earth. Thus, to extract the proper information about the original mineralogy of a body requires the understanding of all these three alteration mechanisms, including the explanation of the new mineral phases formed from such alterations.

This is a real complex matter that should be afforded from the unequivocal characterization of the major, minor and traces mineral phases, identifying all of the alteration products and developing tools to explain their formation. But it makes no sense to start with the study of meteorites without having developed the required analytical methodologies for both (a) unequivocal characterization of major, minor and trace compounds and (b) assignation to each compound as original or formed after any of the three kinds of alteration processes.

This PhD project is our first attempt to develop new analytical methodologies for the characterization of terrestrial analogues and extraterrestrial materials as well as to develop tools to explain the formation of the different alteration products, thinking always in contributing to the research about Mars, planet which is one of the main research areas of our group. From 2015 on we are officially involved in the Science Groups of (a) the Raman instrument of the Exomars2018 Mission (ESA) and (b) the SuperCam (Raman+LIBS+VisNIR) instrument of the Mars2020 Mission (NASA).

The main approach was to test if the methodologies developed by the research group in past PhD projects could be used to study these new types of sensible

materials. The use of micro-destructive and/or non-destructive spectroscopic techniques, which have been used by us in the field of characterization and diagnosis of the conservation state of Cultural Heritage materials (another kind of very sensible materials), in the study of beachrocks, sediments, soils, etc. was considered from the beginning. In particular, SEM-EDX, Raman spectroscopy and X-Ray Fluorescence (XRF) as well as LIBS were selected for this PhD project based in our previous expertise (Raman and XRF) but also in the suggestions of the recommended instruments for planetary research.

To simplify the problem, in this work we have chosen not real meteorites but terrestrial-extraterrestrial materials transformed after the impact (high thermal and pressure event in seconds) of a low airburst or hypervelocity bolide on Earth: the so-called ***impact glasses***. These materials have also suffered from alteration processes. The same as for the meteorites previously mentioned (c), and besides, the alteration products formed after the impact over the Earth of this extraterrestrial body in contact with terrestrial material which originates the impact glass at high pressures and temperatures.

Furthermore, ***slag from steel production (mainly black but also white)*** was considered in this work. Several studies have connected meteorites or glassy materials (tektites) with slag from the steel production[2-5]. Butler (1977)[2] established that the analyses of some compounds from slag produced in blast furnaces could be matched almost exactly with analyses from a meteorite, since there could be a closer analogy to the formation conditions of the blast furnace slag. Martinez-Frias et al. (2004)[3] and Garcia-Guinea et al. (2010)[6] affirmed that there could be confusion among beginners between meteorites and natural or artificial terrestrial rocks because of their external aspect[6] and in addition, a lot of minerals found in meteorites can be artificially

[2] B. C. M. Butler, Al-rich pyroxene and melilite in a blast-furnace slag and a comparison with the Allende meteorite, Mineralogical Magazine 41 (1977) 493-499.
[3] J Martínez-Frías, R. Benito, A. Delgado, J.A. Rodriguez-Losada, Meteoritos *versus* rocas terrestres: el pseudo meteorito de Getafe, Macla 2 (2004) 55-56.
[4] C. Wert, M. Weller, Internal friction of the glassy tektites, Journal of Alloys and Compounds 310 (2000) 54–58.
[5] J. Kempl, P.Z. Vroon, E. Zinngrebe, W. van Westrenen, Si isotope fractionation between Si-poor metal and silicate melt at pressure–temperature conditions relevant to metal segregation in small planetary bodies, Earth and Planetary Science Letters 368 (2013) 61–68.
[6] J.Garcia-Guinea, V. Correcher, L. Recio-Vazquez,E.Crespo-Feo, R. Gonzalez-Martin, L. Tormo, Influence of accumulation of heaps of steel slag on the environment: determination of heavy metals content in the soils, Annals of the Brazilian Academy of Sciences 82 (2010) 267-277.

generated in industrial furnaces, becoming the main components of the slag and ceramic materials of high technology[7]. This was the case of the Getafe-rock, a fall event occurred in 1994 (the 1.5 kg rock impacted on a car when it was running at 100 km/h in the Spanish N-IV road) that was classified after years of research in the Meteoretical Bulletin as a 'pseudometeorite', as it was similar characteristic to industrial EAF slag[8]. Detailed information about the Getafe pseudometeorite can be found in http://tierra.rediris.es/merge/getafe.html .

Impact glasses and slag materials have helped us to perform a complete spectroscopic characterization to identify original and altered compounds and to develop methodologies to understand the weathering processes due to chemical reactivity among original compounds and chemicals belonging to the environment surrounding the materials. The used materials in this work and experimental procedures are briefly described to introduce the topic.

1 IMPACT GLASSES

Impact glasses are natural rich silica-melts produced by impact events of a meteorite, asteroid or comet on any geographic area on the Earth. Such materials have been formed or modified by the hypervelocity of a single extraterrestrial rock impact, probably at pressures higher than 20 GPa, during the initial stages of meteorite crater formation current or past[9]. Impact melt composition depends on target lithology, so target rock composition plays an important role on the characteristics of the impact product.

These impact products are thrown away from the impact site (crater) from meters to kilometers (even more than 200 km) and they are usually named with the location of their origin. In the present work, two different types of impact glasses from the

[7] J Martínez-Frías, R. Benito, A. Delgado, J.A. Rodriguez-Losada, Meteoritos *versus* rocas terrestres: el pseudo meteorito de Getafe, Macla 2 (2004) 55-56.
[8] J. Martinez-Frias, A. Weigel, K. Marti, T. Boyd, G.H. Wilson, T. Jull, The Getafe rock: Fall, composition and cosmic ray records of an unusual ultrarefractory scoriaceous material, Revista de Metalurgia 35 (1999) 308-315.
[9] M.J. Bailey, K.T. Howard, K.J. Kirkby, C. Jeynes, Characterisation of inhomogeneous inclusions in Darwin glass using ion beam analysis, Nuclear Instruments and Methods in Physics Research, *Sect. B*. 267 (2009) 2219-2224.

Meteorites Collection of the Basque Country University (UPV/EHU) were considered: Libyan Desert Glass or LDGs, and Darwin Glass or DGs.

Libyan Desert Glass fragments are scattered in the Western Desert of Egypt (near the Libyan border) in the soils' surfaces lying in interdune channels, and they are commonly small irregular pieces with yellow to whitish translucent color together with brownish inclusions that are estimated to be 28.5 million years old[10].

The other interesting type of impact melt, Darwin glass, is located on the West coast of Tasmania (Australia). It was dated using the $^{40}Ar/^{39}Ar$ single-grain laser fusion technique, yielding isochron ages of 796-815 millions years old with an overall weighted mean of 816 ± 7 million years old[11].

2 TERRESTRIAL ANALOGUES

Terrestrial analogues are defined as environments on Earth that present one or more geological or environmental conditions similar to those found on a given extraterrestrial body (Moon, Mars, etc.), either current or past[12] . Their characterization has been an integral part of comparative planetary science, space exploration and astrobiology for over a half-century[13]. Today, analogue studies continue to be important for understanding data from space missions, and also for planning strategies, developing and testing hardware, selecting targets for future missions, etc., and will continue to be an essential component of planetary science and exploration for the years to come[13].

In this PhD work we selected black (and white) slag from Electric Arc Furnace production of steel (EAF slag), thinking of them as terrestrial analogues to meteorites. But they were likewise used to compare their analysis with our impact glasses. Slags have been artificially formed after a high temperature industrial

[10] J.A. Barrat, B.M. Jahn, J. Amossé , R. Rocchia, F. Keller, G.R. Poupeau, E. Diemer, Geochemistry and origin of Libyan Desert glasses, Geochimica Cosmochimica Acta 61 (1997) 1953–1959.
[11] C.H. Lo, K.T. Howard, S.L. Chung, S. Meffre, Laser fusion argon-40/argon-39 ages of Darwin impact glass, Metoritics and Planetary Science 37 (2002) 1555-1562.
[12] G.R. Osinski, R. Léviellé, A. Berinstain, M. Lebeuf, M. Bamsey, Terrestrial analogues to Mars and the Moon: Canada's role, Geoscience Caada 33 (2006) 175-188
[13] R. Léveillé, A half-century of terrestrial analog studies: from craters on the Moon to searching for life in Mars, Planetary and Space Science 58 (2010) 631-638.

process, and have mineral phases such as Si and Ca-rich phases together with high concentration of metals such as Fe, Mg, Cr, Mn, S, etc.

Several types of slag from different producers/locations of the Basque Country (Spain) and Belgium have been studied. Some of them were collected directly from different steel industries (common steel, special steel and stain less steel factories), either after their dumping from the furnaces or after their short term treatment (water washing, iron removing, etc.). Others were sampled from (a) different construction works few weeks after their deposition and (b) different points along forest tracks in where the slag materials were deposited and used as filler under a few centimeters of the soil more than fifteen years ago.

The great variety of slag samples, including the widespread time elapsed after production and before sampling, gave us a real scenario that provided information about the characteristic of the different kinds of slag and their evolution with the time, having alteration products due to weathering.

We expected to find not only the artificially formed compounds at high temperatures in the steel production process, when studying the samples obtained directly from the dumping of the furnaces, but also the initially transformed products due to the wash treatments (hydration of oxides and other compounds) and stand alone to the open air (CO_2 capture due to their alkalinity). Moreover, we expect to find alteration compounds due to natural weathering of the samples having more than 15 years of deposition in the environment.

This situation about the slag materials was considered to be similar to the impact glasses regarding both their high formation temperatures and the natural weathering once they were deposited over the Earth surface.

3 DEVELOPMENT OF ANALYTICAL PROCEDURES

Among the recommended instruments for future missions on Mars surface, our research group has expertise in the application of SEM-EDX, Raman Spectroscopy and XRF to study other kind of sensible materials like those belonging to Cultural

Heritage[14]. Confocal Raman microscopy was used to study vertical profiles of layered samples like blackish red paint layers[15] and brown bio-patinas over pigments[16] in Pompeian wall paintings. Raman micro-imaging was also used to characterize the vertical profile (from outside to inside) of degraded medieval mural paintings[17] or metal impacted facades of buildings[18]. Moreover, the University of the Basque Country has since 2012 a unique instrument SCA (Structural and Chemical Analyzer), that combines Raman microscopy and SEM-EDX microscopy in the same spot, that has been used to study metal-rich particulate matter samples[19]. All these Raman set ups, combined with XRF and SEM-EDX microscopy will be used to develop new analytical procedures to characterize the EAF slag and impact glasses.

Our research group brought a LIBS instrument in 2013 that started in operation in the middle of 2014. To gain expertise in the use of such instrument, a stage was planed at the Christian Doppler Laboratory for Laser-Assisted Diagnostics (LAD), Institute of Applied Physics, Johannes Kepler University (Linz, Austria), from 24/03/2014 until 27/06/2014, in the group headed by Dr. Pedarnig. After my return, I started the development of a calibration procedure to quantify the elemental concentrations in the studied EAF slag and impact glass materials.

The effect of weathering has been largely studied by our research group on Cultural Heritage assets impacted by natural and anthropic environments. Here, besides, a leaching optimized procedure with Focused Ultrasound Energy that simulates

[14] J.M. Madariaga, K. Castro, I. Martinez-Arkarazo, M.A. Olazabal, G. Arana, M. Maguregui, S. Fdez-Ortiz de Vallejuelo, Diagnóstico de Impactos Ambientales sobre el Patrimonio Cultural (Histórico, Artístico y Natural) mediante análisis in-situ, observaciones micro-espectroscópicas y modelado químico, en Ciencia y Tecnología para la Conservación del Patrimonio Cultural (M.A. Rogerio y C. Saiz-Jimenez eds.), 39-42, Instituto de Recursos Naturales y Agrobiología de Sevilla, CSIC, Sevilla, 2011.

[15] M. Maguregui, U. Knuutinen, I. Martínez-Arkarazo, K. Castro, J.M. Madariaga, Thermodynamic and Spectroscopic Speciation to Explain the Blackening Process of Hematite Formed by Atmospheric SO2 Impact: The Case of Marcus Lucretius House (Pompeii), Analytical Chemistry 83 (2011) 3319-3326.

[16] M. Maguregui, U. Knuutinen, J. Trebolazabala, H. Morillas, K. Castro, I. Martínez-Arkarazo, J.M. Madariaga, Use of in situ and confocal Raman spectroscopy to study the nature and distribution of carotenoids in brown patinas from a deteriorated wall painting in Marcus Lucretius House (Pompeii), Analytical and Bioanalytical Chemistry 402 (2012) 1529-1539.

[17] M. Irazola, M. Olivares, K. Castro, M. Maguregui, I. Martínez-Arkarazo, J.M. Madariaga, In situ Raman spectroscopy analysis combined with Raman and SEM-EDS imaging to assess the conservation state of 16th century wall paintings, Journal of Raman Spectroscopy 43 (2012) 1676-1684.

[18] N. Prieto-Taboada, O. Gomez-Laserna, I. Martinez-Arkarazo, M.A. Olazabal, J.M. Madariaga, Relevance of Cross-Section Analysis in correct Diagnosis of the State of Conservation of Building Materials as evidenced by spectroscopic Imaging, Analytical and Bioanalytical Chemistry 85 (2013) 9501-9507.

[19] N. Goienaga, A. Sarmiento, M. Olivares, J.A. Carrero, L.A. Fernandez, J.M. Madariaga, Emerging Application of a Structural and Chemical Analyzer for the Complete Characterization of Metal-Rich Particulate Matter, Analytical Chemistry 85 (2013) 7173-7181.

extreme leaching processes over others solid silicate materials developed by the group[20] could be used together with chemometric[21], chemical simulations[22] or both data treatments[23] to explain the formation of weathered compounds from the chemical interactions (chemical reactivity) of the original mineral phases with the surrounding chemicals from natural and anthropogenic origin.

This integrated methodology will be used to understand the weathering processes affecting to the Electric Arc Furnace (EAF) slag materials as well as to the millenary impact glasses leaving in the environment.

4 THE EXPERIMENTAL AND ETHICAL ASPECTS

In the development of this PhD project, the expertise of our research group in the study of sensitive Cultural Heritage materials has been of great importance when the experiments were designed and executed. It should be noted that as part of our geological heritage, the study of extraterrestrial and terrestrial analogue materials must be conducted following the rules of Geoethics[24]. Since 2010, Geoethics has been considered a fundamental subject in the context of the activities of the IUGS (International Union of Geological Societies) Commission on Geoscience Education, Training and Technology Transfer. The "International Declaration of Geoethics" was promulgated in Pribram in 2011, and the "International Association for Geoethics (IAGETH)" was established in August 2012.

In accordance with the IAGETH, "Geoethics is an interdisciplinary field, which involves Earth and Planetary Sciences as well as applied ethics, regarding the study of the abiotic world (geoeducation, natural hazards, geo-mining, engineering geology,

[20] S. Fdez-Ortiz de Vallejuelo, A. Barrena, G. Arana, A. de Diego, J. M. Madariaga, Ultrasound energy focused in a glass probe: An approach to the simultaneous and fast extraction of trace elements from sediments, Talanta 80 (2009) 434-439.
[21] I. Martínez-Arkarazo, M. Angulo, L. Bartolomé, N. Etxebarria, M.A. Olazabal, J.M. Madariaga, An integrated analytical approach to diagnose the conservation state of building materials of a palace house in the metropolitan Bilbao (Basque Country, North of Spain), Analytica Chimica Acta 584 (2007) 350–359.
[22] K. Castro, A Sarmiento, I. Martinez-Arkarazo, J.M. Madariaga, L.A. Fernandez, Green Copper Pigments Biodegradation in Cultural Heritage: From Malachite to Moolooite, Thermodynamic Modeling, X-ray Fluorescence and Raman Evidence, Analytical Chemistry 80 (2008) 4103–4110.
[23] N. Prieto-Taboada, M. Maguregui, I. Martinez-Arkarazo, M.A. Olazabal, G. Arana, J.M. Madariaga, Spectroscopic evaluation of the environmental impact on black crusted modern mortars in urban–industrial areas, Analytical and Bioanalytical Chemistry 399 (2011) 2949–2959.
[24] J. Martinez-Frias, J.L. González, F. Rull, Geoethics and Deontology: From fundamentals to applications in Planetary Protection. Episodes 34 (2011) 257-262.

communication, geoconservation, etc). These interactions linking scientific, societal and cultural aspects, consider our planet as a system and as a model. In addition, the necessity of taking into account appropriate protocols, scientific integrity issues and a code of good practice –regarding the study of the abiotic world– is covered by this discipline. Planetary geology and astrobiology also require a geoethical approach".

CHAPTER 1

INTRODUCTION

The Solar System formed from a dusty molecular cloud 4.56 billion years ago. During its first ages, the condensation of materials resulted in the formation of solids that hereafter accreted to form planet embryos. These solids have accreted ices, organic grains and silicate particles recording the signature of the processes occurring during the birth of the Solar System[1]. Our solar system comprises 9 major planets, a number of minor planets, or asteroids, and a multitude of comets[2]. It is thought that environments similar to early Earth can exist or have once existed elsewhere in our Solar system. Therefore, it would be possible that life has evolved on other planets[3].

Mars is viewed as the most likely planet to have once supported life. This is mainly due to its reasonable distance from the Sun and the planet's similar geological history to Earth. Both had high rates of meteoric impact, volcanism, an abundance of liquid water and an atmosphere that contained N_2, H_2 and CO_2. Given that these conditions developed organisms on Earth, it seems reasonable that also Mars could have once supported life. One major difference between the two planets is the smaller size of Mars. This would have caused Mars to cool faster than the Earth, meaning that life could actually have developed sooner than it did on Earth[4].

[1] L. Remusat, Organic material in meteorites and the link to the origin of life, BIO Web of Conferences Sciences 2 (2014) 03001.
[2] E.L. Krinov, Principles of Meteoritics: International Series of Monographs on Earth Sciences, Textbook Publishers, 2003.
[3] A. Imhemed Alajtal, Raman Spectroscopic Application for the Analysis of Organic Compounds and Minerals of Astrobiological Significance, PhD thesis, University of Bradford (UK), 2010.
[4] A. Imhemed Alajtal, Raman Spectroscopic Application for the Analysis of Organic Compounds and Minerals of Astrobiological Significance, PhD thesis, University of Bradford (UK), 2010.

The Mars exploration, with the correspond need to interpret data accessed by rovers in that extraterrestrial environment, have provoked the study of terrestrial analogues materials, such as rock and mineral analogues, but also to consider Mars meteorites as highly interesting materials to this purpose.

Scattered throughout interplanetary space, there are minor or meteoric bodies, which varies enormously in dimensions. Larger meteoric bodies cause the appearance of fire balls which speed across the sky with great brightness. Some of these bolides may fall upon the Earth in the form of stony or iron masses, and they would be the remnants of meteoric bodies which were not completely destroyed in the atmosphere. They are called *meteorites*[5].

In this work we have not considered the study of meteorites because we considered first to go with simpler materials due to our small knowledge in the study of extraterrestrial ones. To simplify the work, terrestrial-extraterrestrial materials like *impact glasses,* namely Libyan Desert Glasses (LDGs) and Darwin Glasses (DGs), have been chosen. Those materials are similar to meteorites (both are formed after an impact) but the terrestrial-extraterrestrial glasses have not the alteration products in the fusion crust due to the atmosphere entry step of the meteorites.

The hypervelocity impact of extraterrestrial bodies, meteorite, comet or asteroid, can form those *impact glasses* at the impact site on the Earth surface; even the formation of impact glasses can occur on the Moon, Mars or any other rocky planetary object having silicates in their surfaces. The assignation of such glasses, in the Earth, to an hypervelocity impact sometimes is not so evident due the tectonic activity and surface processes which tend to erase impact structures from the geological record[6,7].

In the case of impact glass formation on the Earth surface, very high temperatures (>1000 K) and extremely high pressure conditions (>20 or even >40 GPa) are reached, heating and cooling very quickly (K/s) the target material. Thus, part of the vaporized

[5] E.L. Krinov, Principles of Meteoritics: International Series of Monographs on Earth Sciences, Textbook Publishers, 2003.
[6] G. R. Osinski, J. Kieniewicz, J. R. Smith, M.B. E. Boslough, M. Eccleston, H. P. Schwarcz, M. R. Kleindienst, A. F. C. Haldemann, C. S. Churcher, The Dakhleh Glass: Product of an impact airburst or cratering event in the Western Desert of Egypt?, Meteoritics and Planetary Science 43 (2008) 2089-2107.
[7] K. Heide, G. Heide, Vitreous state in nature-Origin and properties, Chemie der Erde 71 (2011) 305–335.

and molten target solidifies as a glass[8,9]. It is noteworthy that these conditions exceed the stress levels (≈1 GPa) experienced by terrestrial rocks undergo normal elastic and plastic deformation[10].

In addition, the formation of the impact glass is either just at the impact crater or transformed when scattered over large areas. These glasses have been discovered at different regions of the Earth, where a possible crater has been identified[11]. For instance, Aouelloul impact glass in the Adrar region, Western Sahara Desert (Mauritania, Africa), Lonar impact glasses in Buldana District (Maharashtra, India), Zhamanshin impact glasses in Kazakhstan (Asia), Libyan Desert Glass in the Great Sand Sea (Egypt, Africa), Darwin Glasses in Tasmania (Auntralia), etc.[12-15]. Hence, the impact glass composition will depend mainly on the target lithology of those areas where it has been formed[16], and besides, it will include some features of the projectile[17]. Only a very small amount of the finely dispersed meteoritic melt or vapor is mixed with a much larger quantity of target rock vapor and melt. In most cases, the contribution of extraterrestrial matter to this is very small, mostly less than 1% by weight, leading to only slight chemical changes in the resulting glasses[18]. Therefore, in order to discern between the Earth and extraterrestrial materials, elements that only have high abundances in meteorites and low in terrestrial rocks have been used:

[8] M.J. Bailey, K.T. Howard, K.J. Kirkby, C. Jeynes, Characterisation of inhomogeneous inclusions in Darwin glass using ion beam analysis, Nuclear Instruments and Methods in Physics Research *Sect. B*. 267 (2009) 2219-2224.

[9] K. Heide, G. Heide, Vitreous state in nature-Origin and properties, Chemie der Erde 71 (2011) 305–335.

[10] K.T. Howard, Volatile enhanced dispersal of high velocity impact melts and the origin of tektites, Proceedings of the Geologists' Association 122 (2011) 363–382.

[11] A. Gucsik, C. Koeberl, F. Brandstätter, W.U. Reimold, E. Libowitzky, Cathodoluminescence, electron microscopy, and Raman spectroscopy of experimentally shock-metamorphosed zircon, Earth and Planetary Science Letters 202 (2002) 495-509.

[12] A. Gucsik, C. Koeberl, F. Brandstätter, E. Libowitzky, M. Zhang, Infrared, Raman, and cathodoluminescence studies of impact glasses, Meteoritics and Planetary Science 39 (2004) 1273-1285.

[13] S. Osae, S. Misra, C. Koeberl, D. Sengupta, S. Ghosh, Target rocks, impact glasses, and melt rocks from the Lonar impact crater, India: Petrography and geochemistry. Meteoritics and Planetary Science 40 (2005) 1473-1492.

[14] C. Koeberl, K. Fredriksson, Impact glasses from Zhamanshin crater (U.S.S.R.): chemical composition and discussion of origin, Earth and Planetary Science Letters 78 (1986) 80-88.

[15] K.T. Howard, Geochemistry of Darwin glass and target rocks from Darwin crater, Tasmania, Australia, Meteoritics and Planetary Science 43 (2008) 479–496.

[16] G. R. Osinski, R. A. F. Grieve, G. S. Collins, C. Marion, P. Sylvester, The effect of target lithology on the products of impact melting, Meteoritics and Planetary Science 43 (2008) 1939–1954.

[17] L. Ackerman, K.Žák, Š. Jonášová, J. Ďurišová, R. Skála, T. Magna, A. Deutsch, Highly siderophile element geochemistry of impact-related glasses and target rocks from the Zhamanshin impact structure, Kazakhstan, 46th Lunar and Planetary Science Conference (2015) #1963.

[18] C. Koeberl, A. Shukolyukov, G. W. Lugmair, Chromium isotopic studies of terrestrial impact craters: Identification of meteoritic components at Bosumtwi, Clearwater East, Lappajärvi, and Rochechouart, Earth and Planetary Science Letters 256 (2007) 534-546.

siderophile elements (Au, Co, Cr, Fe, Ir, Mn, Mo, Ni, Os, Pd, Pt, Re, Rh and Ru) coupled with $^{187}Os/^{188}Os$ isotopic composition[19,20], since osmium isotopic compositions are not likely to be altered during meteorite impact[21].

In general, these impact materials are commonly irregular bodies with textures that vary from dense to vesicular and slaggy, some contain mineral rock inclusions, and colors varied from blackish to pale green[22].

Apart from studying those compounds with material not entirely of terrestrial origin, since they contain an extraterrestrial part, this PhD work has contemplated to analyze artificially synthesized compound, produced at high temperatures as well and normal pressure: the steel slag coming from steelmaking industry. As it has been mentioned in the Preface, in this work steel slag is considered a terrestrial analogue to meteorites for the mineral composition, appearance and high temperature formation of both of them.

Moreover, steel slag was used to compare their analysis with our impact glasses. Thus, it was created a connection between terrestrial and extraterrestrial material and it was used to evaluate analytical instrumentation that will constitute future exploratory missions to the Martian surface.

The description of the LDG, DG and steel slag formation and materials is described below.

[19] C. Koeberl, A. Shukolyukov, G. W. Lugmair, Chromium isotopic studies of terrestrial impact craters: Identification of meteoritic components at Bosumtwi, Clearwater East, Lappajärvi, and Rochechouart, Earth and Planetary Science Letters 256 (2007) 534-546.
[20] L. Ackerman, K.Žák, Š. Jonášová, J. Ďurišová, R. Skála, T. Magna, A. Deutsch, Highly siderophile element geochemistry of impact-related glasses and target rocks from the Zhamanshin impact structure, Kazakhstan, 46th Lunar and Planetary Science Conference (2015) #1963.
[21] C. Koeberl, S.B. Shirey, Detection of a Meteoritic Component in Ivory Coast Tektites with Rhenium-Osmium Isotopes, Science 261 (1993) 595-598.
[22] A. Gucsik, C. Koeberl, F. Brandstätter, W.U. Reimold, E. Libowitzky, Cathodoluminescence, electron microscopy, and Raman spectroscopy of experimentally shock-metamorphosed zircon, Earth and Planetary Science Letters 202 (2002) 495-509.

1.1 LIBYAN DESERT GLASS (LDG)

Libyan Desert Glass (LDG) is a mysterious impact glass that was firstly documented by Patrick A. Clayton in 1933[23]. However, there are abundant evidences to show that LDG was used by prehistoric men to make various artefact, as it can be seen in the finding of an ancient manufacture site in the Great Sand Sea, and also in dynastic times, as raw material to carve the scarab-shaped central motif in one Tutankhamon's pectorals[24].

Since Clayton and Spencer first published a scientific report on LDG, which led to its official discovery, many field expeditions have been performed and more than $2 \cdot 10^5$ kg of LDG have been found. These materials are scattered over an area of 6500 km^2, along wide corridors between the sand dunes of the southwestern corner of the Great Sand Sea (South West of Egypt, near the Libyan border) and the Gilf Kebir Plateau[25,26] (see Fig. 1.1).

[23] P.A. Clayton, L.J. Spencer, Silica-glass from the Libyan desert, Mineralogical Magazine 23 (1934) 501-508.
[24] C. Cipriani, M. Corazza, G. Giuli, V. M. Cecchi, G. Pratesi, P. Rossi, E. Vittone, Ion beam study of a possible extraterrestrial body signature in Libyan desert glass, Nuclear Instruments and Methods in Physics Research Section B: Beam Interactions with Materials and Atoms 170 (2000) 187-192.
[25] M. Swaenen, E.A. Stefaniak, R. Frost, A. Worobiec, R.Van Grieken, Investigation of inclusions trapped inside Libyan desert glass by Raman microscopy, Analytical and Bioanalytical Chemistry 397 (2010) 2659-2665.
[26] J.A. Barrat, B.M. Jahn, J. Amosse, R. Rocchia, F. Keller, G.R. Poupeau, E. Diemer, Geochemistry and origin of Libyan Desert glasses, Geochimica et Cosmochimica Acta 61 (1997) 1953-1959.

Fig.1.1. Map locating of the southwestern Egyptian desert and details of Geological sketch of the area. The rectangle of dashed white lines together in the south and west borders of Egypt indicates the area where LDGs had been found. Red pins indicate craters of that area. * Silica, quartz matrix; *Cretaceus sandstone, "Nubia" Formation cropout; * Sand dunes, sabkhas, cultivated Nile deposits, wadi and playa deposits, beach and corals, calcarenite bars (Quaternary); * Clastics, phosphate and carbonate rocks (Cretaceous); * Marine and fluviomarine beds, clastics (Jurassic); * Mostly clastic rocks (Paleozoic).

That area has sandstones of the Cretaceous Nubia Formation cropout. It was suggested that, the glass precursor material could have existed on or near a surface which was stratigraphically about 400 m higher than the present ground surface, or it is possible that the glass was formed from another silica-rich rock formation within the whole of the Great Sand Sea area as well[27]. Similarities between sandstones and the LDG composition clarify the fusion of the ground material. But the lytologic variation of these sandstones make difficult to identify them as the origin of LDGs[28,29].Excavation works indicated that LDG were found to a depth of ~ 2 m[30].

[27] T. Aboud, Libyan Desert Glass: has the enigma of its origin been resolved? , Physics Procedia 2 (2009) 1425-1432.
[28] A. Greshake, C. Koeberl, J. Fritz, W.U. Reimold, Brownish inclusions and dark streaks in Libyan Desert Glass: Evidence for high-temperature melting of the target rock, Meteoritics and Planetary Science 45 (2010) 973-989.
[29] G. Giuli, E. Paris, G. Pratesi, C. Koeberl, C. Cipriani, Iron oxidation state in the Fe- rich layer and silica matrix of Libyan Desrt Glass: A high- resolution XANES study, Meteoritics and Planetary Science 38 (**2003**) 1181-1186.
[30] T. Aboud, Libyan Desert Glass: has the enigma of its origin been resolved? , Physics Procedia 2 (2009) 1425-1432.

Pieces of silica glass in the form of strongly wind-eroded rounded to irregular fragments having broad ranges of sizes and masses have been found. Some of them reach up to several kilograms in weight. Commonly, the small sized and irregular pieces are found lying on the surface, medium pieces are partially buried and the larger pieces are usually buried. Therefore, the deeper is located, the bigger is the glass, since it is less exposed to the erosion[30]. Regarding the color LDG pieces range from yellow to whitish or translucent color (see Fig.1.2).

Fig.1.2. Images of different LDG samples.

The age of their formation has been estimated to be 28.5 million years old, in the Oligocene[31]. Chemically, LDG is pure silica; actually it is 95.5-99% wt SiO_2[32]. But it is also composed by other compounds, which are sometimes forming bubbles, black or brownish inclusions possibly derived by melting or decomposition of Fe oxides, dark or brown streaks and white cristobalite spherulites. The concentration of impurities is

[31] G. Pratesi, C. Viti, C. Cipriani, M. Mellini, Silicate-Silicate liquid immiscibility and graphite ribbons in Libyan desert glass. Geochimica et Cosmochimica Acta 66 (**2002**) 903-911.
[32] A. Greshake, C. Koeberl, J. Fritz, W.U. Reimold, Brownish inclusions and dark streaks in Libyan Desert Glass: evidence for high-temperature melting of the target rock, Meteoritics and Planetary Science 45 (2010) 973-989.

highly variable. For instance, some samples are free of bubbles and inclusions, being of transparent gemstone quality, while a few have high content of small bubbles, giving them a white and opaque aspect[33-36].

From the time when impact glasses were discovered, 74 scientific publications related to them have been spread. Particularly, in the last 10 years, there have been 15 research documents. With respect to the LDG origin, most of works determine that its genesis is likely due to a high temperature impact of an extraterrestrial body into a sand or sandstone layer causing its fusion and subsequent solidification[36-39]. In fact, it should be pointed out that in the Sahara desert (both in Libya and Algeria) more than 2000 meteorite fragments (including several of lunar and Martian origin) have been recovered during the last ten years[40]. Hence, a meteorite impact could have been the origin. In order to confirm this theory, a crater should be localized in the zone. However, it is evident that the location and confirmation of craters is difficult to resolve because they could be covered by the Great Sand Sea desert or they would be destroyed by erosion[41]. Despite this fact, a very large impact structure in the eastern desert at the border between Libya and Egypt was discovered, the *Kebira* (in Arabic means large) impact crater (see Fig. 1.3).

[33] J.A. Barrat, B.M. Jahn, J. Amosse, R. Rocchia, F. Keller, G.R. Poupeau, E. Diemer, Geochemistry and origin of Libyan Desert glasses, Geochimica et Cosmochimica Acta 61 (1997) 1953-1959.
[34] G. Giuli, E. Paris, G. Pratesi, C. Koeberl, C. Cipriani, Iron oxidation state in the Fe- rich layer and silica matrix of Libyan Desrt Glass: A high- resolution XANES study. Meteoritics and Planetary Science 38 (**2003**) 1181-1186.
[35] M. Swaenen, E.A. Stefaniak, R. Frost, A. Worobiec, R.Van Grieken, Investigation of inclusions trapped inside Libyan Desert Glass by Raman microscopy, Analytical and Bioanalytical Chemistry 397 (2010) 2659-2665.
[36] B. Kleinmann, P.Horn, F. Langehorst, Evidence for shock metamorphism in sandstones from the Libyan Desert Glass strewn field, Metoriritics and Panetary Sciences 36 (2001) 1277-1282.
[37] A. Longinelli, G. Sighinolfi, V. Michele, E. Selmo, δ^{18}O and chemical composition of Libyan Desert Glass, country rocks, and sands: New considerations on target material. Meteoritics and Planetary Science 46 (**2011**) 218–227.
[38] T. Aboud, Libyan Desert Glass: has the enigma of its origin been resolved?, Physics Procedia 2 (2009) 1425-1432.
[39] F. Fröhlich, G. Poupeau, A. Badou, F.X. Le Bourdonnec, Y. Sacquin, S. Dubernet, J.M. Bardintzeff, M. Véran, D.C. Smith, E. Diemer, Libyan Desert Glass: New field and Fourier transform infrared data, Meteoritics and Planetary Science 48 (2013) 2517-2530.
[40] G. Crozaz, M. Wadhwa, The terrestrial alteration of Saharan Shergottites Dar al Gani 476 and 489: A case study of weathering in a hot desert environment, Geochimica et Cosmochimica Acta 65 (2001) 971-977.
[41] J.A. Barrat, B.M. Jahn, J. Amosse, R. Rocchia, F. Keller, G.R. Poupeau, E. Diemer, Geochemistry and origin of Libyan Desert glasses, Geochimica et Cosmochimica Acta 61 (1997) 1953-1959.

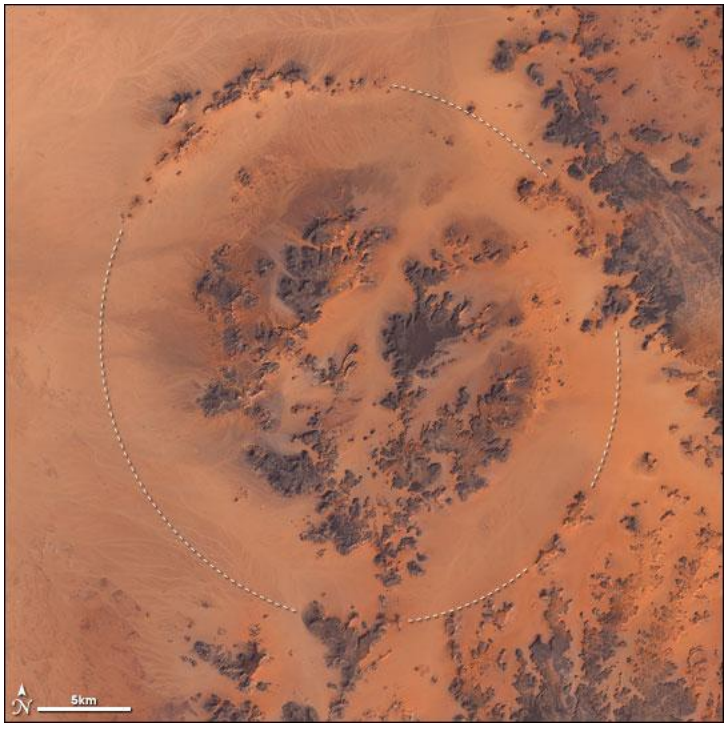

Fig. 1.3. Kebira crater in Libyan Desert. Source: Earth Observatory of NASA[42].

It is the largest impact crater identified in the Sahara with 31 km of diameter[43]. *Kebira* crater existence has been led to the conclusion that could have been created by a meteorite impact, and that the shock of the highly energetic impact would have resulted in melting the quartz-rich sand or sandstone deposits at the impact site yielding to the formation of the LDG[44]. Nevertheless, the study of the crater concluded that the impact probably happened 100 million years ago approximately[42], and the LDG was formed 28.5 million years ago, therefore they would not coincide in time. The Libyan Desert Glasses are younger.

Kebira is the closest impact crater to the area where the LDG were found, but there are others impact structures around that area[45]. In this way, the glasses could have

[42] Earth Observatory of NASA: http://earthobservatory.nasa.gov/IOTD/view.php?id=6351.
[43] W. U. Reimold, C. Koeberl, Impact structures in Africa: A review, Journal of African Earth Sciences 93 (2014) 157–175.
[44] T. Aboud, Libyan Desert Glass: has the enigma of its origin been resolved?, Physics Procedia 2 (2009) 1425-1432.
[45] W. U. Reimold, C. Koeberl, Impact structures in Africa: A review, Journal of African Earth Sciences 93 (2014) 157–175.

been spread from the impact structures during the Oligocene, epoch in which a drainage system dominated the west part of the Egypt Desert[46,47].

Among the confirmed impact structures in Libya and also Egypt, due to the vicinity with the area of the LDG, are *BP*, *Oasis* and *Kamil. BP* and *Oasis* were discovered by petroleum exploration geologists, and their names are due to their respective oil companies. Both occupy the same stratigraphic position in Nubia Sandstone Formation, but the Oasis structure is located about 85 km south of the BP. These structures have been thought to be possibly of the same age as the LDG. Nonetheless, their age are only constrained by the ill defined age of the Nubia Sandstone Formation (90–120 Ma). There is no information to date their crater areas[48]. On the other hand, the *Kamil* crater in southern Egypt is a less than 5000 year old and exceptionally well preserved small impact crater[48]. However, it is too young to be related with the LDG.

As a result of the absence of a nearby corresponding impact crater, it has been generated another hypothesis about the LDG origin by an extraterrestrial body impact. This theory is based on that the melting process could have occurred as a result of a low-altitude explosion of an extraterrestrial body in the atmosphere, generating a thermal pulse (airburst) and causing the melting of surface and nearby silica deposits[49,50] (see Fig.1.4).

[46] M. Ramirez-Carmona, A. El-Barkooky, M. Hamdan. K. Flores-Castro, N.I. Jimenez-Martinez, M. Mendoza-Espinosa International Geological Congress Oslo (2008) PIS-01.
[47] N. Jimenez-Martinez, M. Ramirez, R.Diaz-Hernandez, G. Rodriguez-Gomez, Fluvial Transport Model from Spatial Distribution Analysis of Libyan Desert Glass Mass on the Great Sand Sea (Southwest Egypt): Clues to Primary Glass Distribution, Geosciences 5 (2015) 95-116.
[48] W. U. Reimold, C. Koeberl, Impact structures in Africa: A review, Journal of African Earth Sciences 93 (2014) 157–175.
[49] C. Koeberl, Libyan Desert Glass: formation by meteorite impact or airburst?, CAG 23 2011, Abstract #7.
[50] M. Swaenen, E.A. Stefaniak, R. Frost, A. Worobiec, R.Van Grieken, Investigation of inclusions trapped inside Libyan desert glass by Raman microscopy, Analytical and Bioanalytical Chemistry 397 (2010) 2659-2665.

Fig.1.4. Comet exploding above Egypt. Source: http://www.sci-news.com.

In a low-altitude airburst, surface materials are also affected by both supersonic winds and thermal pulses (up to about 5000 K) and the melted material is blown over a large surface area[51]. In this case, the possibility of a crater-forming event cannot be eliminated. However, once again the crater could have been eroded or buried under sediment[52].

In both impact theories, the impact origin of the LDG is supported by the presence of schlieren structures (flow structure), planar deformation features, partly digested mineral phases, high pressure-temperature mineral phases and non-crystalline (vitreous) phases formed during impact thermal metamorphism. In addition, platinum-group element abundance patterns (Ru, Rh, Pd, Os, Ir and Pb), a reduced state of iron-rich portions, graphite-rich bands in the glasses, iridium content and osmium ($^{187/188}$Os), strontium ($^{87/86}$Sr), argon ($^{40/36}$Ar) and neodymium ($^{143/144}$Nd)

[51] A. Longinelli, G. Sighinolfi, V. Michele, E. Selmo, δ^{18} O and chemical composition of Libyan Desert Glass, country rocks, and sands: New considerations on target material, Meteoritics and Planetary Science 46 (**2011**) 218–227.

[52] M.B.E. Boslough, D.A. Crawford, Low-altitude airbursts and the impact threat, International Journal of Impact Engineering 35 (2008) 1441–1448.

isotopic values have been regarded as fingerprints of primitive meteoritic matter in LDG[53-61].

1.2 DARWIN GLASS (DG)

This impact glass was discovered by aboriginal people in western Tasmania, Australia before its discovery by Europeans in the middle of the 19th century[62].

There are 41 scientific publications about Darwin Glass (DG) so far, and in the last 10 years there have been 8 research documents related to DG. However, despite the lack of conclusive evidence for an impact origin, and a paucity of published information, the source of DG seems to be a buried structure located in a densely forested valley: the Darwin Crater (impact circular structure of 1.2 km in diameter), in the Wild Rivers National Park/Southwest World Heritage Area (Tasmania, Australia)[62-64] (see Fig. 1.5).

[53] P. SChaap, D. Muller-Sohnius, Strontium and neodymium isotopic study of Libyan Desert Glass: Inherited Pan-African age signatures and new evidence for target material, Meteoritics and Planetary Science 37 (2002) 565-576.
[54] J.A. Barrat, B.M. Jahn, J. Amosse, R. Rocchia, F. Keller, G.R. Poupeau, E. Diemer, Geochemistry and origin of Libyan Desert glasses, Geochimica et Cosmochimica Acta 61 (1997) 1953-1959.
[55] G. Giuli, E. Paris, G. Pratesi, C. Koeberl, C. Cipriani, Iron oxidation state in the Fe- rich layer and silica matrix of Libyan Desrt Glass: A high- resolution XANES study, Meteoritics and Planetary Science 38 (**2003**) 1181-1186.
[56] G. Pratesi, C. Viti, C. Cipriani, M. Mellini, Silicate-Silicate liquid immiscibility and graphite ribbons in Libyan desert glass, Geochimica et Cosmochimica Acta 66 (**2002**) 903-911.
[57] M. Ebert, L.Hecht, A. Deutsch, T. Kenkmann, R.Wirth, J.Berndt, Geochemical processes between steel projectiles and silica-rich targets in hypervelocity impact experiments, Geochimica et Cosmochimica Acta, 133 (2014) 257-279.
[58] J. D. Kramers, M. A.G. Andreoli, M.Atanasova, et al. Unique chemistry of a diamond-bearing pebble from the Libyan Desert Glass strewnfield, SW Egypt: Evidence for a shocked comet fragment, Earth and Planetary Science Letters 382 (2013) 21-31.
[59] B. Kleinmann, P.Horn, F. Langehorst, Evidence for shock metamorphism in sandstones from the Libyan Desert Glass strewn field, Metoriritics and Panetary Sciences 36 (2001) 1277-1282.
[60] G. P. Sighinolfi, C. Elmi, R. Serra, G. Contini, High density silica phases as evidence of small-scale hypervelocity impacts: the Gebel Kamil Crater (Egypt), Periodico di Mineralogia 83 (2014) 299-312.
[61] W. U. Reimold, C. Koeberl,Impact structures in Africa: A review, Journal of African Earth Sciences 93 (2014) 157–175.
[62] C.H. Lo, K.T. Howard, S.L. Chung, S. Meffre, Laser-fusion $^{40}Ar/^{39}Ar$ ages of Darwin impact glass, Meteoritics and Planetary Science 37 (2002) 1555-1562.
[63] M.J. Bailey, K.T. Howard, K.J. Kirkby, C. Jeynes, Characterisation of inhomogeneous inclusions in Darwin glass using ion beam analysis, Nuclear Instruments and Methods in Physics Research Sect. B. 267 (2009) 2219-2224.
[64] K. T. Howard et al. Biomass preservation in impact melt ejecta, Nature Geoscience 6 (2013) 1018-1022.

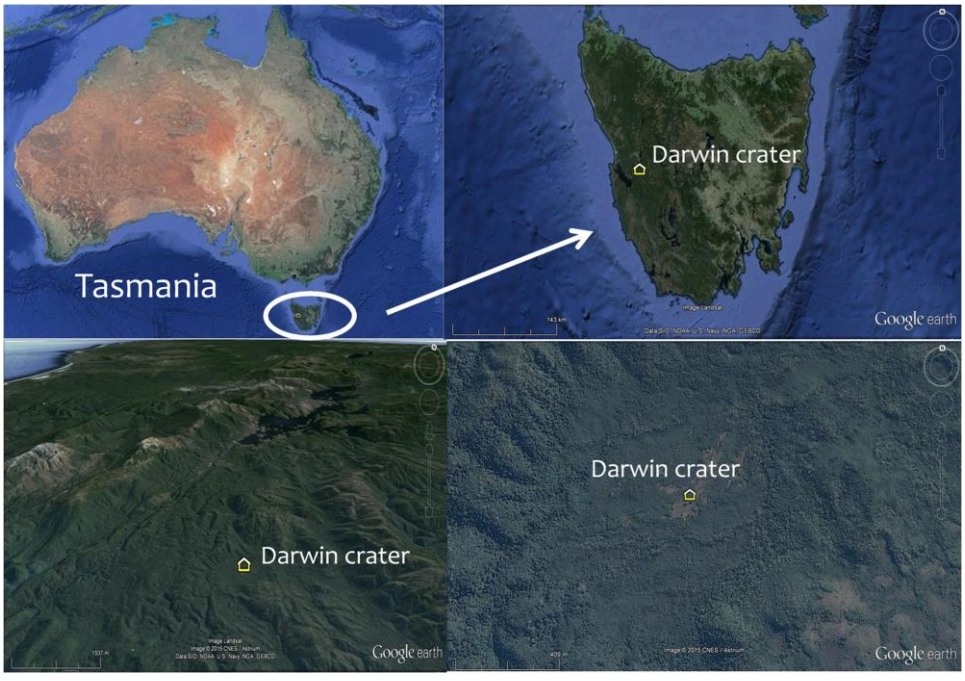

Fig.1.5. Localization of the Darwin Crater in Tasmania (Australia). Source: Google Earth.

In this case, there is an age concordance between DG and glasses found in the Darwin Crater[65], so there is no doubt about the impact origin of DG. According to argon isotope data, they were formed around 816 thousand years ago[66].

Glass fragments were recovered 20 km from the source crater and within a 400 km^2 strewn field. Moreover, the impact hypothesis is supported by the distribution of glasses relative to the Darwin crater, that is, there is a decrease in glass abundance away from the crater[67]. Such widespread distribution is typical of high-velocity impact melt ejecta; in contrast to low-velocity ejecta that tends to remain proximal (<5 crater radius) to the source crater[68]. Furthermore, the idea of a Darwin crater with lacustrine sediments and the presence of swamps infiltrating water at the time of impact is other explanation for the spatial distribution[67].

[65] C.H. Lo, K.T. Howard, S.L. Chung, S. Meffre, Laser-fusion $^{40}Ar/^{39}Ar$ ages of Darwin impact glass, Meteoritics and Planetary Science 37 (2002) 1555-1562.
[66] M.J. Bailey, K.T. Howard, K.J. Kirkby, C. Jeynes, Characterisation of inhomogeneous inclusions in Darwin glass using ion beam analysis, Nuclear Instruments and Methods in Physics Research Sect. B. 267 (2009) 2219-2224.
[67] K.T. Howard, Physical distribution trends in Darwin glass, Meteoritics and Planetary Science 44 (2009) 115-129.
[68] K. T. Howard et al. Biomass preservation in impact melt ejecta, Nature Geoscience 6 (2013) 1018-1022.

There are four color classes encompass the range of variation observed in DG: white; light green; dark green and black (see Fig.1.6). The proportion of white melt is greatest closest to the crater and the proportion of the black melt and splashform increase with distance from the crater. The largest fragments of glass are found closest to the crater. This distribution and the high abundance is sign of the transport of melt products during the impact processes[69].

Fig.1.6. Images of DG samples.

Physically, they are often irregular fragments, twisted masses or chunks up to 10 cm in size. Moreover, DG is generally vesicular and shows flow/layering structures without strain in thin section marked by bands of elliptical bubbles or vesicles[70]. Basically, the glass population can be subdivided on the basis of shape (the majority ~94% are irregular and ropy, and the remainder have either a spheroid, droplet or elongate shape) and colour (53% dark green, 31% light green, 11% black and 5% white)[69].

[69] K.T. Howard, Physical distribution trends in Darwin glass, Meteoritics and Planetary Science 44 (2009) 115-129.
[70] C.H. Lo, K.T. Howard, S.L. Chung, S. Meffre, Laser-fusion $^{40}Ar/^{39}Ar$ ages of Darwin impact glass, Meteoritics & Planetary Science 37 (2002) 1555-1562.

Impact glasses inherit the isotopic and geochemical signals of the source rocks melted during their formation. The target rocks at Darwin crater are quartzites and slates (Siluro Devonian, Eldon Group (along Eldon Rivers))[71]. Chemical composition and REE (Rare Earth Elements) patterns indicate DG consists of a number of major and trace elements originating from upper crustal sediments, such as argillaceous sandstones (quartz grains with clay minerals). There is compatibility of the suspected target rocks at Darwin crater and the materials melted under impact conditions to form DG[71-73].

From the geochemical point of view, there are two groups of glasses. The first group is composed of: SiO_2 (85%), Al_2O_3 (7.3%), TiO_2 (0.05%), FeO (2.2%), MgO (0.9%), and K_2O (1.8%). The second group has lower average SiO_2 (81.1%) and higher average Al_2O_3 (8.2%), FeO (1.5%) and MgO (1.3%) abundances[74].

All studies of Darwin Glass indicate a terrestrial origin after a meteorite impact[73,75]. This argument was also supported by argon and oxygen isotope data and the discovery of coesite within the glass, a high pressure mineral phase[76]. Moreover, the impact is also suggested by the degree of shattering and plastic deformation of the clasts, not observed in rocks in the surrounding region[71]. In addition, the Cr, Ni and Co content (considerably higher than in target rocks) in the DG could imply an extraterrestrial body contribution[75].

[71] K.T. Howard, P.W. Haines, The geology of Darwin Crater, western Tasmania, Australia, Earth and Planetary Science Letter 260 (2007) 328-339.
[72] J. Matsuda, H. Yajima, Noble Gases in Darwin Glass: Anomalous Neon Enrichment, Lunar and Planetary Science conferences 20th (1989) 628-629 #1319.
[73] K.T. Howard, Geochemistry of Darwin glass and target rocks from Darwin crater, Tasmania, Australia, Meteoritics and Planetary Science 43 (2008) 479-496.
[74] K.T. Howard, Physical distribution trends in Darwin glass, Meteoritics and Planetary Science 44 (2009) 115-129.
[75] T. Meisel, C. Koeberl, R.J. Ford, Geochemistry of Darwin impact glass and target rocks, Geochimica et Cosmochimica Acta 54 (1990) 1463-1474.
[76] C.H. Lo, K.T. Howard, S.L. Chung, S. Meffre, Laser-fusion $^{40}Ar/^{39}Ar$ ages of Darwin impact glass, Meteoritics and Planetary Science 37 (2002) 1555-1562.

1.3 STEEL SLAG

Slag is a "waste material produced when coal is dug from the ground, or a substance produced by mixing chemicals with metal that has been heated until it is liquid in order to remove unwanted substances from it" [77].

Steel is a key industrial product whose industry has always had importance for the economy. It can be defined as an alloy of iron and small amounts of carbon with others elements[78]. During its history it has been generated in different kinds of process: Bessemer steel production, Open Hearth production, Basic Oxygen Furnace (BOF) production and Electric Arc Furnace (EAF) production[79]. Nowadays, steel production can be mainly divided into two processes: the BOF, which represents about 60–70% of the world steel production and the EAF, with the remaining production[80]. Moreover, it is employed the Ladle Furnace (LF) to the refine the steel[81]. In the case of Spain, the steel production by EAF exceeds widely the BOF one. Concretely, in the Basque Country (North of Spain), after the disappearance of Altos Hornos de Vizcaya in 1996, the total steel produced is made in EAF[82,83]. Therefore, due to the easier access to this type of steel production, this work is more focused on the slag which is/was generated by the EAF process (see Fig.1.7).

[77] Cambridge dictionary (http://dictionary.cambridge.org/es/)
[78] G. Krauss, Steels: processing, structure and performance, ASM International editorial, USA, 2005.
[79] A. Ghosh, A. Chatterjee, Ironmaking and steelmaking: theory and practice, *PHI* editorial, New Delhi, 2008.
[80] S. Mauthoor, R. Mohee, P. Kowlesser, An assessment on the recycling opportunities of wastes emanating from scrap metal processing in Mauritius, Waste Management 34 (2014) 1800-1805.
[81] IHOBE, S. A. Libro Blanco para la minimización de residuos y emisiones, Servicio Central de Publicaciones del Gobierno Vasco, Vitoria-Gasteiz, Spain, 1999.
[82] IHOBE, S. A. Libro Blanco para la minimización de residuos y emisiones, Servicio Central de Publicaciones del Gobierno Vasco, Vitoria-Gasteiz, Spain, 1999.
[83] I. Berridi Aguirre, Thesis: Análisis de la influencia de residuos metalúrgicos como áridos en las propiedades del hormigón, Barcelona, 2008.

Fig.1.7. Images of steel slags.

The main chemical constituents of EAF slag are normally FeO (10–40%), CaO (22–60%), SiO_2 (6–34%), Al_2O_3 (3–14%) and MgO (3–13%)[84]. Others minor components are MnO (2-6%) and Cr_2O_3 (1-2%)[85,86]. In addition, C, Cu, Cd, Pb, Zn, Ni, Hg, Se, As, Be, Tl, Co, Sb, Sn, Mo, V, S, P, Ag, Ba, La, Li, Na, Nb, Sc, K, Ti, Sr, W,Y, Zr and B have been detected in this kind of slag[87-93]. These chemical components can vary according to the steel

[84] I. Z. Yildirim, M. Prezzi, Chemical, Mineralogical, and Morphological Properties of Steel Slag, Advances in Civil Engineering 2011 (2011) 1-13.
[85] G. Wang, Y. Wang, Z. Gao, Use of steel slag as a granular material: Volume expansion prediction and usability criteria, Journal of Hazardous Materials 184 (2010) 555–560.
[86] E. Vazquez Ramonich, M. Barra, Reactivity and expansion of electric arc furnace slag in their application in construction, Materiales de Construcción 51 (2001) 263-264.
[87] M. Pasetto, N. Baldo, Performance comparative analysis of stone mastic asphalts with electric arc furnace steel slag: a laboratory evaluation, Materials and Structures 45 (2012) 411–424.
[88] M. Tossavainen, F. Engstrom , Q. Yang, N. Menad, M. Lidstrom Larsson, B. Bjorkman, Characteristics of steel slag under different cooling conditions, Waste Management 27 (2007) 1335–1344.
[89] D. Mombelli, C. Mapelli, S. Barella, A. Gruttadauria, G. Le Saout, E. Garcia-Diaz, The efficiency of quartz addition on electric arc furnace (EAF) carbon steel slag stability, Journal of Hazardous Materials 279 (2014) 586–596.
[90] D.M. Proctor, K.A. Fehling, E.C. Shay, J.L. Wittenborn, J.J. Green, C. Avent, R.D. Bigham, M. Connolly, B. Lee, T.O. Shepker, M. A. Zak, Physical and Chemical Characteristics of Blast Furnace, Basic Oxygen Furnace, and Electric Arc Furnace Steel Industry Slags, Environmental Science and Technology 34 (2000) 1576-1582.
[91] M.P. Luxán, R. Sotolongo, F. Dorrego, E. Herrero, Characteristics of the slags produced in the fusion of scrap steel by electric arc furnace, Cement Concrete Research 30 (2000) 517-519.
[92] P. Suer, J.E. Lindqvist, M. Arm, P. Frogner-Kockum, Reproducing ten years of road ageing-Accelerated carbonation and leaching of EAF steel slag, Science of the Total Environment 07 (2009) 5110–5118.
[93] S.Sorlini, A. Sanzeni, L. Rondi, Reuse of steel slag in bituminous paving mixtures, Journal of Hazardous Materials 209– 210 (2012) 84– 91.

grades and pretreatment methods[94], even in the same plant, depending on raw materials[95].

According to the composition of the steel, there are two main groups: carbon steel (i) and alloy steel (ii)[96]:

(i) Carbon steel or common steel is mainly formed by iron and carbon. And its composition varies between C: 0.1-0.8%, Mn: 0.3-0.7%, Si: 0.15-0.3% and P and S: <0.04%.

(ii) Alloy steel or special steel that contains, apart from carbon and impurities, alloy elements such as Cr, Ni, Mo, V and W. This group includes stainless steel, whose chromium percentage can reach up to 24% of the total.

The steel slag materials are named based on the furnace from which it is generated: blast/basic oxygen furnace slag, electric arc furnace (EAF) slag or ladle (LF) slag (see Fig.1.8.a)[97].

In the EAF production, the furnace is charged mainly with steel scrap, some amounts of pig iron, lime/dolomite and oxygen (see Fig.1.8.b), and it is covered of basic refractory compounds. This furnace uses high power electric arcs, instead of gaseous fuels, which melt the recycled steel scrap by means of electric energy and graphite electrodes. The electric arc and the resistance of the metal to this flow of electricity generate the heat[96,97]. It is reached a temperature around 1300-1600°C[98]. As the scrap melts, the electrodes are driven deeper through the layers of scrap. When it is observed the molten liquid at the bottom of the furnace, oxygen is injected through a lance to oxidize the metals (some iron, other impurities, including aluminum, silicon, manganese, phosphorus, and carbon) in the liquid: *oxidant phase*. The iron

[94] H.Yi, G. Xu, H. Cheng, J. Wang, Y. Wan, H. Chen, An overview of utilization of steel slag, Procedia Environmental Sciences 16 (2012) 791 – 801.
[95] G. Wang, Y. Wang, Z. Gao, Use of steel slag as a granular material: Volume expansion prediction and usability criteria, Journal of Hazardous Materials 184 (2010) 555–560.
[96] IHOBE, S. A. Libro Blanco para la minimización de residuos y emisiones, Servicio Central de Publicaciones del Gobierno Vasco, Vitoria-Gasteiz, Spain, 1999.
[97] I. Z. Yildirim, M. Prezzi, Chemical, Mineralogical, and Morphological Properties of Steel Slag, Advances in Civil Engineering 2011 (2011) 1-13.
[98] J. M. Mesa Fernandez, V. Alvarez Cabal, V. Rodríguez Montequin, J. Villanueva Balsera, Online estimation of electric arc furnace tap temperatura by using fuzzy neural networks, Engineering Applications of Artificial Intelligence 21 (2008) 1001–1012.

present in the scrap is the first metal to oxidize, because of its great amount in the scrap. The chemical reaction is as follows[99,100]:

$$Fe + ½\ O_2 \rightarrow FeO \qquad (1.1)$$

Then, the iron oxide oxidizes the silicon and manganese according to[99]:

$$2FeO + Si \rightarrow SiO_2 + 2Fe \qquad (1.2)$$

$$FeO + Mn \rightarrow MnO + Fe \qquad (1.3)$$

The iron, manganese and silicon oxides are part of the slag that covers the molten liquid, reaching temperatures up to 700°C in the body of the slags[99].

Also lime is introduced to the furnace in order to remove the dissolved detrimental phosphorous from the molten liquid (*dephosphorization phase*), because it causes fragility of the cold steel. The chemical reactions of the dephosphorization are the following, together with the formation of calcium silicates[99,100]:

$$2P + 5FeO \rightarrow P_2O_5 + 5Fe \qquad (1.4)$$

$$P_2O_5 + 4CaO \rightarrow (CaO)_4P_2O_5 \qquad (1.5)$$

$$P_2O_5 + 3\ CaO \rightarrow (CaO)_3P_2O_5 \qquad (1.6)$$

$$y\ SiO_2 + x\ CaO \rightarrow (CaO)_x(SiO_2)_y \qquad (1.7)$$

This combination phosphorous-lime with the oxidized components forms the slag: *electric arc furnace slag* (EAF slag). This slag is known as black slag or oxidizing slag as well[99,100].

Finally, carbon powder is also injected through the slag phase floating on the surface of the molten steel, provoking the CO formation. This CO gas formed causes the slag to foam, which increases the thermal energy transfer[99]:

$$FeO + C \rightarrow CO + Fe \qquad (1.8)$$

[99] IHOBE, S. A. Libro Blanco para la minimización de residuos y emisiones, Servicio Central de Publicaciones del Gobierno Vasco, Vitoria-Gasteiz, Spain, 1999.
[100] I. Z. Yildirim, M. Prezzi, Chemical, Mineralogical, and Morphological Properties of Steel Slag, Advances in Civil Engineering 2011 (2011) 1-13.

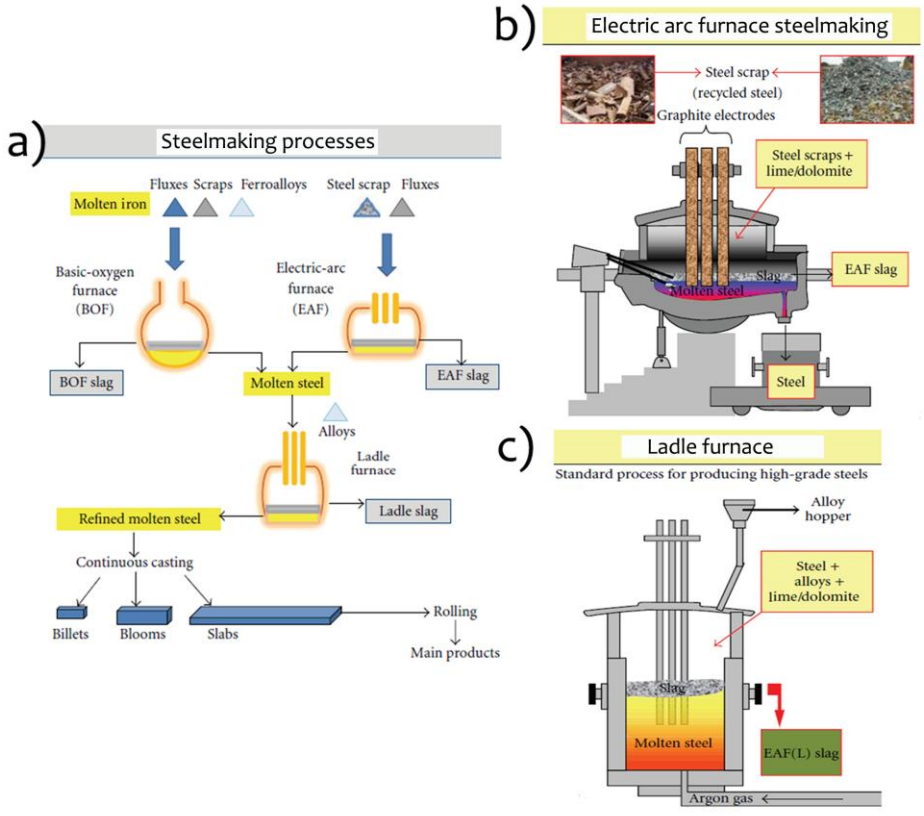

Fig. 1.8. Types of steel slag according to the furnace used (a), EAF process (b) and LF process (c). Source: I. Z. Yildirim et al. (2011)[101].

Once the desired chemical composition of the steel is obtained, the slag and steel are removed from the furnace. This last one is transferred to a secondary steelmaking station for further refining[101,102].

After primary metallurgy, steel produced by BOF or EAF processes can be further refined in the LF to obtain the desired chemical composition. These refining processes are called secondary steelmaking operations: secondary metallurgy. Refining processes are common in the production of high-grade steels. The aim of this phase is to obtain steel with low content of oxygen and to remove the most of the sulfur[101,102].

[101] I. Z. Yildirim, M. Prezzi, Chemical, Mineralogical, and Morphological Properties of Steel Slag, Advances in Civil Engineering 2011 (2011) 1-13.
[102] IHOBE, S. A. Libro Blanco para la minimización de residuos y emisiones, Servicio Central de Publicaciones del Gobierno Vasco, Vitoria-Gasteiz, Spain, 1999.

Ladle furnaces have also graphite electrodes connected to an arc transformer used to heat the steel (see Fig.1.8.c). In this case, the operating temperature is higher than 1700ºC, and the new slag are produced at higher temperature[103]. In the bottom of these furnaces, there is a pipeline that injects argon gas for stirring and homogenization the chemical composition of the liquid steel introduced in the furnace[104,105].

The steel liquid is covered by a reducing slag, named *ladle furnace slag* (LF slag) or white slag. It is formed by lime, fluorite (CaF_2) and coke or graphite, which allows the reduction of the metallic oxides present in the liquid. This is the phase of *deoxidation.* Here, the molten liquid tends to oxidize the slag, which deoxidizes the molten liquid. The addition of iron-alloys of silicon and manganese achieves the definitive deoxidation of the steel[104,105].

Parallel to the previous phase, the *desulfuration phase* of the molten liquid with the contact with the white slag is started. This is due to the fact that the presence of sulfur is unfavourable to the steel performance, causing hot fragility to the resulting steel. When very low levels of sulfur are required, lower than 0.008%, it is added compounds with Si-Ca[104,105].

Furthermore, in order to adjust precisely the chemical composition of the steel in function of the different grades of steel, the desired alloys are added to the molten steel through an alloy hopper connected to the ladle furnace[104,105].

Both type of slag (EAF and LF) are quite different, particularly in the temperature reached during their formation. Black/oxidizing slag is mainly composed of more metal content: oxides, especially of iron (such as hematite, magnesioferrite, magnetite, etc.), calcium and silicon compounds (like larnite, merwinite, bredigite,

[103] K. Banik, S.K. Hazra, S. Adak, P.B. Panda, A.K. Chattopadhyay, Dunite - A versatile and cost effective refractory raw material for different applications, Proceedings UNITECR 2011 Congress: 12th Biennial Worldwide Conference on Refractories - Refractories-Technology to Sustain the Global Environment, 785-788.
[104] I. Z. Yildirim, M. Prezzi, Chemical, Mineralogical, and Morphological Properties of Steel Slag, Advances in Civil Engineering 2011 (2011) 1-13.
[105] IHOBE, S. A. Libro Blanco para la minimización de residuos y emisiones, Servicio Central de Publicaciones del Gobierno Vasco, Vitoria-Gasteiz, Spain, 1999.

etc.), and minor amounts of magnesium, aluminium and manganese oxides[106,107]. Particularly, EAF slag lacks clay and organic ingredients in its composition[108]. Whereas, the principal composition of white/reducing slag is close to Portland cement (whose main mineral is silicate)[109].

The typical applications of steel slag in Europe are as aggregate for: bituminous and hydraulically bound mixtures (asphalt, concrete, road binder, etc.), top layers for high skid resistance, unbound mixtures (unbound surface layers and wearing courses, etc.), dams (road construction and noise protection), embankments and fill, sealing in surface layers to protect deposits roofing, , gabions and noise absorbing walls, ground stabilization, waste water treatment, railway ballast, industrial neutralization product, etc. and for the manufacture of: cement and other hydraulic binders, stone wool, glass (blended with others components)and as fertilizer[110].

It should be pointed out that in the case of the Basque Country (Northern Spain), the black steel slag is considered an inert industrial waste after a valorization process such as carbonation pretreatment (3 months of continuous water washing), i.e. a waste that does not experiment significant transformations and it can be used in certain industrial activities or processes[111].

[106] C. Pellegrino, V. Gaddo, Mechanical and durability characteristics of concrete containing EAF slag as aggregate, Cement and Concrete Composites 31 (2009) 663-671.
[107] M. Frías Rojas, M.I. Sánchez de Rojas, Chemical assessment of the electric arc furnace slag as construction material: Expansive compounds, Cement and Concrete Research 34 (2004) 1881–1888.
[108] D. Mombellia, C. Mapellia, S. Barellaa, A. Gruttadauriaa, G. L. Saoutb, E. Garcia-Diaz, The efficiency of quartz addition on electric arc furnace (EAF) carbon steel slag stability, Journal of Hazardous Materials 279 (2014) 586-596.
[109] G. Chinhsiang, H. Chaolung, L. Tingyi, Activity of Reducing Steel Slag of EAF, Journal of Wuhan University of Technology-Mater. Sci. Ed. 26 (2011) 165-171.
[110] Euroslag (European Slag Association) and Eurofer (European Steel Association), Position Paper on the Ferrous Slag complying with the Waste Framework Directive (Articles 5/6) and the REACH regulation, 2012.
[111] IHOBE, S. A. *Libro Blanco para la minimización de residuos y emisiones*, Servicio Central de Publicaciones del Gobierno Vasco, Vitoria-Gasteiz, Spain, 1999.

CHAPTER 2

OBJECTIVES

As request of NASA, in 2001 the US National Research Council laid down recommendations to the solar system exploration. Some of them were focused on Terrestrial Analogues to Mars, that is, interpretations of Mars must begin with the Earth as a reference. But, the Mars study must go beyond the global mapping and center on detailed analysis at the regional to outcrop level. It was recommended process studies at analogue sites, field workshops, instrument and operations tests, and laboratory measurements. To optimize the choice of instruments and their operating parameters by means of testing and interpretation of their data in Terrestrial analogue materials and environments on Earth was also considered crucial. Scanning electron microscopy/Energy Dispersive X-ray spectroscopy (SEM-EDX), Raman Spectroscopy and Laser-Induced Breakdown Spectroscopy (LIBS) were among the recommended instruments, whose measurements should be focused on Mars analogue materials such as rock and mineral analogues, and Mars meteorites. All of them will be useful for instrument tests.

Our research group has a long past experience in micro-destructive and/or non-destructive spectroscopic techniques in a wide field of materials: Cultural Heritage materials, beachrocks, sediments, soils, etc. However, this PhD project is our first challenge to develop new analytical methodologies for the characterization of terrestrial analogs to Mars and terrestrial-extraterrestrial materials.

In the last 10 years, there have been 15 research documents about Libyan Desert Glass (LDGs) and 8 related to Darwin Glasses (DGs). Perhaps because of the special characteristic of these terrestrial-extraterrestrial materials, which need exhaustive

studies to characterize them, or due to the fact that they are not common materials that you can get in anywhere, anytime, their study is not so widespread.

Therefore, based on US National Research Council recommendations to the Mars exploration, given our previous knowledge and the lack of information about LDGs and DGs, the main objectives in this research were (a) to develop innovative methodologies to the characterization of terrestrial-extraterrestrial materials and terrestrial analogues to meteorites, using LDGs and DGs, and steel slag as target materials respectively, which in turn allowed us to test the analytical instruments that we had at our disposal, and (b) the study of the terrestrial weathering over this type of materials.

In order to achieve the main aims, several operational objectives were defined:

- To test several elemental and molecular analytical techniques over LDG, DG and steel slag, among them some recommended for planetary research.
- To characterize LDG, DG and steel slag by means of a combination of non-destructive and micro-destructive spectroscopic techniques, obtaining experimental evidences of the formation of different compounds in LDG, DG and steel slag.
- To take advantage of the Raman spectroscopy technique to determine pressure, temperature and water effects over the studied materials. And thus, to corroborate the impact origin of the LDG and DG.
- To compare the composition of LDG and DG, originated in different environments.
- To study the possible presence of organic compounds and biologic activity in LDG, DG and steel slag, given the lack of information about it in these kinds of samples.
- To test the viability of employing portable LIBS equipment to the elemental quantification by calibration approach using multivariate statistical tools.

- To study the weathering of LDG, DG and steel slag to differentiate compounds produced after the generation of the samples and in different Earth climates.

- To simulate weathering processes based on the interaction of steel slag with water, a soft acid and a strong acid, with later use of chemometric tools to extract possible relationships between steel slags of different provenance.

- To evaluate the simulated weathering process methodology, proposed from the study over the steel slag, on the weathering of impact glasses.

- From the extracted knowledge of all previous experiments, to establish a methodology that facilitates the choice of analytical instruments and the steps to follow in this type of singular materials.

CHAPTER 3

MATERIALS AND METHODS

3.1 SAMPLES AND SAMPLING PROCEDURE

3.1.1 Libyan Desert Glasses (LDGs)

Several specimens of LDG from the Meteorites Collection of the Basque Country University (UPV/EHU) were analyzed. They were collected in the Libyan Desert (Africa) area mentioned in the Introduction, their dimensions range between 1-5 x 2-4 cm and 5-23 g weight (see Fig. 3.1) and they have a translucent glassy matrix, with whitish spherical, brownish and dark inclusions in some cases.

Fig.3.1. Studied Libyan Desert Glasses belonging to the Meteorites Collection of the Basque Country University (UPV/EHU).

3.1.2 Darwin Glasses (DG)

Some specimens of Darwin Glasses belonging to the meteorite samples of the collection of the University of the Basque Country (UPV/EHU) were studied (see Fig. 3.2). They were collected in Tasmania (Australia), in an area near the Darwin crater, as it has been described in the Introduction, and present different hues and geometrical forms. Our DG samples are mainly spheroid, and with different shades: a green brownish dark colour, black or very light and translucent and most of them have some bubbles inside the bulk. Most of the specimens are mainly not higher than 1×1 cm, but some of them have dimensions of 4.5×3.7 cm, 3×1 cm and 2.8×1 cm,

Fig.3.2. Studied Darwin Glasses belonging to the Meteorites Collection of the Basque Country University (UPV/EHU).

3.1.3 Steel slag collected in steel factories and in civil constructions works

Several Electric Arc Furnace black slag coming from different industries and locations of the Basque Country (Spain) and Belgium have been analyzed. Some of them came directly from steel producers, but two were sampled in two civil construction works where slags were used as filling for vehicle roads. Slag samples are listed in the Table 3.1.The majority of them suffered from a treatment consisting of outdoor cooling and

irrigation with water. The origin and treatment of the M3 and M4 samples collected from two different civil building constructions in the Basque Country (Spain) was unknown. However, we assumed that they were treated since slag must be treated to be used in construction sites according to the Basque legislation[1].

Table 3.1. List of the analyzed black steel slag.

Sample	*Type*	*Inerting/stabilization treatment*	*Localization*
M1	Common steel factory	Outdoor cooling	Basque Country (Spain)
M1 T	Common steel factory	Outdoor cooling, irrigation with water, crushing, sifting and magnetic separation of ironed materials	Basque Country (Spain)
M2	Special steel factory	Outdoor cooling	Basque Country (Spain)
M2 T	Special steel factory	Outdoor cooling and irrigation with water	Basque Country (Spain)
M3	Unknown	Unknown (supposedly treated)	Civil building construction in Getxo (Basque Country, Spain)
M4	Unknown	Unknown (supposedly treated)	Civil building construction in the Campus of Bizkaia (Leioa, Basque Country, Spain).
M5	Other common steel factory	Outdoor cooling and irrigation with water	Basque Country (Spain)
M6	Stainless steel factory	Outdoor cooling and irrigation with water	Belgium

All of the steel slag samples have a grey dark color, but with time the slag goes to a whitish color. In the Fig. 3.3, it can be observed several of the analyzed slag samples.

[1] BOPV Official Bulletin of the Basque Country, 2003. N° 4. Decreto 34/2003 por el que se regula la valorización y posterior utilización de escorias procedentes de la fabricación de acero en hornos de arco eléctrico, en el ámbito de la Comunidad Autónoma del País Vasco. (http://www.euskadi.net).

Fig.3.3. Images of some treated and non treated black steel slag. (a) M1T, (b) M2, (c) M4 and (d) M2T.

3.1.4 Steel slag collected in forest tracks

Black and white steel slag were collected along two nearby forest tracks in a pass through the mountains of Gipuzkoa (Basque Country, Northern Spain) (see Fig. 3.4):

- 0.5 km long forest track, only filled with black steel slag 18 years ago. It is named as short forest track (SFT), and the slag samples S.

- 6 km long forest track, filled with a mixture of black steel slag and white steel slag approximately 34 years ago. Besides, it was added a layer of white slag about 18 years ago in order to repair some areas. It is named as long forest track (LFT), and the slag samples LS.

The steel slag samples of both forest tracks come from two different steelworks; however, all black steel slags were generated in Electric Arc Furnace and the white ones in a Ladle Furnace. They were used as filler in the driving surface of the forest tracks. Black steel slag samples were taken from both forest tracks, and some white ones from the longer forest track. They were collected in different points throughout the two forest tracks (see Fig. 3.4).

Fig.3.4. Images of: (a) forest track with mixture of black and white steel slags (LS), (b) and (c) samples distribution along the forest track with mixture of slag types (LS) and that with only black slags (S), (d) black steel slags in the forest track with only blacks slags, (e) location of both forest tracks, (f) black and white steel slags, (g) forest track with only black steel slags and (h) image of water accumulated in the soil of the forest track with mixture of black and white steel slag (LFT).

3.1.4.1 Rain water collected from the forest track with mixture of black and white steel slag

Rain water was picked up directly from the atmosphere and accumulated water on the LFT soil (see Fig. 3.4.h). The accumulated water was collected in the upper zone of the LFT, near where the LS4 was sampled, whereas water from the atmosphere was collected in an area between the sampling of LS1 and LS2.

3.2 PRE-TREATMENT OF THE SAMPLES

Depending on the procedure of each analysis, different pre-treatments were carried out.

3.2.1 Thick and thin sections preparations

LDG and DG were sliced. Thick and thin sections were prepared to get samples of small thickness and thus, to facilitate subsequent analysis. Sections were obtained by

slicing the samples with a cutting (Buehler-PetroThin) with a diamond saw. As it is necessary a perfectly flat surface without deformations, the fragments were polished using silicon carbide powder of different grain size on frosted glasses. The thick of the fragments was approximately 800 µm. Once obtained the flat surface, in the case of thin sections, samples were mounted on glass slides (dimensions of 27 x 46 x 1.5 mm) with epoxy resin (a fixer compound composed of polyurethane, acrylic and cyanoacrylate) and then, the samples were smoothed using progressively finer abrasive grit until they were only 30 µm thick.

3.2.2 Grinding and weighing of samples

i) Libyan Desert Glasses (LDG) and Darwin Glasses (DG): small fragments detached from LDG and DG samples were ground in the agate mortar. Once obtained homogenized samples, they were put in glass recipients until analysis.

ii) Steel slag: steel slag samples were crushed, ground, lyophilized, sieved and put in glass recipients until analysis (see Fig. 3.5). The grinding step was done first by hand and then mechanically by using a Fristch Pulverisette 6 (Indar- Orberstein, Germany) with an agate ball mill, during 15 min., with two repetitions at 700 rpm. These conditions were changing according to the hardness of the slag. Later, grinded samples were lyophilized (Cryodos, Telstar, Spain) for 48 h to 150 mb and -52°C approximately. Finally, the samples were sieved in an Octagon sieve shaker (Endecotts, UK). The grains with less than 2 mm were used in the corresponding analysis.

Fig.3.5. Images of the agate ball mill, the mill, the lyophilizer and the sieve shaker.

Powder samples were weighed using an AJ150L analytical balance (Mettler Toledo, Ohio, USA) with ± 0.0001 g of precision in the quantitative analyses.

3.3 QUALITATIVE AND QUANTITATIVE ANALYSIS

The results of this work are centred in three chapters; the first one is related to the *elemental and molecular characterization* of the LDG, DG and steel slag (Chapter 4), the second is focused on the *elemental quantification* of the samples by means of calibration approach using multivariate statistical tools (Chapter 5), and the last one is about the study of the *terrestrial weathering* suffered by the samples (Chapter 6). For those purposes, the instruments described below were employed.

3.3.1 Microscopic and elemental characterization

Optical polarizing microscope and cathodoluminiscence: thin sections of the impact glasses were examined under NIKON optical polarizing microscope equipped with a digital camera in order to observe the structural and textural composition. Moreover, a technosyn Cold cathode luminescence system, model 8200MKII with a vacuum chamber coupled to a polarizing microscope working under standard operating conditions at 12-15kV of accelerating potential, 0.5-0.6 mA beam current, and a beam diameter of 4.5 mm was used on impact glasses thin sections to observe the internal structure of the matrix and the texture of the melt based mainly on elements luminescence of the melt.

Elemental characterization: in order to perform a screening of the elemental composition of the samples, it was used the following non destructive techniques: (a) Micro-Energy Dispersive X-Ray Fluorescence Spectroscopy (μ-EDXRF) , (b) Electron Microscopy/Energy Dispersive X-Ray Spectroscopy (SEM-EDX), (c) Electron Microprobe Analysis (EPMA) and (d) X-Ray Photoelectron Spectroscopy (XPS).

(a) Micro-Energy Dispersive X-Ray Fluorescence Spectroscopy (μ-EDXRF): samples were analyzed directly without any pretreatment. However, in order to measure the

inner part of the samples, steel slags and DGs were broken. In the case of LDGs, thick sections obtained previously were analysed.

It was used a Bruker AG ArtTax portable Micro-Energy Dispersive X-Ray Fluorescence (μ-EDXRF) equipment (Berlin, Germany) consisting on a X-ray tube with a molybdenum anode working at maximum voltage of 50 kV and a maximum current of 700 μA (Fig. 3.6). The instrument is provided with an electro-thermally cooled Xflash® detector (5 mm^2). The X-rays were collimated by a tantalum 0.65 mm diameter collimator. The measuring head of the equipment integrates a Charge Coupled Device (CCD) camera that allows focusing on the sample by a motorized XYZ positioning unit controlled by the computer and to obtain 8 mm x 8 mm images of the sample analyzed. The instrument was daily calibrated with the Cu and Sn Kα lines of bronze reference standard (Bruker, Berlin, Germany).

The operating conditions varied between 1000-1500 s of exposition time at a voltage of 50 kV and a current of 700 μA. A helium flow was used in order to identify elements with Z<20. This method avoids the use of vacuum conditions. However, elements with Z<11 cannot be identified. Instrument control, data collection, processing and analysis were carried out using the ARTAX 4.9.13.2 software (Bruker, Berlin, Germany).

Furthermore, when the previous equipment was not available, a handheld Electron Dispersive X-Ray Fluorescence (EDXRF) portable analyzer X-MET5100 (OXFORD Instruments) was employed (see Fig. 3.6). It is equipped with an X-ray rhodium tube that provides a 40 kV voltage and it includes a high resolution silicon drift detector (SSDD). The used exposition time was of 50 seconds.

Numerous measurements were performed in all of the samples in order to obtain reliable results, and only Kα lines of the elements were considered in both instruments.

Fig.3.6. X-Ray Fluorescence (XRF) instruments. ArtTax portable Micro-Energy Dispersive X-Ray Fluorescence (μ-EDXRF) equipment on the left and the handheld Electron Dispersive X-Ray Fluorescence (EDXRF) analyzer on the right.

(b) Electron Microscopy/Energy Dispersive X-Ray Spectroscopy (SEM-EDX): structural (electron image acquisitions) and elemental distribution data at high magnifications was accomplished by Scanning Electron Microscopy coupled to Energy Dispersive X-Ray Spectroscopy (SEM-EDX). These analyses were performed over steel slag fragments as well as thick and thin sections of the LDGs and DGs. In the steel slag samples any pretreatment was applied since they were considered to be conductive due to their high iron and other metals content. However, LDG and DG sections were coated with carbon to a better conduction.

Two SEM-EDX instruments were employed. On one hand, it was used an EVO 40 Scanning Electron Microscope (Carl Zeiss NTS GmbH,Germany) coupled to an X-Max Energy-Dispersive X-Ray spectroscopy (EDX) system (Oxford Instruments, UK) for the elemental mapping. The equipment is also installed on an antivibratory table inside a temperature controlled room. SEM images were acquired at high vacuum employing an acceleration voltage of 20 KV. Magnifications up to 10 000× were reached using a Secondary Electron (SE) detector for image acquisitions. Moreover, elemental mappings were performed using an 8.5 mm working distance, a 35° take-off angle and an acceleration voltage of 20 KV (see Fig. 3.7).

Fig. 3.7. Images of the SEM-EDX system (left) and detail of the EDX instrument (right).

On the other hand, it was used a JEOL JSM-6400 SEM with an Oxford Pentafet photon energy instruments Link Isis X-Ray (EDX) system. SEM images were acquired at high vacuum employing an acceleration voltage of 20 KV as well as in the elemental mapping. Magnifications up to 10 000× were reached using a Secondary Electron (SE) detector for image acquisitions, and elemental mappings were performed using an 15 mm working distance.

The analysis and the treatment of the data were performed with the INCA Microanalysis Suite 4.3 (Oxford Instruments, UK).

(c) Electron Microprobe Analysis (EPMA): thin sections of LDG and DG were employed for EPMA analysis. A CAMECA SX-100 electron microprobe (EPMA) was used. The operating conditions for X-ray mapping were 15 kV accelerating potential, 15 nA beam current, 2 µm scan distance, and 100 ms acquisition time of X-ray peak per point and a lower detection-limit of 600 mg/Kg for a mapped element. The beam diameter was 0.6 µm at 15 kV and 100 nA.

(d) X-Ray Photoelectron Spectroscopy (XPS): this also is a non destructive technique that provided information about the elements present on the surface and on its oxidation state. Analyses were carried out on the SGIker analyses service of the UPV-EHU. The measured samples were small steel slag fragments. The analysis was performed in a SPECS system (Berlin, Germany) equipped with a Phoibos analyzer 150 1D-DLD and a monochromatic radiation source Al Kα (1486.6 eV). The spot over the sample was 1-2 mm. An initial analysis of the elements (wide scan: step 1 eV energy,

dwell time 0.1 s, pass energy 80 eV) was carried out and then the detailed analysis (detail scan: step energy 0.1 eV, dwell time 0.1 s, pass energy 30 eV) at an electron exit angle of 90°, fitting the spectra to Gaussian-Lorentzian functions (CasaXPS 2.3.16 software) after background subtraction.

3.3.2 Molecular characterization

Three non-destructive instrumental techniques were used to perform the molecular characterization: (a) Raman spectroscopy, (b) Structural and Chemical Analyser (SCA) and (c) X-Ray Diffraction (XRD).

(a) Raman micro-spectroscopy: several Raman spectrometers were used for the development of the present research work. To guarantee representativeness and reproducibility, more than 100 measurements were performed per sample/spectrometer. Samples were analysed directly without any pretreatment. However, in order to measure the inner part of the samples, broken fragments of the steel slags and the thick and thin sections of the LDG and DG samples previously obtained were analyzed.

InnoRaman^{TM} spectrometer

The search for major compounds was done using two InnoRaman^{TM} handheld spectrometers (B&WTEK$_{INC}$, Newark, USA) provided with a 785 nm and 532 nm diode excitation lasers respectively and Charge Coupled Device (CCD) detectors (Peltier cooled) (see Fig. 3.8). The equipments have a laser power software controller from 0 % to 100 %, being the nominal laser power of the 785 nm laser instrument 330 mW± 15 % at the source and 255 mW ± 15 % at the surface of the analyzed samples; and 50 mW at the source and 33 mW at the surface of the samples using the equipment with the 532 laser. In order to avoid thermodecomposition of the samples, the laser power was modulated.

The microprobe (spots around 100 microns of focus when working alone) can be mounted on a microscope to perform micro-Raman spectroscopy. Two long-range focusing lenses with 20x and 50x magnification (respective 5 µm and 2 µm lateral

resolutions) can be used. Depending on the objective used, the laser was focused on a 5-200 μm spot in diameter.

Data acquisition was done by BWSpec^{TM} 3.26 and BWSpec 4.02_15 software (B&WTEK$_{INC}$, Newark, USA), and the analysis, treatment and interpretation of the results was carried out by Omnic 7.2 software (Thermo Fisher-Nicolet, Madison, USA). Spectra were obtained with a resolution of 3–4 cm^{-1} and 5 cm^{-1} in a spectral range of 200–2000 cm^{-1} and 62–3750 cm^{-1} in the 785 nm and 532 nm laser equipments respectively. Moreover, in order to improve the relation signal-to-noise, the accumulations were modified too.

Renishaw RA100 spectrometer

The analysis of minor (and trace) compounds was performed with a Raman microprobe device, a Renishaw RA 100 Raman Spectrometer (Renishaw, UK), coupled to an Oxford fibre optic microprobe, equipped with 785nm excitation diode laser and a CCD detector (Peltier cooled). The nominal power laser is 150 mW at the source and neutral filters allow working at 1 % (5 mW at the source and 1 mW at the sample), 10 % (50 mW at the source and 10 mW at the sample) and 100 % (150 mW at the source and 30 mW at the sample) of the total power. In order to avoid thermodecomposition of the samples, the laser power was modulated at 1, 10 and 100%.

The microprobe mounted on a tripod (see Fig. 3.8) was joined to different long range lenses: 4x, 20× and 50× (25 μm, 5 μm and 2 μm of lateral resolution respectively), which allowed us to focus the laser beam between 5 μm and 100 μm at the sample. The instrument is also coupled to a micro-camera whose positioning is controlled by a micrometric stage which permits a perfect focusing of the areas of interest. Spectra were obtained in a spectral range of 200–2000 cm^{-1} approximately with a spectral resolution of 2 cm^{-1}. In order to improve the relation signal-to-noise, the number of accumulations and integration time were modified too. The data were acquired with WIRE 3.2 software (Renishaw, UK), and the analysis and treatment of these were realized with the previously mentioned Omnic software.

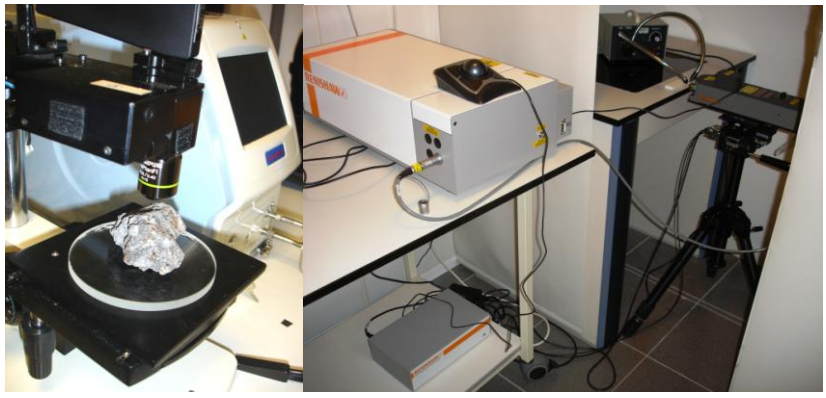

Fig.3.8. The InnoRaman^{TM} B&W TEK$_{INC}$ spectrometer provided with the 785 nm laser analyzing a steel slag on the left and the Renishaw RA100 spectrometer on the right.

Renishaw InVia confocal micro spectrometer

This instrument was relevant for deeper analysis of the samples, since the system can be used with different laser excitation sources, detectors and can be coupled to different devices.

The fine micro-Raman analysis of the samples was carried out using a Renishaw InVia confocal micro Raman spectrometer (Renishaw, UK) provided by a 514 nm and a 785 nm lasers as excitation sources (at highest powers, the nominal laser powers at the source are 50 mW and 350 mW for each of the laser beams, and at the samples 20 mW and 150 mW respectively) and a Peltier cooled CCD detector (-70°C). The equipment is coupled to a Leica DMLM microscope (Bradford, UK). For visualization and focusing 5x N PLAN (0.12 aperture) and 20x N PLAN EPI (0.40 aperture) lenses were used. The spectra were acquired using 50x N PLAN (0.75 aperture, lateral resolution of 2 µm) long-range objectives. At high magnifications, the laser spot was reduced to 1 µm diameter. The microscope implements a Prior Scientific motorized XYZ positioning stage with a joystick and is equipped with a micro-camera for searching points of interest. Moreover, the equipment is installed on an antivibratory table inside a temperature controlled chamber.

The spectral range was 100-3500 cm^{-1} with a resolution of 1 cm^{-1}. In order to achieve the best signal-to-noise ratio the number of accumulations and integration time were

varied. WIRE 3.2 software (Renishaw, UK) was used to the data obtaining and their analysis and treatment was realized with the Omnic software as well.

In addition, this equipment was used to obtain Raman chemical image acquisitions of specific areas of the samples, outlining the distribution of several chemical components in those areas. It was collected great quantity of spectra and processing images. As a result it was created false-colour Raman chemical imaging analyses.

In the steel slag, it was used the 514 nm excitation source and the Stream Line mode to obtain the Raman chemical images. Laser was set at 20 mW at the sample, since it was not observed thermal decompositions. The InVia equipment implements a motorized microscope stage which moves the sample under the lens, to be the line raster across the area of interest. As the line moves across the sample, data are swept synchronized across the StreamLine UVDD CCD detector and read out continuously. The spectra were obtained with the 50x N PLAN (0.75 aperture) objective. For higher magnification objectives, such as 100x, significant defocusing was observed which precluded mapping experiments. The spectral range chosen was 108–2000 cm^{-1}, the acquisition time was 5 s with one accumulation per each spectrum, which ensured a suitable signal-to-noise ratio, and the step size was set in 3.2 μm. Finally, it was obtained between 1560-4891 spectra.

In the impact glasses, it was used the 514 nm and the 785 nm excitation sources to obtain the Raman images and it was set at 20 mW and 150 mW at the sample. The spectra were obtained with the 20x N PLAN EPI (0.40 aperture) and 50x N PLAN (0.75 aperture) objective. The spectral range varied between 100 and 3000 cm^{-1}. The acquisition time was 1-40 s with 1-5 accumulation per each spectrum, which ensured a suitable signal-to-noise ratio, and the step size was set in 3.2 or 3.5 μm. At the end, each Raman image was composed from 483-5285 spectra.

In the data collected for each map it was carried out a cosmic ray removal and a noise filter by means of the WIRE 3.2 software. After performing the baseline correction, the spectra were filtered based on the integration of the main Raman bands for each molecular phase in order to represent their chemical image in the selected mapping area. In case of mineral phases sharing band positions secondary Raman bands were taken into account for peak integration.

It should be noted that this equipment can be coupled to a SEM instrument composing the Structural and Chemical Analyser (SCA) that will be explained later on (see Fig. 3.9).

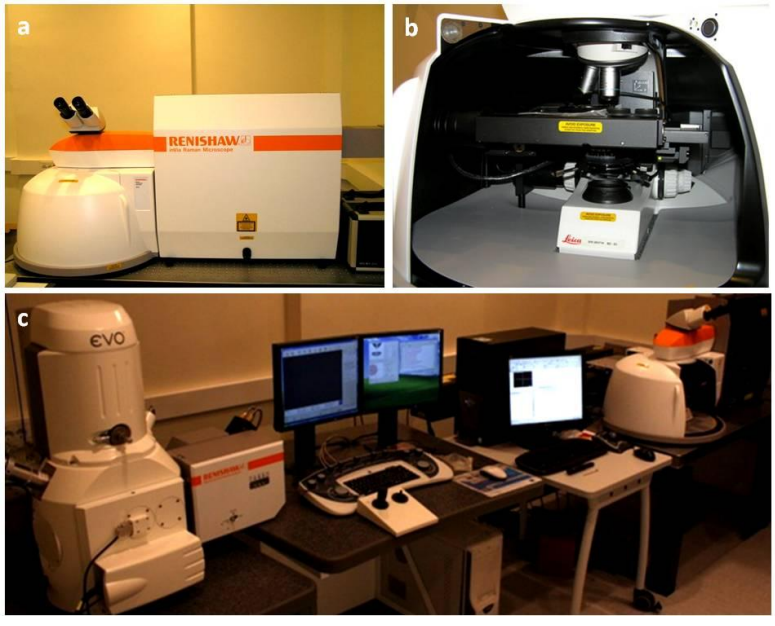

Fig.3.9. Images of the Renishaw InVia confocal micro Raman spectrometer (a and b), and general view of the temperature controlled room with the contiguous SEM instrument to which can be coupled (c).

WITEC microscope a300RA+

The WITEC Company realized these analyses in order to differentiate and measure the bubbles of LDG thick section by means of Raman images. For recording the data it was used a WITEC microscope a300RA+ with a back illuminated Electron Multiplying CCD (EMCCD) camera, a deep-depletion CCD camera, an UHTS300 spectrometer for visible and for NIR, a frequency doubled Nd-YAG laser used for 532 nm excitation, a diode laser used for 785 nm excitation and a Zeiss 100x air objective (0.9 aperture). The measurements were acquired using the WITecControl software and analyzed with the WITecProject software.

Final considerations for Raman spectroscopic measurements

The quality of measurements of the different Raman equipments used was guaranteed by means of an internal calibration and a diary calibration using the

Raman signal of Si at 520.5 cm^{-1} of a crystalline silicon chip. All the Raman spectroscopic measurements were carried out in darkness, due to the fact that the artificial light photons and sunlight can reach the spectrometer detector and their signal can be confused with the Raman signals from the sample. Despite this, occasionally cosmic rays were observed.

The acquisition of the spectra was conducted following a protocol mainly consisting on starting at lower laser powers and then increasing it until a good signal to noise ratio was obtained, varying also the integration time and the accumulations as it has been mentioned. After recording each spectrum, a visual inspection through a micro-video camera was performed on the measurement and on the microscope stage in order to detect any phase transitions caused by the laser.

The analysis and treatment of the Raman spectra using the mentioned Omnic software basically consisted on cosmic rays removal and sometimes baseline correction or smoothing, in order to correct fluorescence or noise interferences to a greater or lesser extent. Furthermore, when broadening effects of the peaks were observed, deconvolutions were performed with the Grams 8.0 software (Thermo Fisher Scientific $_{INC.}$, Waltham, USA) based on Lorentzian and Gaussian functions.

The interpretation of the results was accomplished by comparison with standard Raman spectra from the e-VISARCH[2] and e-VISART[3] libraries and with spectra obtained from the on-line database RRUFF (http://rruff.info/)[4].

(b) Structural and Chemical Analyser (SCA): structural and Chemical Analyser (SCA) (Renishaw, UK), that is the previous Raman instrument (see section Renishaw InVia confocal micro spectrometer) coupled to the SEM-EDX equipment (see section Electron Microscopy/Energy Dispersive X-Ray Spectroscopy (SEM-EDX)) was used to know the elemental and molecular information in a same micrometric spot (spots of

[2] M. Pérez-Alonso, K. Castro, J.M. Madariaga, Vibrational spectroscopic techniques for the analysis of artefacts with historical, artistic and archaeological value, Analytical Chemistry 2 (2006) 89-100.
[3] K. Castro, M. Perez-Alonso, M. D. Rodriguez-Laso, L. A. Fernandez, J. M. Madariaga, On-line FT-Raman and dispersive Raman spectra database of artists' materials (e-VISART database), Analytical and Bioanalytical Chemistry 382 (2005) 248-258.
[4] Downs R.T, *The RRUFF Project: an integrated study of the chemistry, crystallography, Raman and infrared spectroscopy of minerals*. Program and Abstracts of the 19th General Meeting of the International Mineralogical Association in Kobe, Japan, 2006, O03-13. http://rruff.info/.

less than 5 microns) of the sample surface, without moving the sample from one instrument to another.

The SEM-EDX analysis helped to select areas and identify what elements were present in the exact point of Raman measurements of steel slag samples. Despite this advantage, the analyses performed with this equipment are expensive, so it is not entirely suitable for the routine characterization of major and minor compounds. This can be more economically achieved with the handheld spectrometer or with the Raman microprobe.

Grains sieved between 2 mm and 250 μm for each steel slag were deposited on the surface of a special aluminum pin and glued to the surface by using a carbon adhesive tape. SEM images were acquired at high vacuum employing an acceleration voltage of 20 KV, as the voltage in the elemental mapping.

The SCA interface uses in-SEM retractable collection optic to introduce the laser light and focus it into the sample as well as to collect the Raman signal through the in-Via micro-Raman spectrometer described earlier. The laser light and Raman signal are both transmitted between the Raman spectrometer and the SCA via 2 m fibre-optic cables.

Although the SCA used in this study is configured for use with 514 and 785 nm laser excitations, only the 785 nm laser was used to measure the slag samples, with the highest power. The exposure time was 30 s with 5 accumulations. As previously, the Raman spectral interpretation was done by comparison with pure standard compounds contained in the databases mentioned before.

(c) X-Ray Diffraction (XRD): complementary information about the mineral composition was obtained from X-Ray Diffraction. Analyses were carried out on the SGIker analyses service of the UPV-EHU. Prior to the analysis, small fragments of slag samples and small pieces detached from LDG and DG LDG in the hitting with a hammer were crushed and homogenized manually with an agate mortar.

It was used a powder diffractometer PANalytical Xpert PRO that incorporates a copper tube ($\lambda Cu_{K\alpha media}$= 1.5418 Å, $\lambda Cu_{K\alpha 1}$= 1.54060 Å, $\lambda Cu_{K\alpha 2}$= 1.54439 Å), vertical goniometer (Bragg-Brentano geometry), programmable divergence aperture,

automatic interchange of samples, secondary monochromator from graphite and PixCel detector.

The measurement conditions were 40 kV of voltage and a current of 40 mA, with an angular range (2θ) scanned between 5 and 70°. The treatment of the diffractograms and the identification of the mineral phases was performed with the specific software X`pert HighScore (PANalytical) in combination with the specific powder diffraction file (PDF2) database (International Centre for Diffraction Data - ICDD, Pennsylvania, USA).

3.3.3 Elemental quantification by Laser-Induced Breakdown Spectroscopy (LIBS)

A portable EasyLIBS IVEA system (model Easy 2C) was employed for these measurements (see Fig. 3.10). It employs a pulsed Nd:YAG laser, with the possibility to dual pulse mode, and emits at the fundamental wavelength of 1064 nm. The laser energy per pulse on the sample is higher than 25 mJ with a repetition rate of 1 Hz and the duration of laser pulse is 4-5 ns. In this work, the measurements were realized with double pulse mode. An optimized delay time of 50 μs (both single to double pulse) to the laser pulse and a gate width of 5 ms were employed. All spectra were accumulated over 1-3 laser-shots.

The Easy 2C model consists of an optic probe in form of gun that allows focusing the laser in the material to analyze. The gun goes connected to a computer and to two spectrometers, one corresponding to the Ultraviolet (UV) spectral range (196-419 nm) and that of the near Infrared (NIR) (580-1000 nm) (Czerny-Turner Ocean Optics HR 2000+). This spectral range is covered in each acquisition process. The optical resolution in both is 0.2 nm (Full Width at Half Maximum, FWHM) (spectral resolution of about 1000). The laser spot is around 193 μm in diameter and the crater is 250 μm. Two laser pointers to check the focus, associated with LED, lighting the sample surface, and a compact color camera at the back of the gun, allow the operator to choose the shot position. Moreover the gun has three bottoms of contact to security of the laser. The plasma light generated by the laser shot is collected with an aspheric lens (from Ocean Optics), directly coupled to a transport fiber. All these optical

elements are mounted within the gun-shaped box. The "laser gun" is connected by an umbilical (1 m) to a second box containing the spectrometers and the batteries and also to a computer, which controls the system. A CCD detector collects the signal.

Fig.3.10. The portable EasyLIBS IVEA system.

The software used for automatic acquisition, control, visualization and processing of the spectra was the AnaLIBS version 6.3. It also incorporates two databases to an automatic detection mode able to associate spectral lines to their corresponding chemical elements. One of them is the IVEA database and the other is the NIST database[5].

3.3.4 Terrestrial weathering analysis by leaching tests

Quantitative analyses were carried out to know the elemental quantitative compositional data after several leaching tests. It was employed two different leaching tests over the steel slag: the EN 12457-2 standard leaching test, commonly used in steel slag to determine the release of trace elements from the sample[6-9]; and

[5] NIST database of atomic spectral data. http://physics.nist.gov/PhysRefData/ASD.
[6] S. Barella, A. Gruttadauria, F. Magni, C. Mapelli, D. Mombelli, Survey about Safe and Reliable Use of EAF Slag, ISIJ International 52 (2012) 2295–2302.
[7] S. Sorlini, A. Sanzeni, L. Rondi, Reuse of steel slag in bituminous paving mixtures Journal of Hazardous Materials 209-210 (2012) 84-91.
[8] F. Engström, M. L. Larsson, C. Samuelsson, Å. Sandström, R. Robinson, B. Björkman, Leaching Behavior of Aged Steel Slags, Steel Research International 85 (2014) 607-615.
[9] D. Mombelli, C. Mapelli, S. Barella, A. Gruttadauria, G. Le Saout, E. Garcia-Diaz, The efficiency of quartz addition on electric arc furnace (EAF) carbon steel slag stability, Journal of Hazardous Materials 279 (2014) 586–596.

a previously optimized procedure with Focused Ultrasound Energy that simulates extreme leaching processes over solid silicate materials[10]. After choosing the optimal leaching methodology with the steel slag samples, it was applied to the impact glasses. Then, the dissolutions were measured through Inductively Coupled Plasma-Mass Spectrometry (ICP-MS) and Ionic Chromatography (IC).

3.3.4.1 EN 12457-2 standard leaching test

This leaching test is based on the dissolution of slag of particular size less than 4 mm diameter, with deionized water, which results in a liquid-to-solid (l/Kg) ratio of 10:1. Furthermore, the dissolution is stirred by a rotary mixer during 24h at 10 rpm[11]. The purpose of making this leaching test was to compare it with our own leaching test described in the next section. Therefore, it was weighed 2 g of a Reference Material (RM) steelmaking slag (NH 146, Brammer standard, Mittal Steel Oslava, Czech Republic) mixed with 20 ml of Milli-Q water (18.2 MΩ cm, Millipore, Billerica, Massachusetts, USA). At least 3 replicates and 3 blanks were obtained per sample. All the dissolutions were filtered with 0.45 μm filters (Whatman PVDF W/GMF) and stored in polypolyethylene vials of 50 ml at 4°C before analysis.

3.3.4.2 Focused UltraSound Energy leaching test

Focused Ultrasound (FUS) was used to accelerate the extraction of compounds organic metals, organometallics, etc. of many matrices, yielding greater efficiencies than other types of extraction. Besides, it should be considered that this technique has low instrumental requirements, is repetitive and fast compared to other advanced techniques such as microwave extraction[12,13].

[10] S. Fdez-Ortiz de Vallejuelo, A. Barrena, G. Arana, A. de Diego, J. M. Madariaga, Ultrasound energy focused in a glass probe: An approach to the simultaneous and fast extraction of trace elements from sediments, Talanta 80 (2009) 434-439.
[11] EN 12457-2: Characterization of waste –leaching – compliance test for leaching of granular waste materials and sludges – Part 2: one stage batch test at a liquid to solid ratio of 10 l/kg for materials with particle size below 4 mm (without or with size reduction), European Committee for Standarization, 2002.
[12] S. Fdez-Ortiz de Vallejuelo, A. Barrena, G. Arana, A. de Diego, J. M. Madariaga, Ultrasound energy focused in a glass probe: An approach to the simultaneous and fast extraction of trace elements from sediments, Talanta 80 (2009) 434-439.
[13] R. Azuola, P. Vargas, Extracción de sustancias asistida por ultrasonidos (EUA), Tecnologia en Marcha 20 (2007) 30-40.

In this case, the samples of particular size less than 2 mm diameter were sonicated during 6 minutes with a HD 2070 Sonopuls Ultrasonic Homogenizer (Bandelin, Germany) equipped with a GM 2070 generator (70 W, 20 kHz), an UW 2070 ultrasonic converter, a SH 70 GQ horn and GS 6 glass probe (6 mm), whose immersion was 1.5 cm. The applied power was 35% with 5 cycles. Simultaneously, the dissolutions were stirred continuously with a magnetized bar in a magnetic agitator. To avoid any cross contamination, after each experiment, the glass probe was sonicated with Milli-Q water during one minute at the same conditions as the samples.

To compare its performance against the EN 12457-2 method, 0.5 g of the RM steelmaking slag together with 20 ml of Milli-Q water were used (in the following tests 0.5 g of each steel slag were also used).

Later, in other leaching tests, 20 ml of acetic acid 0.11 M (100%, Merck) or 20 ml of nitric/hydrochloric acid 6.8M (69%/36%, Merck) were used as extractant instead of Milli-Q water, using the same FUS conditions, in order to perform a stronger extraction and to observe the leaching elements in more adverse conditions. Once the sonication was over, all the dissolutions were filtered with 0.45 μm filters (Whatman PVDF W/GMF) and stored in polypolyethylene vials of 50 ml. Again three replicates per sample and three blanks per extractant (water, acetic acid or nitric/hydrochloric acid) were carried out.

Finally, our leaching test with Milli-Q water was applied to several LDG and DG samples as an adequate accelerated weathering test.

3.3.4.3 pH and redox determination in the water extracts

The redox potential and the pH of the Milli-Q water extracts from the steel slag and impact glasses were also measured. This was carried out by using Crison electrodes. Crison 52-02 electrode for pH measurements provided with a AgCl reference electrode and Crison 52-61 for the redox potential which uses platinum as an indicator metal and AgCl as reference electrode.

3.3.4.4 Instruments for measuring leached ions

Owing to the nature of the leached ions, two quantitative techniques were used, ICP-MS for dissolved cations and IC for the dissolved anions.

(a) Inductively Coupled Plasma-Mass Spectrometry (ICP-MS): prior to the elemental quantification measurement, the dissolutions (different kind of extracts) were acidified until 1% of HNO_3, just to avoid equipment affections.

It was used an Elan 9000 ICP-MS spectrometer from PerkinElmer (Ontario, Canada), equipped with a Ryton cross-flow nebulizer, a Scott-type double pass spray chamber and standard nickel cones (see Fig. 3.11).

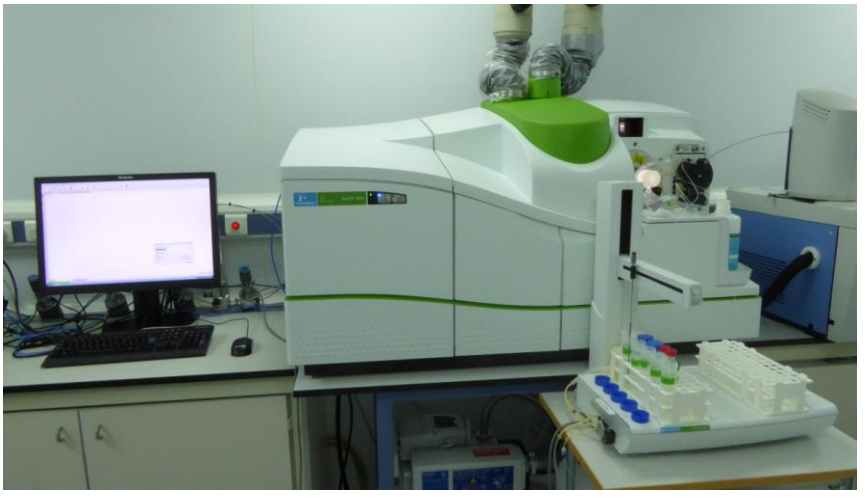

Fig. 3.11. Mass spectrometer.

The preparation of calibrates and the samples analysis were done inside a clean room (class 100). Calibrates were carried out by using standard solutions from Alfa Aesar (Specpure (Germany)). ^{9}Be, ^{45}Sc, ^{115}In and ^{209}Bi stock standard solutions (1000 mg/L in 5% HNO_3) (Specpure, Alfa Aesar, USA) were added to blank, standard and sample solutions as internal standard to yield a 10 µg/L concentration level. Argon (99.999%, Praxair, Spain) was used as carrier gas. Moreover, the accuracy of the analysis was checked using the RM steelmaking slag mentioned previously. And the precision associated to the used analytical method was estimated with the repetitions of the measurements of the studied elements in the sample replicas, according to the

previous analytical procedure. In the Table 3.2 are summarized the operating conditions for the quantitative analysis. The analysis and the data acquisition were performed using the Elan 3.2 software (Perkin Elmer, Ontario, Canada).

Table 3.2. ICP-MS analysis experimental conditions.

Variables	Experimental conditions
Plasma gas flow rate (L.min $^{-1}$)	15
Auxiliary gas flow rate (L.min $^{-1}$)	1
Nebulizer gas flow rate (L.min $^{-1}$)	0.8-0.9
Sample uptake rate (mL..min $^{-1}$)	1
RF power (W)	1100
Integration time (ms)	1000
Mass range (amu)	6-240
Data acquisition	Peak hopping
Dwell time (ms)	50
Sweeps per reading	3
Readings per replicate	1
Replicates per sample	3
Blanks per sample	3

It was measured the following elements in the steel slag samples: ^{107}Ag, ^{27}Al, ^{75}As, ^{11},B, ^{137}Ba, ^{43}Ca, ^{114}Cd, ^{59}Co, ^{52}Cr, ^{63}Cu, ^{57}Fe, ^{202}Hg, ^{39}K, ^{7}Li, ^{24}Mg, ^{55}Mn, ^{98}Mo, ^{23}Na, ^{60}Ni, ^{208}Pb, ^{78}Se, ^{121}Sb, ^{120}Sn, ^{88}Sr, ^{47}Ti, ^{51}V, ^{184}W and ^{66}Zn. Also, in the impact glasses it was analyzed the following Rare Earth Elements (REE): ^{139}La, ^{140}Ce, ^{141}Pr, ^{142}Nd, ^{152}Sm, ^{153}Eu, ^{158}Gd, ^{159}Tb, ^{164}Dy, ^{165}Ho, ^{166}Er, ^{169}Tm, ^{174}Yb, ^{175}Lu, ^{232}Th and ^{238}U.

Furthermore, given the different concentration ranges of the elements analysed in the acetic acid extractions of the steel slag samples, a second dilution (1:25) was necessary to determine the concentration of the major elements: Ca, Al, Ba, Fe, Mg, Mn and Na; in the case of nitric/hydrochloric acid extractions 1:45 (from a previous dilution of 1:28 used for the rest of the elements). Even, it was necessary to dilute the Milli-Q dissolutions of the RM slag (0.1:10) in both leaching tests to quantify Ca, Fe and Al.

The detection limits were calculated as three times the standard deviation of 8 replicates of the blank, taking into consideration the intercept and the slope of the calibration.

It could be thought the possible unreliability of determination of calcium by ICP-MS (in response to the isobaric interferences caused in the mass detector by the argon ions, which has a similar atomic mass, ~ 40 g/mol). However, according to the results of a previous thesis from our group, where a comparison of the Ca quantification data measured by ICP-MS and IC was performed, there are not significant differences (uncertainty around 10 %) between both analyses if the Ca concentrations are not too low[14].

Therefore, we measured Ca with ICP-MS because IC was more expensive and time consuming (sample and reagent consuming in this case). Moreover, the ICP-MS technique offers the possibility of carrying out the Ca study together with the rest elements measured. This implies that in a simple unique analysis we could obtain the concentration values of a wide range of elements, with the corresponding advantages regarding time effectiveness, reagent consumption, etc.

(b) Ionic Chromatography (IC): it was used a Dionex ICS 2500 Ion Chromatographic system (Thermo Fisher Scientific INC., Waltham, USA) connected to an AS40 autosampler (Dionex Corporation, Sunnyvaley, California, USA), which provided the automatic analysis of the sample series, and to a conductimetric detector (ED50 Dionex) with postcolumn suppression (Dionex Corporation, Sunnyvaley, California, USA). An IonPac AS23 (4x250 mm) column and an IonPac AG23 (4x50 mm) precolumn were used for the separation of anions, together with a mobile phase of 5 mM Na_2CO_3/0.8 mM $NaHCO_3$ (Merck), 25 mA of supression current and 1 ml/min flow (see Fig. 3.12).

This instrument was used to measure F^-, Cl^-, NO_3^-, Br^-, SO_4^{2-} and $C_2O_4^{2-}$ in the Milli-Q water extracts of the steel slag, LDG and DG samples prepared previously in the focused ultrasound leaching test. Three replicates and three blanks per type of steel slag and impact glass were analysed. Calibrates were preparing using standard solutions (1000 mg/l) from Fluka Analytical (Sigma Aldrich, USA). All data were acquired and integrated through Chromaleon 6.60-SPIa software (Dionex Corporation, Sunnyvaley, California, USA).

[14] N. Arrieta, The study of an unusual temperate latitude beachrock formation,PhD thesis, University of Basque Country (UPV/EHU), 2014.

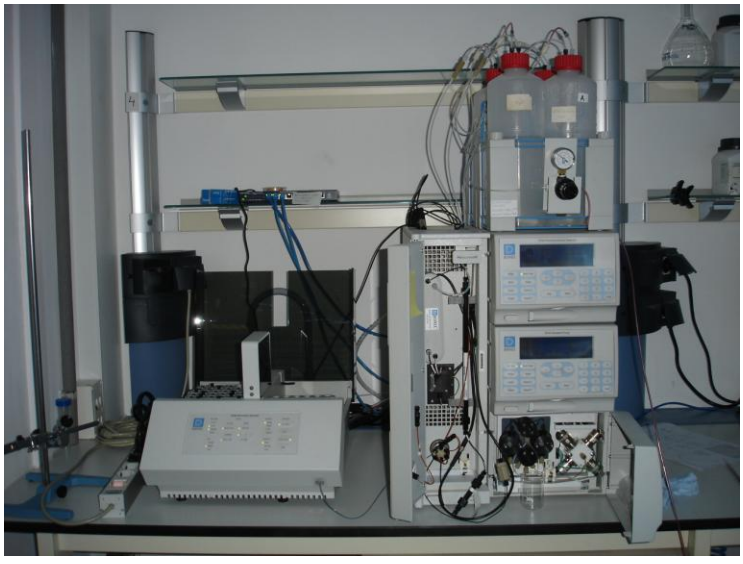

Fig.3.12. Dionex ICS 2500 Ion Chromatographic system with an ED50 conductivity detector coupled to an AS40 autosampler.

3.3.5 Characterization of organic compounds

Apart from the identification of organic compounds by Raman spectroscopy, it was also employed (a) Pyrolisis-Gas Chromatography-Mass Spectrometry (Py-GC-MS) over few grains of steel slag, LGD and DG samples and (b) Solid Phase Microextraction (SPME)/Head Space (HS)-GS-MS on the Milli-Q water extracts of the impact glasses.

(a) Pyrolisis-Gas Chromatography-Mass Spectrometry (GC-MS): the used equipment consisted of a Agilent 7890A gas chromatograph (Agilent Technologies, Palo Alto, CA, USA) coupled to a Agilent 5975C mass spectrometer (Agilent Technologies, Palo Alto, CA, USA). The solid samples were measured using Pyrolysis-GC-MS (Py-GC-MS).

Pyrolysis unit

Py-GC-MS was performed using a CDS PYROPROBE 5250 (Ingenieria Analitica, Spain) pyrolysis unit. The samples were contained in a 1 cm quartz tube which could be heated up by a 2–3 mm diameter platinum filament, and that enables a temperature increase up to 1200 °C at a heating rate of 20°C/ms. Every sample was subjected to the same pyrolysis program sequentially (the increase of temperature went from 280°C, 600°C and finally 750°C), and GC ran automatically under each temperature

step. The average weight charged into the pyrolysis unit was approximately 0.5 mg and occupied about 1–1.5 mm of the quartz tube. Quartz wool was properly packed at the top and bottom to avoid possible leakage, or that the sample being blown out. Three replicates of each sample were run. Moreover, the quartz tubes with quartz wool were employed like blanks, which did not show any significant chromatographic signal.

Initially, samples reached 50°C during 1 s and then, 100°C during 2 s in order to remove the humidity correctly. Afterwards, they reached the corresponding temperatures (280°C, 600°C and 750°C), keeping the sample for 15 s at each temperature. At the end of the process it was carried out a cleaning at 1200°C during 15 s. The evaporated samples were introduced into the analysis system through a transfer line at 300°C. Helium (flux of 1.7 ml/min) was used as the carrier gas for the GC-MS to purge off the air from the sample before pyrolysis, and send the gas generated during the course of pyrolysis to the GC for testing. Extracts were injected in the split mode to the GC-MS with a ratio of 1:10. The GC oven temperature program began with 2 min hold at 40°C followed by a temperature increase of 12°C/min to 330°C with a hold time of 5 min. The mass spectra were recorded in scan mode for m/z 40-550.

The identification of volatile compounds was performed by comparing the mass spectra of the peaks obtained with standard spectra of other compounds using the NISTOS database with which the equipment software itself is equipped (Chemstation), in order to obtain the most probable matches of retention times and mass spectra. The percentage was set at 70% match. Compounds from the chromatographic system or those with a signal lower than 0.1 % in percentage area were removed.

(b) Solid Phase Microextraction (SPME) and Head Space (HS)-Gas Chromatography-Mass Spectrometry (SPME/HS-GC-MS): the Milli-Q extracts obtained from the leaching tests on the LDG and DG samples were measured by SPME and HS injections coupled to Gas Chromatography and Mass Spectrometry detection (Agilent 7890A gas chromatograph (Agilent Technologies, Palo Alto, CA, USA) coupled to the Agilent 5975C mass spectrometer (Agilent Technologies, Palo Alto, CA, USA). According to the availability of the extracted samples, 2-5 ml of each LDG and DG Milli-Q water

extracts were taken. 3 ml of Milli-Q water were used as the blank solution in all the cases. All dissolutions and the blanks were injected following a standard procedure to detect volatile organic acids (VFA).

Solid Phase Microextraction (SPME) operation conditions

The Milli-Q dissolutions of the impact glasses were heated at 80°C during 5 min. After, the dissolutions with the SPME fiber (50/30m DVB/CAR/PDMS) inside were maintained at 80°C during 1 min. Then, the fiber was introduced into the injection port of the GC system for thermal desorption (1.5 min) before GC-MS analysis.

Head Space (HS) operation conditions

An Agilent Model G1888 Head Space Sampler (Agilent Technologies, Santa Clara, California, USA) was used, and the injection was carried out in the injection part of the GC-MS at 120°C.

In both cases, SPME and HS, the helium flux used as the carrier gas was set at 1.2 ml/min. The injection to the gas chromatograph, coupled to the mass spectrometer, was carried out considering splitless mode. The GC oven temperature program began with 3 min hold at 50°C with a heating rate of 12°C/min up to 250°C. Also, the GC is equipped with a DB-5 capillary column (30 m × 0.25 mm, 0.25 µm film thickness, Agilent Technologies) to the SPME and a capillary column 19091P-Q04 HP-PLOT/Q, 30 m x 0.32 mm x 20 µm (film) to the HS. Mass spectra were recorded in scan mode for m/z 50-550.

The identification of volatile compounds in the water extracts was performed by comparing the mass spectra of the peaks obtained with standard spectra of other compounds using the NIST12 database with which the equipment software itself is equipped (Chemstation), in order to obtain the most probable matches of retention times and mass spectra. The percentage was set at 70% match. However, in many cases the match was lower, so it was not possible to define the identity of a lot of chromatographic signals with reliability. Furthermore, in this case, the results of blank samples were taken into consideration because sometimes showed some

signal. Thus, compounds that may result from the chromatography column, the chromatography system itself or from the injection were not considered.

All these analyses of the organic compounds were performed by the SCAB unit (Servicio Central de Analisis de Bizkaia) of the SGIker (UPV/EHU).

3.4 CHEMOMETRICS AND STATISTICS

To obtain the maximum of the information from the results provided by some of the quantitative techniques, integrated chemometric analyses of all the dataset were also carried out.

The statistic treatment of the data was performed by means of Correlation Analysis (CA) and Principal Component Analysis (PCA), using The Unscrambler® Version 9.2 software (CAMO Process ASA, Trondheim, Norway)[15] and MATLAB 2010 with PLS Toolbox, version 7.0.2 (Eigenvector Technologies). CA was used to identify correlations between the studied variables, to characterize the samples and to help in the interpretation and the comprehension of the data. PCA is a multivariate statistical technique capable of discerning patterns and classify samples from large datasets[16-18].

3.5 CHEMICAL AND THERMODYNAMIC MODELING

The understanding of the terrestrial weathering on the studied materials requires the use of chemical based knowledge to interpret the experimental evidences.

In order to predict the formation of the some compounds present in the steel slag, LDG and DG, thermodynamic models were performed using information of stability constants included in the free academic software HYDRA (Hydrochemical

[15] Unscrambler v 9.2, Camo Process As., 2005, Norway.
[16] S. Fdez-Ortiz de Vallejuelo, Gorka Arana, Alberto de Diego, Juan Manuel Madariaga, Risk assessment of trace elements in sediments: The case of the estuary of the Nerbioi–Ibaizabal River (Basque Country), Journal of Hazardous Materials 181 (2010) 565–573.
[17] J. A. Carrero, I. Arrizabalaga, J. Bustamante, N. Goienaga, G. Arana, J. M. Madariaga, Diagnosing the traffic impact on roadside soils through a multianalytical data analysis of the concentration profiles of traffic-related elements, Science of the Total Environment 458-460 (2013) 427-434.
[18] A. Gredilla, S. Fdez-Ortiz de Vallejuelo, J.M. Amigo, A. de Diego, J.M. Madariaga. Unsupervised pattern-recognition techniques to investigate metal pollution in estuaries, Trends in Analytical Chemistry 46 (2013) 59-69.

Equilibrium-Constant) and Medusa 32 bit Version (Make Equilibrium Diagrams Using Sophisticated Algorithms)[19] to make chemical equilibrium diagrams.

These models must be based on the possible chemical reactions between original compounds present in the samples and some reactants present in the surrounding environment where the samples have been for years (few to millions of years depending on the samples).

[19] I. Puigdomenech, MEDUSA (Make Equilibrium Diagrams Using Sophisticated Algorithms), v-15; Department of Inorganic Chemistry, The Royal Institute of Technology, Stockholm, Sweden, 2012.

CHAPTER 4

ELEMENTAL AND MOLECULAR CHARACTERIZATION OF THE MATERIALS

In this chapter the elemental and molecular characterization of different materials produced at high temperature or/and pressure is described. These materials include: two impact glasses, Libyan Desert Glasses (LDGs) and Darwin Glasses (DGs), and several steel slags collected (a) directly from factories (after their dumping from the furnaces and after a short term treatment), (b) from different construction works few weeks after their deposition and (c) from two forest tracks where they had been used as filler around 18 and 34 years ago. For that purpose, a combination of analytical techniques was employed. In all the studied materials X-Ray Fluorescence and Raman micro spectroscopy were mainly used. Both techniques are non-destructive, which allowed us to conserve the materials (samples), especially the impact glasses to further analysis (positive aspect since they are samples that could not be acquired easily), do not require sample preparation and have the potential to undertake single inclusion analysis, often present in the case of impact glasses. X-Ray

Diffraction analysis, Scanning Electron Microscopy coupled to Energy Dispersive X-Ray, Electron Probe Micro Analysis, Structural and Chemical Analyser (SCA), X-Ray Photoelectron Spectroscopy and Pyrolisis-Gas Chromatography-Mass Spectrometry (Py-GC-MS) completed the characterization.

The use of Raman micro spectroscopy goes beyond with the possibility to determine the effect of the pressure, temperature, humidity, etc. over the mineral compounds present in the samples. This fact is possible because it can be distinguished characteristics Raman bands of hydrated compounds and those of H_2O and OH bonds and compounds associated to certain temperatures or pressure. Moreover, the detection of Raman bands displacements due to high-low pressure and temperature, which change the vibration modes of the molecular bonds and therefore the positions in Raman spectra[1], allows determining those pressures or temperatures in which the samples have been subjected. In addition, Raman spectroscopy allows us to differentiate polymorphs owing to their different vibrations caused by their different crystal structure[2].

The characterization of the impact glasses formed by the action of an extraterrestrial body and steel slags, considered like terrestrial analogues to meteorites and connected to impact glasses (both are formed at high temperatures), was performed also to evaluate analytical instrumentation that will be part in future exploratory missions to the Martian surface.

[1] G. Lucazeau, Effect of pressure and temperature on Raman spectra of solids: anharmonicity, Journal of Raman Spectroscopy 34 (2003) 478 – 496.
[2] A. A. Bunaciu, H. Y. Aboul-Enein, V. Dang Hoang, Vibrational spectroscopy used in polymorphic analysis, Trends in Analytical Chemistry (2015), http://dx.doi.org/doi:10.1016/j.trac.2015.02.006.

A. CHARACTERIZATION OF LIBYAN DESERT GLASS (LDG)

This part of the chapter was divided into external and internal characterization of the samples, due to the different methodologies used.

A.1. EXTERNAL CHARACTERIZATION

Several impact glass fragments found in Great Sand Sea of Libyan Desert (Egypt) (see Fig. 4.1), belonging to the Collection of Meteorites of the University of the Basque Country (UPV/EHU), were analyzed by Raman micro-spectroscopy (RS), assisted by X-Ray Diffraction (XRD) and Micro-Energy Dispersive X-Ray Fluorescence Spectroscopy (μ-EDXRF).

Despite the choices previously mentioned about RS and XRF, only a few of works have used X-Ray Fluorescence[3,4] and Raman spectroscopy to research the composition of LDG[3,5-9].

[3] A. Greshake, C. Koeberl, J. Fritz, W.U. Reimold, Brownish inclusions and dark streaks in Libyan Desert Glass: evidence for high-temperature melting of the target rock, Meteoritics and Planetary Science 45 (2010) 973-989.
[4] H.A. Sallam, N.A. Eissa, I. Dézsi, D.L. Nagy, Mössbauer effect study of Libyan Desert Silica Glass, Acta Physica Hungarica 57 (1985) 125-129.
[5] J.D. Kramers et al., Unique chemistry of a diamond-bearing pebble from the Libyan Desert Glass strewnfield, SW Egypt: Evidence for a shocked comet fragment, Earth and Planetary Science Letters 382 (2013) 21-31.
[6] M. Swaenen, E.A. Stefaniak, R. Frost, A. Worobiec, R. Van Grieken, Investigation of inclusions trapped inside Libyan desert glass by Raman microscopy, Analytical and Bioanalytical Chemistry 397 (2010) 2659-2665.
[7] A. Gucsik, C. Koeberl, F. Brandstätter, E. Libowitzky, M. Zhang, Infrared, Raman and cathodoluminescence studies of impact glasses, Meteoritics and Planetary Science 39 (2004) 1273-1285.
[8] J. F. McHone, M. Killgore, A. Kudryavtsev, Cristobalite inclusions in Libyan Desert Glass; confirmation using Raman spectroscopy, Abstracts of the Lunar and Planetary Science Conference 31 (2000) 1877.
[9] K. Halvorson, J. F. McHone, Vredefort, Coesite Confirmed with Raman Spectroscopy, Abstracts of the Lunar and Planetary Science Conference 23 (1992) 477.

Fig.4.1. Image of two studied LDG specimens belonging to the Collection of Meteorites of the University of the Basque Country (UPV/EHU).

The main aim of this part of the chapter was to characterize the surface of the LDG samples, both the matrix and the dark inclusions, in order to initiate us into the world of compounds formed under extreme conditions of temperature and pressure.

1. ELEMENTAL RESULTS

1.1 Micro-Energy Dispersive X-Ray Fluorescence Spectroscopy (μ-EDXRF)

The elemental analysis consisted of measurements over the LDG surface samples and revealed the presence of Si, K, Ca, Ti, Mn, Fe, and Sr, together with other elements like Al, V, Cl, Cu, Zn and S at trace levels, according to K_α lines (see Fig. 4.2). Most of the research works reported that the LDG matrix was composed mainly by Si[10-16], but

[10] M. Swaenen, E.A. Stefaniak, R. Frost, A. Worobiec, R. Van Grieken, Investigation of inclusions trapped inside Libyan desert glass by Raman microscopy, Analytical and Bioanalytical Chemistry 397 (2010) 2659-2665.
[11] J.A. Barrat, B.M. Jahn, J. Amosse, R. Rocchia, F. Keller, G.R. Poupeau, E. Diemer, Geochemistry and origin of Libyan Desert glasses, Geochimica et Cosmochimica Acta 61 (1997) 1953-1959.
[12] T. Aboud , Libyan Desert Glass: has the enigma of its origin been resolved?, Physics Procedia 2 (2009) 1425-1432.
[13] C. Cipriani, M. Corazza, G. Giuli, V. M. Cecchi, G. Pratesi, P. Rossi, E. Vittone, Ion beam study of a possible extraterrestrial body signature in Libyan desert glass, Nuclear Instruments and Methods in Physics Research Section B: Beam Interactions with Materials and Atoms 170 (2000) 187-192.
[14] A. Greshake, C. Koeberl, J. Fritz, W.U. Reimold, Brownish inclusions and dark streaks in Libyan Desert Glass: Evidence for high-temperature melting of the target rock, Meteoritics and Planetary Science 45 (2010) 973-989.
[15] A. Gucsik, C. Koeberl, F. Brandstätter, E. Libowitzky, M. Zhang, Infrared, Raman, and cathodoluminescence studies of impact glasses, Meteoritics and Planetary Science 39 (2004) 1273-1285.
[16] B. Kleinmann, P.Horn, F. Langehorst, Evidence for shock metamorphism in sandstones from the Libyan Desert Glass strewn field, Metoriritics and Panetary Sciences 36 (2001) 1277-1282.

here Ti, Mn and Fe (apart from Si, K, Sr and Ca of the silicate matrix) were clearly seen in the LDGs, together with Cl and S in some of the spectra.

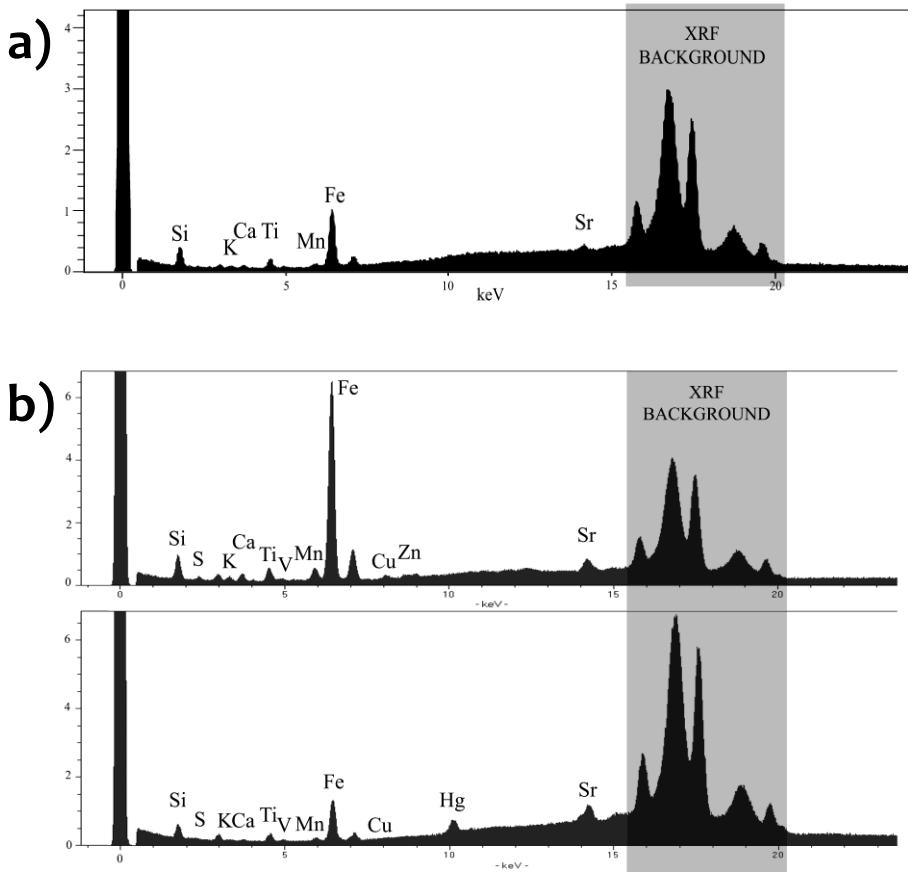

Fig. 4.2. Some μ-EDXRF spectra of LDGs: (a) matrix and (b) brownish inclusions.

In the case of the brownish inclusions, it was also observable that iron seemed to be linked to them due to the intensification of their signals in the μ-EDXRF analysis (see Fig.4.2.b), although Fe was also noticeable through the matrix in some occasions (see Fig. 4.2.a). Zn and Cu seem to be also related to the nature of the inclusions. The case of mercury was unique since it was detected only in a brownish-reddish inclusion (see Fig. 4.2.b). The presence of this element will be discussed later on.

2. MOLECULAR RESULTS

2.1 Raman Spectroscopy

More than 100 measurements were performed over the superficial matrix of the LDG samples by Raman analysis. In areas without any inclusions three different spectra were obtaining, depending on the matrix but also on the excitation laser used to obtain the Raman spectrum.

The first of them, obtained with the 785 nm excitation laser, presented three intense and broad (br) bands at 1374, 1554, and 1636 cm^{-1} (see Fig. 4.3). A second type of spectrum, also obtained with the same excitation laser, showed five Raman bands at 1277vs (very strong), 1382vs, 1517s (strong), 1662br and 1842br cm^{-1} (see Fig. 4.3) (this spectrum was close to that reported by M. Swaenen et al. (2010)[17] on other LDG samples).

The third one, obtained with the 514 nm excitation laser, presented bands at 447br, 602w (weak), 810br, 1061br and 1322br cm^{-1} (see Fig. 4.4), which was described in the same work mentioned before as having broad Raman bands around 480 and 820 cm^{-1} [17].

The bands in the 1200-1900 cm^{-1} range of the first two spectra (see Fig.4.3) are due to the luminescence emission produced by the effect of the red laser (785 nm) over transition metals or REE (Rare Earth Element), possibly present in the glassy matrix[18,19]. These spectral features were not observed with the green lasers (514 and 532 nm), so in all of the spectra collected with the 785 nm laser, those signals in the 1200-190 cm^{-1} range were not considered for characterisation purposes.

[17] M. Swaenen, E.A. Stefaniak, R. Frost, A. Worobiec, R. Van Grieken, Investigation of inclusions trapped inside Libyan desert glass by Raman microscopy, Analytical and Bioanalytical Chemistry 397 (2010) 2659-2665.
[18] J.A. Barrat, B.M Jahn, J. Amossé, R. Rocchia, F. Keller, G.R. Poupeau, E. Diemer, Geochemistry and origin of Libyan Desert glasses, Geochimica et Cosmochimica Acta 61 (1997) 1953-1959.
[19] T. Magna, A. Deutsch, K. Mezger, R. Skala, H.M. Seitz, J. Mizera, Z. Randa, L. Adolph, Lithium in tektites and impact glasses: Implications for sources, histories and large impacts, Geochimica et Cosmochimica Acta 75 (2011) 2137-2158.

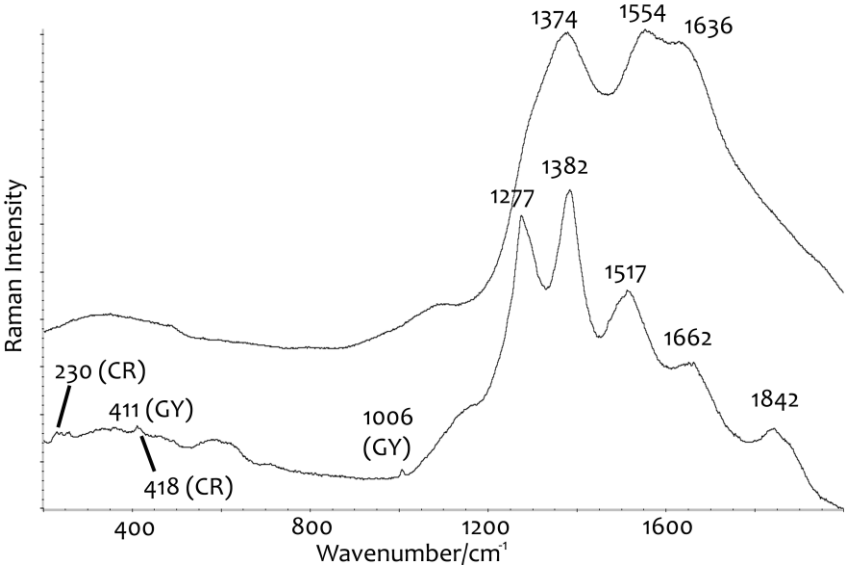

Fig. 4.3. Raman spectra of the matrix in two LDG specimens CR: cristobalite (α-SiO_2), GY: gypsum ($CaSO_4 \cdot 2H_2O$) (Laser: 785 nm).

The last Raman spectrum (see Fig. 4.4) can be considered the real one of the LDG matrix and it was obtained with the 514 nm laser. In some occasions, that spectrum varied a little bit with its Raman bands at 447br, 810br, 956br, 1049br, 1195br and 1630br cm^{-1}. Hence, we differentiated between spectrum A, the former, and spectrum B, this last one. In bibliography, the broad band at 447 cm^{-1} is claimed to be due to bending modes of the Si–O–Si bonds within the tetrahedral units; the band at 400–600 cm^{-1} varies with degree of polymerization of the glass and with Si-O-Si (and Si-O-Al) bridging bond angles[20], besides ~600 cm^{-1} band is ascribed to Si-O bending vibration modes. Near 800 cm^{-1} position involves symmetric motions of Si-O-Si bending and around 800-1200 cm^{-1} is associated with symmetric Si-O stretching vibrations. The doublet at 955 and 1052 cm^{-1} is specific of glassy matrix with alkali

[20] A. Gucsik, C. Koeberl, F. Brandstätter, E. Libowitzky, M. Zhang, Infrared, Raman and cathodoluminescence studies of impact glasses, Meteoritics and Planetary Science 39 (2004) 1273-1285.

content; and finally the band at 1630 cm^{-1} seems to be related with the presence of H-O-H bonds[21-23]. Although these last spectra have not been identified before in previous works, their wavenumbers and the presence of broad bands indicated the amorphous nature of the glass bulk.

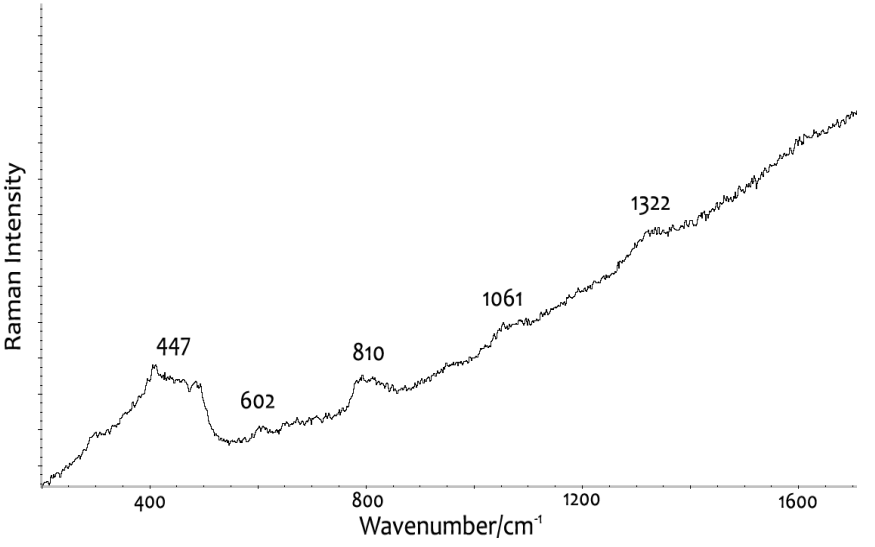

Fig. 4.4. Raman spectra of the LDG matrix (Laser: 514 nm).

Colomban et al. used the Raman intensity of these broad bands to determine the degree of crystallisation of amorphous/crystalline silicates glasses as well as their temperatures of formation[24-26]. They defined the Polymerization index (I_p) as the ratio of the areas under the broad bending band (~ 500 cm^{-1}) and the stretching band (~ 1000 cm^{-1}) of the silicate group, because that ratio is strongly correlated to the processing temperature[26]. In our case, two different ranges of index were found in

[21] E. Faulques, E.Fritsch, M. Ostroumov. Spectroscopy of natural silica-rich glasses. Journal of Mineralogical and Petrological Sciences 96 (2001) 120-128.
[22] M. Swaenen, E.A. Stefaniak ,R. Frost, A.Worobiec, R.Van Grieken, Investigation of inclusions trapped inside Libyan Desert glass by Raman microscopy, Analytical and Bioanalytical Chemistry 397 (2010) 2659–2665.
[23] W. B. White, D.G. Minser, Raman spectra and structure of natural glasses, Journal of Non-Crystalline Solids 67 (1984) 45–59.
[24] P.Colomban, A. Slodczyk, Raman intensity: An important tool to study the structure and phase transitions of amorphous/crystalline materials, Optical Materials 31 (2009) 1759–1763.
[25] P. Colomban. Polymerization degree and Raman identification of ancient glasses used for jewelry, ceramic enamels and mosaics, Journal of Non-Crystalline Solids 323 (2003) 180–187.
[26] P. Colomban, Raman spectroscopy in archaeology and art history, Case study: glasses, glazes and ceramics: recognition of ancient technology from the Raman spectra, In Raman spectroscopy in archaeology and art history (eds H. G. M. Edwards & J. M. Chalmers), 192–206. New York, NY: Marcel Dekker, 2000.

the LDG matrix. In the matrix spectrum *A*, I_p was in the range of 6.1-6.8 (<7), typical of glasses formed at 600-1400ºC. And in the matrix spectrum *B*, I_p was in the range of 10.2-16.9, which corresponds to a greater glass formation temperature than 1400ºC.

It was described that siliceous sandstones of the Libyan Desert were transformed into glass without involving melting at 40-60 GPa[27] as a consequence of the impact from a high velocity bolide. However, at temperature higher than 1700ºC, the silica glass is transformed to silica melt (as a supercritical fluid). Therefore, the two different spectra of amorphous silica in the matrix of our LDGs, as it has been differentiated with the Polymerization index, can be considered as an indication of the complex process leading to the formation of the LDG samples.

Furthermore, through the matrix clear signals of anatase (TiO_2, main Raman band at 143s cm^{-1}), α-cristobalite (SiO_2; Raman bands at 230vs and 418vs cm^{-1} as seen in Fig. 4.3), gypsum ($CaSO_4{\cdot}2H_2O$; Raman bands at 411w and 1006w cm^{-1} as seen in Fig. 4.3) and coesite (SiO_2; Raman bands at 270vw and 521sh (shoulder) cm^{-1}), together with a microcline feldspar ($KAlSi_3O_8$; Raman bands at 328vw, 406w, 513m and 1096vw cm^{-1}), were detected.

The presence of α-cristobalite proves that the temperature of glass formation was above 1470ºC[28], supporting the hypothesis of a high-temperature fusion process caused by an impact structure[29,30]. Coesite is a silica polymorph produced at high pressures (>30GPa)[31-33], commonly present in materials from large-scale impact craters[31]. These pressures are not created during volcanic or tectonic processes in the Earth's crust, so the presence of coesite is also a strong indication of production

[27] A. Gucsik, C. Koeberl, F. Brandstätter, E. Libowitzky, M. Zhang, Infrared, Raman and cathodoluminescence studies of impact glasses, Meteoritics and Planetary Science 39 (2004) 1273-1285.
[28] D.C. Smith, J.D. Vernioles, The Temperature of Fusion of a Celtic Vitrided Fort: a Feasibility Study of the Application of the Raman Microprobe to the Non-Destructive Characterization of Unprepared Archaeological Objects, Journal of Raman Spectroscopy 28 (1997) 195-197.
[29] T. Aboud, Libyan Desert Glass: has the enigma of its origin been resolved?, Physics Procedia 2 (2009) 1425-1432.
[30] M. Ramirez-Cardona, A. El-Barkooky, M. Hamdan, K. Flores-Castro, N.I. Jimenez-Martinez, M. Mendoza-Espinosa, On the Lybian Desert Silica Glass (LDSG) transport model from a hypothetical impact structure, International Geological Congress Oslo 2008, PIS-01.
[31] G.P.Sighinolfi, C. Elmi, R. Serra, G. Contini, High density silica phases as evidence of small-scale hypervelocity impacts: the Gebel Kamil Crater (Egypt), Periodico di Mineralogia 83 (2014) 299-312.
[32] J.T. Wasson, Large Aerial Bursts: An Important Class of Terrestrial Accretionary Events, Astrobiology 3 (2003) 163-179.
[33] T. Henderson, K. A. Milam, XRD analyses of silurian dolostones from the central uplift of the Kentland impact structure, Newton County, Indiana, USA, 46th Lunar and Planetary Science Conference (2015) 2989.

during an extraterrestrial impact[32]. Under normal conditions, rocks in Earth's crust and upper mantle are subjected to static load pressures produced by the weight of overlying rocks. These pressures are less than a few gigapascals[34]. The rapid release of large amounts of energy in impact events puts too much sudden stress on the target rocks for them to respond in the normal way[34]. Typical impact velocities of tens of kilometers per second far exceed the velocities of sound in the target rocks (typically 5–8 km/s), where the resulting impact-produced shock waves travel through the target rocks at supersonic velocities, and they impose intense stresses on the rocks without giving them time to give way by normal deformation[34]. In the shock-wave environment, momentary pressures may exceed 500 GPa at the impact point and may be as high as 10–50 GPa throughout large volumes of the surrounding target rock[33]. At >60 GPa, shock-produced temperatures can exceed 2000°C, and immediately after the shock wave has passed, a rapid large-scale melting occurs[34].

In the analysis of the brownish inclusions α-quartz (SiO_2; Raman bands at 205m (medium), 263w, 354w, 398vw, 464vs, 696vw, 806w, 1081w and 1160vw cm^{-1}; as seen in Fig. 4.5) and also α-cristobalite (SiO_2; Raman bands at 230vs and 418vs cm^{-1} as seen in Fig. 4.6) were found. Both compounds are typically found in LDG samples[35-38]. However, in spite of being α-cristobalite the silica form most often mentioned as LDG inclusion[36], in this work, α-quartz was identified more frequently in the inclusions near the studied LDG surfaces. This α-quartz can be converted to coesite at >30 GPa[34]. Thus, it seems like the α-quartz trapped was partially converted to α-cristobalite and/or coesite.

[34] B. M. French, Traces of Catastrophe: A Handbook of Shock-Metamorphic Effects in Terrestrial Meteorite Impact Structures, Lunar and Planetary Institute (1998), LPI Contrib. No 954, Houston.
[35] G. Giuli, E. Paris, G. Pratesi, C. Koeberl, C. Cipriani, Iron oxidation state in the Fe- rich layer and silica matrix of Libyan Desrt Glass: A high- resolution XANES study, Meteoritics and Planetary Science 38 (2003) 1181-1186.
[36] M. Swaenen, E.A. Stefaniak, R. Frost, A. Worobiec, R. Van Grieken, Investigation of inclusions trapped inside Libyan desert glass by Raman microscopy., Analytical and Bioanalytical Chemistry 397 (2010) 2659-2665.
[37] T. Magna, A. Deutsch, K. Mezger, R. Skála, H.M. Seitz, J. Mizera, Z. Řanda, L. Adolph, Lithium in tektites and impact glasses: Implications for sources, histories and large impacts, Geochimica et Cosmochimica Acta 75 (2011) 2137-2158.
[38] A. Longinelli, G. Sighinolfi, V. Michele, E. Selmo, δ18 O and chemical composition of Libyan Desert Glass, country rocks, and sands: New considerations on target material, Meteoritics and Planetary Science 46 (2011) 218–227.

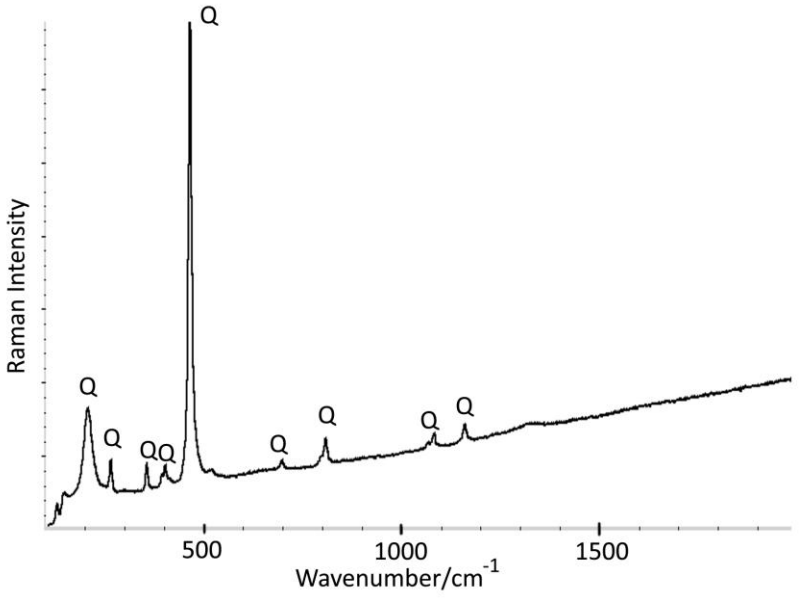

Fig. 4.5. Raman spectrum of quartz (Q) identified in a brownish inclusion of the LDG surface. (Laser: 785 nm).

Moreover, other compounds were identified in the brownish inclusions: anhydrite ($CaSO_4$; main Raman bands at 1018w and 1161w cm^{-1}), amorphous carbon (C; Raman bands at ≈1300br and ≈1600br cm^{-1}), corundum (α-Al_2O_3, Raman band at 416m cm^{-1} as seen in the deconvolution of Fig. 4.6), which is the most thermodynamically stable form of aluminum oxide at all temperatures and whose transformation from metastable phases of alumina occurs at a high temperature (over 1000-1200 °C)[39], and also anatase (TiO_2, main Raman band at 143s cm^{-1}), which reverts to rutile (TiO_2) at temperatures around 800-900°C[40-42].

[39] Y. Wang, C. Suryanarayana, L. An, Phase Transformation in Nanometer-Sized γ-Alumina by Mechanical Milling, Journal of the American Ceramic *Society* 88 (2005) 780–783.
[40] M. Swaenen, E.A. Stefaniak, R. Frost, A. Worobiec, R. Van Grieken, Investigation of inclusions trapped inside Libyan desert glass by Raman microscopy., Analytical and Bioanalytical Chemistry 397 (2010) 2659-2665.
[41] C. Zeng, Y. Ling, S. Li, Y. Rao, Y. Chen, The effect of chromium on the gamma to alpha phase transition of alumina coating formed on 316L SS by a cathodic micro arc deposition (CMAD) process, Surface and Coatings Technology 263 (2015) 15-20.
[42] V.B. Tezza, M. Scarpato, L.F.S. Oliveira, A.M. Bernardin, Effect of firing temperature on the photocatalytic activity of anatase ceramic glazes, Powder Technology 276 (2015) 60–65.

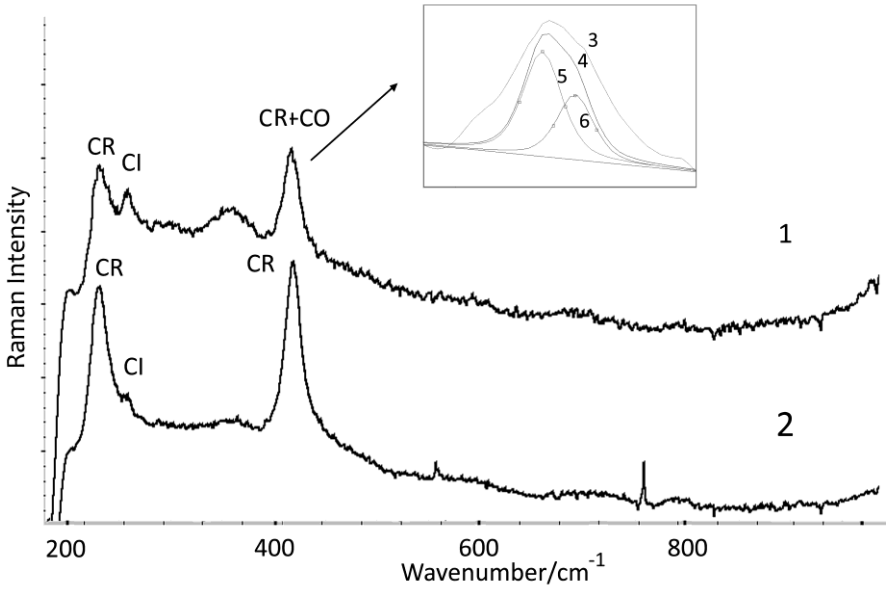

Fig. 4.6. Raman spectra of CR: cristobalite, CI: cinnabar and CO: corundum identified in the brownish inclusions of the LDG surfaces. (Laser: 785 nm).

On the other hand, new compounds not determined in other studies were found in our study of the LDG samples. Regarding the brownish inclusions the next compounds were identified: calcite ($CaCO_3$; Raman bands at 153w, 279m, 710w and 1085vs cm^{-1}; see Fig. 4.7), magnesite ($MgCO_3$; Raman bands at 330w, 739w and 1095m cm^{-1}) and cinnabar (HgS; main Raman band at 252m cm^{-1}; see Fig. 4.6), which was uniquely detected in a brownish-reddish inclusion but in several measurements. Indeed, this inclusion analyzed by μ-EDXRF gave also the Hg signal (see Fig. 4.2). This sulfide could be a compound belonging to the sediments of the environment that has been adhered to the surface of the LDG, but it has not been changed to other form (the melting of sulfide minerals may also provide evidence of unusually high impact-produced temperatures[43]) because the temperature at the moment of its trapping was not highly enough.

[43] B.M. French, Christian Koeberl, The convincing identification of terrestrial meteorite impact structures: What works, what doesn't, and why, Earth-Science Reviews 98 (2010) 123-170.

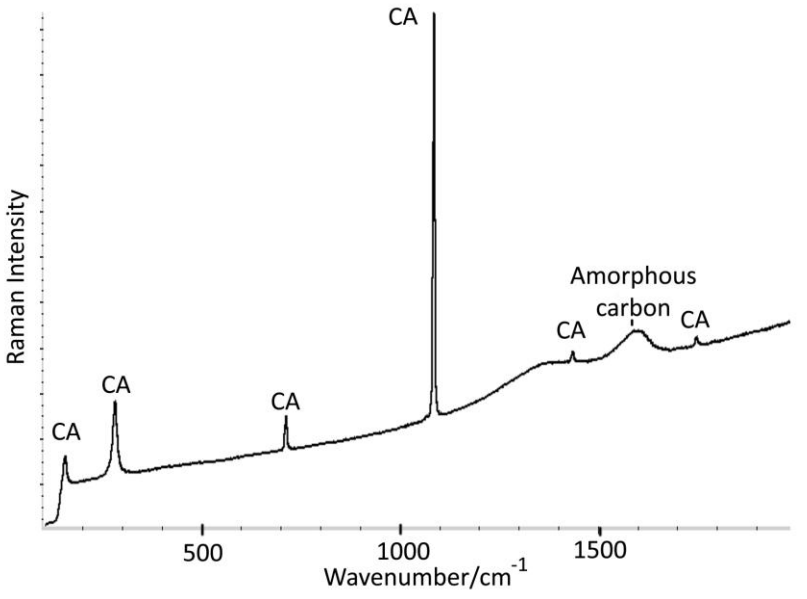

Fig. 4.7. Raman spectrum of calcite (CA) and amorphous carbon identified in a brownish inclusion of the LDG surface. (Laser: 785 nm).

Calcite ($CaCO_3$) (and dolomite, $CaMg(CO_3)_2$) are the most common species, occurring as the principal mineral components in limestone and Mg-rich limestone sedimentary rocks. Carbonate minerals have limited stability at high temperature unless high carbon dioxide (CO_2) pressure exists. This explains their great presence in environments near the Earth's surface and in sedimentary rocks. On heating to sufficiently high temperature, carbonate minerals decompose, giving off CO_2 gas and forming a metal oxide or a mixed solid. The temperature at which decarbonation occurs varies with mineral composition and CO_2 pressure, among other factors. At ambient pressure in air, calcite and magnesite begin to decompose at approximately 700 and 500°C, respectively. Consequently, carbonate minerals generally persist under high-temperature conditions only when sufficiently deep in the crust that the high confining pressure prevents decomposition[44].

It is remarkable that the age in which the LDG impacted the Earth coincided with Oligocene, the age when the drainage system was active. Therefore, the identified carbonates could belong to the Gilf fluvial system soils and could have been trapped into the external structure of LDG after a second or third impact, when the melted

[44] R.J. Reeder, Carbonate Minerals. McGraw-Hill Encyclopedia of Science & Technology 3, 10th ed. New York: McGraw-Hill Companies, Inc. 2007.

fragments were still flying whilst cooling after the first impact, in the surrounding soils/rocks.

One of the most astonishing finding occurred in one superficial inclusion, where a spectrum with Raman bands at 462vw, 635w, 724w, 860vw, 1101w, 1189w, 1273w, 1367br, 1443w, 1464sh, 1608s, 1716m, 2871sh, 2937vs and 3074m cm^{-1} (see Fig. 4.8) was found. A similar spectrum has not been described in previous studies of LDG materials. The spectrum exhibited peaks in the range about 3000-3100 cm^{-1}, characteristic of aromatic C-H stretching modes; the range from 1300-1650 cm^{-1} includes various aromatic C-C stretching vibrations and the range from approximately 1000 to 1250 cm^{-1} contains bands commonly attributed to C-H bending modes. All of these modes can be assigned to polycyclic aromatic hydrocarbons (PAHs) [45-47].

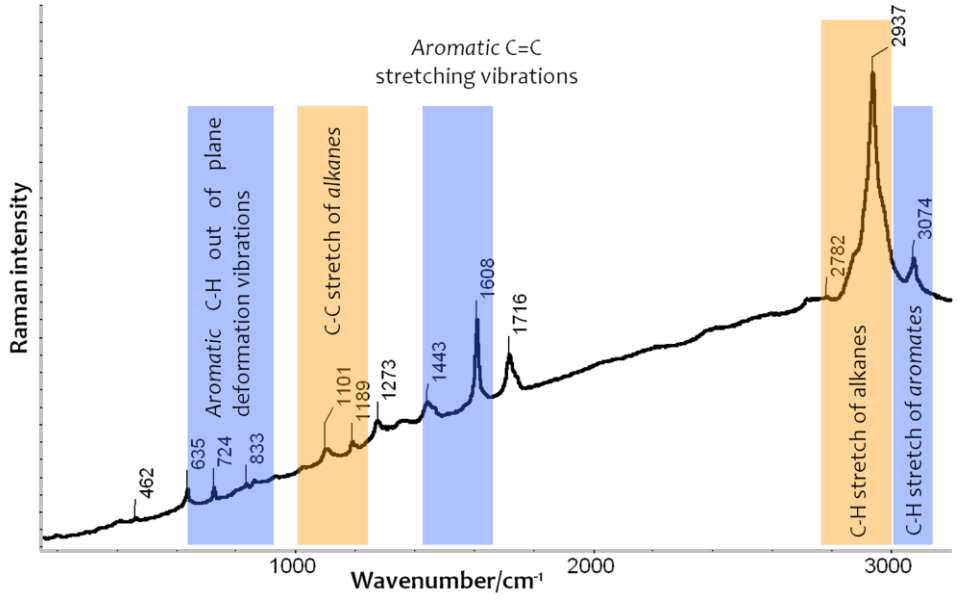

Fig.4.8. Raman spectrum of a possible organic compound in LDG sample (Laser: 514nm).

[45] L. Colangeli, V. Mennella, G.A. Baratta, . Bussoletti, G. Strazzulla. Raman and Infrared specta of polycyclic aromatic hydrocarbon molecules of possible astrophysical interest. The astrophysical Journal 396 (1992) 369-377.

[46] O. Frank, J. Jehlicka, H. G. M. Edwards, Raman spectroscopy as tool for the characterization of thio-polyaromatic hydrocarbons in organic minerals, Spectrochimica Acta A 68 (2007) 1065-1069.

[47] L. Colangeli, V. Mennella, G.A. Baratta, E. Bussoletti, G. Strazzulla, Raman and ingrared spectra of plycyclic aromatic hydrocarbon molecules of possible astrophysical interest, The Astophysical Journal 396 (1992) 369-377.

The origin of these hydrocarbons in the LDG should be attributed to a terrestrial natural source. Organic matter present in the desert sands can be transported by winds, migrate within and between the atmosphere, and interchange between the soil and aquatic compartments[48]. Incomplete oxidation (low temperature combustion) processes of such organic matter (enormous gradients in temperature during thousands or millions of years) would act as precursors of such PAHs. But PAHs leaching and biological or chemical degradation processes, which may be influenced by environmental factors, can play also an important role in the decomposition of the initially trapped PAHs in the LDGs[49-51]. According to Howard et al. (2013) the organic components inside impact glass were trapped into the impact melt and preserved when the melt quenched to glass, avoiding the organic decomposition since the impact[52]. Moreover, the occurrence of PAHs in non-common materials has been reported in the literature, like in amorphous superheated glassy mineraloid[53], asteroid, comet and meteorites[54].

In another dark inclusion of the analysed LDG surfaces a Raman spectrum showing only a band at 1572m cm^{-1} was found, suggesting the presence of a high ordered fullerene-type compound. This is supported by several studies collected in literature. These ordered structures have been observed in C_{60} single crystals of fullerene subjected to pressure or in the 3D-polymerization of C_{60} and C_{70} fullerenes at 15 GPa and 670 K conducting to a material that has only one Raman band at 1572 cm^{-1} [55,56]. Some Raman studies on the so-called onion-like fullerene spherical nanostructures have identified also a Raman band at 1572 cm^{-1} when a high degree of structural

[48] C. Balducci, R.Ladji, V. Muto, P. Romagnoli, N. Yassaa, A. Cecinato. Biogenic and anthropogenic organic components of Saharan sands. Chemosphere 107 (2014) 129–135.
[49] B. Maliszewska-Kordybach, The effect of temperature on the rateo of disappearance of PAHs from soils, Environmental Pollution 79 (1993) 15-20.
[50] A.K. Haritash, C.P. Kaushik, Biodegradation aspects of Polycyclic Aromatic Hydrocarbons (PAHs): A review, Journal of Hazardous Materials 169 (2009) 1–15.
[51] G. Purcaro, S.Moret, L. S. Conte, Overview on polycyclic aromatic hydrocarbons: Occurrence, legislation and innovative determination in foods, Talanta 105 (2013) 292-305.
[52] K. T. Howard, Biomass preservation in impact melt ejecta, Nature Geoscience 6 (2013) 1018-1022.
[53] E. A. Carter, M.D. Hargreaves, T.P. Kee , M. A. Pasek , H. G. M. Edwards. A Raman spectroscopic study of a fulgurite. Philosophical Transactions of the Royal Society A 368 (2010) 3087-3097.
[54] M.R. Wing. J. L. Bada, The origin of the polycyclic aromatic hydrocarbons in meteorites, Origins of Life and Evolution of the Biosphere 21 (1992) 375-383.
[55] S.Porwal, A. Diwedi, M. Kamal. 13C NMR and Raman Studies of Fullerene-Based Poly (Acrylamides). International Journal of Organic Chemistry 2 (2012) 377-386.
[56] V.D. Blank, S.G. Buga, G.A. Dubitsky, N.R. Serebryanaya, V.M. Prokhorov, B.N. Mavrin, V.N. Denisov, L.A. Chernozatonskii, S. Berezina, V.M. Levin, Synthesis of superhard and ultrahard materials by 3D-polymerization of C60, C70 fullerenes under high pressure (15 Gpa) and temperatures up to 1820 K, Zeitschrift für Naturforschung 61b (2006) 1547-1554.

perfection of the graphitic network is attained, like subjecting nanodiamonds to temperatures in the range 1800-1900 K [57,58].

Two inorganic compounds found in inclusions of the matrix surface, gypsum and microcline feldspar previously mentioned, require an especial comment. Feldspar glasses are widespread constituents of terrestrial, lunar and meteoritic impact formations[59]. However, our detected microcline feldspar may come from the material that was trapped into the matrix, or can be a compound belonging to the body that impacted with the Earth surface. This last aspect is not clear because it was not possible to identify microscopically if our compound has deformation features due to the impact[60].

Regarding gypsum, on one side, we may assign its bands to normal gypsum according to bibliography[61]. It would have adhered from the soil to the LDG surface after the second or third impact during the cooling or whenever in the LDG existence. On the other hand, Knittle et al. (2001)[62] assigned its 1006 cm^{-1} Raman peak to low pressure (around 6 GPa) gypsum; so it could be trapped during the successive impacts after the first one. It is also conceivable that the pressures of these subsequent impacts were much lower. To sum up, as gypsum appeared with cristobalite (see Fig. 4.3), which involves high temperatures (1470°C) while gypsum starts to lose the crystallization waters at around 100°C[63], then it could be trapped after the first impact (formation of cristobalite at high temperature). Other option could be the formation of gypsum as a secondary product from a soluble anhydrite hydration with time. This anhydrite could be terrestrial or pre-terrestrial, and could be formed by extreme heating from gypsum trapped during the first impact as well.

[57] D. Obraztsova, M. Fujii, S. Hayashi, V.L. Kuznetsov, Yu.V. Butenko, A.L. Chuvilin, Raman identification of onion-like carbon, Carbon 36 (1998) 821-826.
[58] V.L. Kuznetsov and Yu.V. Butenko, Nanodiamond graphitization and properties of onion-like carbon, in D.M. Gruen, O.A. Shenderova and A.Y. Vul eds. Synthesis, Properties and Applications of ultracrystalline diamong, pp. 199-216, Springer, Amsterdam, The Nederlands, 2005.
[59] D. Stoffler, U. Hornemann, Quartz and Feldspar Glasses Produced by Natural and Experimental Shock, Meteoritics 7 (1972) 371-394.
[60] B. M. French, Traces of Catastrophe: A Handbook of Shock-Metamorphic Effects in Terrestrial Meteorite Impact Structures, Lunar and Planetary Institute (1998), Houston, LPI Contrib. No 954.
[61] H. G. M. Edwards, F. Sadooni, P.Vitek, J. Jehlicka, Raman spectroscopy of the Dukhan sabkha: identification of geological and biogeological molecules in an extreme environment, Philosophical Transactions of the Royal *Society A* 368 (2010) 3099-3107.
[62] E. Knittle, W. Phillips, Q. Williams, An infrared and Raman spectroscopic study of gypsum at high pressures, Physics and Chemistry of Minerals 28 (2001) 630-640.
[63] P.S.R. Prasad, A. Pradhan, T.N. Gowd, In situ micro- Raman investigation of dehydration mechanism in natural gypsum, Current Science 80 (2001) 1203-1207.

More analysis inside the LDG samples was necessary to deep in this topic. In addition, calcium sulphates present in the LDG surface could have been formed by the reaction of the LDG superficial carbonates and the atmospheric SO_x.

All compounds with their Raman bands identified in the surface of the LDG samples are summarized as follows in Table 4. 1.

Table 4.1. Raman characteristic bands of mineral compounds found in LDG.

Compound	This study (Wavenumber/cm^{-1})	Other LDG studies (Wavenumber/cm^{-1})
LDG matrix	447br, 602w, 810br,956br,1049br,1061br,1195br, 1322br,1630br	Glassy matrix: 480br, 820br[64]
Coesite (SiO2)	270vw, 521sh	Not found by Raman
α-Quartz (SiO_2)	205m, 263w, 354w, 398vw, 464vs, 696vw, 806w, 1081w, 1160vw	208w, 465m[64]
α-Cristobalite (SiO_2)	230vs, 418vs	230s, 418s, 780w, 1076w[65]
Rutile (TiO_2)	Not found	445m, 607s[64]
Anatase (TiO_2)	143s	142vs, 227vw, 395vw, 515vw, 637w[64]
Gypsum ($CaSO_4 \cdot 2H_2O$)	411w, 1006w	Not Found
Anhydrite ($CaSO_4$)	1018w, 1161w	418vw, 1018vs, 1130w[64]
Zircon ($ZrSiO_4$)	Not found	1147s, 1201vs, 1223vs[64]
Amorphous carbon	≈1300br, ≈1600br	≈1300br, ≈1600br[64]
Fullerene	1572s	Not Found
Microcline feldspar ($KAlSi_3O_8$)	328vw, 406w, 513m, 1096vw	Not Found
Cinnabar (HgS)	252m	Not Found
Corundum (Al_2O_3)	416m	Not found by Raman
Calcite ($CaCO_3$)	153w, 279m, 710w, 1085vs	Not Found
Magnesite ($MgCO_3$)	330w, 739w, 1095m	Not Found

***** br: broad, v: very, w: weak, m: medium, s: strong

[64] M. Swaenen, E.A. Stefaniak, R. Frost, A. Worobiec, R. Van Grieken, Investigation of inclusions trapped inside Libyan desert glass by Raman microscopy, Analytical and Bioanalytical Chemistry 397 (2010) 2659-2665.

[65] A. Greshake, C. Koeberl, J. Fritz, W.U. Reimold, Brownish inclusions and dark streaks in Libyan Desert Glass: evidence for high-temperature melting of the target rock, Meteoritics and Planetary Science 45 (2010) 973-989.

2.2 X-Ray Diffraction (XRD)

The XRD analysis of the LDGs was carried out over a portion of its matrix, without inclusions, in order to know more about its mineral phases. Unfortunately, there was not XRD signals and any mineral compound could be identified. In conclusion, the matrix is almost completely amorphous, vitreous.

The presence of non-crystalline phases can be other parameter, apart from high pressure-temperature phases, to identify structures formed during impact thermal metamorphism[66].

The crystalline phases present in the inclusions of the matrix are not major materials, thus they did not appear in the diffractograms, although Raman spectroscopy identified them (see Table 4.1), probably because it was possible to measure Raman properties at micro scale level, increasing the possibilities to identify the given mineral phases.

3. DISCUSSION

The combination of μ-EDXRF and Raman spectroscopy was an excellent analytical approach since it allowed us to characterize the surface of the LDG samples and to identify new compounds for high-temperature glasses that have not been heretofore described (gypsum, microcline feldspar, calcite, magnesite and cinnabar) in the literature. The XRD analysis was not so useful for this kind of samples.

The μ-EDXRF analyses supported the presence of α-quartz, α-cristobalite, coesite, microcline feldspar, anatasa, anhydrite, gypsum, calcite, corundum and cinnabar, identified by Raman measurements. In spite of the evident presence of Fe, any iron compounds were identified in the LDG surface.

In the brownish inclusions it was possible to find α-quartz, α-cristobalite, calcite, and occasionally amorphous carbon, magnesite, anatase, anhydrite, corundum and cinnabar. They could indicate that the trapping process continue after the first

[66] G. P.Sighinolfi, C. Elmi, R. Serra, G. Contini, High density silica phases as evidence of small-scale hypervelocity impacts: the Gebel Kamil Crater (Egypt), Periodico di Mineralogia 83 (2014) 299-312.

impact (α-cristobalite requires high temperature to be formed from quartz), when thousands of melt fragments start flying and impacting again with the soil/sand/rock, trapping new materials if the melt was still liquid enough to catch them as inclusions, till just before the end of the cooling process. Thus, we can imagine two, three or more impacts for each melt fragment (each new one having lower temperature and pressure than the previous one) until the formation of the current glass phases of the recovered LDG objects.

The identification of PAHs compounds through Raman analysis must be highlighted, reinforcing the idea of the presence of organic molecules in the LDGs.

Moreover, it was detected the presence of a fullerene-type compound in a black inclusion sustains, compound that can be formed at high temperatures (> 1800K) or at low temperature and medium pressure (15 GPa and 670K).

As for the matrix, its Raman bands were different from those reported in other studies[67]. This fact can be due to the width of the broad bands, since all are in the same range of wavenumbers (around 400 and 800 cm^{-1}). Also, it was seldom distinguished gypsum and anatase through it.

A.2. INTERNAL CHARACTERIZATION

In this part we present a detailed study of LDG samples using an integrated methodology of several techniques such as optical microscopy, cathodoluminescence, Electron Microscopy-Energy Dispersive X-Ray Spectroscopy (SEM-EDX), Electron Microprobe Analysis (EPMA), Micro-Energy Dispersive X-Ray Fluorescence (μ-EDXRF) and Raman spectroscopy.

Due to the size and the irregularities of the studied specimens, it was not possible to analyze the external part (surface) of the LDGs with SEM-EDX. Therefore, the elemental data in the external areas were acquired only with μ-EDXRF (as it has been

[67] M. Swaenen, E.A. Stefaniak, R. Frost, A. Worobiec, R. Van Grieken, Investigation of inclusions trapped inside Libyan desert glass by Raman microscopy, Analytical and Bioanalytical Chemistry 397 (2010) 2659-2665.

seen in the Chapter 4: Part A.1). However, after slicing and polishing, SEM-EDX can be used to analyze the inner matrix and their inclusions.

All the techniques allowed the detection and comparison of different elements and compounds located in the inner and outer part of LDG specimens, which provided some clues about their origin.

After LDG lamination, in the inner part it could be observed that the brownish inclusions were not so widely spread, whereas whitish inclusions enclosed in the matrix could be easily perceived and predominated over the brownish ones (Fig. 4.9). Moreover some discarnate little dark inclusions were microscopically observed (see Fig. 4.9.c).

Thus, in this part of the chapter it was differentiated between the inner matrix and whitish, brownish and dark inclusions analysis. In some occasions measurements were performed close to the LDG border in order to have information of the surface. But, those cases are emphasized all along the text.

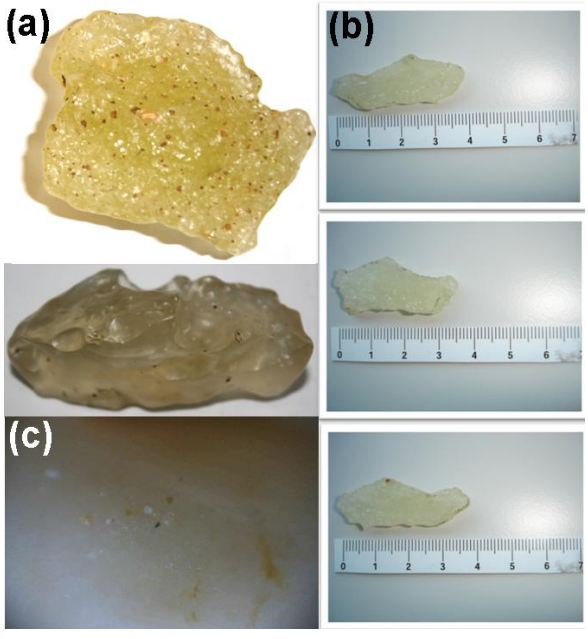

Fig. 4.9. Photographs of (a) two of the studied LDGs, (b) thick sections of a LDG and (c) microimage of one of the studied thick sections (5 mm width).

The results now present are separated in matrix, inclusions and bubbles analyses, to enhance their comprehension.

1. INNER MATRIX OF THE LDGS

Comparing the EDXRF spectra of the inner matrix and the superficial one, Si was the main element, and the main difference was in the relative presence of the elements. Fe, Sr and Ti presented higher signals in the inner matrix than in the surface, and in contrast, Mn, Ca, Cl and S were more intense in the surface.

In order to know the general distribution of the elements in the inner part of LDG samples, an elemental distribution area mapping was carried out over a thick lamina of one of the LDG samples (Fig. 4.10).

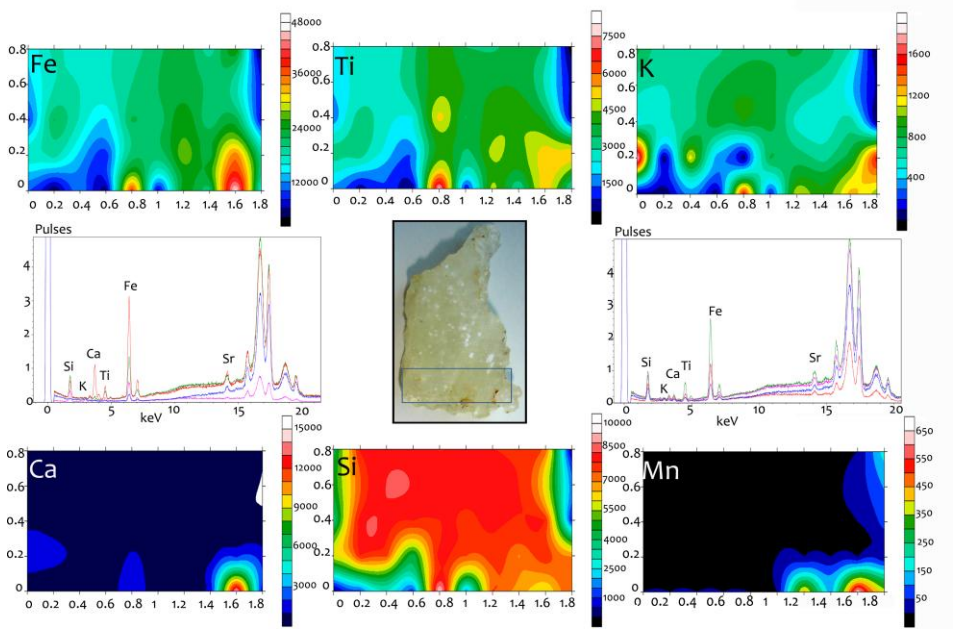

Fig.4.10. In the centre of the Figure, a photograph of the studied sample appears, indicating the analyzed area of the LDG sample, as well as μ-EDXRF images of the distribution of Fe, Ti, K, Ca, Si and Mn in that area, and EDXRF spectra of measurements where the difference in the area of K_α lines is appreciated from the measurements.

In the EDXRF spectra of Fig. 4.10, the mentioned high peak intensities of Fe, Ti and Sr (compare it with Fig. 4.2) was observed in the analyzed inner parts of the LDG sample. Moreover, the highest presence of iron appeared in the inclusions, both

inner and outer inclusions. In contrast, light elements (Cl, S, Mn and Ca) had higher presence in the surface. Potassium did not shown differences between the surface and the inner part but in the image distribution of Fig. 4.10 a zone of higher presence of K near the surface was observed. Cu and Zn were only identified in the central area of the LDG matrix. This distribution difference is an indication of the great heterogeneity of the LDG samples. The presence of some of these elements in the LDG matrix could be related to minerals from desert target sandstones (Cretaceous sandstones of the former "Nubian Group")[68].

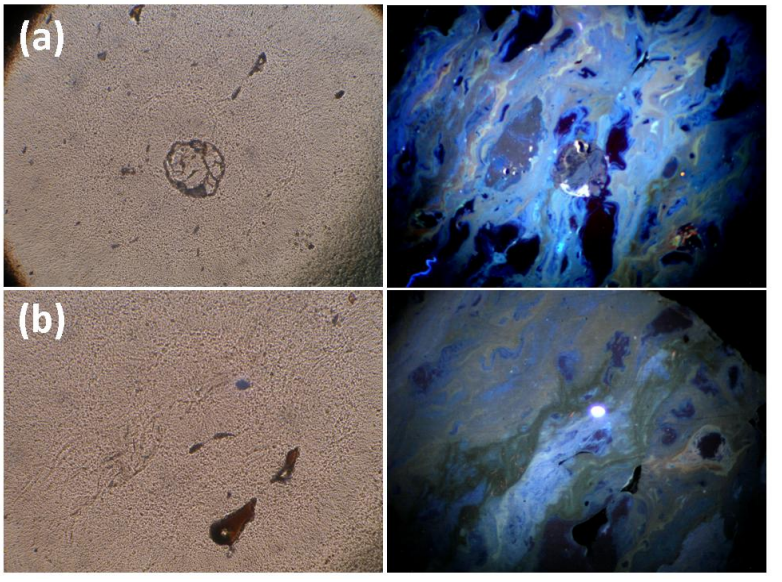

Fig.4.11. Optical microscope and cathodoluminescence microphotograph in the thin lamina of a LDG sample showing a spherule enclosed in the matrix (a) and complex flow-banded structures in the glass (b) (Width of the all microphotographs: 2mm).

This heterogeneity was also observed by cathodololuminiscence (see Fig. 4.11); in whose images it could be observed a variation of elements due to the differences tonalities in the flow structures of the melt (see images on the right in the Fig. 4.11). This flow texture was also discerned by SEM (see Fig. 4.12 as an example of the multiple images collected in this work).

[68] P. Schaaf, D. Müller-Sohnius. Strontium and neodymium isotopic study of Libyan Desert Glass: Inherited Pan-African age signatures and new evidence for target material, Meteoritics and Planetary Science 37 (2002) 565–576.

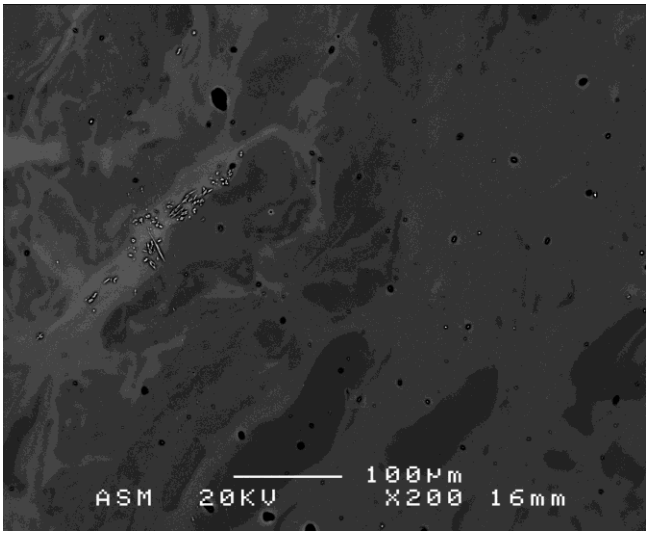

Fig. 4.12. SEM image with turbulent flow structures of the matrix found in a thin lamina of a LDG. Light grey colour: richer in Al and dark grey colour: richer in Si.

In general, the inner matrix exhibited a semi-crystalline texture with porphyritic crystals by optical microscope observation (see Fig. 4.11). Regarding the molecular composition by Raman spectroscopy, the inner matrix exhibited the same characteristic Raman spectrum as described previously in the outer matrix. Besides, in this case, some of the Raman spectra were obtained with the red laser (785 nm) as well.

In addition, glass spherules of size 40-100 μm (considered as the whitish inclusions dispersed within the silica glass matrix) were found with internal cracks and with spheroid bodies similar to grapes[69]. These spherules were identified as α-cristobalite (SiO_2, Raman bands at 230vs and 418vs cm^{-1}), a compound of high temperature formation (above 1470ºC) as it has been described earlier.

Although, scanning electron and optical microscopy showed a homogeneous pure silica composition of cristobalite crystals, EPMA analysis revealed that their inner and the outer part had distinct elemental composition. The inner part contained 99.19 wt% SiO_2 and the outer 96.76 wt%; Al_2O_3 varies from 0.20 wt% at the inner to 2.04 wt% at the outer part, as well as Fe_2O_3 that showed a variation from 0.01-0.22 wt%; TiO_2 from 0.018-0.51 wt% and CaO varies from 0-0.12 wt% in the inner and the outer part.

[69] L. Ferriere, C. Koeberl, W. Reimold, Characterisation of ballen quartz and cristobalite in impact breccias: new observations and constraints on ballen formation, European Journal of Mineralogy 21 (2009) 203–217.

Different cooling rate could be the responsible for cristobalite habit, or/and the chemistry of the melt, given that cristobalite could develop in response to a specific reaction within the melt.

Within a cristobalite area, a zircon ($ZrSiO_4$) inclusion was observed, with a crystalline form completely developed (idiomorphic) indicating that this inclusion could be earlier in the crystallization sequence to cristobalite (see Fig. 4.13.a and b). Traces of Hf were found in this inclusion by SEM-EDS as well. Furthermore, zircon crystals trapped in the matrix were also detected by Raman spectroscopy ($ZrSiO_4$; Raman bands at 351m, 435m, 973vw, 1000vs, 1050w, 1085m and 1140vw cm^{-1}; Fig. 4.13.c).

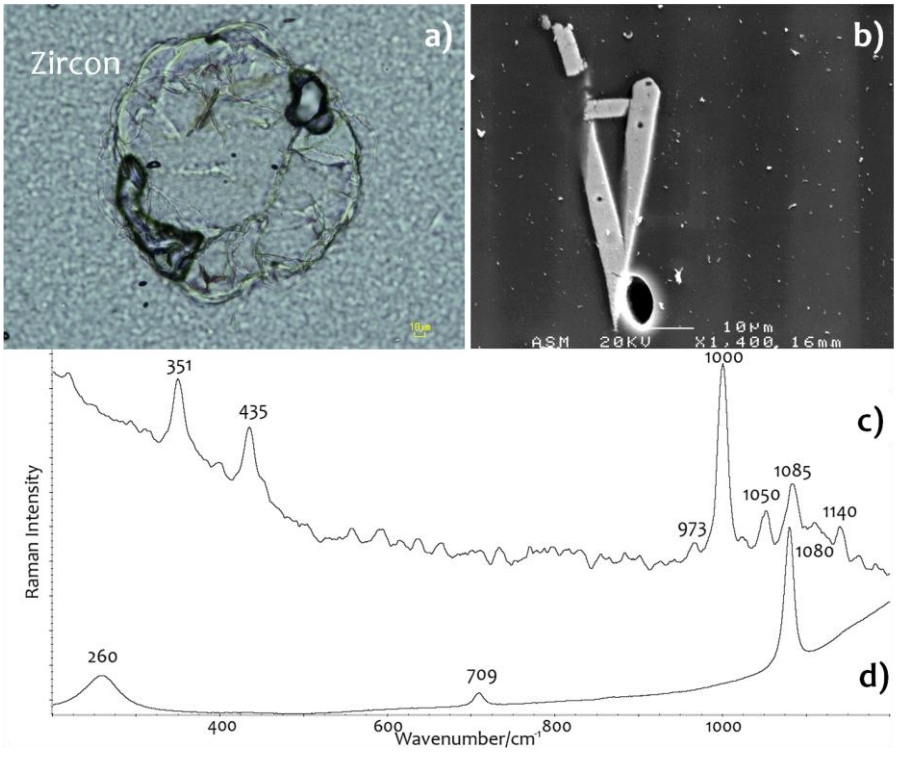

Fig.4.13. Optical image of zircon inclusion within of a cristobalite in LDG (a), SEM image of zircon in the LDG melt (b), and Raman spectra of zircon (c) and amorphous calcite (d) found in the matrix of a LDG sample (Laser: 514 nm).

In those cases, the Raman spectrum of zircon allowed us to determine the conditions in which these LDGs were formed. In this way, the main Raman band of the zircon appeared at 1000 cm^{-1}, which corresponds to a metamict/amourphous zircon (see Fig. 4.13.c). The change in the position of its usually main band (~1008 cm^{-1}) means

that it has been subjected at a pressure of 20 GPa[70]. Also, as long as the temperature increases (it can reach above 1470°C) the band is displaced to 1000 cm^{-1} [71,72]. Thus, high temperature and pressure are perfectly reasonable with the impact event[73]. Also, calcite ($CaCO_3$; Raman bands at 153w, 279m, 710w and 1085vs cm^{-1}) and ($CaCO_3$; Raman bands at 149w, 260m, 709w and 1080vs cm^{-1}) (see Fig. 4.13.d) were found through the inner matrix.

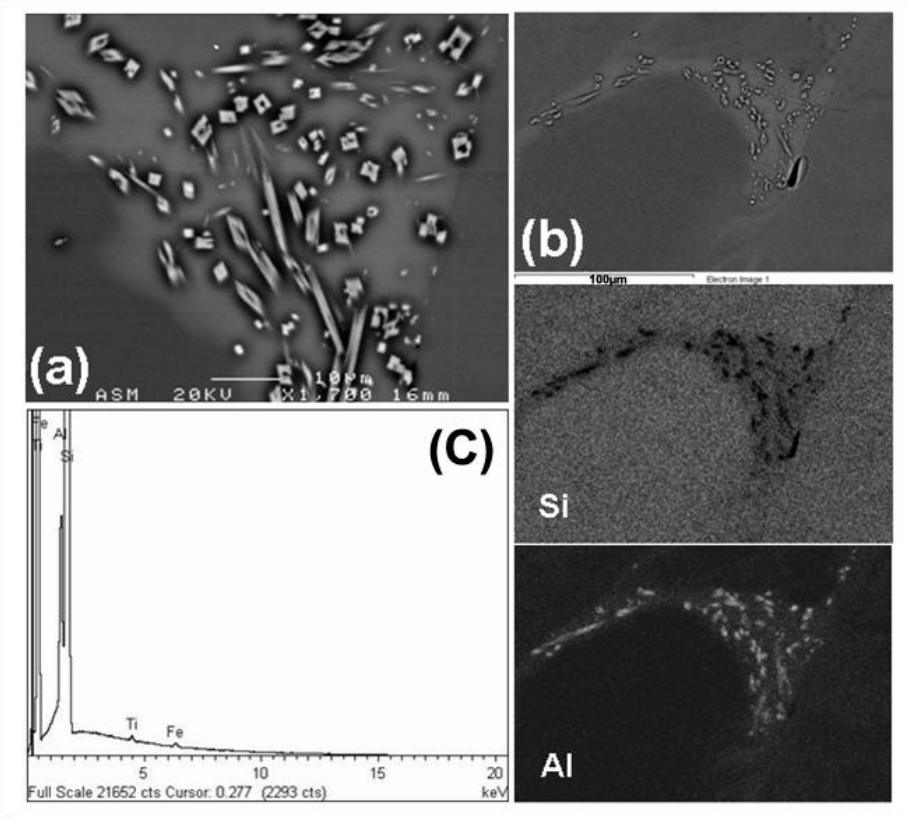

Fig.4.14. Optical microscope image of euhedral crystallites over the matrix of a LDG (a), SEM image of an area with crystallite aggregations together with EDX maps of silicon and aluminium, and one of the spectrum obtained by EDX where traces of Fe and Ti are shown (c).

[70] A. Gucsik, M. Zhang, C. Koeberl, E. K. H. Salje , S. A. T. Redfern, J. M. Pruneda. Infrared and Raman spectra of ZrSiO4 experimentally shocked at high pressures, Mineralogical Magazine 68 (2004) 801–811.
[71] M. Zhang, E.K.H. Salje, I. Farnan, A. Graeme-Barber , P. Daniel, R.C. Ewing, A.M. Clark, H. Leroux, Metamictization of zircon: Raman spectroscopic study, Journal of Physics: Condensed Matter 12 (2000) 1915-1925.
[72] L. Nasdala, G. Irmer, D. Woelf, The degree of metamictization in zircon: a Raman spectroscopic study, European Journal of Mineralogy 7 (1995) 471-478.
[73] D.C. Smith, J.D. Vernioles, The Temperature of Fusion of a Celtic Vitrified Fort: a Feasibility Study of the Application of the Raman Microprobe to the Non-Destructive Characterization of Unprepared Archaeological Objects, Journal of Raman Spectroscopy 28 (1997) 195-197.

Euhedral crystallites were found dispersed over the matrix. These crystallites were generally randomly oriented forming aligned clouds and/or aggregations of crystallites defining flow patterns (see Fig. 4.14.a). Besides, they showed skeletal structure (i.e. crystals with cavities) and swallowtail ends similar to typical structures of those formed during rapid crystallization from a melt[74]. A high degree of undercooling (become supercooled) during the crystal formation could explain the shape of these tiny size crystals. Besides, they were identified as aluminium rich crystallites with traces of Ti and Fe by SEM-EDX analysis (see Fig. 4.14.b and c).

Given these SEM-EDX results and the detection of corundum (α-Al_2O_3) in the LDG surface, we tried to find these structures in the inner parts using Raman spectroscopy. However, there was no signal; we did not found the characteristic bands of corundum, so it was only present in the inclusions of the surface. There are more than 15 distinct crystalline forms of aluminum oxide and can undergo a variety of transitions ((γ, δ, κ, ρ, η,θ, β, etc.) until it reaches the most thermodynamically stable corundum structure (α-Al_2O_3)[75-77]. The alumina heated at temperatures under 1100°C are considered amorphous or non-crystalline materials[76], and do not exhibit any Raman bands[78]. However, corundum, which is formed at around 1200°C[78], is considered a crystalline phase and we could identify it[77]. Therefore, LDG may have transition aluminas in the inner part and the stable phase, corundum, in the outer part. To confirm the no-signal of those crystallites, an area of 200 x 200 μm with them was measured by Raman image, without finding the characteristic bands around 413-416 cm^{-1} of corundum. Only it was obtained the characteristic Raman bands of the LDG matrix.

Rutile crystals (TiO_2; Raman bands at 445s and 610s cm^{-1}) (see Fig.4.15) were also found enclosed in the matrix as well as coesite (SiO_2), due to the Raman bands at

[74] G.E. Lofgren, Experimental studies on the dynamic crystallization of silicate melts, Hargraves, R.B. Ed. Physics of Magmatic Processes pp.487-551. Princeton University Press, New Yersey ,1980.
[75] Y. Wang, C. Suryanarayana, L. An, Phase Transformation in Nanometer-Sized □-Alumina by Mechanical Milling, **Journal of the American Ceramic Society**88 (2005) 780–783.
[76] P. Souza Santos, H. Souza Santos, S.P. Toledo, Standard Transition Aluminas. Electron Microscopy Studies, Materials Research 3 (2000) 104-114.
[77] C. Zeng, Y.Ling, S. Li, Y. Rao, Y. Chen, The effect of chromium on the gamma to alpha phase transition of alumina coating formed on 316L SS by a cathodic micro arc deposition (CMAD) process, Surface & Coatings Technology 263 (2015) 15–20.
[78] , J. Breza, M. Veselý, Raman spectra of synthetic sapphire., Microelectronics Journal 32 (2001) 955–958.

521m cm^{-1} (its most fundamental vibration[79]) and 270w cm^{-1} (see Fig.4.15), the high pressure polymorph of α–quartz as stated before.

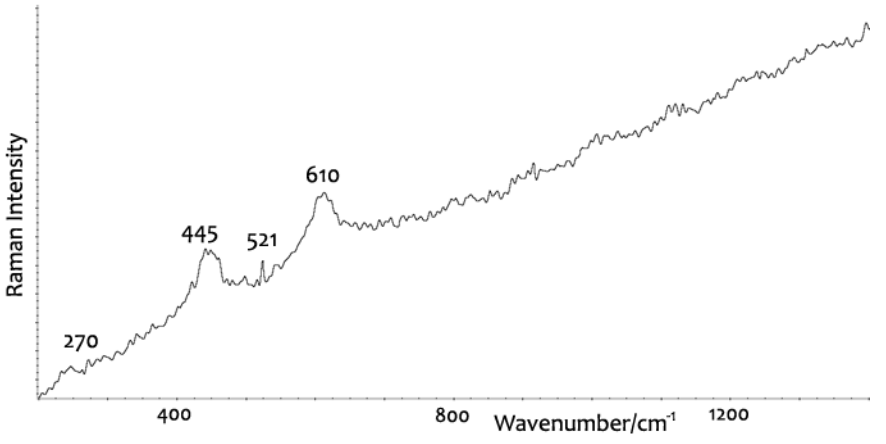

Fig.4.15. Raman spectrum of rutile and coesite (Laser: 532 nm).

Rutile is a TiO_2 polymorph formed in ultra high temperature (exceeding 1800ºC) and pressure conditions[80]. In the formation of the LDG matrix, it could have happened that during the initial high temperature moment the glass trapped rutile or the metastable anatase (other polymorph of TiO_2). In case of trapping anatase this mineral phase should pass irreversibly to the stable rutile in the range of 400–1200ºC. But today, there is a controversy on the presence of both titanium oxide polymorphs as stated from the disagreements in the published papers[81-83].

Comparing the outer and inner matrix, it could be observed that some compounds were only detected inside, such as zircon, rutile, calcite (although it was detected in

[79] T. Kobayashi,T. Hirajima, T. Hiroi, M. Svojtka, Determination of SiO_2 Raman spectrum indicating the transformation from coesite to quartz in Gfohl migmatitic gneisses in the Moldanubian Zone, Czech Republic, Journal of Mineralogical and Petrological Sciences 103 (2008) 105-111.
[80] P. Horn, D. Muller-Sohnius, P. Schaaf , B. Kleinmann , D. Storzer . Potassium-argon and fission-tracks dating of Libyan Desert Glass, and strontium-neodynium isotope constraints on its source rock. Proceedings of the "Silica 96" Meeting on Silica Glass and related desert events, edited by de Michele V. Milano: Pyramids, pp. 59–73, Bologna, 1997.
[81] D.A.H. Hanaor, C. C. Sorrell, Review of the anatase to rutile phase transformation, Journal of Materials Science 46 (2011) 855–874.
[82] A. Matthews. The crystallization of anatase from amorphous titanium dioxide under hydrothermal conditions, American Mineralogist 61 (1976) 419-424.
[83] V.B. Tezza, M. Scarpato, L.F.S. Oliveira, A.M. Bernardin, Effect of firing temperature on the photocatalytic activity of anatase ceramic glazes, Powder Technology 276 (2015) 60–65.

outer inclusions) and amorphous calcite. Others only appeared outside, like gypsum, anatase and microcline feldspar.

2. DARK AND BROWNISH GLASSY INCLUSIONS IN THE INNER PART OF THE LDGS

After the lamination of the LDG specimens the brownish and black inclusions were not so clearly perceived in the inner part, only near the LDG border, and were irregular-shaped (see Fig .4.16). Some particles present in the inclusions of the glass could be interpreted as sedimentary minerals from the target rocks (Cretaceous sandstone of the "Nubia Group") that were captured and condensed inside the silica glass during the explosion due to the impact and the formation of the melt.

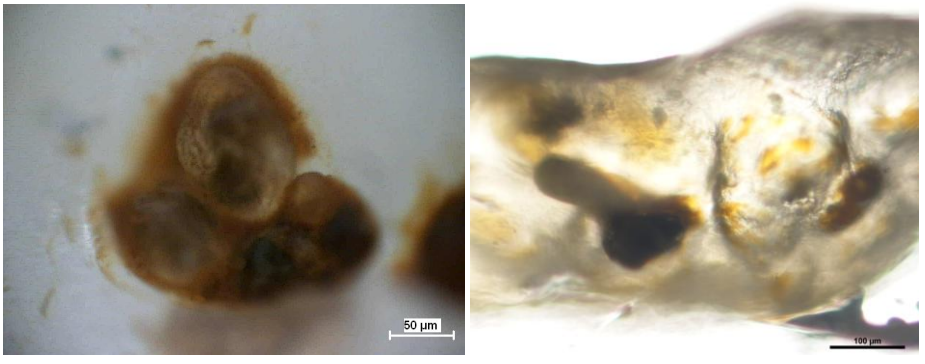

Fig.4.16. Optical image of two brownish inclusions near the border in the thick section of one of our LDG samples.

The elemental composition of the brownish inclusions situated in the LDG border of the thick sections coincided with that described in the Chapter 4: Part A.A1 to the brownish inclusions of the surface.

Nonetheless, in order to study how the elements were distributed in the inner brownish inclusions, several elemental composition mappings as well as a semi-quantitative determination were carried out by SEM-EDX. In general, the silicon is the main element, as in the superficial brownish inclusions. However, in this analysis over a LDG thick section, Fe, Sr and Ti signals were increased and improved inside. Furthermore, it was undoubtedly enhanced the detection of light elements; for example, the previously not detected Mg (despite magnesium carbonate was

identified by Raman spectroscopy in an outer brownish inclusion) was present in the inner inclusions. As an example of the results from SEM-EDX analysis of inner inclusions, Fig. 4.17 shows an inclusion mainly formed by Si and several elements such as O, Ca, Al and Fe. Also Na, Mg, P, Cl, K and Ti were detected but their signals were very low.

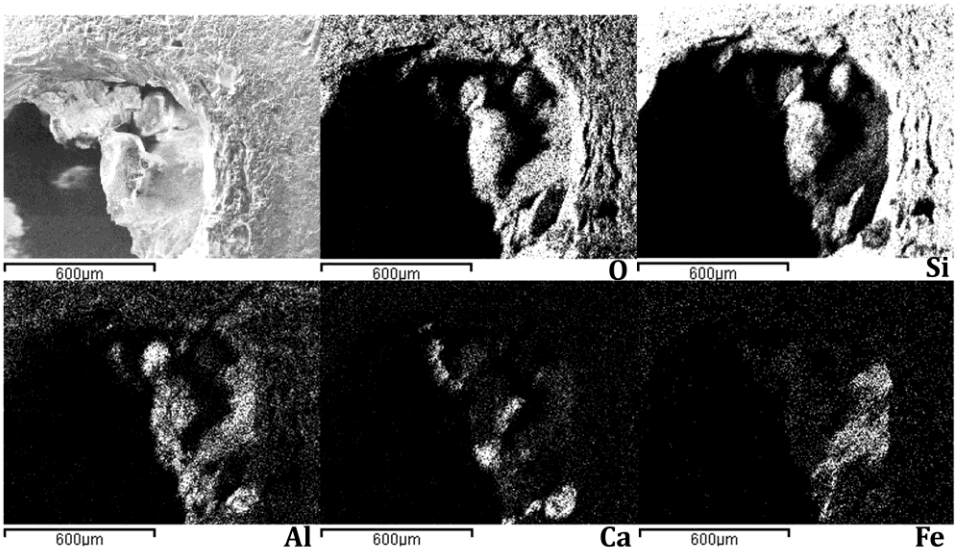

Fig. 4.17. SEM image of an inner inclusion of a sliced LDG sample together with oxygen map, silicon map, aluminum map, calcium map and iron map.

It can be noticed the correlations between elemental maps, where the presence of elements is represented in white colour and the absence in black. Fig. 4.17 shows correlations between O, Si and Al, and correlations among Fe, O and Al. Also some points shown similarities of Ca with Al and O.

Fig. 4.18 displays the SEM-EDX analysis of other inner inclusion but located in the border. It was mainly composed by silicon as well, and some elements were concentrated in certain areas such as: C, O, Mg, Al, K, Ca and Fe. In this case there were correlations between O, Si and Al; Fe, Mg, K and Ca; and the C map with Ca.

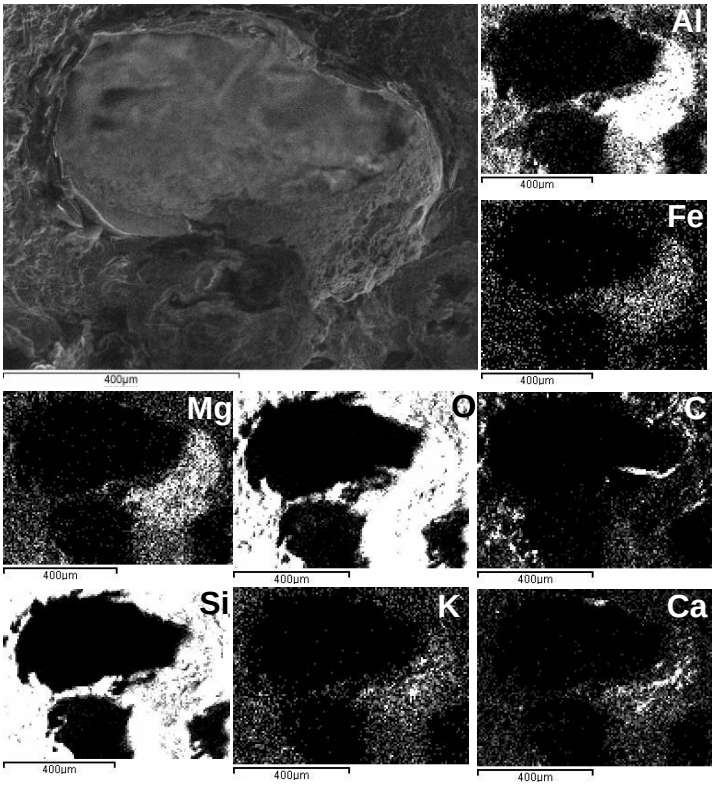

Fig.4.18. SEM image of an inner inclusion near the border of a LDG thick section, together with Al, Fe, Mg, O, C, Si, K and Ca maps.

The observed correlations among different elements suggest the presence of given mineral phases. But their presence can only be confirmed through a molecular vibration spectroscopic technique, like Raman spectroscopy. The Raman analyses identified calcite ($CaCO_3$; Raman bands at 153w, 279m, 710w, and 1085vs cm^{-1}) and aragonite ($CaCO_3$, Raman band at 207w, 704w and 1083m cm^{-1}) in the inner brownish inclusions near the border. It should be noted that by SEM-EDX it was detected similarity between calcium and carbon maps, as observed in Fig. 4.18 where the sites more concentrated in carbon and calcium are the same. Calcite was found in outer and inner part, but aragonite was only found in the inner inclusions of the border.

Calcium carbonate occurs in five different crystalline polymorphs at ambient pressure, anhydrous phases (calcite, aragonite, and vaterite), and hydrated phases (monohydrocalcite and ikaite); but there are also several amorphous forms. Amorphous calcium carbonate is transient and transforms into one of the crystalline

forms in presence of water or when heated[84]. Below 1200°C and approximately at 10 GPa, possible conditions due to the high temperature and pressure of the impact during the LDG formation, the metastable disordered calcite (amorphous calcite) in the melt could be the precursor of the aragonite enclosed in the glass, then a rapid cooling and decrease of temperature could transformed this aragonite to calcite, stable at ambient conditions[85,86]. Also, aragonite transforms to calcite with time, and it becomes more stable than calcite only at high pressure (approximately 350 MPa at 25°C and 700 MPa at 300°C)[87].

Apart from calcium carbonate polymorphs, Raman spectroscopy detected other mineral phases that appeared in both type of brownish inclusions (inner and outer) such as α-quartz (SiO_2; Raman bands at 205m, 263w, 354w, 398vw, 464vs, 696vw, 806w, 1081w and 1160vw cm^{-1}), anatase (TiO_2, Raman band at 141vs, 394m, 512w and 636s cm^{-1}) and cristobalite (α-SiO_2, Raman bands at 230vs and 418vs cm^{-1}).

It was noted that in the inner inclusions of the LDG sample, in some occasions the main Raman band of α-quartz (464 cm^{-1} for ambient pressure and temperature) appeared slightly displaced at 461 cm^{-1} (see Fig. 4.19). Besides, shifts from 205 to 202, 263 to 261 and 806 to 802 cm^{-1} were observed as well. This displacement is commonly attributed to molecules of crystalline quartz that have been subjected to shock pressures of 26 GPa[88].

[84] A. V. Radha, T. Z. Forbes, C. E. Killian, P. U. P. A. Gilbert, A. Navrotsky, Transformation and crystallization energetics of synthetic and biogenic amorphous calcium carbonate, Proceedings of the National Academy of Sciences 107 (2010) 16438–16443.
[85] L. Black, C. Breen, J. Yarwood, K. Garbev, P. Stemmermann, B. Gasharova, Structural features of C–S–H(I) and its carbonation in air – a Raman spectroscopic study. Part II: carbonated phases, *Journal of the American* Ceramic Society 90 (2007) 908–917.
[86] K. Suito, J.Namba, T. Horikawa, Y. Taniguchi, N. Sakurai, M. Kobayashi, A. Onodera, O.Shimomura, T. Kikegawa, Phase relations of $CaCO_3$ at high pressure and high temperature, American Mineralogist 86 (2001) 997–1002.
[87] R.J. Reeder, Carbonate Minerals. McGraw-Hill Encyclopedia of Science & Technology 3. 10th ed. New York, 2007.
[88] P.F. McMillan, G. H. Wolf, P. Lambert, A Raman Spectroscopic Study of Shocked Single Crystalline Quartz, Physics and Chemistry of Minerals 19 (1992) 71-79.

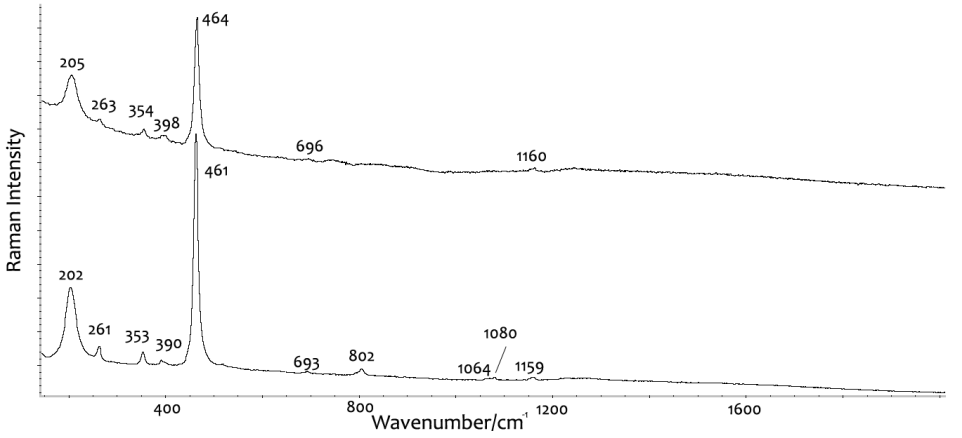

Fig.4.19. Raman spectrum of quartz with its displaced bands by shock pressures, measured in the same conditions. (Laser: 785 nm).

Anhydrite also appeared in both type of inclusions, but in the inner ones various types of anhydrite could be differentiated from the Raman mapping images obtained on several areas. Here the advantages of mapping over point-by-point analyses must be highlighted (you cannot find a minor compound in the point-by-point mode if you do not have the chance to focus over it). Gypsum ($CaSO_4 \cdot 2H_2O$, Raman bands at 411m, 618vw, 668vw and 1006m cm^{-1}) was also detected in the inner brownish inclusions, unlike that found through the superficial matrix. So, anhydrite and gypsum were found both on the surface and inside.

Anhydrite can present different Raman spectra due to the different structures of its polymorphous species[89]. Anhydrite III (A-III either soluble anhydrite or γ-$CaSO_4$) is formed from hemihydrates above temperatures close to 110°C. Anhydrite II (A-II either insoluble anhydrite or β-$CaSO_4$) is formed at approximately 300 °C and it corresponds to the mineralogical form of anhydrite. Its rehydration is unusual, depending on the temperature reached. And the last polymorph, anhydrite I (A-I or α-$CaSO_4$), a high temperature form that is stable above 1180 °C[90], below 1200°C reverts to insoluble anhydrite[90]. Then, according to their Raman bands identified in bibliography[89] and in these samples, it was possible to recognize a probable mixture of A-II and A-I in the LDG. In the surface of the LDG over a brownish inclusion and

[89] N. Prieto-Taboada, O. Gomez-Laserna, I. Martínez-Arkarazo, M. A. Olazabal, J.M. Madariaga, Raman Spectra of the Different Phases in the CaSO4–H2O System, Analytical Chemistry 86 (2014) 10131–10137.
[90] P. Barnes, J. Bensted, Structure and Performance of Cements, Second Edition, Spon Press, New York 2002.

together with quartz, it was found A-II (β-$CaSO_4$, Raman bands at 610vw, 624vw, 1018m, 1128vw and 1161w cm^{-1}). Whereas A-I was identified inside, on one hand, through the matrix (α-$CaSO_4$, Raman bands at 170w, 417w, 1017m, 1110w, 1128w and 1160vw cm^{-1}) and on the other hand, in a brownish inclusion (α-$CaSO_4$, Raman bands at 624w, 970w, 1010m, 1110m and 1158br cm^{-1}) together with calcite and hematite. This last A-I could be mixed with gypsum (overlapping of Raman bands) due to displacement of the A-I Raman bands from 628 to 624 cm^{-1} and from 1017 to 1010 cm^{-1}.

In relation to the temperature, it is rather reasonable to find this distribution of anhydrites in the LDG. A-I, stable above 1180 °C, would be inside where it could have been formed by the high temperatures of the impact. And A-II, stable from 300 to 1180 °C, would be in the surface of the LDG, where the temperature would not have been so high especially in the second (or third) impact of the initially formed LDG, when the melt was in a cooling process (favoured by the LDGs flying after the explosion) but still remaining partially melted and with capacity to trap materials from soils or rocks.

It is difficult to say what compound was the precursor, gypsum, anhydrite or maybe both. Besides, it may depend on the type of substrate where the impact occurred. According to recent studies[91], anhydrite was seen in white deposits inside the sand of the Libyan Desert. For that reason, the anhydrite found in the LDG samples could belong to these latest deposits. The same situation could have happened with gypsum, which could be also present in the substrate. However, other option could be the formation of gypsum from the anhydrite hydration (despite mineral anhydrite (A-II) is insoluble) given the long period of time from LDG formation. Cracks and fissures connected to the surface of the glass could explain the presence of water of crystallization in the interior of the LDG.

[91] F. Fröhlich, G. Poupeau, A. Badou, F. X. Le Bourdonnec, Y. Sacquin, S. Dubernet, J. M. Bardintzeff, M. Veran, D. C. Smith, E. Diemer, Libyan Desert Glass: New field and Fourier transform infrared data, Meteoritics and Planetary Science 48 (2013) 2517–2530.

The Oligocene (33.9 to 23.0 million years ago, epoch that coincide with the appearance of the LDG) was a period of dramatic climate change[92], and there were significant tectonic events: Red Sea opening, formation of the East African Rift Valley, formation of the Dead Sea rift, etc. and also the Gilf Khebir uplift[92,93]. In this period one of the three main drainage systems of southwestern Egypt was the Gilf system, which consisted of a northward flowing stream and was originated in the Gilf Khebir Plateau[92,94]. Besides, during Miocene time (23-5.3 million years ago), the Gilf Khebir Plateau could have been eroded by catastrophic floods[95]. This fact was established due to the geomorphology of that area[96]. The terminal depression of palaeo-channels is used as an indicator of areas with ground-water accumulation[96]. So sand was fluvially derived and subsequently reshaped by aeolian activity in periods of dry climate[97]. The LDG formation occurred just after the Gilf Khebir Plateau uplift and during its subsequent mechanical erosion by strong floods along the depression formed during the late Oligocene and Miocene times[96], like it was shown for the aqueous alteration of the well known Nakhla meteorite[97]. Thus, it is confirmed the presence of large quantity of water in this area in certain periods of time, and therefore, hydrated mineral compounds such as gypsum could be present in those times.

In the referred study of the Nakhla meteorite, Gooding et al. (1991)[97] explained also that the outer calcium sulphates could come from the interior ones. This compound could be pre-terrestrial and during the impact over the Earth, they could have been partially leached from the inner and reprecipitated in the outer part. This situation could have also occurred in our LDG samples.

[92] L. L. Lavier, M.S. Steckler, F. Brigaud, Climatic and tectonic control on the Cenozoic evolution of the West African margin, Marine Geology 178 (2001) 63-80.
[93] G.C. Begg, W.L. Griffin, L.M. Natapov, Suzanne Y. O'Reilly, S.P. Grand, C.J. O'Neill, J.M.A. Hronsky, Y. Poudjom Djomani, C.J. Swain, T. Deen, P. Bowden, The lithospheric architecture of Africa: Seismic tomography, mantle petrology, and tectonic evolution, Geosphere 5 (2009) 23–50.
[94] A. S. Goudie, The drainage of Africa since the Cretaceous, Geomorphology 67 (2005) 437-456.
[95] I.A. Brookes, Possible miocene catastrophic flooding in Egypt's Western Desert, Journal of African Earth Sciences 32 (2001) 325-333.
[96] F. El-Baz, M. Maingue, C. Robinson, Fluvio-aeolian dynamics in the north-eastern Sahara: the relationship between fluvial/aeolian systems and ground-water concentration, Journal of Arid Environments 44 (2000) 173–183.
[97] J. L. Gooding, M.E. Zolensky, S.J. Wentworth, Aqueous alteration of the Nakhla meteorite, Meteoritics 26 (1991) 135-143.

With respect to the origin of the quartz identified in the inclusions, it was known that the Lybian Desert has deposits of soft sandstones from the Paleozoic (542-252.2 millions of years ago), Mesozoic (252.2-65.5 millions of years ago) and Quaternary (1.8 million years ago till nowadays) periods, where the ground surface was covered with sandstones/quartzite gravels within a layer of sand, which overlie reddish silts (rounded quartz and quartzite grains)[98]. Some authors[99] mentioned that these reddish silts are lacustrine in origin. Therefore, quartz could have been trapped within the LDG from gravels of the Libyan Desert just during the impacts.

Furthermore, in the inner brownish inclusions hematite (α-Fe_2O_3, Raman bands at 226w, 292m, 410w, 612w and 1300br cm^{-1}) and limonite ($FeO(OH).n\ H_2O$, Raman bands at 171w, 208m, 243m, 300s, 399vs, 471br, 551s and 1282br cm^{-1}) (see Fig. 4.20) were identified. Limonite was also observed in the inner inclusions near the LDG border. These compounds are in concordance with the Fe and O maps of SEM-EDX, as it can be seen in Fig. 4.17 and 4.18, where their more concentrated areas are very similar.

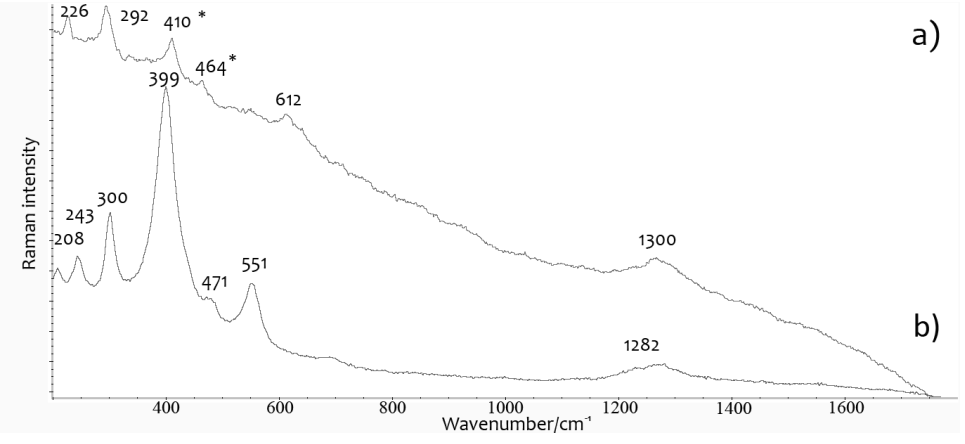

Fig.4.20. Raman spectrum of hematite (a) and limonite together with quartz* (b) found in inner inclusions of a LDG sample. (Laser: 785 nm).

[98] F. Fröhlich, G. Poupeau, A. Badou, F. X. Le Bourdonnec, Y. Sacquin, S. Dubernet, J. M. Bardintzeff, M. Veran, D. C. Smith, E. Diemer, Libyan Desert Glass: New field and Fourier transform infrared data, Meteoritics and Planetary Science 48 (2013) 2517–2530.

[99] P. A. Clayton, L. J. Spencer, Silica-Glass from the Libyan Desert, Mineralogical Magazine 23 (1934) 501–508.

The Raman image obtained in an inner brownish inclusion confirmed the distribution of hematite, together with quartz and calcite, showing again the heterogeneous nature of the inclusions (see Fig. 4.21).

Additionally, like in the inner matrix, rutile was also found in the brownish inner inclusions. As it has been explained previously, its presence could be due to the heating of anatase at 400-1200ºC, situation that it could be given during the LDG formation. In that moment, rutile would stay inside and those zones closer to the surface would maintain the titanium oxide as anatase (detected in the outer matrix and inclusions) due to the cooling of the initial melt. Anatase was identified in the brownish inner inclusions as well, so perhaps all the areas were not cooled or heated in the same way.

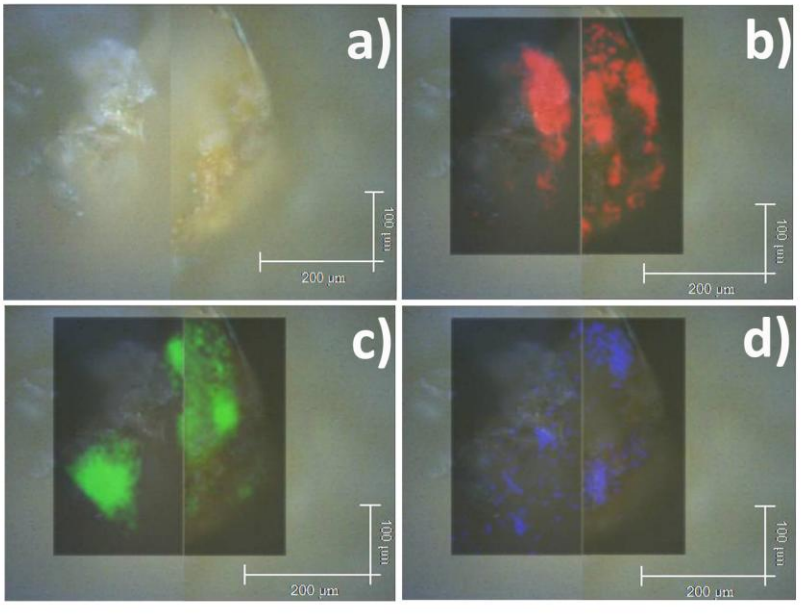

Fig.4.21. Raman image of an inner brownish inclusion: microscopic image of the analyzed inclusion (a), calcite signal (b), quartz signal (c) and hematite signal(d).

In addition, carbon was detected by Raman spectroscopy in some little dark areas of brownish inclusions, areas where the carbon signal in SEM-EDX was not correlated with any other element. Carbon was identified both in outer (C; Raman bands at ≈1300br and ≈1600br cm^{-1}) and inner inclusions (C, Raman bands at 1346br and 1580-1605br cm^{-1}). The band at ≈1580-1600 cm^{-1} is assigned as the G band of the C

(originates from the stretching vibration of sp^2 carbon atoms C-C). And the band at ≈1300 cm^{-1} is attributed to D band (from the stretching vibration of sp^3 carbon atoms, which induces defects and disorders)[100,101].

The origin of this carbon may be in the impact of the meteorite or asteroid, or in the target rocks. Kramers et al. (2013)[102] found carbon phases with G broad band at a high wave number (1597 cm^{-1}) in a stone that called "Hypatia" sampled from the same area of LDG. Other theory that they considered was that this stone was a remnant of a cometary nucleus fragment that it could have been part of a bolide that formed the LDG.

In our case, the Raman bands suggested amorphous carbon, which is typical from sedimentary rocks[103]. However, it is noteworthy that Abate et al. (1999)[104] did not find traces of carbon in the target rocks of the LDG area.

On the other hand, in the inner part of the LDG it was also found Raman bands at 914m, 1331s, 1363br, 1432m, 1471m and 1586m cm^{-1}, as the spectrum shown in Fig. 4.22.

[100] Y.Wang, D. C. Alsmeyer, R. L. McCreery, Raman Spectroscopy of Carbon Materials: Structural Basis of Observed Spectra, Chemistry of Materials. 2 (1990) 557-563.
[101] A.C. Ferrari, J. Robertson, Interpretation of Raman spectra of disordered and amorphous carbon, Physical Review B 61 (2000) 14095–14107.
[102] J. D. Kramers, M.A.G. Andreoli, M.Atanasova, G. A. Belyanin, D.L. Block, C. Franklyn, C. Harrisf, M. Lekgoathi, C.S. Montross, T. Ntsoane, V.Pischedda, P.Segonyane, K.S. (Fanus) Viljoen, J.E. Westraadt, Unique chemistry of a diamond-bearing pebble from the Libyan Desert Glass strewnfield, SW Egypt: Evidence for a shocked comet fragment, Earth and Planetary Science Letters 382 (2013) 21–31.
[103]G. Pratesi, C. Viti, C. Cipriani, M. Mellini, Silicate-silicate liquid inmiscibility and graphite rribons in Libyan desert glass, Geochimica et Cosmochicima Acta 66(2002) 903-911.
[104] B Abate, C Koeberl, F.J Kruger, J.R Underwood Jr BP and Oasis impact structures, Libya, and their relation to Libyan Desert Glass ,in: B.O Dressler, V.L Sharpton (Eds.), Large Meteorite Impacts and Planetary Evolution II, Geological Society of America 339 (1999) 177–192 Special Paper.

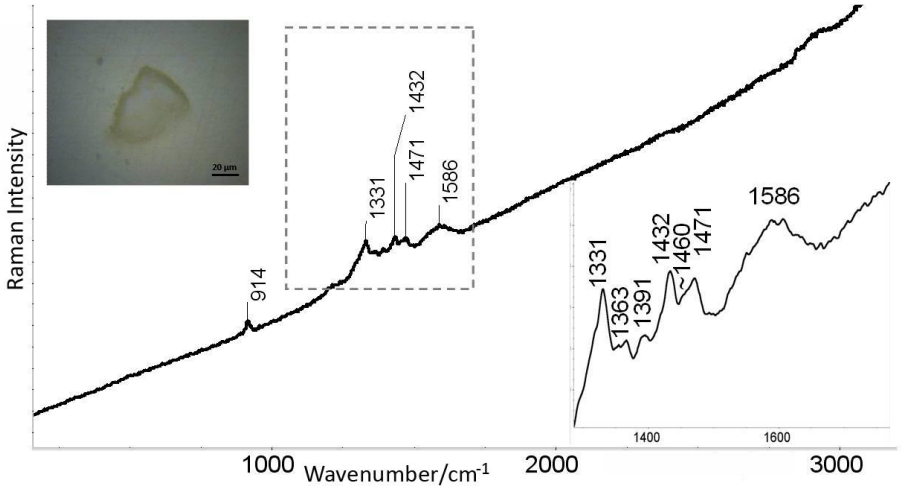

Fig. 4.22. Raman spectrum of an oxalate, together with carbon, in the inner part of a LDG sample. (Laser: 514 nm).

The 914 cm^{-1} Raman band corresponded to ν(C-C) stretching mode[105], that at 1331 cm^{-1} to the D band of carbon as well as that at 1585 cm^{-1} corresponding to the G band of carbon[106], and the Raman bands at 1432 and 1471 cm^{-1} could be assigned to the ν(C-O) stretching mode, which could imply two independent oxalate anions in the crystal[106]. The presence of oxalates is widespread in nature and they are formed by reaction of metals and oxalic acid excreted from fungi, lichens and plants[106]. It was not possible to identify exactly those oxalates; however, it could be observed that LDG samples could be colonized by microorganisms, something that it has not been reported so far in this type of samples. By contrast, microbial activity has been found in Martian meteorites[107].

[105] R.L.Frost, M.L. Weier, Thermal decomposition of humboldtine - a high resolution thermogravimetric and hot stage Raman spectroscopic study. Journal of Thermal Analysis and Calorimetry 75 (2004) 277-291.
[106] Y. Wang, D.C. Alsmeyer, R.L. McCreery, Raman Spectroscopy of Carbon Materials: Structural Basis of Observed Spectra, Chemistry of Materials. 2 (1990) 557-563.
[107] A. Steele, D.T. Goddard, D. Stapelton, J. K. W. Toporski, V. Peters, V. Bassinger ,G. Sharples, D.D. Wynn-Williams, D. S. McKay, Investigations into an unknown organisms on the Martian meteorite Allan Hills 84001, Meteoritics and Planetary Science 35 (2000) 237–241.

3. CAVITIES AND EMBEDDED BUBBLES

Empty or full irregular cavities were also observed in the LDG matrix. According to microscopic observations, some individual grains in these cavities could be pyroxenes (silicate group) due to their crystallography (see Fig. 4.23). In order to verify their composition, Raman spectroscopy, SEM-EDX and EMPA analysis were performed. Correlations between Fe, Mg and Si, and Al, K, Ca and Si were found in SEM-EDX maps. By Raman spectroscopy it was possible to identify different kinds of silicates, such as tephroite (Mn_2SiO_4; Raman bands at 811m and 843m cm^{-1}), forsterite (Mg_2SiO_4; Raman bands at 303w, 430w, 604m, 820s, 854s and 961m cm^{-1}) and enstatite ($MgSiO_3$; Raman bands at 231w, 296vw, 336m, 389w, 657s, 678vs and 1005vs cm^{-1}) (see Fig. 4.23). These results confirmed the pyroxene existence (fosterite and enstatite) suggested by the SEM-EDX analyses. Moreover, these pyroxenes went with rutile or hematite in some of the analyzed cavities.

Pyroxenes are considered major rock-forming primary minerals[108], but they can suffer from weathering. It is said that the chemical weathering of pyroxenes leads either to Fe-rich products and then to goethite, or to a phyllosilicate clay[109].

In addition, there were others cavities more circular in shape, which suggested the presence of vesicles, gaseous or fluids, which could have been exploded with the slicing.

[108] M. J. Wilson, Weathering of the primary rock-forming minerals: processes, products and rates, Clay Minerals 39 (2004) 233-266.
[109] A. Decarreau,F. Colin, A. Herbillon, A. Manceau,D. Nahon, H. Paquet, D. Trauth-Badaud,J. J. Trescase, domain segregation in ni-fe-mg-smectites, Clays and Clay Minerals 35 (1987) 1-10.

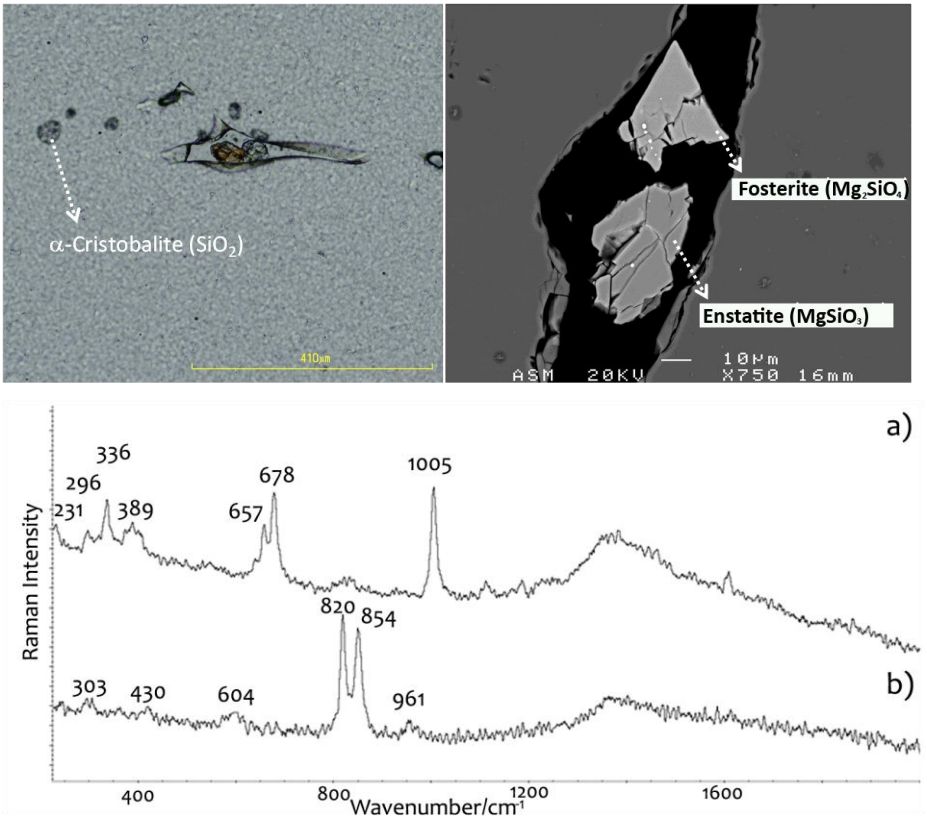

Fig.4.23. Microphotographs of two pyroxenes in the LDG matrix, and their Raman spectra: a) enstantite and b) fosterite (Laser: 785 nm).

Fluid inclusions could have been trapped during boiling of geothermal/hydrothermal fluids. And gaseous vesicles could have been formed in the melt with a decrease of the solubility of dissolved gases, due to changes of the physical conditions (temperature, pressure, oxygen fugacity). Therefore, the formation of bubbles should have occurred during the impact moment. During this event, water, nitrogen and organics could be released. Besides, the temperature could have been locally high enough to partially melt low melting-temperature phases, while other neighboring phases (olivine, pyroxenes) remained solid. If pressure was elevated, water and nitrogen could dissolve in the liquids. Upon pressure decrease, water and nitrogen soon degassed again, leaving trapped bubbles after solidification[110,111].

[110] N. J.F. Blamey, Composition and evolution of crustal, geothermal and hydrothermal fluids interpreted using quantitative fluid inclusion gas analysis, Journal of Geochemical Exploration 116–117 (2012) 17–27.
[111] C.Perron, C. Fiéni, N. Guilhaumou, Nitrogen and water bubbles, oxygen isotopes, shock effects: Deciphering the history of the Bencubbin meteorite breccia , Geochimica et Cosmochimica Acta 72 (2008) 959–977.

It was discerned differences in the number of bubbles between the studied LDG samples. Perhaps in the specimens with more bubbles, the pressure decreased to a larger extent during the solidification. This could be the case of LDG deposited further from the impact zone, which had more way to go and therefore more possibilities to get cold away from the hot impact area.

Apart from this theory where these gases or fluids bubbles could have been formed during the impact, the contact with the terrestrial atmosphere could have also introduced terrestrial heavy noble gases to the samples[112].

To ascertain the nature of the materials in the bubbles, an analysis was performed over these bubbles. Firstly, a Raman image analysis with the 532 nm excitation laser was carried out, observing a different composition between matrix and bubbles, but due to the fluorescence it was impossible to identify the compound that distinguished them (see Fig. 4.24.a). It is noticeable that the only signal identified is that belonging to the matrix (see Fig. 4.24.a.3).

For this reason, another Raman image analysis was carried out but with the excitation laser of 785 nm. In this case, the signal of the bubbles was not intense enough to assign to some compound (see Fig.4.24.b.3). This could have been attributable to the presence of a compound in gaseous phase whose concentration was too low to be detected by Raman spectroscopy. Also, these cavities could have contained fluid bubbles; however, it was not detected Raman signals of water bands or CH bands. Therefore, these gaseous or fluid bubbles could have been released during the heating in the impact.

[112] G.Crozaz, M. Wadhwa, The terrestrial alteration of Saharan Shergottites Dar al Gani 476 and 489: A case study of weathering in a hot desert environment, Geochimica et Cosmochimica Acta 65 (2001) 971–978.

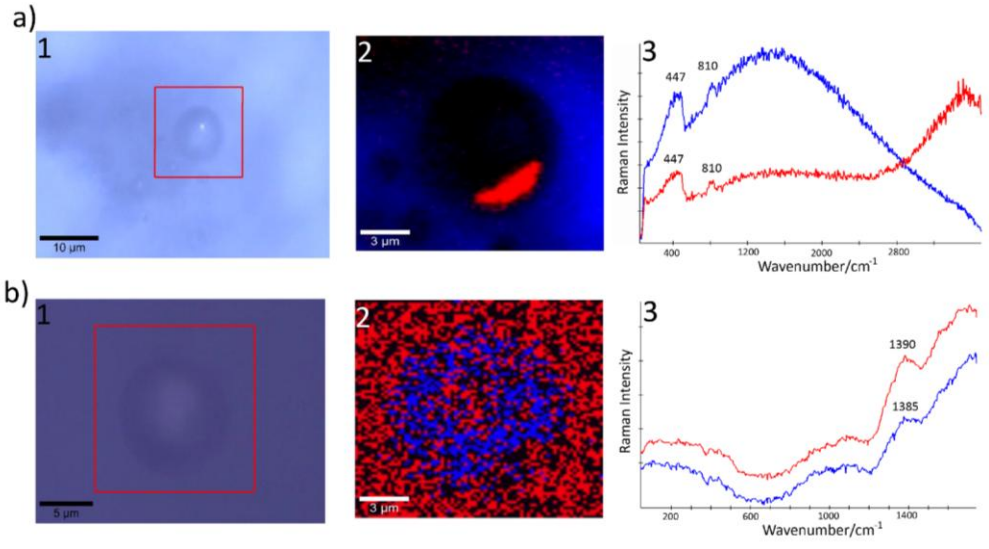

Fig.4.24. Analysis of some bubbles (a) and (b) in the LDG samples. a.1. and b.1: Optic images of the bubbles, a.2 and b.2: Raman images of the indicated area and a.3 and b.3: average spectra of the red and blue areas of a.2 and b.2 images. Laser: 532 nm (a) and 785 nm (b).

In addition, the SEM-EDX analyses showed other empty bubbles, like it can be observed in Fig. 4.25.

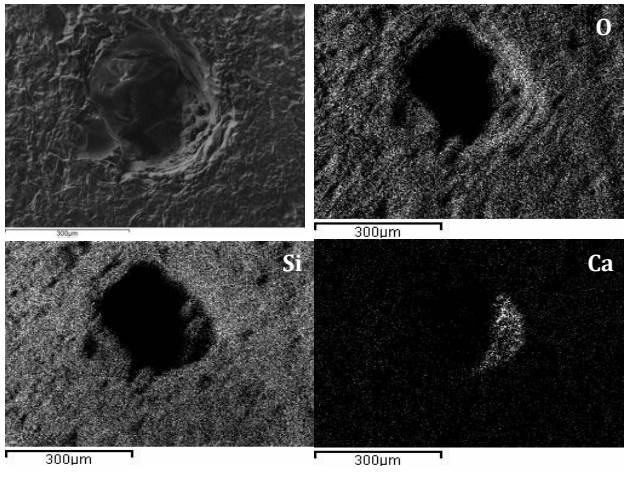

Fig.4.25. SEM image of a bubble of a LDG thick lamina, together with oxygen, silicon and calcium map.

Finally, other point-by-point Raman analysis were performed on different bubbles, and in this case, it was possible to identify oxygen gas (O_2(g), Raman band at 1554w

cm^{-1})[113] and nitrogen inside them (see Fig. 4.26). It should be emphasized that by means of this technique, it is possible to differentiate several nitrogen forms. On one hand, nitrogen gas can be identified by its Raman band at 2328w cm^{-1} (its position at atmospheric pressure)[114], and on the other hand, the liquid nitrogen shows a Raman band at 2326w cm^{-1} [115]. Other peaks associated with gaseous nitrogen (2342w cm^{-1})[116], and also a Raman band at 2337w cm^{-1} attributable to stretching mode C≡N[117] were also seen.

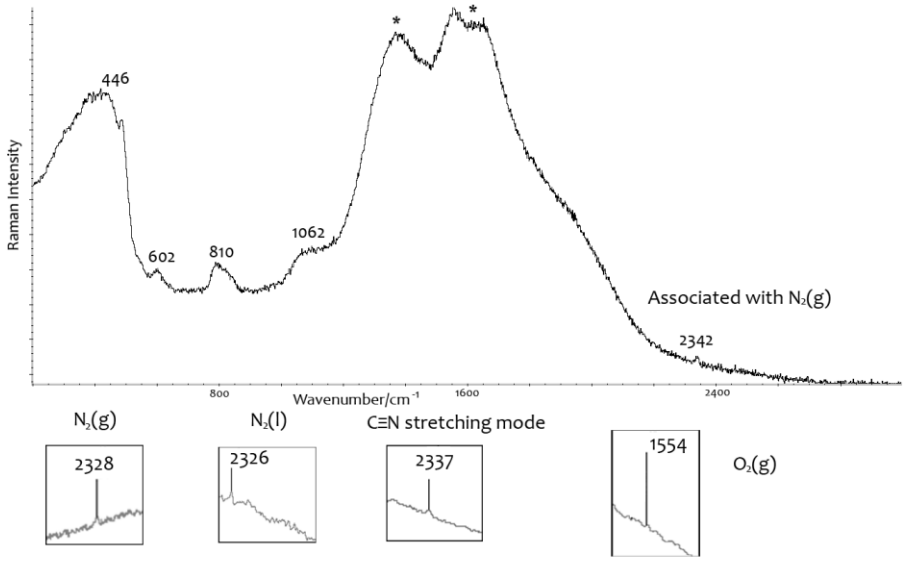

Fig.4.26. Analysis of bubbles in the LDG samples by Raman spectroscopy. Raman band associated with N_2(g) together with the LDG matrix Raman signal and luminescence (*); and Raman signals of N_2(g), N_2(l),C≡N and O_2(g). (Lasers: 514 nm for N_2(g), 532 nm for N_2(l), and 785 nm).

[113] M.P. Buric, Gas phase raman spectroscopy using hollow waveguides, Thesis of University of Pittsburgh, 2010.
[114] C.Perron, C. Fiéni, N. Guilhaumou, Nitrogen and water bubbles, oxygen isotopes, shock effects: Deciphering the history of the Bencubbin meteorite breccia , Geochimica et Cosmochimica Acta 72 (2008) 959–977.
[115] S.A. Akhmanov, N.I. Koroteev, R.Y. Orlov, I.L. Shumai, Active spectroscopy of Raman scattering of light in the continuous regime; possibility of ultrahigh resolution spectroscopy of Raman transition, Journal of Experimental and Theoretical Physics Letters 23 (1976) 249-252.
[116] G. Turrell, J. Corset, Raman Microscopy: Developments and Applications, 1ST Edition, Academic Press, London, 1996.
[117] P.M. Anbarasan, P. Senthil Kumar K. Vasudevan, S. Moorthy Babu, V. Aroulmoji, DFT and TD-DFT Calculations of Some Metal Free Phthalonitrile Derivatives for Enhancement of the Dye Sensitized Solar Cells, Acta Physica Polonica A 119 (2011) 395-404.

4. PYROLYSIS - GAS CHROMATOGRAPHY MASS SPECTROMETRY (PY-GC-MS)

The detection of organic compounds by Raman spectroscopy in the LDGs, moved us to use Pyrolisis-Gas Chromatography-Mass Spectrometry (Py-GC-MS) to identify the compounds present in the LDG samples. All samples were subjected to the same pyrolysis program sequentially. The first temperature of analysis was 280°C, followed by an analysis at 600°C and finally to 750°C.

At 280°C, 1-nonanol (a fatty alcohol derived from natural oils[118],) nonanal and decanal (aldehydes related to essential oils[118]) were identified. At 600°C appeared: 1-heptene; toluene (aromatic hydrocarbon); bycyclo (3.2.0) heptanes,cis; styrene (aromatic hydrocarbon that can be produced naturally by plants, bacteria, and fungi, it is also present in combustion products and is used to make plastics and rubber[119]); 1,2-cyclopentanedione; phenol and 2-methyl-phenol (aromatic hydrocarbons); p-cresol (aromatic hydrocarbon that occur naturally in oils of various plants, also is a product of combustion from natural fires and volcanic activity, and there are microorganisms that produce cresols when degrade organic matter of the environment[120]); nonyl-cyclopropane; 2-ethyl-1-Hexanol; 1-ethyl-2-methyl- cis -cyclopentane; indole (polycyclic aromatic hydrocarbon related to bacterial life[121]); 2-dodecene,(Z)-; 3-chloropropionic acid, dodecyl ester and carbonic acid, hexadecyl 2,2,2-trichloroethyl ester (see Fig. 4.27).

[118] PubChem, http://pubchem.ncbi.nlm.nih.gov/compound/.
[119] ATSDR (Agency for Toxic Substances and Disease Registry) - Public Health Statement: Styrene (http://www.atsdr.cdc.gov/phs/phs.asp).
[120] ATSDR (Agency for Toxic Substances and Disease Registry) - Public Health Statement: Cresols (http://www.atsdr.cdc.gov/phs/phs.asp)
[121] M. Hu, C. Zhang, Y. Mu, Q. Shen, Y. Feng, Indole Affects Biofilm Formation in Bacteria, Indian Journal of Microbiology 50 (2010) 362–368.

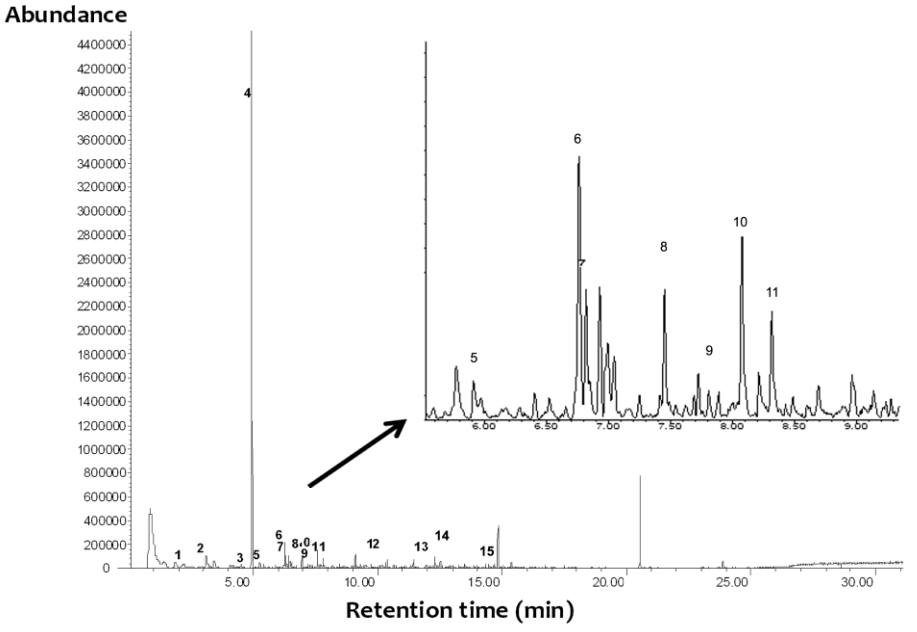

Fig.4.27. Chromatogram for LDG at 600°C 1: 1-heptene; 2: toluene; 3: bycyclo (3.2.0) heptanes,cis; 4: styrene; 5: 1,2-cyclopentanedione; 6: phenol; 7: nonyl-cyclopropane; 8: 2-ethyl-1-Hexanol; 9: 2-methyl-phenol; 10: p-cresol; 11: 1-ethyl-2-methyl-, cis- cyclopentane; 12: indole; 13: 2-dodecene,(Z)-; 14: 3-chloropropionic acid, dodecyl ester; 15: carbonic acid, hexadecyl 2,2,2-trichloroethyl ester. Zoom at 5-10 min.

At 750°C it was recognized again styrene and phenol but also three new compounds: 1,4,5,6-tetrahydro-pyridine-3-carbonitrile, and 1-ethyl-2-heptyl- cyclopropane**.**

In general, the lower pyrolysis temperature step (280°C) releases fewer compounds than the other temperatures (600 and 750°C). At 600°C, it was detected more range of compounds. Among the identified compounds there were mainly hydrocarbons (long-chain hydrocarbons, cyclic and aromatics), some related to components of plants such as 1-nonanol, decanal, styrene and p-cresol, and on the other hand, others representative of bacterial life like also p-cresol and indole. It is astounding the resistance of these compounds at the temperatures used in the analysis. Therefore, it is unclear whether their origin is before or after the impact of the extraterrestrial body on the Libyan Desert.

5. DISCUSSION

In the following table (Table 4.2) the mineral compounds identified in the LDG samples and their Raman bands are summarized.

The presence of several compounds related to high and low temperatures and pressures may be a clue to elucidate the origin for their formation and the stress suffered by the LDG samples. There were α-quartz, the low-temperature stable polymorph of SiO_2, which is converted by heating into β-cristobalite at 1470 °C; α-cristobalite, which is normally created on cooling process by transformation of its internal crystal structure from the previously formed β-cristobalite formed at higher temperature. Therefore, the presence of α-cristobalite indicated the former presence of β-cristobalite and hence a temperature greater than 1470 °C and the following cooling process.

Moreover, the effect of high temperature on the LDGs was also supported by the presence of rutile.

On the other hand, the high pressure conditions in the formation of the LDGs were corroborated by the presence of coesite (high-pressure polymorphs of quartz) and aragonite. And the low pressure, settled state, was confirmed by calcite.

This entire means that the compounds belonging to high pressure and temperature were formed during the meteorite/asteroid impact and subsequently, with the cooling, the low pressure and temperature mineral phases appeared. Firstly, we thought that high pressure and temperature compounds would be inside, since they would be trapped in the inner part during the impact, whereas the superficial part in contact with the atmospheric conditions would be cooled and subjected to normal conditions pressure, and therefore it would have low pressure and temperature compounds. However, coesite, corundum (stable at 1200°C) and anatase were found in inclusions of both inner and outer part of the LDG. Hence, we did not find a logical distribution of these compounds unless the LDGs suffered more than one impact when cooling but still in a melt form just to trap more materials in the second (or third) impact to the surface of the Libyan Desert.

Table 4.2. Identification and the characteristic Raman positions (cm^{-1}) of different mineral phases present in LDG, where the intensity of the bands are represented by v: very, s: strong, m: medium, w: weak and br: broad.

		Location			
		Matrix		*Inclusion*	
Compounds	**Raman bands** (cm^{-1})	*Inner*	*Outer*	*Inner*	*Outer*
Matrix	447br,602w,810br,956br,1049br, 1061br,1195br,1322br,1630br	X	X		
Microcline feldspar ($KAlSi_3O_8$)	328vw, 406w, 513m, 1096vw		X		
Zircon ($ZrSiO_4$)	351m,435m,973vw,1000vs,1050w,1085m, 1140vw	X			
Rutile (TiO_2)	445s, 610s	X		X	
Anatase (TiO_2)	141vs, 394m, 512w, 636s		X	X	X
Coesite (SiO_2)	177vw, 270w, 521m	X	X		
Quartz ($\alpha-$ SiO_2)	205m, 263w, 354w, 398vw, 464vs, 696vw, 806w, 1081w and 1160vw			X	X
Cristobalite ($\alpha-SiO_2$)	230vs, 418vs	X	X	X	X
Corundum (Al_2O_3)	416m				X
Calcite ($CaCO_3$)	153w, 279m, 710w, 1085vs	X		X	X
Amorphous Calcite($CaCO_3$)	149w, 260s, 709w, 1080vs	X			
Aragonite ($CaCO_3$)	207w, 704 w, 1083m			X	
Magnesite($MgCO_3$)	330w,739w, 1095m				X
Anhydrite ($CaSO_4$): type I and II	AI (α-CaSO4): 170w, 417w, 1017m, 1110w, 1128w, 1160vw			X	
	AII (β-CaSO): 610vw, 624vw, 1018m, 1128vw , 1161w				X
Gypsum ($CaSO_4{\cdot}2H_2O$)	411m, 618vw, 668vw, 1006m		X	X	
Amorphous carbon (C)	≈1340-1350br, ≈1580-1600br			X	X
Cinnabar (HgS)	252m				X
Hematite (Fe_2O_3)	226w, 292m, 410w, 612w, 1300br			X	
Limonite (FeO(OH))	171w, 208m, 243m, 300s, 399vs, 471br, 551s, 1282br			X	
Fosterite (Mg_2SiO_4)	303w, 430w, 604m, 820s, 854s, 961 m			X	
Enstatite ($MgSiO_3$)	231w, 296vw, 336m, 389w, 657s, 678vs, 1005vs			X	
Tephroite (Mn_2SiO_4)	811m, 843m			X	

In this sense, the atmosphere, deposits and sands of the Libyan Desert could be responsible for some compounds identified in the LDG, incorporated in the moment of the impact(s).

Besides, depending on the time of fly, the areas of the LDG could not be cooled in the same way. Thus, the cooling could have been inhomogeneous and this is translated to the nature of the mineral phases trapped in the inclusions of the different LDGs that arrived to us.

It was also possible to identify O_2(g), N2(g), N2(l), other Raman peak associated with gaseous nitrogen and a Raman band attributable to C-N bond. These gases or fluids bubbles could have been formed during the impact. Fluid inclusions could have been trapped during boiling of geothermal/hydrothermal fluids. And gaseous vesicles could have been formed in the melt with a decrease of the solubility of dissolved gases, due to changes of the physical conditions (temperature, pressure, oxygen fugacity).

Furthermore, the presence of organic compounds, previously suggested by Raman spectroscopy, was confirmed by means of Py-GC-MS at three temperatures (280°C, 600°C and 750°C). A wide range of hydrocarbons was recognized, detecting the presence of components related to plants and life. This suggests a further incorporation for some of the organic compounds from the surrounding environment to the LDGs specimens, provably through the porous of the glassy materials.

B. CHARACTERIZATION OF DARWIN GLASSES (DG)

The literature survey shown that Darwin Glasses (DGs) have been analyzed using different instrumental techniques such as Particle Induced X-Ray Emission (PIXE)[122], Elastic Backscattering Spectrometry (EBS)[122], $^{40}Ar/^{39}Ar$ single-grain laser fusion technique[123], optical microscopy[124], Scanning Electron Microscopy-Energy Dispersive X-Ray Spectroscopy (SEM-EDX)[124], Direct Current Plasma (DCP)[125], Atomic Absorption Spectrometry (AAS)[125], Electron Probe Micro Analysis (EPMA)[125], Instrumental Neutron Activation Analysis (INAA)[125]. However, there is only one study[126] where Raman spectroscopy was used for the analysis but it was not a Darwin glass specific study.

The literature search showed also the scarce information about the molecular composition of inclusions and matrix of DGs. Thus, with the aim of characterizing them and understanding more about the formation process of these glasses, a complete Raman spectroscopic study has been carried out, together with Micro-Energy Dispersive X-Ray Fluorescence Spectroscopy (μ-EDXRF), X-Ray Diffraction (XRD), SEM-EDS and EPMA, to provide elemental and molecular information of our Darwin Glasses collection (see Fig. 4.28).

[122] M.J. Bailey, K.T. Howard, K.J. Kirkby, C. Jeynes, Characterisation of inhomogeneous inclusions in Darwin glass using ion beam analysis, Nuclear Instruments and Methods in Physics Research Sect. B. 267 (2009) 2219-2224.
[123] C.H. Lo, K.T. Howard, S.L. Chung, S. Meffre, Laser-fusion 40Ar/39Ar ages of Darwin impact glass, Meteoritics & Planetary Science 37 (2002) 1555-1562.
[124] L. Neil, K.T. Howard, Rare Inclusions in Darwin Glass: Partial Melts, 45th Lunar and Planetary Science Conference, Texas, 2014; 1932.
[125] T. Meisei, C. Koeberl, J. Ford, Geochemistry of Darwin impact glass and target rocks, Geochimica et Cosmochimica Acta 54 (1990) 1463-1474.
[126] E. Faulques, E. Fritsch, M. Ostroumov, Spectroscopy of natural silica-rich glasses, Journal of Mineralogical and Petrological Sciences 96 (2001) 120-128.

Fig.4.28. Images of Darwin Glasses belonging to the University of Basque Country (UPV/EHU) collection: a) DW4, b) DW1, c) DW2 and d) DW3.

The specimens were analyzed both in the surface and internally. Some of the specimens were laminated, like the LDG samples, and several thin laminas were obtained and used for the analyses. Moreover, some samples were subjected to Py-GC-MS to characterize the possible organic compounds.

1. ELEMENTAL RESULTS

1.1 Energy Dispersive X-Ray Fluorescence Spectroscopy (EDXRF)

The EDXRF results, based on more than 10 measurements per sample, revealed that the same major elements were found to be present in all of the samples. Differences in the higher or lower presence of these elements were attributed to the variation in sample colour. The elements found in all the studied samples were Si, Al, Fe, K and Ca together with some minor elements like Ti, Ba, S, Cr, Mn, Ni and Sr.

The darkest specimens are those with the lower presence of silicon and higher presence of iron and aluminium. In the case of DW4, the EDXRF data suggested that the colour differences could be due to the different elemental composition of the particular DG specimen. This elemental composition found in our samples is

consistent with the referred geochemistry of the target rocks at Darwin Crater[127]. Finally, DW3 represents a special case due to the presence of a high amount of copper inside; also, its inner matrix contained calcium.

1.2 Scanning Electron Microscopy/Energy Dispersive X-Ray Spectroscopy (SEM-EDX)

The SEM images (Fig. 4.29 shows one of such images) of the thin sections revealed that Darwin Glass is highly vesicular with a glassy groundmass. The glassy groundmass is mainly holohyaline (> 80% glass) ranging from colourless to brownish in colour, defining Schlieren structures. Schlieren structures indicate different flow/layering zones of the silicate matrix as impact melts display. These structures are characterised by the presence of abundant elliptical vesicles.

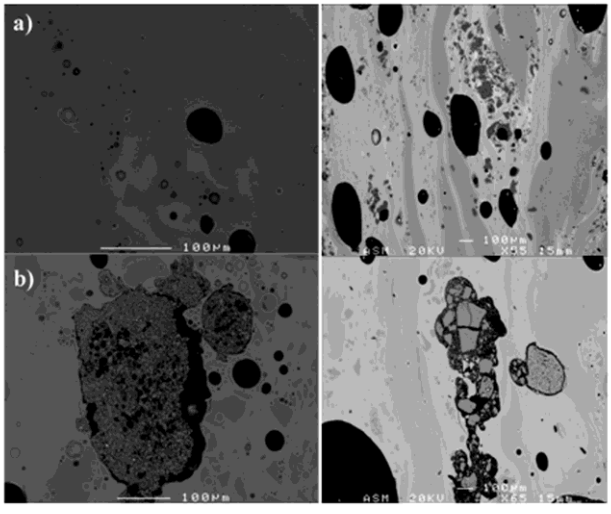

Fig.4.29. SEM images of Darwin glass with: (a) schlieren structures defined by different grey colour zones (the darker area corresponds to silica); (b) different filled vesicles in the matrix. Black elliptical are empty vesicles. Angular grey inclusions surrounded generally by a light grey or whitish colour are silica pure inclusions.

The SEM-EDX results revealed variations in the matrix. SEM back scattered images and various mapping by EDX determined evident compositional differences (see Fig. 4.30). In the Si EDX map, the white area corresponds to silica rich inclusions or pure

[127] K.T. Howard, Physical Distribution Trends in Darwin *Glass,* Meteoritics and Planetary Science *44* (**2009**) 115-129.

silica, and it is surrounded by gradient concentrations of other elements such as Al, Fe, K and Mg.

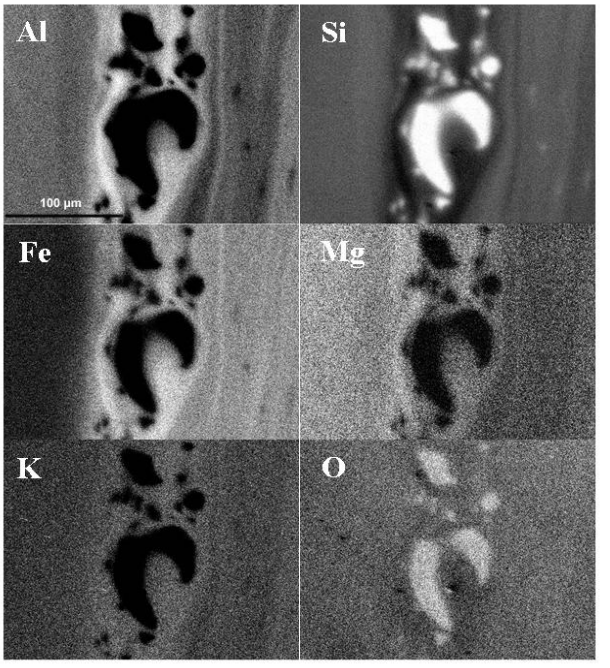

Fig.4.30. EDX mapping images of a silica rich inclusion and the distribution of major elements around it.

According to the results, the aluminium and iron distribution maps are very similar, suggesting the formation of aluminium iron-silicate, a very common compound of sediments[128], which probably was incorporated to the matrix during the impact.

In addition, Fig.4.29.b shows some areas of the DG thin sections rich in vesicles indicating disequilibrium and rapid quenching conditions, characteristics of impact glasses. Others vesicles are filled with angular mineral fragments that represent target sedimentary material[129]. For instance, in some of these vesicles nickel-iron or iron oxide (see the following Raman spectroscopy section) was identified around the entire vesicle. They always appeared as perfect elliptical vesicles.

[128] J. Komlos, R.K. Kukkadapu, J.M. Zachara, P.R. Jaffé, Biostimulation of iron reduction and subsequent oxidation of sediment containing Fe-silicates and Fe-oxides: Effect of redox cycling on Fe(III) bioreduction, Water research *41* (**2007**) 2996-3004.
[129] K.T. Howard, Geochemistry of Darwin glass and target rocks from Darwin crater, Tasmania, Australia, Meteoritics and Planetary Science 43 (**2008**) 479-496.

1.3 Electron Probe Micro Analysis (EPMA)

To confirm the elemental distribution found by SEM-EDX, semi-quantitative analysis by EPMA were carried out in different areas of the Darwin Glass glassy matrix (as an example, see some details in Fig. 4.31). The concentration ranges for the compositions of the main elements were the following: SiO_2 varies from 80% to 90% wt (excluding the SiO_2 pure inclusions detected in point #1, see Fig. 4.31), Al_2O_3 (5.0 to 9.1 %wt), FeO/Fe_2O_3 (2.0 to 4.0 %wt), MgO (0.30 to 0.80 %), K_2O (1.8 to 2.3), CaO (0.010 to 0.030 %) and TiO_2 (0.35 to 0.60%).

The high heterogeneous composition, in a micrometer scale, reflects the melting heterogeneity process as well as the existence of differences during the transport (flying) before the solidification.

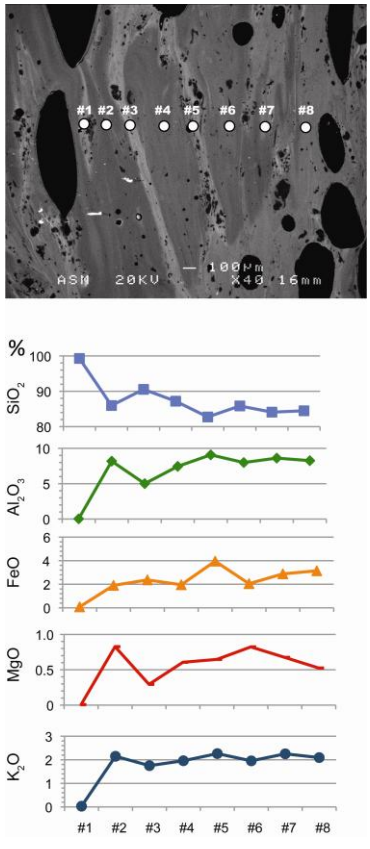

Fig.4.31. SEM image of a thin section of a Darwin glass with the points where the electron microprobe analysis were performed. Below, scatter diagrams for the analyzed major elements. Point #1 is a silica pure inclusion.

2. MOLECULAR RESULTS

2.1 Raman Spectroscopy

More than 100 Raman measurements were performed and it was determined that the dark bulk of all Darwin glasses was a silica vitreous matrix, with its main Raman bands at 110vw, 480s, 810w, 930sh and 1021s cm^{-1}, very similar features to those obtained for Libyan Desert Glass matrixes (see Fig. 4.32).

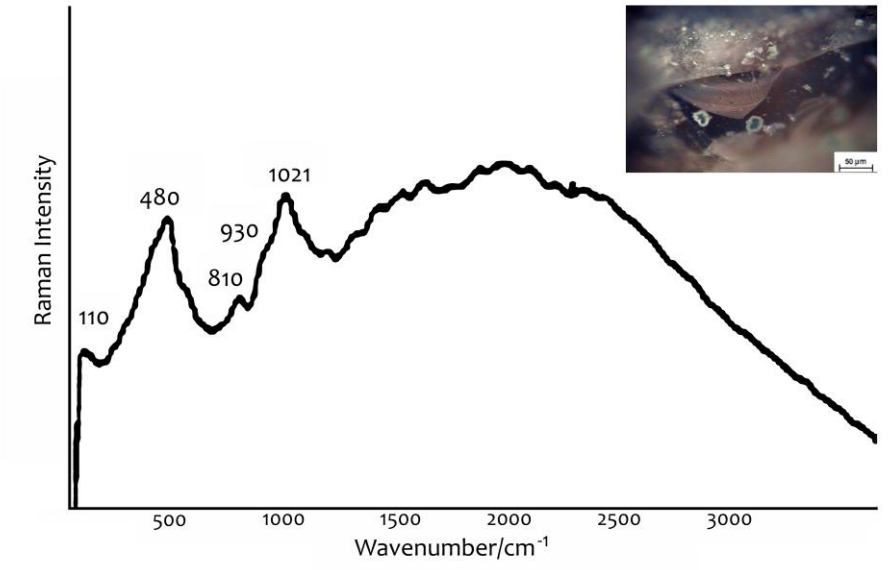

Fig.4.32. Microimage of DW3 with details of the crystals and Raman spectrum of the black matrix (Laser: 514 nm).

However, the relative intensities of the Raman bands of Darwin Glass are really different to LDG. In the case of LDG, the 480 cm^{-1} band is the most intense one. In contrast, in Darwin glass, apart from the band at 480 cm^{-1}, there is also another major band at 1021 cm^{-1}, whilst in LDG, that band is very weak. As it has been mentioned in the LDG section, the band around 400–600 cm^{-1} varies with the degree of polymerization of the glass and with Si-O-Si (and Si-O-Al) bridging bond angles[130]. The

[130] A. Gucsik, C. Koeberl, F. Brandstätter, E. Libowitzky, M. Zhang, Infrared, Raman and cathodoluminescence studies of impact glasses, Meteoritics and Planetary Science 39 (2004) 1273-1285.

position near 800 cm^{-1} involves symmetric motions of Si-O-Si bending and around 800-1200 cm^{-1} is associated with symmetric Si-O stretching vibrations[131].

In addition, some large white crystals were seen in the margins of the bulk and in the centre within the glassy matrix with the naked eye. These white crystals were composed of α-cristobalite (SiO_2), identified by Raman peaks at 230s, 417vs, 783m and 1076m cm^{-1} (see Fig. 4.33.a).

As stated before, the α-quartz, which is the low temperature stable polymorph of SiO_2, is converted into β-cristobalite at >1470 °C. And in the cooling process, β-cristobalite transforms into α-cristobalite. Therefore, the presence of α-cristobalite normally indicates the former presence of β-cristobalite and, hence, a temperature greater than 1470 °C[132]. Besides, in the Fig. 4.33.a together with α-cristobalite, it can be observed a group of Raman bands around 2800-3000 cm^{-1}, attributed to C-H stretching vibrations[133].

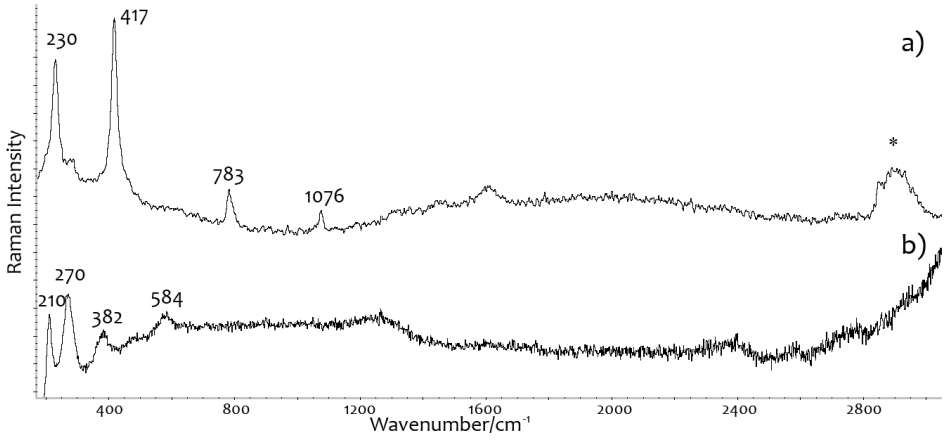

Fig. 4.33. Raman spectra of cristobalite (a) and typical vibration signal of –CH at around 2900 cm^{-1} (*), and Iron or Nickel and iron oxide (b) (Laser: 785 nm).

[131] E. Faulques, E.Fritsch, M. Ostroumov. Spectroscopy of natural silica-rich glasses. Journal of Mineralogical and Petrological Sciences 96 (2001) 120-128.
[132] D. C Smith, J. D. Vernioles, The Temperature of Fusion of a Celtic Vitrified Fort: a Feasibility Study of the Application of the Raman Microprobe to the Non-Destructive Characterization of Unprepared Archaeological Objects, Journal of Raman Spectroscopy *28* (1997) 195-197.
[133] M.W. Ducey, Jr., C. J. Orendorff, J.E. Pemberton, Structure-Function Relationships in High-Density Octadecylsilane Stationary Phases by Raman Spectroscopy. 1. Effects of Temperature, Surface Coverage, and Preparation Procedure, Analytical Chemistry 74 (2002) 5576-5584.

Some areas of the Darwin Glass are rich in vesicles, as it has been observed by SEM image, and in several of these vesicles nickel-iron or iron oxide was identified around the entire vesicle (Fig. 4.33.b), with Raman bands at 210m, 270s, 382br and 584br cm^{-1} [134]. Taking into account the identified bands, this compound could be hematite or also an iron-nickel compound which has been previously identified in meteorites, specifically in ordinary chondrites, where they appeared also filling pore spaces[135].

Furthermore, a blue-turquoise crystal was observed macroscopically in the centre of one of the biggest α-cristobalite inclusions, inside the DW3 specimen (see Fig. 4.28.d for details). The presence of this type of crystal is unusual in these melt specimens. The Raman spectroscopic analysis revealed the presence of a mixture of copper compounds, such as malachite ($Cu_2CO_3(OH)_2$) (see Fig. 4.34.a) and ponsjankite ($Cu_4SO_4(OH)_6{\cdot}H_2O$) (see Fig. 4.34.b). In addition to the white crystals of α-cristobalite, and not necessarily related to those blue crystals, covellite (CuS) was often found as evidenced by its characteristic Raman band at 471 cm^{-1} (see Fig. 4.34.c).

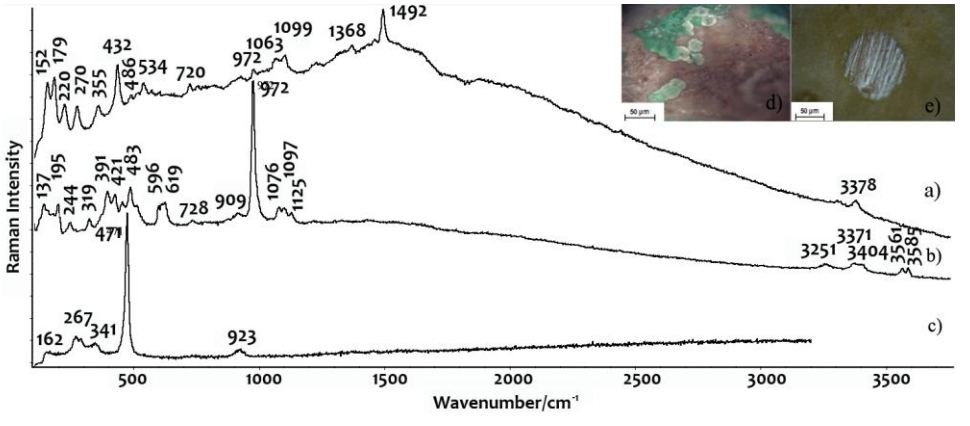

Fig. 4.34. Raman spectrum of a) malachite, b) ponsjankite and c) covellite. Microphotographs of d) ponsjankite (intense turquoise colour) and malachite (spherical structure) and e) covellite with its spherical structure (Laser: 785 nm).

Raman spectroscopic analysis of the Darwin Glass samples revealed a number of mineral phases which can be used to estimate the temperature of formation. SiO_2 is

[134] A. Weselucha-Birczynska, M. Zmudzka, Micro-Raman spectroscopy characterization of selected meteorites, Journal of Molecular Structure 887 (2008) 253-261.
[135] D. C Smith, J. D. Vernioles, The Temperature of Fusion of a Celtic Vitrified Fort: a Feasibility Study of the Application of the Raman Microprobe to the Non-Destructive Characterization of Unprepared Archaeological Objects, Journal of Raman Spectroscopy 28 (1997) 195-197.

transformed into β -cristobalite at 1470ºC, thus, it would have to be formed during the impact. In contrast, the malachite carbonate would disappear at temperatures higher than 800ºC, which could mean that this compound was formed (trapped) after the first impact.

All mineral phases detected in our Darwin Glasses samples have been listed in the Table 4.3.

Table 4.3. Raman bands of the compounds identified in the analyzed Darwin Glasses.

Compounds	***Raman bands***
Vitreous matrix	110vw, 480s, 810w, 930sh, 1021s
Cristobalite (SiO_2)	230s, 417vs, 783m, 1076m
Malachite ($Cu_2CO_3(OH)_2$)	152m, 179m, 220w, 270w, 355w, 432s, 486vw, 534vw, 720vw, 972vw, 1063vw, 1099vw, 1368vw, 1492s
Ponsjankite ($Cu_4SO_4(OH)_6 \cdot H_2O$)	137m, 195m, 244vw, 319vw, 391m, 421m, 483m, 596m, 619m, 728vw, 909vw, 972vs, 1076w, 1097w, 1125vw, 3251vw, 3371vw, 3404vw, 3561vw, 3585vw
Covellite (CuS)	162vw, 267w, 341vw, 471vs, 923vw
Ni-Fe oxide	210m, 270s, 382m, 584w

On the other hand, it was discerned some bands probably related to organic compounds in the Darwin Glasses, as it has been found in the LDG samples. They appeared at 1301w, 1438w, 1608w, 1653w, 2724vw, 2851s, 2882s, 2930s and 3065vw cm^{-1} (see Fig. 4.33.a and Fig. 4.35). It was thought that they could belong to aromatic compounds, since various aromatic C-C stretching vibrations are included around

1350-1700cm^{-1}. Moreover, C-C bands at 1400 cm^{-1} and 1625–1675 cm^{-1} are both present in PAHs with at least five aromatic rings in the core[136].

The aromatic hydrocarbons could be composed of a few base groups such as methyl and methylene. In our case, Raman bands at 2851 and 2882 cm^{-1} could correspond to symmetric stretching vibrations of CH_2 and CH_3 respectively, and at 2930 cm^{-1} to antisymmetric stretching vibrations of CH_2[137]. C-H bonds were already displayed in Raman spectra, where bands at 2851, 2885 cm^{-1} and 2930 cm^{-1} as well (see Fig. 4.33) were detected.

The origin of these hydrocarbons would be by any organic material that has been transformed at high temperature. PAHs can be formed by incompletely carbonized or combusted organic matter at high temperature (500–700°C) over very short time periods[138,139].

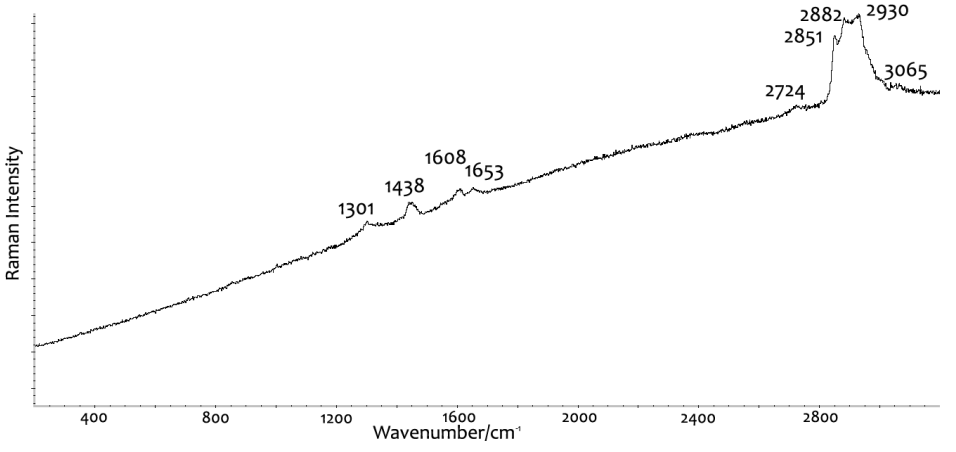

Fig.4.35. Raman spectrum of organic compounds (Laser: 785 nm).

[136] A. Ballard Andrews, D. Wang, K.M. Marzec, O.C. Mullins, K. B. Crozier, Surface enhanced Raman spectroscopy of polycyclic aromatic hydrocarbons and molecular asphaltenes, Chemical Physics Letters, 620 (2015) 139–143.

[137] G. Socrates. Infrared and Raman Characteristic Group Frequencies: Tables and Charts. Wiley 3rd Edition, 2004

[138] T. Wenzl, R.Simon, E. Anklam, Analytical methods for polycyclic aromatic hydrocarbons (PAHs) in food and the environment needed for new food legislation in the European Union, Trends in Analytical Chemistry 25 (2006) 716–725.

[139] G.Purcaron , S.Moret, L.S. Conte, Overview on polycyclic aromatic hydrocarbons: Occurrence, legislation and innovative determination in foods, Talanta 105 (2013) 292–305.

2.2 X-Ray Diffraction (XRD)

The XRD analyses on the DG matrix showed only one crystalline phase, α-cristobalite (see Fig. 4.36).

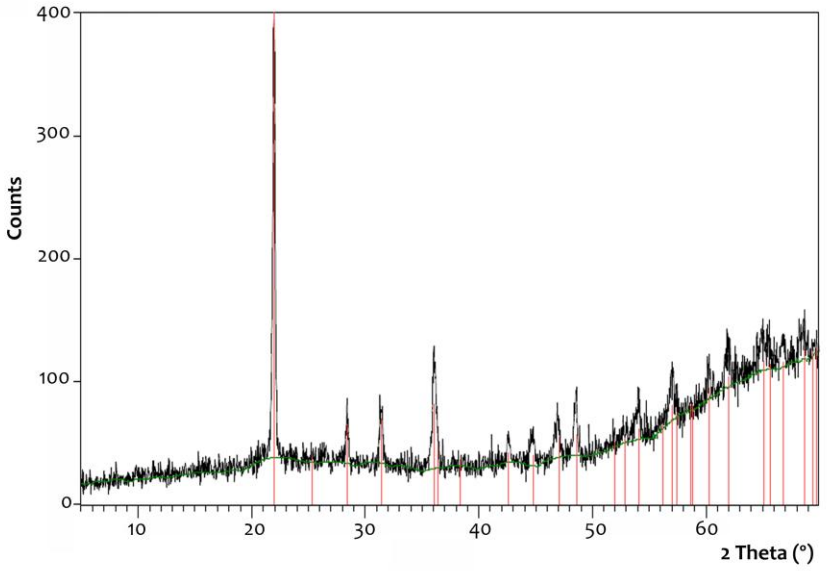

Fig.4.36. Diffractogram of DG sample (red: α-cristobalite).

3. Pyrolysis - Gas Chromatography Mass Spectrometry (Py-GC-MS)

As in the case of LDG samples, due to the probably presence of organic compounds in the DG as detected by Raman spectroscopy, samples were analyzed by Py-GC-MS. All samples were subjected to the same sequential pyrolysis program previously used. The first temperature of analysis was 280°C, followed by another analysis at 600°C and finally to 750°C.

At 280°C, nonanal; decanal; oxalic acid, monoamide, N-(3-(N-morpholinyl)propyl)-, butyl ester and β-d-mannofuranoside, O-geranyl were identified**.** This last compound

plays a functional role in the chemical defense against microbial invasion in plants[140]. At 600°C, it was distinguished 1-heptene; 1H-pyrrole, 3-methyl- (aromatic hydrocarbon); styrene (aromatic hydrocarbon); 1,2-cyclopentanedione; 2-furancarboxaldehyde, 5-methyl-; phenol (aromatic hydrocarbons); 2-methyl-phenol; 1-decene; p-cresol (aromatic hydrocarbon); 1-dodecene; 1,4:3,6-Dianhydro-.alpha.-d-glucopyranose (sugars from plants); n-tridecan-1-ol; indole (polycyclic aromatic hydrocarbon); 5-Octadecene, (E)-; pentafluoropropionic acid, undecyl ester; acetic acid, chloro-, octadecyl ester; 7-Hexadecene, (Z)-; pentanedioic acid, dibutyl ester; cyclododecane; 1-nonadecene and cholesta-3,5-diene (related to cellular tissues of animals[141]); toluene (aromatic hydrocarbon); 2-propenoic acid, 2-methyl-, 2-methylpropyl ester; benzene, 1-propenyl- (aromatic hydrocarbon); cetene; trichloroacetic acid, undecyl ester;dichloroacetic acid, heptadecyl ester; 1-tetradecanol; carbonic acid and octadecyl 2,2,2-trichloroethyl ester (see Fig. 4.37).

Finally, at 750°C the chromatogram shown the presence of: benzene; benzene, 1-isocyano-2-methyl-; styrene (aromatic hydrocarbon); phenol (aromatic hydrocarbon); p-cresol (aromatic hydrocarbon); 1-nonanol; naphthalene, 1-methyl- (aromatic hydrocarbon).1-Decene; n-Tridecan-1-ol; Benzonitrile, 3-methyl-; cyclopentane, 1,1,3-trimethyl-; naphthalene, 2-methyl-; benzocycloheptatriene ;cyclotetradecane and n-Heptadecanol-1 (see Fig.4.38).

[140] A. Manilal, B. Merdekios, J. Kambivelikkakath Velappan, J.P. Veliyath Paul, A. Idhayadhulla, C. Muthukumar, M. Melkie, An in vitro efficacy validation of mangrove associates, Journal of Coastal Life Medicine 2 (2014) 560-565.

[141] P. J. Weldon, B. Flachsbarth, S. Schulz, Natural products from the integument of nonavian reptiles, Natural Product Reports 25 (2008) 738–756.

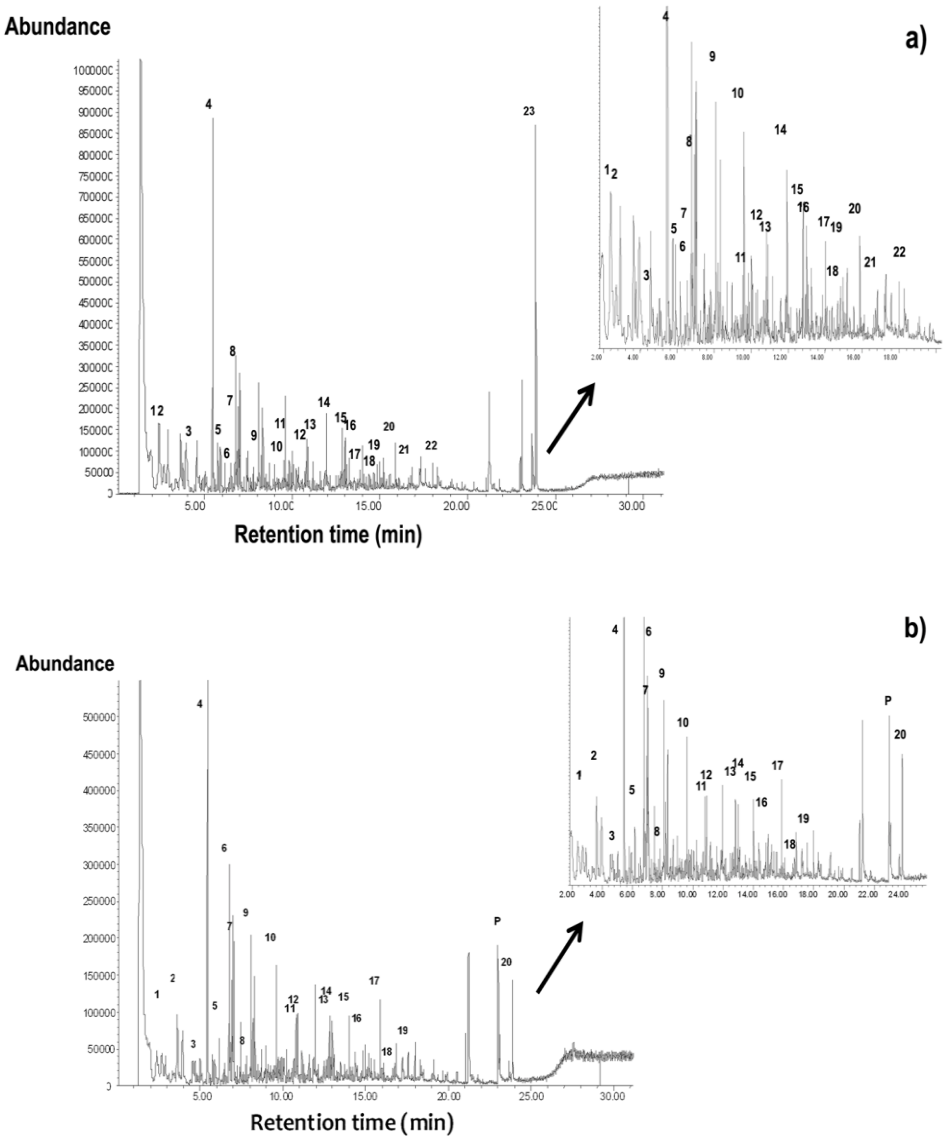

Fig.4.37. DG chromatograms for 600°C. (a) 1: 1-heptene; 2: methyl methacrylate (possible contamination of the sample during storage) ; 3: 1H-pyrrole, 3-methyl-; 4: styrene; 5: 1,2-cyclopentanedione; 6: 2-furancarboxaldehyde, 5-methyl-; 7: phenol; 8: 1-decene;9: p-cresol; 10: 1-dodecene; 11: 1,4: 3,6-Dianhydro-.alpha.-d-glucopyranose; 12: n-tridecan-1-ol; 13: indole; 14: 5-Octadecene, (E)-; 15: pentafluoropropionic acid, undecyl ester; 16: acetic acid, chloro-, octadecyl ester; 17 and 20: 7-Hexadecene, (Z)-; 18: pentanedioic acid, dibutyl ester; 19 and 21: cyclododecane; 22: 1-nonadecene; 23: cholesta-3,5-diene. Zoom at 2-18 min (right image). (b) 1: 1-Heptene; toluene; 2: 1H-Pyrrole, 3-methyl-; 3: styrene; 5: 2-propenoic acid, 2-methyl-, 2-methylpropyl ester; 6: phenol; 7: benzene, 1-propenyl-; 8: 2-methyl-phenol; 9: p-cresol; 10,13,16: cyclododecane; 11: trichloroacetic acid, undecyl ester; 12: indole; 14: dichloroacetic acid, heptadecyl ester; 15: 1-tetradecanol; 17: cetene; 18: carbonic acid, octadecyl 2,2,2-trichloroethyl ester; 20: Cholesta-3,5-diene. Zoom at 2-24 min (right image). P: plasticizers (modern contamination).

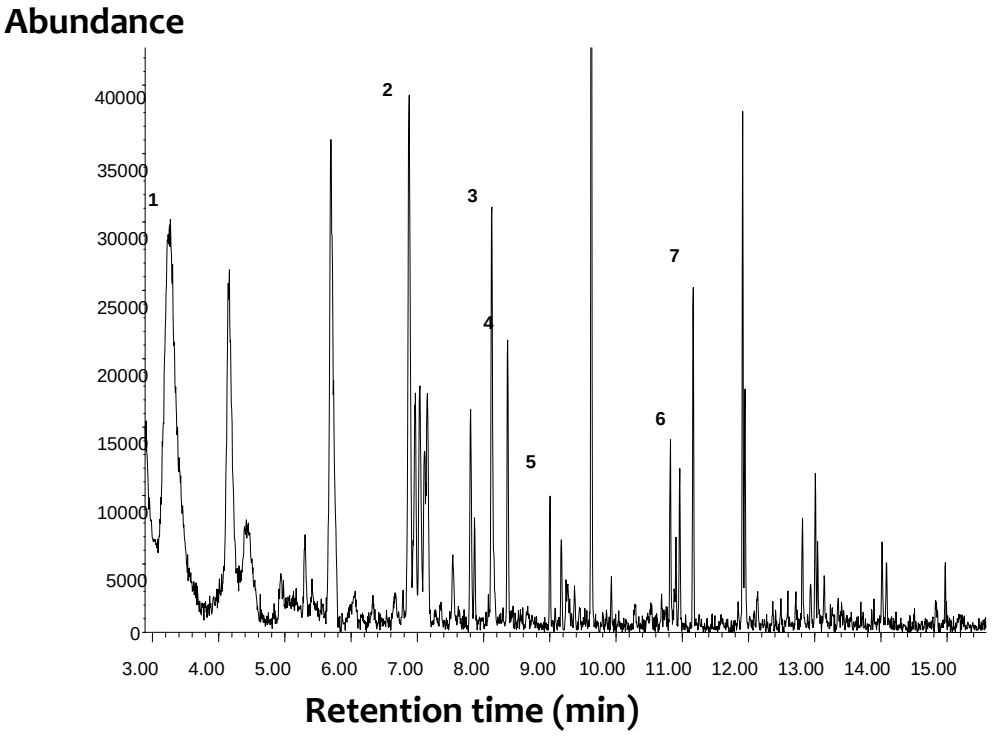

Fig.4.38. DG chromatogram for 750°C. 1: benzene; 2: phenol; 3: p-cresol; 4: 1-nonanol; 5: benzene, 1-isocyano-2-methyl-; 6,7: naphthalene, 1-methyl-.

As observed with the LDG samples, the DG ones showed a high number of detected compounds at 600 °C. Among the identified compounds there were mainly hydrocarbons (long-chain hydrocarbons, cyclic and aromatics), some of them related to components of plants such as 1-nonanol, decanal, styrene, p-cresol, β-d-mannofuranoside, O-geranyl and 1,4:3,6-Dianhydro-.alpha.-d-glucopyranose. Moreover, compounds associated with bacterial life and animals were detected, such as p-cresol, indole and cholesta-3,5-diene. It should be pointed out that it was also detected m-guaiacol, a compound related to bacteria as well[142]. Although its identification did not reach the 70% of match, its presence in this type of samples was corroborated by a similar finding in a paper published in 2013[143]. The organic compounds resistance at those temperatures could mean that the compounds may predate the impact.

[142] I. Shimomura, R. E. Hammer, S. Ikemoto, M. S. Brown, J. L. Goldstein, Brief communication, Pheromones: Exploitation of gut bacteria in the locust, Nature 40 (2000) 851.
[143] K. T. Howard, Biomass preservation in impact melt ejecta, Nature Geoscience 6 (2013) 1018-1022.

Apart from these organic compounds, modern organic compounds related to plastic were detected, suggesting a possible contamination of the samples due to its not adequate storage conditions, previous to our acquisition.

4. DISCUSSION

Darwin Glasses presented a heterogeneous composition where the major elements found in the Darwin Glass samples were Si, Al, Fe, K and Ca, and minor Ti, Ba, S, Cr, Mn, Ni and Sr. A particular case was the higher presence of Cu in DW3 sample. On the other hand, SEM-EDX and EPMA results revealed variations in the matrix composition. Cathodoluminiscence analysis was performed but the results did not give conclusive results.

By means of Raman spectroscopy it was identified the characteristic silica vitreous matrix, together with α-cristobalite (SiO_2) inclusions, which indicated that the glasses were formed at high temperatures. Moreover, the presence of malachite ($Cu_2CO_3(OH)_2$), ponsjankite ($Cu_4SO_4(OH)_6 \cdot H_2O$), covellite (CuS) and possibly organic compounds suggested that they were formed or incorporate to the matrix after the impact.

By means of Py-GS-MS it was possible to detect those organic compounds, which were mainly hydrocarbons. They endured high temperatures in the analysis (280°C, 600°C and 750°C), so it could be thought that they may be prior to the impact. In addition, it was observed the presence of components associated with plants and bacterial life.

C. CHARACTERIZATION OF ELECTRIC ARC FURNACE (EAF) STEEL SLAG

According to literature, we have considered the steel slag materials, from Electric Arc Furnace (EAF) production, as a terrestrial analogue to meteorites and connected to impact glasses because their composition is expected to be similar due to the fact that both have silicate matrixes and are produced at high temperatures[144].

Unlike impact glasses, the number of research papers about steel slag is high, and it is increasing to a greater extent. Possibly, because of the need to improve the knowledge about its chemical composition, and thus, it can be used correctly in any of its applications as secondary product. In the last ten years, X-Ray Fluorescence (XRF) has been one the most used technique for slag analysis, with more than 50 research papers[145-150].

[144] B. C. M. Butler, Al-rich pyroxene and melilite in a blast-furnace slag and a comparison with the Allende meteorite, Mineralogical Magazine 41 (1977) 493-499.
[145] I. Liapis, I. Papayianni, Advances in chemical and physical properties of electric arc furnace carbon steel slag by hot stage processing and mineral mixing, Journal of Hazardous Materials 283 (2015) 89-97.
[146] M. Dri, A. Sanna, M.M. Maroto-Valer, Mineral carbonation from metal wastes: Effect of solid to liquid ratio on the efficiency and characterization of carbonated products, Applied Energy 113 (2014) 515-523.
[147] L.K. Bankole, S.A. Rezan, N.M. Sharif, Crystallization of potassium calcium silicate from modified industrial EAF slag, Advanced Materials Research 620 (2013) 66-71.
[148] J. Xie, S. Wu, J. Lin, J. Cai, Z. Chen, W. Wei, Recycling of basic oxygen furnace slag in asphalt mixture: Material characterization & moisture damage investigation, Construction and Building Materials 36 (2012) 467-474.
[149] R. Yellepeddi, D. Bonvin, X. Li, XRF analysis of metallurgical slags in the iron and steel industry, Yejin Fenxi/Metallurgical Analysis 31 (2011) 34-37.
[150] C. Navarro, M. Díaz, M.A. Villa-García, Physico-chemical characterization of steel slag. study of its behavior under simulated environmental conditions,Environmental Science and Technology 44(2010)5383-5388.

However, Raman spectroscopy has been little used for characterization purposes [151-154].

Hence, in this work Raman spectroscopy was selected as the analytical technique of choice, and different Raman spectrometers were used. On one hand, a hand-held Raman spectrometer was used, which allows field analysis *in situ* (thanks to the small size that makes easier the transport by only one person[155]). However, in our case it was used in the laboratory to check its future use and to characterize major (and minor) mineral phases. To assist hand-held Raman analysis (spots around 100μm), Micro-Energy Dispersive X-Ray Fluorescence Spectroscopy (μ-EDXRF) (spots around 650 μm) and X - Ray Diffraction (measured area of 10x10 mm) were used. Moreover, a micro-Raman spectrometer was used in order to characterize minor and trace compounds, because of the possibility to use magnification microscope objectives to focus the laser beam on the selected material layer.

Also, the so-called Structural and Chemical Analyzer (SCA) was used to observe other compounds at the trace level. SCA (Raman plus SEM/EDS) allows to merge the analytical advantages of several individual techniques in the same system (the EDS analysis helped to select what elements were present in the exact point of Raman measuring of the black slag) but at trace levels (spots of less than 5 μm).

Finally, Raman Image and X-Ray Photoelectron Spectroscopy (XPS) analysis were used to study the effect induced by the water rinse (come from the slag pre-treatment or the atmosphere during its storage) in the chemical composition of the treated slag surface.

In this part of the chapter, the selected samples were steel slags from common, special and stainless steel factories located in the Basque Country and in Belgium.

[151] S.S. Jung, I. Sohn, Crystallization control for remediation of an FetO-rich CaO-SiO_2-Al_2O_3-MgO EAF waste slag , Environmental Science and Technology (2014) 48 1886-1892.
[152] J. Liao, Y. Zhang, S. Sridhar, X. Wang, Z. Zhang, Effect of Al_2O_3/SiO_2 ratio on the viscosity and structure of slags, ISIJ International 52 (2012) 753-758.
[153] L. Jianxin, Y. Qijun, W. Jiangxiong, Z. Tongsheng, Structural characteristics and hydration kinetics of modified steel slag, Cement and Concrete Research 41 (2011) 324-329.
[154] J. Waligora, D. Bulteel, P. Degrugilliers, D. Damidot, J.L. Potdevin, M. Measson, Chemical and mineralogical characterizations of LD converter steel slags: A multi-analytical techniques approach, Materials Characterization 61 (2010) 39-48.
[155] I. Martínez-Arkarazo, D.C. Smith,O. Zuloaga, M. A. Olazabal, J.M. Madariaga, Evaluation of three different mobile Raman microscopes employed to study deteriorated civil building stones, Journal of Raman Spectroscopy 39 (2008) 1018-1029.

They were collected directly after their dumping from the furnaces, after a short term treatment and from different construction works few weeks after their deposition (see Fig. 4.39).

M1 is a slag coming from a common steel producer, obtained directly after its extraction from the Electric Arc Furnace unit, once cooled. M1T is the same king of slag but it has been left outside for three months with periodical water washing. M2 and M2T have the same meaning but are coming from special steel productions. M3 and M4 are two different slag in appearance, sampled in two different building constructions (civil works), where the slag materials (it should be treated slags) are used to support the heavy traffic around the construction. M6 is a slag from stainless steel but produced in a factory located in Belgium.

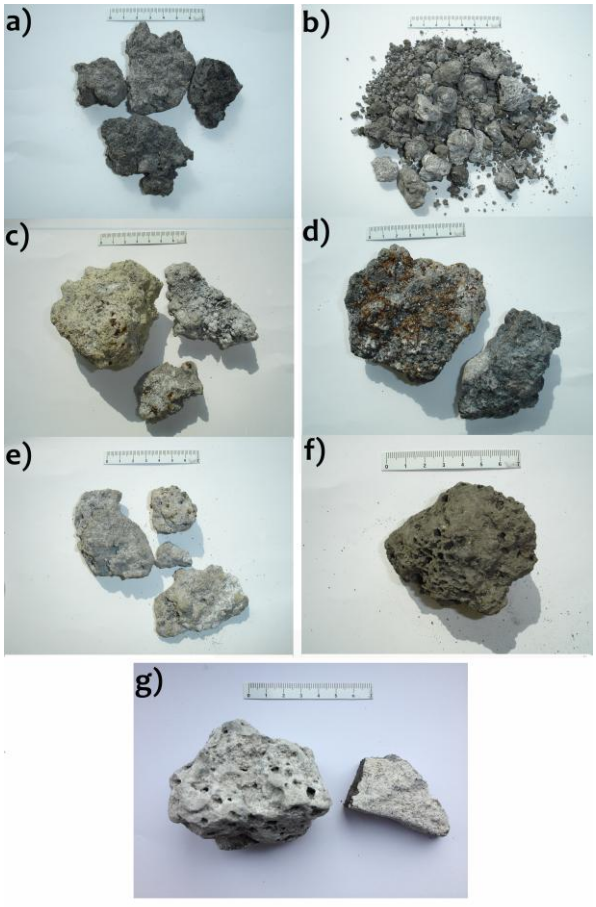

Fig. 4.39. Black slag studied samples: (a) M1, (b) M1 T, (c) M2, (d) M2 T, (e) M3, (f) M4 and (g) M6.

The proposed novel approach was designed to perform a complete characterization of the samples, from major till minor and trace compounds, mainly based on spectroscopic techniques, and allowed us to establish an analytical procedure for future works.

1. ELEMENTAL RESULTS

1.1 Micro-Energy Dispersive X-Ray Fluorescence Spectroscopy (μ-EDXRF)

The elemental characterization of slag at micro level was made through μ-EDXRF over several points of the raw samples. It was selected one slag of each type (M1, M1T, M2, M2T, M3, M4, and M6), and more than 10 measurements were done per slag.

The characteristic elements present in all the analysed samples were: Si, Al, Ca, Ti, Cr, Mn, Fe, Cu, Zn, Sr, Ba, S, P and V. Whereas As, Se, Sn, Rb and Ni were occasionally observed. Ni appeared more often in the special (M2, M2T) and stainless (M6) steel slag.

When the XRF spectra of non treated and treated samples were compared, some important differences in the relative peak area of the elements were observed (see Fig. 4. 40), probably as a consequence of the appearance of new mineral phases (many metallic oxides present in the original slag materials will be transformed in the corresponding hydroxides and/or carbonates) after the treatment suffered by these slags. Thus, a comparative molecular analysis is required among treated and non treated samples to confirm this observation.

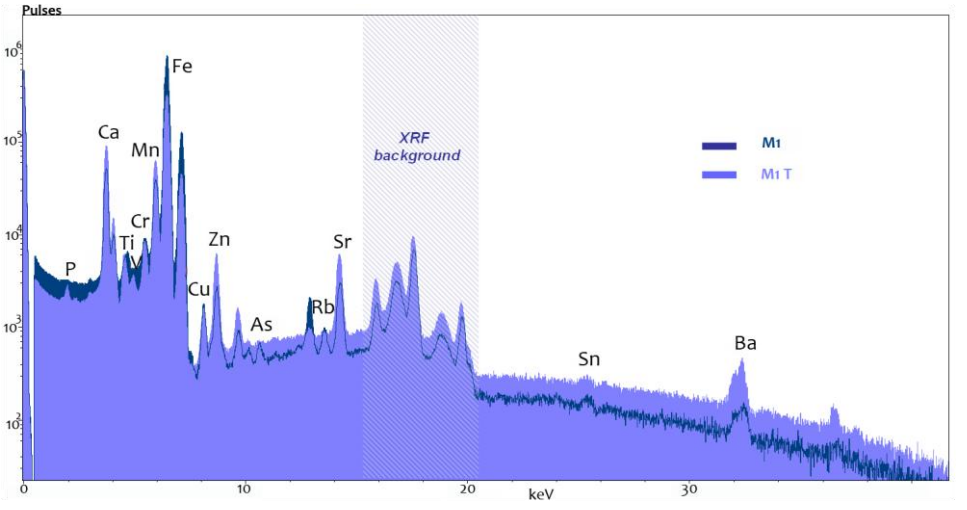

Fig. 4.40. XRF spectra of M1 and M1T slag samples.

Once the elements present in the slag was known, their distribution was observed by means of μ-EDXRF mapping. Therefore, it could be discerned their higher or lower presence along the selected areas, distinguishing between the inner and the outer part. For that purpose, slags were broken in half. Fig. 4.41 shows a group of maps (area of 45 mm^2 from the inner part of the slag -point zero in the maps- to the nearest point to the surface of the slag -point 15 in the maps-) belonging to several elements identified in the same area of a M2 T sample: Ca, P, S, V, Ba, Cr, Cu, Fe, Mn, Si, Sn, Sr, Ti and Zn. The white zones in the maps mean absence of that element. Each map has a color scale according to the higher or lower presence of each element.

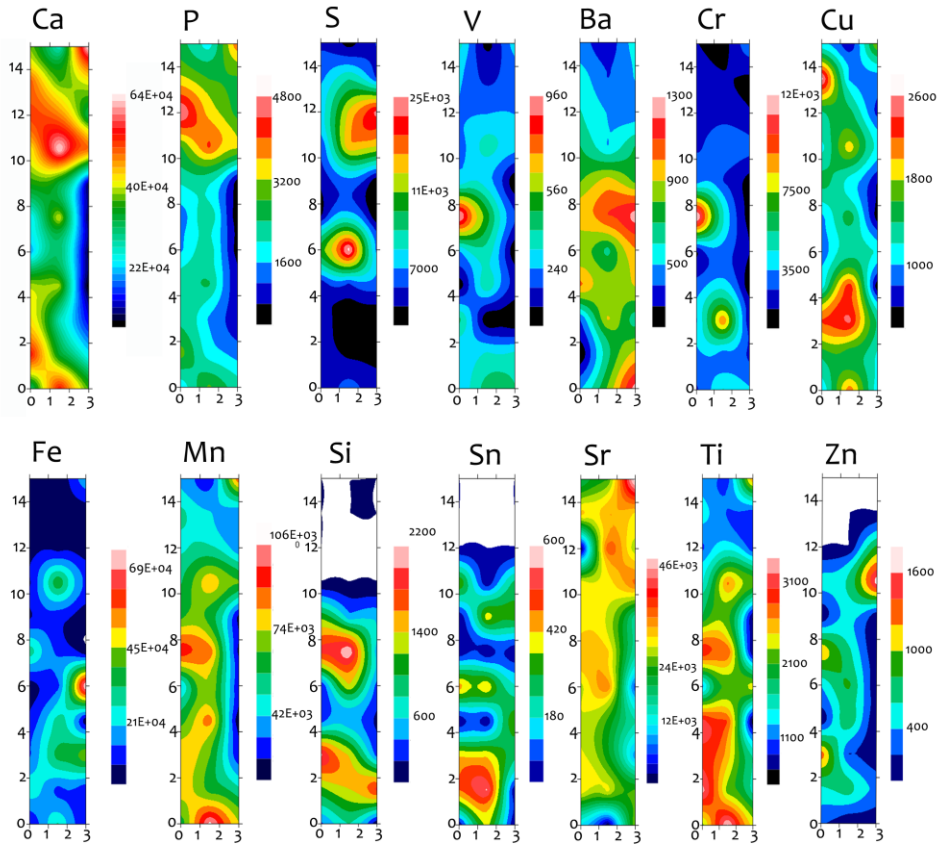

Fig. 4.41. μ- EDXRF mapping (Ca, P, S, V, Ba, Cr, Cu, Fe, Mn, Si, Sn, Sr, Ti and Zn elemental maps) over the same area of a M2T slag from its inner part (point 0) up to its outer part (point 15).

Several interesting conclusion can be drawn from these element distribution images. For example, calcium (and Sr in a lower extent) is mainly present in the most superficial zone. Also, P and S have higher presence in the outer part. The highest presence of S in the surface can be attributable to the attack by SO_X gases, which would react firstly with the part nearer to the atmosphere.

Si, Sn and Zn do not appear in the outer part. In the case of the Si map, it has a zone with high presence that coincides with the zone of high presence of Mn. Here the tephroite (Mn_2SiO_4) could be present (later, Raman spectroscopy identified that compound).

Apart from Ca, Fe is the element that has more presence along the analyzed area (look at the counts in the color frame of the element and compare with other elements), but its distribution is not homogeneous, with a lower presence in the surface. V, Ba and Cr also have the lowest presence in the zone nearer surface. Cu, Ti and Zn have a homogeneous distribution with the exception of some points where they can be more present. However, Sr has the most homogeneous distribution.

Consequently, examining these results, slag samples can be considered materials with a heterogeneous elemental distribution and thus, the point-by-point analysis should be performed carefully, repeating the measurements in several spots of the slag sample.

1.2 X-Ray Photoelectron Spectroscopy (XPS)

This technique was used to perform the elemental analysis in the surface of the raw slag samples. Table 4.4 and 4.5 display the elements identified, their positions in the XPS spectrum and their relative atomic percentages.

Table 4.4. Estimation of the atomic relative percentage of M2.

	Name	***Position***	***Conc.(%)***	***Rel. at.%***
C	C 1s	284.6	5.637	12.6
	C 1s	287.1	0.935	
	C 1s (carbonate)	289.4	6.057	
O	O 1s	532.2	60.045	60.0
Mg	Mg 1s	1304.5	0.959	1.0
Si	Si 2p	102.4	7.299	7.3
Al	Al 2p	73.9	3.736	3.7
F	F 1s	685.8	0.671	0.7
Ca	Ca 2p	347.3	12.81	12.8
S	S 2p	168.5	1.593	1.6
Na	Na 1s	1073.3	0.26	0.3

Table 4.5. Estimation of the atomic relative percentage of M2T.

	Name	*Position*	*Conc.(%)*	*Rel. at.%*
C	C1s	284.6	28.427	37.5
	C 1s (carbonate)	289.3	9.108	
O	O 1s	531.5	45.135	45.1
Mg	Mg 1s	1304.8	0.341	0.3
Al	Al 2p	74.1	4.201	4.2
Ca	Ca 2p	347.0	12.787	12.8

It is appreciable that the treated slag presents higher relative atomic percentage of carbon, which is due to the higher carbonation of the treated samples, and aluminium, but there is not a big difference. On the other hand, the non treated slag exhibits higher relative atomic percentage of Mg and O, perhaps this oxygen belongs to oxides that had not been hydrated and carbonated yet, unlike treated ones. Besides, it was detected Si, F, S and Na. Ca was in the same proportion in both cases.

2. MOLECULAR RESULTS

2.1 Raman Spectroscopy

More than 60 measurements were performed per raw sample/spectrometer. The major mineral phases, summarized in the Table 4.6, were identified by hand-held Raman spectroscopy in the black slag samples. As it can be seen, all slag samples have the same major components. In this work, a major mineral phase is a compound that appears more than 20% in the whole set of spectra collected with the hand-held Raman spectrometer (spots around 100 microns).

Calcite ($CaCO_3$; Raman bands at 155m, 281s, 712m, 1085vs, 1433w and 1747w cm^{-1}) was detected in all the samples, the ones without treatment, which they had only suffered from cooling (M1 and M2 samples), the ones sampled after the stabilization treatment (M1T and M2T samples) and those sampled at the civil works (M3 and M4 samples). Its presence is due to the use of caustic lime (CaO) in the formation of the

slag during the production of the steel, in order to eliminate the phosphorous[156] from the raw materials. When cooling, the remaining caustic lime suffers a hydration process that transforms it into calcium hydroxide:

$$CaO(s) + H_2O \rightarrow Ca(OH)_2(s) \qquad (4.1)$$

and then calcium hydroxide reacts with atmospheric CO_2 to give calcium carbonate (calcite):

$$Ca(OH)_2(s) + CO_2(g) \rightarrow CaCO_3(s) + H_2O \qquad (4.2)$$

The difference among samples is the relative abundance of calcite, as it can be observed in the Raman images shown in Fig. 4.42. Also the intensity of the Raman bands of calcite in the normalized spectra is lower in the non-treated than in the treated ones. The abundance observed for the M2 and M2T sample was similar to that is shown in Fig.4.42. Moreover, the abundances in M3 and M4 samples were similar to the obtained for the M1T and M2T samples, confirming that M3 and M4 samples belong to treated slag material.

[156] IHOBE, S. A. Libro Blanco para la minimización de residuos y emisiones, Servicio Central de Publicaciones del Gobierno Vasco, Vitoria-Gasteiz, 1999.

Table 4.6. Raman bands list of original or degradation compounds found in the different black slag studied (M1: common steel industry; M1 T: treated from common steel industry; M2: special steel industry; M2 T: treated from special steel industry; M3: from Getxo town; M4: from Leioa town).

Compound		Formula	M1	M2	M1T	M2T	M3	M4	Wavenumbers/cm^{-1}
Calcite	*PR*	$CaCO_3$	X	X	X	X	X	X	155m, 281m, 712m, 1085vs, 1433w, 1747w
HMC	*PR*	$Ca(Mg)CO_3$	X	X	X	X	X	X	154s, 281m, 713m, 1087vs
Aragonite	*PR*	$Ca(Mg)CO_3 + CaCO_3$	X	X	X	X	X	X	277m, 709m, 1090vs
Lepidocrocite	*PR*	γ- FeO(OH)	X	X	X	X	X	X	215m, 248vs, 305m, 346m, 375s, 525m, 646m
Magnetite	*PR*	Fe_3O_4	X	X	X	X	X	X	314m, 477m, 558m, 680vs
Magnesioferrite	*PR*	$MgFe_2O_4$	X	X	X	X	X	X	327m, 435m, 613vs
Larnite	*PR*	β-Ca_2SiO_4	X	X	X	X	X	X	846sh, 857vs, 976m
Walstromite	*PR*	$BaCa_2Si_3O_9$	X	X	X	X	X	X	664s, 990m
Hematite	*PR*	α-Fe_2O_3	X	X	X	X	X	X	223s, 288vs, 408m, 497w, 608w
Goethite	*MR*	α-FeOOH		X	X	X	X	X	248m, 300m, 384vs, 475vw, 529w
Tephroite	*MR*	Mn_2SiO_4	X	X	X		X		810m, 843m
Limonite	*MR*	$FeO(OH)\cdot nH_2O$				X		X	296m, 396vs, 470vw
Ilesite	*MR*	$(Mn, Zn, Fe)\ SO_4\cdot 4H_2O$		X			X		427s, 488s, 622s, 1024vs
Amorph. Carbon	*PR*	C		X		X			1306br, 1608br
Gypsum	*MR*	$CaSO_4\cdot 2H_2O$		X					414m , 492m, 619m, 670m, 1008s, 1135m
Bassanite	*MR*	$CaSO_4\cdot 1/2H_2O$		X					429m, 487m, 627m, 668m, 1015s
Rasvumite	*MR*	KFe_2S_3				X			152 vs, 186w, 218 vs, 246m, 436m, 471s
Rutile	*MR*	TiO_2	X						237m, 448vs, 611s
Natron	*MR*	$Na_2CO_3\cdot 10\ H_2O$				X			1070m
Nitratine	*MR*	$NaNO_3$		X		X			190m, 724m, 1067vs
Brucite	*MR*	$Mg(OH)_2$		X					278m, 443m
Magnesiochromite	*SCA*	$MgCr_2O_4$			X				570w, 699s
Chromite	*SCA*	$FeCr_2O_4$		X					279m, 680vs
Hashemite	*SCA*	$BaCrO_4$				X			351s, 859vs
Crocoite	*SCA*	$PbCrO_4$			X				843vs

***** s: strong; m: medium; w: weak; v: very; br: broad; sh: shoulder / HMC: calcite with high content in magnesium/ PR: Portable Raman spectroscopy/MR: micro-Raman spectroscopy/SCA: Structural Chemical Analyser (SEM/EDS + micro-Raman)

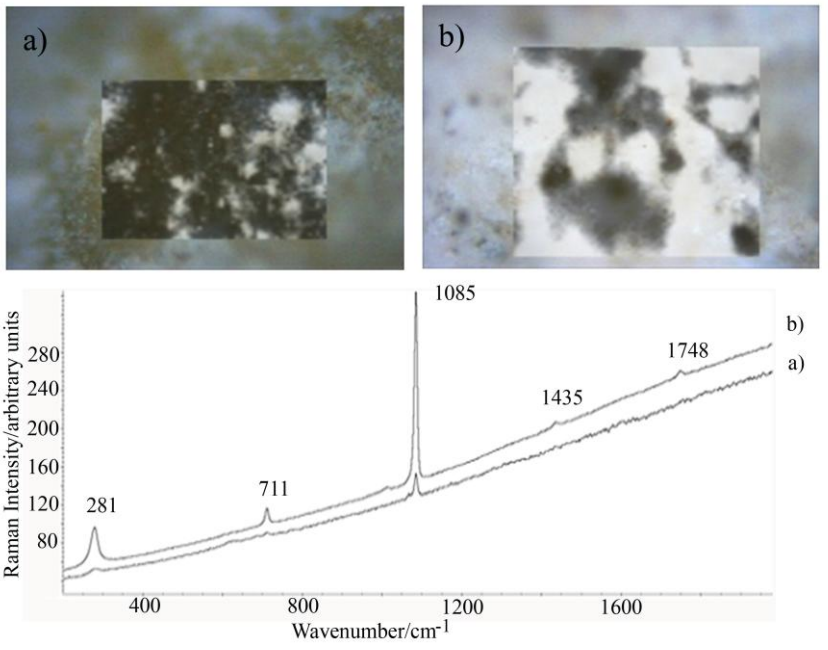

Fig. 4.42. Raman images showing the relative abundance of calcite in samples M1 (a) and M1T (b). The indicated spectra belong to a pixel of each image for the calcite Raman intensities (mapping area: 30-40 mm^2)

To sum up, the experimental evidence shown in Fig. 4.42.a allowed us to conclude that calcite is formed after cooling the slag, without any special treatment. When the slag is removed from the Electric Arc Furnace, the material is at a temperature of 800ºC or above, thus no carbonate can be present. But as the cooling process proceeds in open air, the presence of atmospheric humidity and CO_2 is enough to transform part of the remaining CaO into $Ca(OH)_2$, according to reaction (4.1), and then to $CaCO_3$, following reaction (4.2). Thus, before starting the stabilization process of the slag, some calcite is always formed. After the stabilization treatment all the CaO should be transformed to calcite ($CaCO_3$, reactions 4.1-4.2), like it is observed in the M1T Raman image (Fig.4.42.b), where calcite occupies practically all the Raman image.

However, calcite was not the only calcium carbonate observed. In fact, aragonite ($CaCO_3$, Raman bands at 206m, 705m and 1085vs cm^{-1}) was also detected. But, it was always found mixed with other compounds (the aragonite bands never appeared alone) and it is not a major compound because it appears only in less than 5% of the

collected spectra. Some authors report the formation of aragonite when the concentration of magnesium is relatively high with regard to calcium. This is the case of the black slag, into which magnesium could move from the refractory bricks of the furnace[157,158].

In some cases, the Raman peaks of the calcite were found shifted few wavenumbers (see Fig. 4.3.a-d).

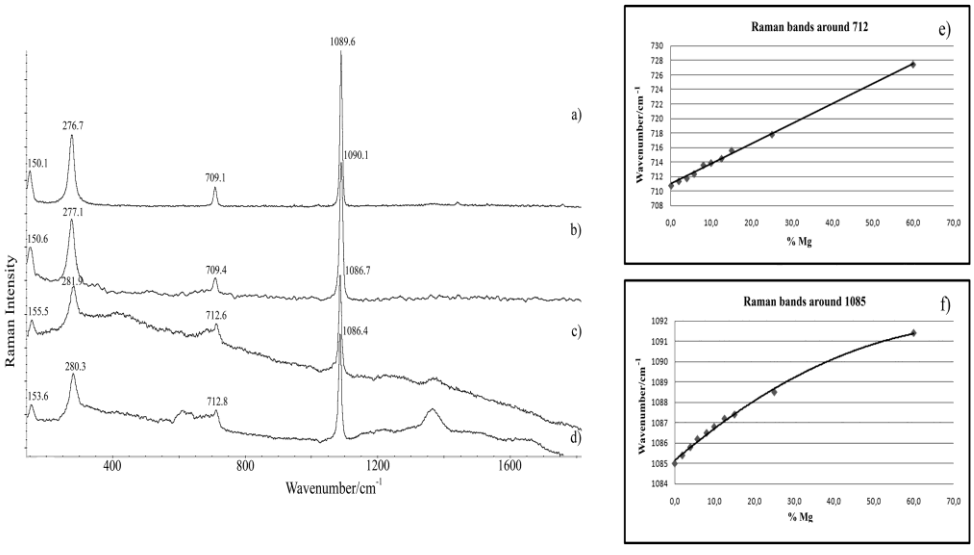

Fig. 4.43. Raman spectra obtained with the portable device of high magnesium calcite with aragonite: a), b); and only high magnesium calcite c), d) with around 7% Mg. Tendency of Raman bands according to the percentage of magnesium in the calcite for the 712 and 1085 peaks (e, f).

This could be also due to the presence of magnesium, which replaces the calcium atoms of the calcite, forming calcite with high magnesium content (HMC) ($Ca(Mg)CO_3$; Raman bands at 153-155s, 279-282m, 711-714m and 1085-1087vs cm^{-1}). Depending on the magnesium percentage, the peaks are more or less shifted. The greater displacement of the peaks is observed in the case of higher magnesium

[157] IHOBE, S. A. Libro Blanco para la minimización de residuos y emisiones, Servicio Central de Publicaciones del Gobierno Vasco, Vitoria-Gasteiz, 1999.
[158] J. Hernández Puy. Estudio de la estabilidad volumétrica, propiedades físicas y químicas de la escoria negra de acero de horno de arco eléctrico. MSc. Thesis, Universitat Politècnica de Catalunya, Barcelona, 2007.

percentages[159]. The relation of the wavenumbers of the υ_4 and υ_1 Raman bands of HMC as a function of the magnesium percentage in the HMC is shown in Fig. 4.43.e and f as described elsewhere[159].

Those Raman shifts in HMC as a function of a mean magnesium percentage can be fitted (both fits are shown in both figures) to a polynomial function and can be used to calculate the magnesium percentage in HMC. Thus, our Raman bands of the original and pretreated slag, summarized in Table 4.7, were introduced in the mathematical functions (Fig. 4.43.e and 4.43.f) to obtain a mean of the magnesium percentage values. As seen, the estimated magnesium ranged between 5% and 10%, concluding that the amount of magnesium is not constant for all the samples.

Table 4.7. High magnesium calcite (HMC) Raman bands (T, L, υ_4 and υ_1) of several black slag samples (M1, M2, M1T and M2T) and their magnesium percentage calculated.

	M1	*M2*	*M1T*	*M2T*
T	155.5	153.7	153.6	155.1
L	281.9	279.7	280.3	282.0
υ_4	712.6	712.1	712.8	712.8
υ_1	1086.7	1086.3	1086.4	1086.9
% Mg	7.7	5.6	7.0	8.6

The HMC appeared not only in the slag sampled in the steelworks (treated and non-treated) but also in those sampled in the civil construction sites, confirming its presence as one of the major mineral phases (like in the case of calcite) of the slag materials.

Black slag contains residual iron originated from the scrap used in the fabrication of the steel[160]. In this production, the reduction process of hematite ores in the Electric Arc Furnace, due to the action of mixtures of CO and CO_2, produces metallic iron by

[159] W.D. Bischoff, S.K. Sharma, F.T. Mackenzie, Carbonate ion disorder in sinthetic and biogenic magnesian calcites: A Raman spectral study, American Mineralogist 70 (1985) 581-589.
[160] IHOBE, S. A. Libro Blanco para la minimización de residuos y emisiones, Servicio Central de Publicaciones del Gobierno Vasco, Vitoria-Gasteiz, 1999.

means of a series of intermediate oxides. At high temperatures (> 570 °C) the reduction of iron oxides follows the order:

$$Fe_2O_3 \text{ (hematite)} \rightarrow Fe_3O_4 \text{ (magnetite)} \rightarrow FeO \text{ (wüstite)} \rightarrow Fe$$

At lower temperatures (<570°C), Fe is produced without FeO[161,162]. The metallic iron can be oxidized in the cooling process of the slag and in contact with open atmosphere it turns into Fe^{+2} and Fe^{+3} forms. Some reactions of transformation are the following ones[163]:

$$Fe^{+2} + 2OH^- \rightarrow Fe(OH)_2$$

$$4Fe(OH)_2 + O_2 + 2H_2O \rightarrow 4Fe(OH)_3$$

In the Raman analysis of the slag the main Fe oxides and hydroxides observed were (see Fig. 4.44): lepidocrocite (γ-FeOOH; Raman bands at 215m, 248vs, 305m, 346m, 375s, 525m and 646m cm^{-1}), goethite (α-FeOOH; Raman bands at 248m, 300m, 384vs, 4785vw and 529w cm^{-1}), limonite (FeO (OH).nH_2O; Raman bands at 296m, 396vs and 470vw cm^{-1}), hematite (α-Fe_2O_3; Raman bands at 223s, 288vs, 408m, 497w and 608w cm^{-1}) and magnetite (Fe_3O_4; Raman bands for this material at 314m, 477m, 558m and 680vs cm^{-1}). In the last case, the main peak of magnetite should be at 667 cm^{-1}, but in the majority of the collected spectra it is displaced due to be stoichiometric substitution of the iron for cobalt, nickel and traces of aluminium, present in its structure[164]. Also, this displacement could be attributed to differences in the average oxidation state of the iron[165,166].The presence of hydroxides was higher in the treated

[161] R.Y. Chen, W.Y.D. Yuen, Oxide-Scale Structures Formed on Commercial Hot-Rolled Steel Strip and Their Formation Mechanism, Oxidation of Metals 56 (2001) 89-118.
[162] W.K. Jozwiak, E. Kaczmarek , T.P. Maniecki, W. Ignaczak, W. Maniukiewicz, Reduction behavior of iron oxides in hydrogen and carbon monoxide atmospheres, Applied Catalysis A: General 326 (2007) 17-27.
[163] J. Hernández Puy. Estudio de la estabilidad volumétrica, propiedades físicas y químicas de la escoria negra de acero de horno de arco eléctrico. MSc. Thesis, Universitat Politècnica de Catalunya, Barcelona, 2007.
[164] R.T. Downs. The RRUFF Project: an integrated study of the chemistry, crystallography, Raman and infrared spectroscopy of minerals. Program and Abstracts of the 19th General Meeting of the International Mineralogical Association in Kobe, Japan. O03-13, 2006.
[165] V.S.F.Muralha, T. Rehren, R.J.H. Clark, J Characterization of an iron smelting slag from Zimbabwe by Raman microscopy and electron beam analysis, Journal of Raman Spectroscopy 42 (2011) 2077-2084.
[166] J. Van der Weerd, T. Rehren, S. Firth, R. J. H. Clark, Identification of iron oxide impurities in earliest industrial-scale processed platinum, Materials Characterization 53 (2004) 63-70.

slag than in the slag without treatment, due probably to the action of the added water in the pretreatment.

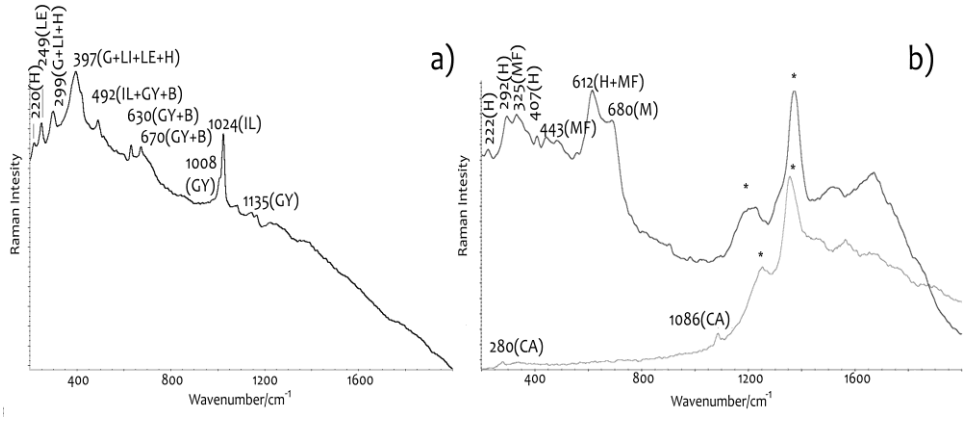

Fig. 4.44. Micro-Raman spectrum of: a) sample M2: mixture of goethite (G), limonite (LI), lepidocrocite (LE), hematite (H), gypsum (GY), bassanite (B) and ilesite (IL); b) sample M1T: hematite (H), magnesioferrite (MF), and magnetite (M). Luminescence signals are also shown (*).

The spectra taken with the micro-Raman system also revealed the presence of magnesioferrite ($MgFe_2O_4$; Raman bands at 327m, 435m and 613vs cm^{-1} as seen in Fig. 4.44.b) and brucite ($Mg(OH)_2$; Raman bands at 278m and 443m cm^{-1}). These compounds can be formed due to magnesium that comes, as it has been mentioned before, from the decaying of the ceramic bricks of the furnaces, during the oxididative phase of steel production, which is a material rich in MgO[167,168].

In addition, several sulfates were detected by micro-Raman analysis (see Fig. 4.44.a), such as ilesite ($(Mn^{2+}, Zn, Fe^{2+})\ SO_4.4H_2O$; Raman bands at 427s, 488s, 622s and 1024vs cm^{-1}), gypsum ($CaSO_4.2H_2O$; Raman bands at 414m, 492m, 619m, 670m, 1008s and 1135m cm^{-1}) and bassanite ($CaSO_4.1/2H_2O$; Raman bands at 429m, 487m, 627m, 668m and 1015s cm^{-1}). These two last compounds appeared always mixed; around 75% bassanite and 25% gypsum (see Fig.4.39.a). Also, rasvumite (KFe_2S_3; Raman bands at

[167] IHOBE, S. A. *Libro Blanco para la minimización de residuos y emisiones*, Servicio Central de Publicaciones del Gobierno Vasco, Vitoria-Gasteiz, 1999.
[168] J. Hernández Puy. Estudio de la estabilidad volumétrica, propiedades físicas y químicas de la escoria negra de acero de horno de arco eléctrico. MSc. Thesis, Universitat Politècnica de Catalunya, Barcelona, 2007.

152vs, 186w, 218vs, 246m, 436m and 471s cm^{-1}) was identified. The sulfur is present in the black slag because when the slag was formed, the desulfuration has not been carried out yet (this process happens in a subsequent phase where the black slag has already left the furnace)[169]. Micro-Raman spectroscopy also provided information about the presence of rutile (TiO_2; Raman bands at 237m, 448vs and 611s cm^{-1}) in most of the analyzed samples but always as a minor compound.

In the same way that in the LDG samples, steel slag also presented the characteristic bands of luminescence (as it can be seen in the Fig. 4.44.b. and Fig. 4.45). Firstly, we thought that the group of Raman peaks at ~1230m and ~1370s cm^{-1} belonged to silicates, but after measuring with the 514 and 532 nm lasers, those peaks were never observed. Besides, these steel slag samples can contain vitrified siliceous crystals with REE or transition metals, so they can be the responsible for that luminescence signal[170].

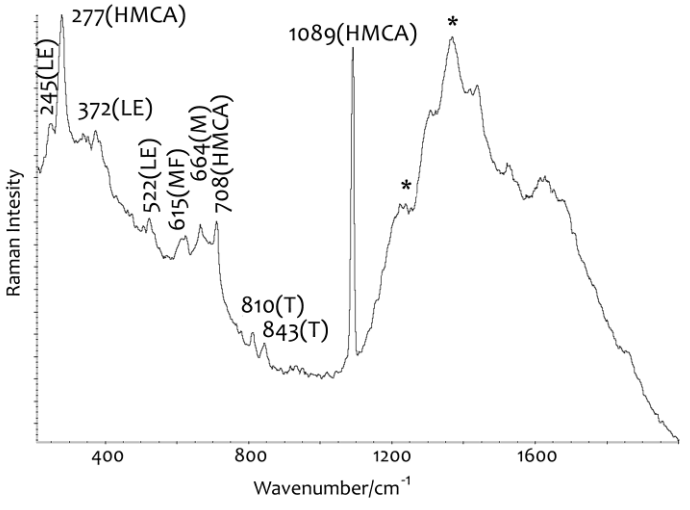

Fig.4.45. Micro-Raman spectrum of sample M1T: lepidocrocite (LE), high magnesium calcite plus aragonite (HMCA), magnesioferrite (MF), magnetite (M) and tephroite (T). Luminiscence (*).

[169] IHOBE, S. A. Libro Blanco para la minimización de residuos y emisiones, Servicio Central de Publicaciones del Gobierno Vasco, Vitoria-Gasteiz, 1999.

[170] C. Lenz, D.Talla, K.Ruschel, R. Škoda, J. Götze, L. Nasdala, Factors affecting the Nd3+(REE3+) luminescence of minerals, Mineralogy and Petrology 107 (2013) 415–428.

The identified silicates were tephroite (Mn_2SiO_4; Raman bands at 810m and 843m cm^{-1}) (see Fig. 4.45), walstromite ($Ba_2Ca_2Si_3O_9$; Raman bands at 664s and 990m cm^{-1}) and larnite (β-Ca_2SiO_4; Raman bands at 846sh, 857vs and 976m cm^{-1}).

Sodium carbonate decahydrated ($Na_2CO_3.10H_2O$; Raman band at 1070vs cm^{-1}) and nitratine ($NaNO_3$; Raman bands at 190m, 724m and 1067vs cm^{-1}) were also found in some treated samples. Their presence could be justified by the possible use of Na_2O as an alkaline melting agent[171] in the melting process to decrease the melting point and eliminate part of the slag of the own process. Na_2O can remain in the slag, and the combination with atmospheric CO_2 or NO_x gas attack (during the cooling process outdoors) and water (during treatment of "inerting" that is performed in the steelworks) can form natron ($Na_2CO_3 \cdot 10\ H_2O$) and nitratine ($NaNO_3$).

Amorphous carbon (C; Raman bands at ~1306s and ~1608s cm^{-1}) has also been identified at trace level in some slag samples.

The slag is very heterogeneous and in many occasions, apparent Raman displacements of some peaks can be seen, probably owing to the overlap of different compounds. This is mainly observed when micro-Raman spectroscopy was used to identify minor compounds; if those minor mineral forms are not perfectly focused, signals for major compounds will appear as the predominant ones, leading the Raman bands of minor compounds as shoulders or as overlapped peaks that must be resolved applying mathematics to define individual bands where two or more peaks overlap in a broad signal.

The case of stainless (inox) steel slag (M6) was special because its spectra presented more fluorescence and it was found almost exclusively the luminescence signal in all the measurements. Perhaps they contain more vitrified siliceous crystals with REE or transition metals than the other slags, and to micro scale the luminescence was more often observed. Only calcite, hematite and magnetite were detected.

[171] S. Sarkar, V.V.V. Subrahmanyam, Method for Estimation of Na2O and K2O in Ores, Fluxes, Coal and Coke Ash by Inductively Coupled Plasma-Atomic Emission Spectroscopy, Journal of Minerals and Materials Characterization and Engineering 8 (2009) 57-71.

2.2 X-Ray Diffraction (XRD)

The XRD results confirmed some of the mineral phases detected by Raman spectroscopy such as calcite, magnetite, larnite, goethite and hematite (see Fig. 4.46 and 47). Nevertheless, it could be identified others as well: gehlenite ($Ca_2Al(AlSiO_7)$), wüstite (FeO), merwinite ($Ca_3Mg(SiO_4)_2$), vaterite ($CaCO_3$) (see Fig. 4.46 and 47), monticellite ($CaMgSiO_4$) and monohidrocalcite ($CaCO_3 \cdot H_2O$). The new crystalline phases detected by XRD are summarized in Table 4.8.

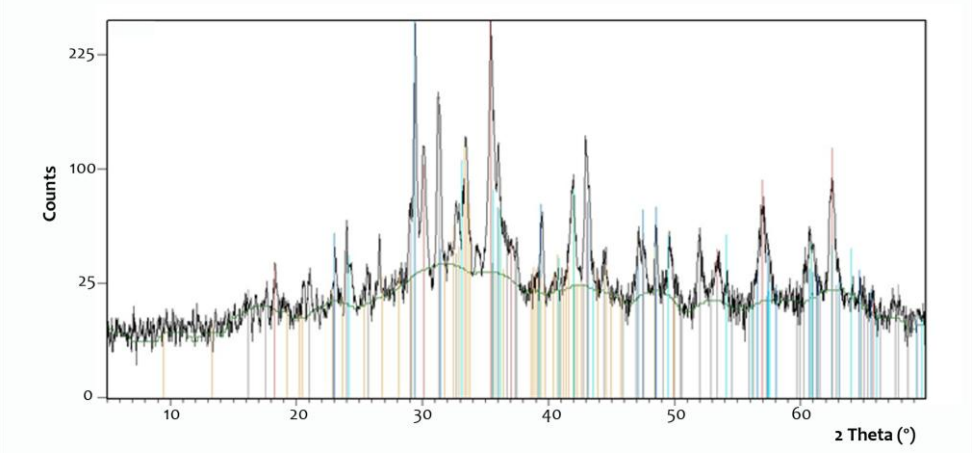

Fig. 4.46. Diffractogram of M2 sample (red: magnetite, green: wüstite, blue: calcite, orange: merwinite, light blue: hematite and grey: gehlenite).

In the stainless steel slag (M6) it was possible to detect also chromite ($FeCr_2O_4$), which we could not found by Raman on such M6 samples due to the high fluorescence observed during the Raman analysis.

In addition, the presence of vitreous, amorphous phase in the samples is proved through the background elevation of the diffractograms (see Fig. 4.47). This fact could not be due to the slides used to hold the sample, since they are of monocrystalline silicon which do not give that signal.

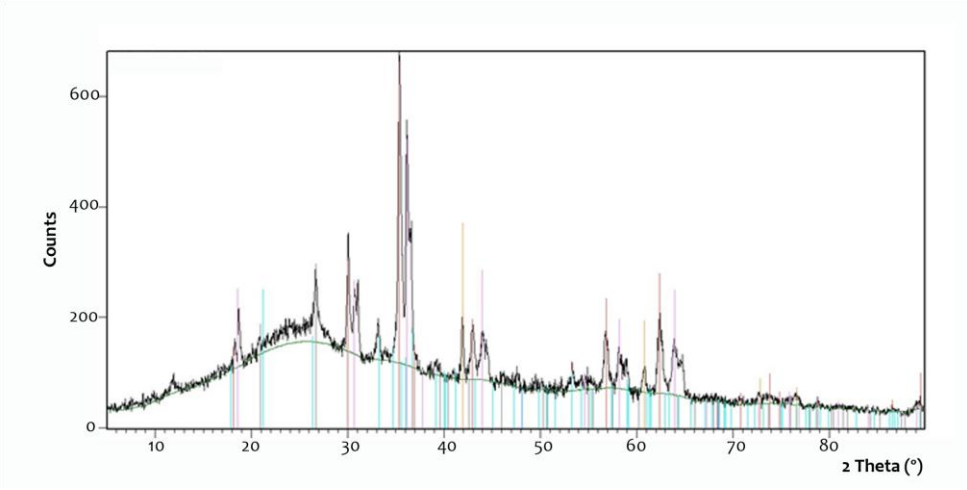

Fig. 4.47. Diffractogram of M1T sample (red: magnetite, orange: wüstite, blue: goethite, pink: spinel and grey: quartz).

Table 4.8. New mineral phases detected by XRD.

Compound	*Formula*	*M1*	*M2*	*M1T*	*M2T*	*M3*	*M4*	*M5*	*M6*
Gehlenite	$Ca_2Al(AlSiO_7)$	x	x	x	x	x	x	x	x
Wüstite	FeO		x	x		x			x
Merwinite	$Ca_3Mg(SiO_4)_2$		x	x				x	
Vaterite	$CaCO_3$				x				
Monticellite	$CaMgSiO_4$		x			x			
Monohidrocalcite	$CaCO_3.H_2O$					x			
Quartz	SiO_2		x	x				x	
Spinel	$MgAl_2O_4$			x					
Fayalite	Fe_2SiO_4							x	
Chromite	$FeCr_2O_4$								x

2.3 Structural and Chemical Analyser (SCA)

The possibility to have other minor compounds not well identified came from the EDS maps, which revealed good correlations among elements not belonging to compounds clearly identified by the portable and micro-Raman devices or by the XRD analyses. Consequently, we concluded on the presence of other compounds,

probably at the trace level, that required further experimentation to clearly detect them.

As these compounds were not identified with the conventional Raman systems, we performed new measurements using the SCA instrument (SEM-EDS plus Raman on the same spot). This technique allowed us to search for trace minerals because the SEM images helped us to select a given point (spot) for analysis, obtaining the elemental distribution maps of interest through the EDS unit. We selected only areas where elements, which were not in the compounds defined till now, shown high correlations. Then the Raman spectra were collected in only such areas.

As an example, Fig. 4.48 shows the results that can be attained: the SEM image of a micro-fraction of M1T sample together with the image of its elemental composition where the relative proportion of each element identified increases the intensity of the white colour (Fig. 4.48.a), and one of the Raman spectra obtained on a spot of the whole area (Fig. 4.48.b).

The EDS images show the main grains (mainly composed by chromium and calcium) and over them a group of micro crystals that could have been formed subsequently, i.e., minerals phases that would have been adhered to the surface of original grains of larger size. It could be said that silicon and calcium maps are quite similar; this suggests the formation of dicalcium silicate, tricalcium silicate or other intermediate silicates, but having the Si and Ca as remarkable elements. This is consistent with the presence of larnite and walstromite (Fig. 4.48.b) identified by Raman analysis.

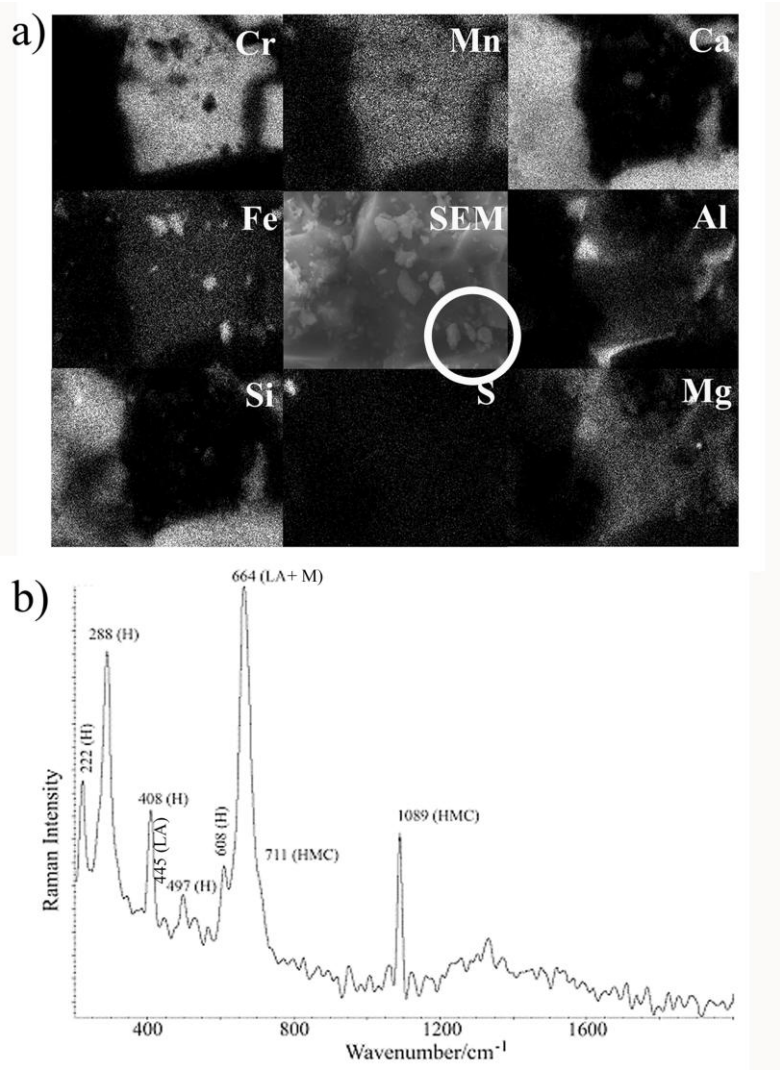

Fig. 4.48.M1 T sample: a) SEM microphotography (100 μm) of a zone of crushed M1T sample (Figure central part) together with the elements: Cr, Mn, Ca, Fe, Al, Si, S and Mg; and b) micro-Raman spectrum of hematite (H), walstromite (W), magnetite (M) and high magnesium calcite (HMC) found in the selected area with a circle.

White zones of the Al and Mg map have great resemblance, although they were not so identical as those of Si and Ca maps. It could be thought in the presence of some crystal of magnesium alumino-silicate or magnesium aluminate (for example spinel $MgAl_2O_4$, detected by the XRD analyses) in order to explain the strong white colour areas in their maps. Besides SEM microphotography suggests that magnesium alumino-silicates or magnesium aluminates would be as crystals in the interior side of slag structure, not in the surface.

Iron is the main compound in the raw materials but its presence in the slag has been identified in different forms. Fig.4.48.a shows four zones very intense in the Fe map that can be associated with four crystals that appear in the SEM microphotograph. As no other element is present in the same zones of white intensity (it is observed four black holes in the Cr map), it is assumed that the Fe would be in the form of oxide (hematite and magnetite) or hydroxide (lepidocrocite and goethite). Hematite and magnetite (see Fig.4.48.b) were identified in their associated Raman spectra. Also, there was a small crystal of Fe situated in the top left part, whose profile coincides with the S and Mn. This corroborates the existence of ilesite crystal ($(Mn^{2+}, Zn, Fe^{2+})SO_4 \cdot 4H_2O$) identified by Raman spectroscopy.

Finally, the grain that contained chromium was perfectly defined, occupying almost the 50% of the microphotograph and its image match mostly with that of manganese and something with magnesium (Fig. 4.48.a). This distribution suggested the presence of Cr and Mn oxides, although a compound like magnesium chromite could not be discarded. It is known that iron, manganese and silicon oxides are integrated in the slag that covers the molten liquid after the beginning of the process of production of steel[172] but other compounds can be formed.

After that screening performed individually with the SEM-EDS and the confocal micro-Raman instruments, the SCA analysis was started. For example, Fig. 4.49 shows the global results of a measurement performed on the M1T sample, where the Raman spectrum reveals the presence of magnesiochromite ($MgCr_2O_4$; Raman bands at 570w and 699s cm^{-1}) (see Fig. 4.49.a), confirming the previous hypothesis from the images of chromium and magnesium in the EDX analysis shown in Fig. 4.49.a. Thus, with the information obtained from the grouping of the results of all these techniques, the presence of magnesiochromite was unequivocally corroborated.

[172] IHOBE, S. A. Libro Blanco para la minimización de residuos y emisiones, Servicio Central de Publicaciones del Gobierno Vasco, Vitoria-Gasteiz, 1999.

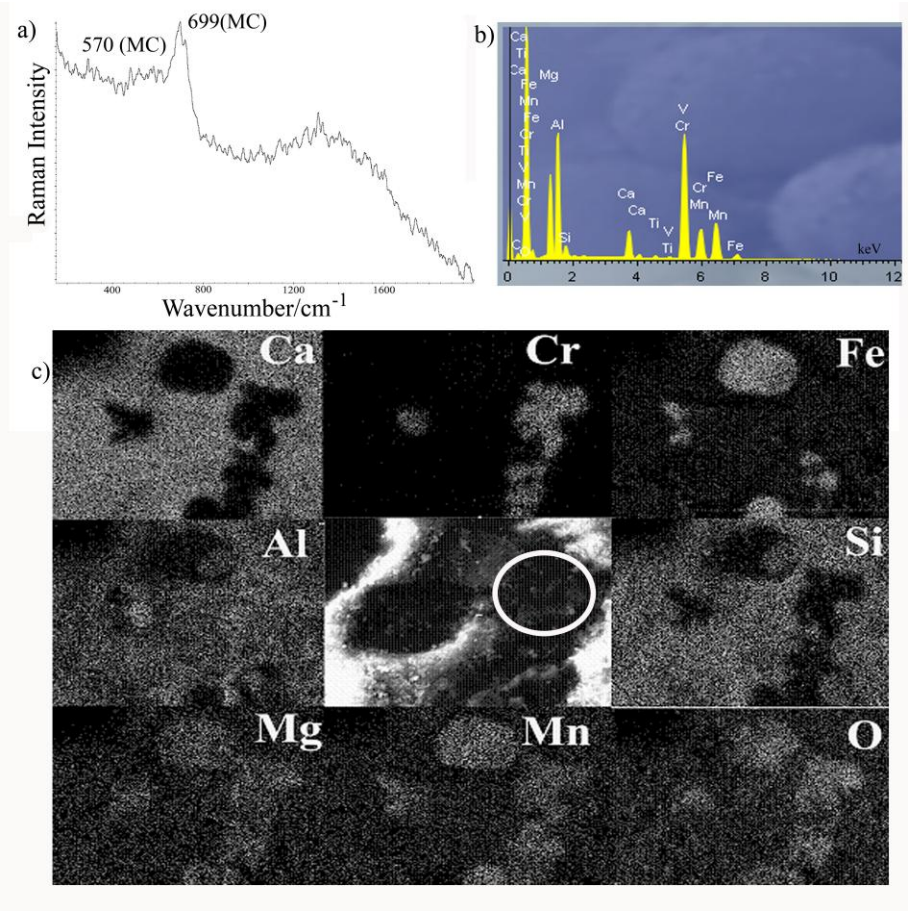

Fig. 4.49. SCA results of magnesiochromite (MC) in M1T sample: a) Raman spectrum, b) EDS analysis and c) SEM image (40 μm) plus EDS mapping for different elements.

Following the same analytical strategy on the SCA analysis, other compounds were identified. In particular, chromite[173] ($FeCr_2O_4$; Raman bands at 279m and 680vs cm^{-1}), crocoite[174] ($PbCrO_4$; Raman bands at 843vs cm^{-1}) and hashemite ($BaCrO_4$; Raman bands at 351s and 859vs cm^{-1}) were detected in the slags coming from special steel production. Any new compound was detected in the slag samples from common and stainless steels.

[173] C. Ming, S. Jinfu, M. Ho-Kwang, Xieite, a new mineral of high-pressure $FeCr_2O_4$ polymorph, Chinese Sicience Bulletin 53 (2008) 3341-3345.
[174] K. Castro, M. Pérez-Alonso, M.D. Rodríguez-Laso, J.M. Madariaga, Pigment analysis of a wallpaper from the early 19th century: *Les Monuments de Paris*, Journal of Raman Spectroscopy 35 (2004) 704-709.

3. PYROLYSIS - GAS CHROMATOGRAPHY MASS SPECTROMETRY (PY-GC-MS)

Steel slags from the factories and from the civil construction works were measured by Py-GC-MS. All samples were subjected to the same pyrolysis program as impact glasses. The first temperature of analysis was 280ºC, followed of an analysis to 600ºC and finally to 750ºC.

Although it was observed some small chromatographic signals in the analyzed slag samples, it was not systematically identified any clear compound. Only it was sporadically identified hydrocarbons of long chain such as 2-Octene, 1-Hexene, 3-methyl- and 5-Methyl-1-heptanol, in the M3 sample (from the Getxo construction work) at 600ºC; and aromatic hydrocarbons such as biphenyl and benzene, and polycyclic aromatic hydrocarbon (PAH) like naphthalene in the M2T sample (from special steel factory) at 750ºC.

4. DISCUSSION

In this part of the chapter an innovative analytical procedure has been developed, based on the combination of Raman spectroscopy, μ-EDXRF and SCA (SEM-EDX+Raman), to perform a complete mineralogical and elemental characterization of any material subject of high temperatures during their formation.

The mineralogical composition of the black steel slag produced in Electric Arc Furnace included above all oxides (and sometimes hydroxides) of iron, silicates, carbonates, sulfates and amorphous carbon.

The treatment suffered by the slag, prior to its reuse as a secondary inert material, did not cause a significant change in the slag composition, only in the relative presence of some compounds. The main difference between "treated slag" (principally washed with water for three months) and "original slag" was the presence of hydroxides (as lepidocrocite, goethite and limonite for iron), formed from the hydration of oxides (hematite mainly for iron) during the addition of water in the treatment carried out in each factory. In spite of this, in some occasions, it

could be appreciated hydroxides in the slag without treatment, possibly owing to their interaction with the environmental atmospheric humidity.

Moreover, nitrates (nitratine), sulfates (ilesite, bassanite and gypsum) and a great amount of carbonates (natron, vaterite and calcite) were observed mainly in the treated slags. Those products that originally are not in the slag and probably they would have appeared with the cooling process outdoors, due to the interaction of the original mineral phases with atmospheric acid gases and water.

With regard to calcite, in some cases its Raman bands were shifted, mostly due to the substitution of Ca atoms by Mg, with the subsequent formation of high magnesium calcite. In their Raman spectra, wavenumbers increased when the magnesium percentage augmented. Apart from this, aragonite was also present, mixed with high magnesium calcite. In these cases, it was not possible to calculate the magnesium percentage because their bands did not follow the same trend that the high magnesium calcite alone.

On the other hand, the presence of chromium (a potentially toxic element) in the Raman spectroscopy, SCA, XRD and EDXRF results was clear.

The analytical approach used in this work was of great usefulness. Major compounds can be easily identified by portable equipments while minor compounds require the use of Raman microscopy. The possibility to analyze the same point with Raman spectroscopy and SEM-EDS (SCA) facilitated the identification of trace compounds. XRD and XRF complemented and corroborated the Raman and SCA analysis.

XPS analysis together with Raman image permitted to show the widespread carbonation produced either by the water treatment in the steel slag surfaces or by the long term simple interaction with atmospheric CO_2 and humidity.

With regard to the organic compounds present in the steel slag, we must conclude on its absence to a large extent. It was only identified some long-chain hydrocarbon and aromatic hydrocarbons in a couple of the analyzed samples.

D. BLACK AND WHITE STEEL SLAG USED AS FILLER IN FOREST TRACKS ABOUT 30 YEARS AGO

Slag materials from the production of steel are considered terrestrial analogs to impact glasses, but the materials studied in the previous section had only days to weeks of interaction with the surrounding environment. If we would have access to old slag materials deposited outside for years, this would brought us a bit closer to the situation experienced by the LDG and DG impact glasses studied in this work.

Such materials are in forest tracks constructed decades ago in the hills and mountains of the Basque Country. After obtaining the corresponding permits, two forest tracks located in Gipuzkoa (Basque Country, Northern Spain), and constructed 18 and 34 years ago, were sampled (see Fig. 4.50).

The characterization of black (from Electric Arc Furnace production) and white (Ladle Furnace production) steel slag, which had been used as filler in such forest tracks, was performed using the same spectroscopy based methodology used to analyze the steel slags collected from the factories (part C of the chapter): Raman Spectroscopy, X-Ray Fluorescence (XRF), X-Ray Diffraction (XRD) and Scanning Electron Microscopy/Energy Dispersive X-Ray Spectroscopy (SEM-EDX).

Fig. 4.50. Black and white steel slag and images of both forest tracks.

1. ELEMENTAL RESULTS

1.1 Energy Dispersive X-Ray Fluorescence Spectroscopy (μ-EDXRF)

The elemental characterization of slag at macro level was performed through EDXRF over several points of the raw samples. Various black slag were selected from both forest tracks and white ones from the longest forest track, which was built with a mixture of black and white steel slag. Around 10 measurements were done per slag sample.

The characteristic elements present in the black steel slags were: Si, Al, Ca, Ti, Cr, Mn, Fe, Ni, Cu, Zn, Sr, Ba, S, P, K, V and Sn. To our surprise, Al and Cl were detected in the black slags of both forest tracks. In the case of white slags, they had fewer elements, mainly Si, Al, Ca, Ti, Fe, Sr, P and K, due to its formation in a second step, when the steel is refined and cleaner, so it contains fewer impurities from the steel production.

Comparing all the elements found in the black slag residues of the forest tracks with the elements present in the slag from the current producers, we did not find any important difference, apart from the presence of Cl, especially if we compare to the black slags from special steel productions. That means the slag materials obtained around 30 years ago are similar in elemental composition to the slag residues produced today.

The presence of Cl in the slag of the forest tracks are clearly related to the interaction of the soil/plant activity of the forest with the residues, concluding that slag suffer some chemical changes with time as a function of the particular environmental conditions affecting the materials. This will be taken into account in the chapter devoted to weathering processes.

1.2 Scanning Electron Microscopy/Energy Dispersive X-Ray Spectroscopy (SEM-EDX)

SEM-EDX analyses corroborated the presence of some compounds described in the next section. For instance, in the Fig. 4.51 it can be observed a SEM image of a black steel slag and their elemental distribution maps of Al, C, Ca, Si, O, S, Mg, Mn, Cr, Fe and K. As it has been mentioned, the white colour indicates the presence of an element and the black one, the absence. The oxygen is practically in all the measured area and is correlated with Fe, Ca, Cr and Mn. Apart from the similitude of Fe-O maps, the Mn map is comparable with the Fe as well. Also, it is observable that where there is Fe, there is not Si. However, Si map has resemblance to Ca map. Moreover, Ca map has some similitude with C map. On the other hand, Al map is similar to Mg map in a certain grain discernible in the right upper part of both maps. Regarding S map, in this area it is not similar to Ca map, but in some grains of the Fe map. K map is different from any other map, it has not resemblance to the rest of elements, perhaps its little upper point with Si map. All this information corroborates the presence of iron oxides (Fe-O), larnite (Ca-Si-O) and calcite (Ca-C-O) identified with Raman spectroscopy and XRD below. Besides, there could be some compounds with Al and Mg or aluminosilicates, but they have not been found by molecular techniques until now.

Unlike black steel slag, the simplest chemical composition of white steel slag can be observed in the Fig. 4.52, where a SEM image on a white steel slag spot and the elemental distribution maps for Al, Ca, Si, O and Fe are shown. In this measured area, it is appreciable that O, Al and Fe maps present a homogeneous distribution. And Ca and Si are distributed similarly in some given points, in agreement with the presence of mullite ($Al_6Si_2O_{13}$) detected in the XRD analyses.

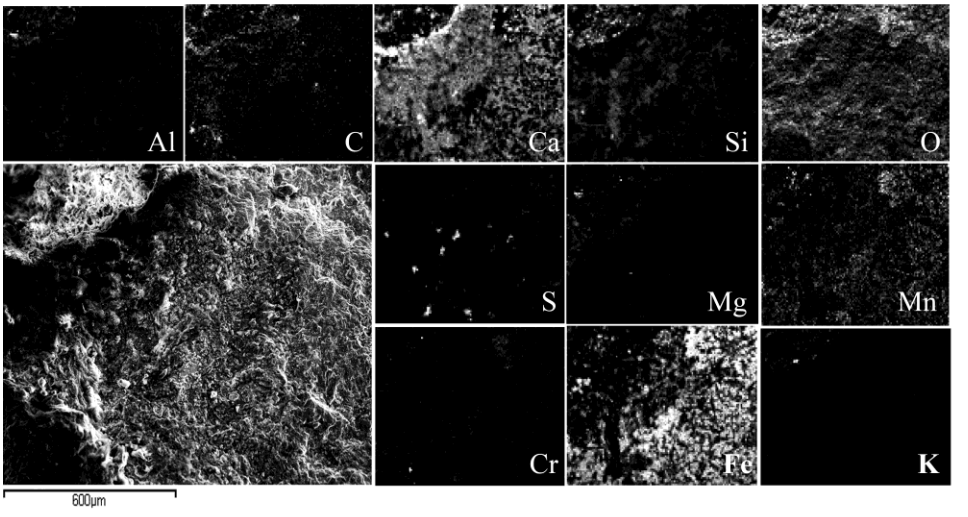

Fig.4.51. SEM image (600 µm) with EDS mapping (600 µm) of different elements present in a black slag: Al, C, Ca, Si, O, S, Mg, Mn, Cr, Fe and K.

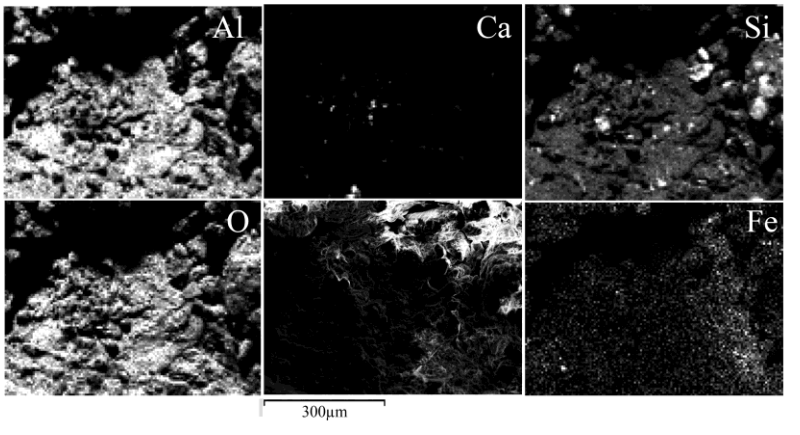

Fig. 4.52. SEM image (300 µm) with EDS mappings (300 µm) of different elements present in a white slag: Al, Ca, Si, O, Fe and K.

2. MOLECULAR RESULTS

2.1 Raman Spectroscopy

More than 100 Raman measurements were performed on black and white slag samples. In the black slag samples most of the iron oxides were identified, such as hematite (α-Fe_2O_3; Raman bands at 223s, 288vs, 408m, 497w and 608w cm^{-1}) (see Fig. 4.53.a) and magnetite (Fe_3O_4; Raman bands for this material at 314m, 477m, 558m and 665s cm^{-1}), iron hydroxides such as goethite (α-FeOOH; Raman bands at 248m, 300m, 384vs, 4785vw and 529w cm^{-1}), lepidocrocite (γ-FeOOH; Raman bands at 215m, 248vs, 305m, 346m, 375s, 525m and 646m cm^{-1}), and in some occasions akaganeite (β-FeOOH; Raman bands at 311sm, 392sw, 488vw, 536m and 715w cm^{-1}) (see Fig. 4.53.b).

Moreover carbonates like calcite ($CaCO_3$; Raman bands at 155m, 281s, 712m, 1085vs, 1433w and 1747w cm^{-1}) , also detected in the white slag samples, and high magnesium calcite (HMC) ($Ca(Mg)CO_3$; Raman bands at 154s, 281m, 713m and 1087vs cm^{-1}) (see Fig. 4.53.a) were identified.

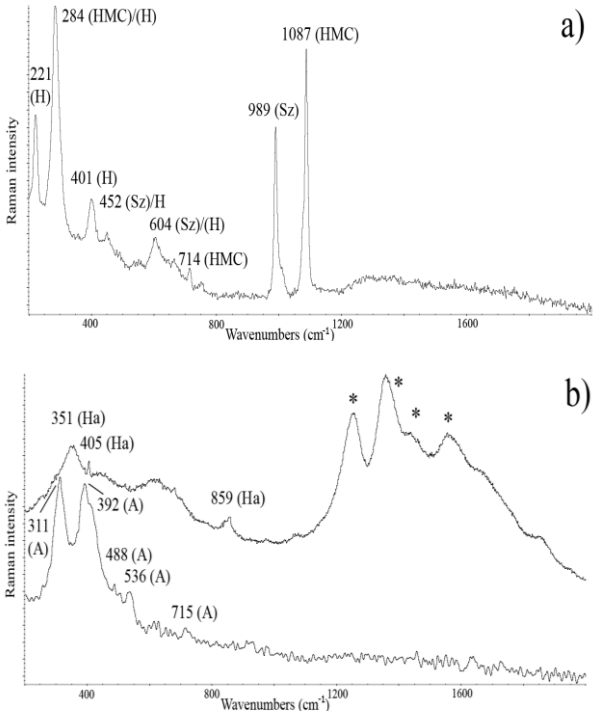

Fig.4.53. Raman spectra identified in black slag samples of: a) hematite (H), high magnesium calcite (HMC) and szomolnokite (Sz); and b) hashemite (Ha), akaganeite (A) and bands belonged to luminiscence (*).

In addition, magnesioferrite ($MgFe_2O_4$; Raman bands at 327m, 435m and 613vs cm^{-1}), larnite (β-Ca_2SiO_4; Raman bands at 846sh, 857vs and 976m cm^{-1}), tephroite (Mn_2SiO_4; Raman bands at 810m and 843m cm^{-1}), quartz (SiO_2; Raman bands at 203w, 263w, 400vw and 463m cm^{-1}) and also szomolnokite ($FeSO_4.H_2O$; Raman bands at 452m, 604m and 989vs cm^{-1}) were recognized (see Fig.4.53.a).

Hashemite ($BaCrO_4$; Raman bands at 351s, 405w and 859vs cm^{-1}) (see Fig. 4.53.b) and crocoite ($PbCrO_4$; Raman bands at 843m cm^{-1}) were detected in the black slag samples. These two Cr(VI) compounds were also found in the steel slags collected directly from the factories, but in this case of slag exposed directly to the

surrounding environment, the Cr(VI) compounds could be leached under acid conditions to the soil, with the corresponding toxic effects[175].

Furthermore, an iron arsenate could be present (Raman band 850 cm^{-1} [176,177]). It was not possible to assign completely what compound was, because the presence of more peaks hid its secondary bands and made difficult its identification. Anyway, the mobility of arsenate anions must be taken into account if these kinds of wastes are going to be settled/deposited to the open environment. The two most important factors that control the speciation and solubility of arsenic are pH and redox potential. But it can be also controlled by either iron or sulfur, according to the iron/ sulfur ratio. Under high iron-conditions, aqueous sulfide is rapidly consumed in the formation of iron sulfide minerals; however, in low iron-conditions, aqueous sulfide is available to complex aqueous arsenic and to form solid arsenic-sulfide minerals, so arsenic would be removed from solutions[178].

It should be noted that the white slag samples gave luminescence signal in almost all the spectra, and less compounds were clearly identified. Among them, calcite, magnesioferrite, rutile and quartz were detected.

2.2 X-Ray Diffraction (XRD)

Unlike Raman spectroscopy, XRD detected wüstite (FeO) (see Fig. 4.54.a), vaterite ($CaCO_3$), merwinite ($Ca_3Mg(SiO_4)_2$), mullite ($Al_6Si_2O_{13}$) (see Fig. 4.52.b), cristobalite (SiO_2) (see Fig.4.54.b), thaumasite ($Ca_3Si(CO_3)(SO_4)(OH)_6.12H_2O$), portlandite ($Ca(OH)_2$) and brucite ($Mg(OH)_2$). But also it was found magnetite, hematite, calcite, larnite and quartz, already identified by Raman spectroscopy.

[175] M.K. Banks, A.P. Schwab, Carlos Henderson, Leaching and reduction of chromium in soil as affected by soil organic content and plants, Chemosphere 62 (2006) 255-264.
[176] S. C. B. Myneni, S.J. Traina, G.A. Waychunas , T.J. Logan. Experimental and theoretical vibrational spectroscopic evaluation of arsenate coordination in aqueous solutions, solids, and at mineral-water interfaces. Geochimica et Cosmochimica Acta 62 (1998) 3285–3300.
[177] R. L. Frost, S.Bahfenne, J.Cejka, J.Sejkora, J. Plásil, S. J. Palmer. Raman spectroscopic study of the hydrogen-arsenatemineral pharmacolite Ca(AsO3OH)· 2H2O – implications for aquifer and sediment remediation. Journal of Raman Spectroscopy 41 (2010) 1348-1352.
[178] A. R. Keimowitz, Y. Zheng, S.N. Chillrud, B.Mailloux, H.B. Jung, M. Stute, H. J. Simpson. Arsenic Redistribution between Sediments and Water near a Highly Contaminated Source, Environmental Science and Technology 39 (2005) 8606-8613.

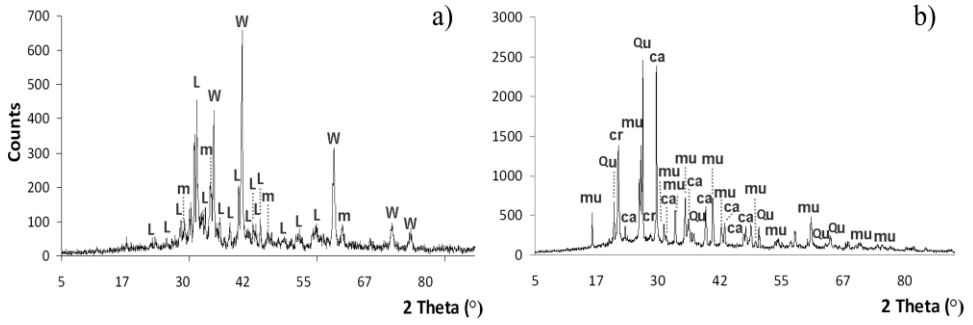

Fig.4.54. X-ray diffractograms of a black slag (a) and a white slag (b): L (larnite), m (magnetite), W (wüstite), mu (mullite), Qu (quartz), cr (cristobalite) and ca (calcite).

The compounds identified by Raman spectroscopy and XRD are listed in the Table 4.9. They can be considered primary compounds (original from the steel production) or secondary compounds (alteration products formed after a certain time due to the environmental conditions).

The presence of cristobalite, the stable form of quartz at high temperature must be highlighted. Both SiO_2 compounds were detected unequivocally through the XRD analyses of the white slag materials.

Table 4.9. Primary (Pr) and secondary (Sc) mineral compounds found in black and white slag by means of Raman spectroscopy and XRD analysis.

	Black slag		***White slag***	
	Pr	Sc	Pr	Sc
Hematite (α-Fe_2O_3)	✓			
Magnetite (Fe_3O_4)	✓			
Goethite (α-FeOOH)		✓		
Lepidocrocite (γ-FeOOH)		✓		
Akaganeite (β-FeOOH)		✓		
Wüstite (FeO)	✓			
Magnesioferrite ($MgFe_2O_4$)	✓		✓	
Calcite ($CaCO_3$)		✓		✓
Vaterite ($CaCO_3$)		✓		
HMC ($Ca(Mg)CO_3$)		✓		
Portlandite ($Ca(OH)_2$)		✓		
Brucite ($Mg(OH)_2$)		✓		
Quartz (SiO_2)	✓		✓	
Cristobalite (SiO_2)			✓	
Larnite (β-Ca_2SiO_4)	✓			
Tephroite (Mn_2SiO_4)	✓			
Merwinite ($Ca_3Mg(SiO_4)_2$)	✓			
Thaumasite ($Ca_3Si(CO_3)(SO_4)(OH)_6.12H_2O$))		✓		
Szomolnokite ($FeSO_4.H_2O$)	✓			
Hashemite ($BaCrO_4$)	✓			
Crocoite ($PbCrO_4$)	✓			
Mullite ($Al_6Si_2O_{13}$)			✓	

3. PYROLYSIS - GAS CHROMATOGRAPHY - MASS SPECTROMETRY (PY-GC-MS)

Steel slag samples from both forest tracks were measured by Py-GC-MS. All samples were subjected to the same pyrolysis program as impact glasses and steel slags from factories and civil construction works. The first temperature of analysis was 280°C, followed of an analysis to 600°C and finally to 750°C.

Although it was observed some chromatographic signals in the analyzed slag samples, it was not identified relevant compounds, their signal was low. Only, at 700°C it was seldom identified a typical chromatogram of aliphatic and aromatic hydrocarbons in a sample of the LFT.

4. DISCUSSION

There are differences in the mineralogical composition of these black and white steel slag samples. The chemical composition of black steel slag is more complex, in terms of the different compounds detected (hematite, magnetite, goethite, lepidocrocite, akaganeite, wüstite, magnesioferrite, calcite, vaterite, HMC, portlandite, brucite, quartz, larnite, tephroite, merwinite, thaumasite, szomolnokite, hashemite and crocoites), than the white one (magnesioferrite, calcite, quartz, cristobalite and mullite), according to Raman spectroscopy, XRD analysis and SEM-EDX.

It should be noted that the presence of brucite, portlandite and thaumasite in the black slag is indicating a high physical stress due to the volume increase prometed by these compounds and therefore, the corresponding damage to the forest track road structure because of its disintegration. In fact, the road breakage is visible right now, and it should be repaired. Moreover, the fractures can provoke that water can access the inner parts of the slags and more compounds can be leached from the slag to the surrounding areas by rain water runoff.

The reactivity of these black steel slags in contact with the atmosphere of this area (humidity, atmospheric CO_2 and SO_X acid gasses) is shown with the identification of

compounds such as goethite, lepidocrocite, akaganeite, calcite, vaterite, HMC and szomolnokite, apart from brucite, portlandite and thaumasite. In the white steel slag is also observable this reactivity through the presence of calcite (carbonation).

In addition hashemite and crocoite were identified in the slag. They should be controlled in order to avoid, or at least minimize, the possible leaching of Cr(VI) and/or Cr(III) in the soil and their corresponding environmental consequences.

But the most interesting finding in this Part D of Chapter 4 is the identification of α-cristobalite in the white slag samples. In all of the compounds identified in the black slag samples, whenever its provenance, nothing related to molecular species formed at high temperature was confirmed. However, the only family of samples related to white slag materials revealed the presence of α-cristobalite, the stable form of quartz at high temperature (>1470^{o}C).

This finding represents a clear indication of the different temperatures reached in the formation of the black slag (<1300^{o}C) during the primary reduction process in the Electric Arc Furnace production of steel, than in the formation of the white slag (>1500^{o}C) in the secondary reduction step.

Again, the excellent information given by the selected spectroscopic analytical techniques (Raman, XRD and SEM-EDX) has been critical to properly characterize the white and black steel slag in the forest tracks, giving specific information on the temperatures reached when the slag were formed in the furnace as well as on the important decay experienced by the materials leaving for years in the forest tracks.

Organic compounds were not present in the steel slag samples collected from the forest tracks, only few aliphatic and aromatic hydrocarbons were slightly detected.

CHAPTER 5

LASER-INDUCED BREAKDOWN SPECTROSCOPY (LIBS) APPLICATION

In this chapter it is displayed a methodology based on quantitative analysis by Laser Induced Breakdown Spectroscopy (LIBS) of the studied samples: impact glasses (Libyan Desert Glasses (LDGs) and Darwin Glasses (DGs)) and steel slags.

LIBS is a spectroscopic multi-elemental analytical technique based on atomic emission spectroscopy (AES). The elements included in the sample are vaporized, atomized and excited in hot plasma generating an atomic and ionic spectrum that is characteristic of the elemental composition of the sample[1]. This technique advantages over other quantitative techniques are the rapid analysis, possible *in situ* analysis, minimal sample preparation and not total destruction of it. Only a little fraction of the material from the sample surface is removed[1].

[1] G.S. Senesi, Laser-Induced Breakdown Spectroscopy (LIBS) applied to terrestrial and extraterrestrial analogue geomaterials with emphasis to minerals and rocks, Earth-Science Reviews 139 (2014) 231–267.

In the last ten years, LIBS has been widely employed in the analysis of steel slag[2-9] and meteorites[10-18]. It is an analytical technique particularly attractive in space explorations because of its *in situ* and remote application and its easily coupling with Raman spectrometers for simultaneous multi elemental and molecular information.

NASA missions to Mars take a compact spectrometer for LIBS analysis. Hence, the LIBS research with terrestrial analogues to Mars materials in laboratory conditions will be useful to improve and develop experimental strategies and prototypes to the

[2] C. López-Moreno, S. Palanco, J.J. Laserna, Quantitative analysis of samples at high temperature with remote laser-induced breakdown spectrometry using a room-temperature calibration plot, Spectrochimica Acta - Part B Atomic Spectroscopy 60 (2005) 1034-1039.

[3] C. Palagas, P. Stavropoulos, S. Couris, G.N. Angelopoulos, I. Kolm, D.C. Papamantellos, Investigation of the parameters influencing the accuracy of rapid steelmaking slag analysis with laser-induced breakdown spectroscopy, Steel Research International 78 (2007) 693-703.

[4] V. Sturm, H.U. Schmitz, T. Reuter, R. Fleige, R. Noll, Fast vacuum slag analysis in a steel works by laser-induced breakdown spectroscopy, Spectrochimica Acta - Part B Atomic Spectroscopy 63(2008)1167-1170.

5 B. Arne, T. Björk, Laser ablation breakdown spectroscopy technique for simultaneous analysis of steel and slags in metallurgical samples Yejin Fenxi/Metallurgical Analysis 29 (2009) 8-13.

[6] J.D. Pedarnig, J. Heitz, B. Praher, P. Kolmhofer, N. Huber, R. Rössler, H. Wolfmeir, E. Arenholz, Analysis of oxide materials in steel industry by calibration-free laser-induced breakdown spectroscopy, Yejin Fenxi/Metallurgical Analysis 32 (2012) 9-12.

[7] J.D. Pedarnig, Application of laser-induced breakdown spectroscopy to the analysis of secondary materials in industrial production, Laser Spectroscopy for Sensing: Fundamentals, Techniques and Applications, (2014) 496-521. Book Chapter.

[8] V. Sturm, R. Fleige, M. De Kanter, R. Leitner, K. Pilz, D. Fischer, G. Hubmer, R. Noll, Laser-induced breakdown spectroscopy for 24/7 automatic liquid slag analysis at a steel works, Analytical Chemistry 86 (2014) 9687-9692.

[9] P.J. Kolmhofer, S. Eschlböck-Fuchs, N. Huber, R. Rössler, J. Heitz, J.D. Pedarnig, Calibration-free analysis of steel slag by laser-induced breakdown spectroscopy with combined UV and VIS spectra, Spectrochimica Acta - Part B Atomic Spectroscopy 106 (2015) 67-74.

[10] J.R. Thompson, R.C. Wiens, J.E. Barefield, D.T. Vaniman, H.E. Newsom, S.M. Clegg, Remote laser-induced breakdown spectroscopy analyses of Dar al Gani 476 and Zagami Martian meteorites, Journal of Geophysical Research [Planets] 111 (2006) E05006/1-E05006/9.

[11] A. De Giacomo, M. Dell'Aglio, O. De Pascale, S. Longo, M. Capitelli, Laser induced breakdown spectroscopy on meteorites, Spectrochimica Acta, Part B: Atomic Spectroscopy 62B (2007) 1606-1611.

[12] R. Gaudiuso, M. Dell'Aglio, O. De Pascale, G.S. Senesi, A. De Giacomo,Laser Induced Breakdown Spectroscopy for elemental analysis in environmental, cultural heritage and space applications: a review of methods and results, Sensors 10 (2010) 7434-7468.

[13] M. Dell'Aglio, A. De Giacomo, R. Gaudiuso, O. De Pascale, G.S. Senesi, S. Longo, Laser Induced Breakdown Spectroscopy applications to meteorites: chemical analysis and composition profiles, Geochimica et Cosmochimica Acta 74 (2010) 7329-7339.

[14] M. Hornackova, J. Plavcan, J. Rakovsky, V. Porubcan, D. Ozdin, P. Veis, Calibration-free laser induced breakdown spectroscopy as an alternative method for found meteorite fragments analysis , European Physical Journal: Applied Physics 66 (2014) 10702/1-10702/10.

[15] M. Dell'Aglio, A. De Giacomo, R. Gaudiuso, O. De Pascale, S. Longo, Laser-induced breakdown spectroscopy of meteorites as a probe of the early Solar system , Spectrochimica Acta, Part B: Atomic Spectroscopy 101 (2014) 68-75.

[16] G.S. Senesi, Laser-Induced Breakdown Spectroscopy (LIBS) applied to terrestrial and extraterrestrial analogue geomaterials with emphasis to minerals and rocks,Earth-Science Reviews 139 (2014) 231-267.

[17] J. Kovacs, I. Sajo, Z. Marton, V. Jager, T. Hegedus, T. Berecz, T. Toth, P. Gyenizse, A. Podobni, Andras, Csatalja, the largest H4-5 chondrite from Hungary, Planetary and Space Science 105 (2015) 94-100.

[18] D. Ozdin, J. Plavcan, M. Hornackova, P. Uher, V. Porubcan, P. Veis, J. Rakovsky, J. Toth, P. Konecny, J. Svoren, Mineralogy, petrography, geochemistry, and classification of the Kosice meteorite, Meteoritics and Planetary Science 50 (2015) 864-879.

Mars exploration. Despite LIBS applications, any research works about its use over LDG and DG has been found.

It is known that LIBS can provide qualitative and quantitative information about the samples[19,20]. Regarding quantitative analysis, which is the aim of this chapter, there are two possible traditional approaches of calibration: a calibration free procedure and a calibration line approach[21]. The former determine the elemental composition of samples directly from measured LIBS spectra using computational methods in analyzing the basic physics of the plasma process. It is estimated the plasma temperature and electron number density, assuming that the plasma composition represents exactly the composition of the sample, i.e. stoichiometric ablation, the plasma is optically thin and it is in local thermodynamic equilibrium (LTE)[22]. The latter approach consists in drawing a calibration line with a set of standards whose composition is similar to that of the unknown sample. The intensity or area of a given emission line is proportional to the number density of emitters, which, in turn, is proportional to the concentration of the emitter (namely, the analyte) in the irradiated sample. Therefore, the emission intensity is linearly correlated to the concentration of a given specie in the sample[21]. So, it is feasible to determine unknown concentration of elements in the sample by comparison with the standard samples of known concentration within the expected range of concentrations.

In recent years, the application of chemometric approaches has increased broadly because of the possibility to evaluate all the information contained in the raw spectra provided by LIBS, not only a limited portion, by means of advanced statistical signal

[19] J.B. Sirven, B. Bousquet, L. Canioni, L. Sarger, S. Tellier, M. Potin-Gautier, I. Le Hecho,Qualitative and quantitative investigation of chromium-pollutedsoils by laser-induced breakdown spectroscopy combined with neural networks analysis, Analytical and Bioanalytical Chemistry (2006) 385: 256–262.

[20] A. Giakoumaki, K. Melessanaki, D.Anglos, Review Laser-induced breakdown spectroscopy (LIBS) in archaeological science-applications and prospects, Analytical and Bioanalytical Chemistry (2007) 387:749–760.

[21] R. Gaudiuso, M. Dell'Aglio, O. De Pascale, G. S. Senesi, A. De Giacomo, Laser Induced Breakdown Spectroscopy for Elemental Analysis in Environmental, Cultural Heritage and Space Applications: A Review of Methods and Results, Sensors 10 (2010) 7434-7468.

[22] V. K .Unnikrishnan, K. Mridul, R. Nayak , K.Alti, V. B. Kartha, C. Santhosh, G. P. Gupta, B. M. Suri, Calibration-free laser-induced breakdown spectroscopy for quantitative elemental analysis of materials, Pramana- Journal of Physics 79 (2012) 299-310.

processing and classification algorithms (see Fig.5.1). These methods were introduced in the early '70s, but the first use in LIBS analysis was done at 1994[23].

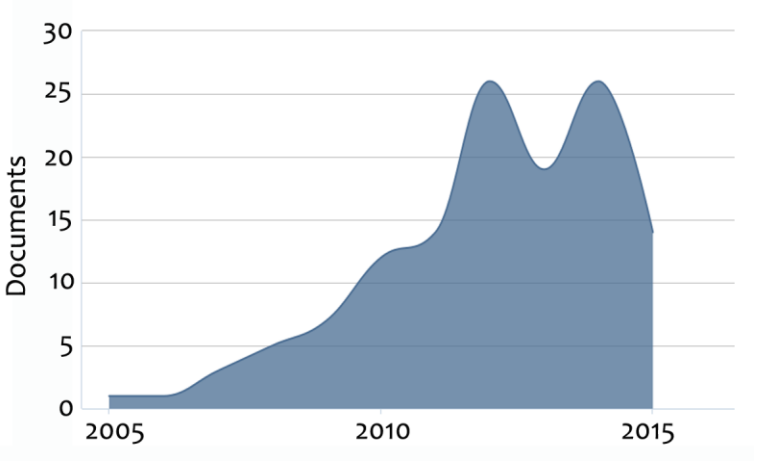

Fig.5.1. Scientific publications about the use of chemometric analysis in LIBS. Source: Scopus.

Univariate analysis is the most traditional calibration method. It only uses a single characteristic spectral line of the measured element as an input variable to set up an univariate regression model. Nevertheless, due to the normally complex spectra of multi-component and multi-matrix samples and the overlapping of spectral lines, multivariable analysis methods are employed to solve these problems and improve the accuracy of quantitative analysis[24]. Multivariate calibration displays the concentration of the analyte with all the variables belonging to the continuous spectrum. Thus, it can be reduced the complexity of spectra, enabling to extract the valuable information when the standard calibration curve method may fail[25]. Multivariate methods may be divided into four main groups: i) data representation, ii) pattern recognition, iii) classification techniques and iv) regression techniques. In general, Partial Least Squares regression (PLS) is the most common chemometric

[23] G. S. Senesi, Laser-Induced Breakdown Spectroscopy (LIBS) applied to terrestrial and extraterrestrial analogue geomaterials with emphasis to minerals and rocks, Earth-Science Reviews 139 (2014) 231–267.
[24] S. Wu, T. Zhang, H. Tang, K. Wang, X. Yang, H. Li, Quantitative analysis of nonmetal elements in steel using laser-induced breakdown spectroscopy combined with random forest, Analytical Methods 7 (2015) 2425–2432.
[25] R. Gaudiuso, M. Dell'Aglio, O. De Pascale, G. S. Senesi, A. De Giacomo, Laser Induced Breakdown Spectroscopy for Elemental Analysis in Environmental, Cultural Heritage and Space Applications: A Review of Methods and Results, Sensors 10 (2010) 7434-7468.

technique applied to concentration measurement by LIBS[26-29]. It has been employed either to calculate the concentrations of a single element (PLS1) or to simultaneously calculate the concentrations of more than one element (PLS2). PLS is a linear method since it is based on linear algebra calculations. Besides, there are other linear methods to the LIBS analysis, such as Multi Linear Regression (MLR), Principal Component Regression (PCR), Least Absolute Shrinkage and Selection Operator (LASSO), Multivariate Regression with Covariance Estimation (MRCE), Soft Independent Modelling of Class Analogy (SIMCA), Multivariate Curve Resolution (MCR), amongst others[30,31]. On the other hand, nonlinear methods such as Artificial Neural Networks (ANN)[32] are also applied by few authors to take into account the possible nonlinear relationship between the X and Y values.

It should be noted that prior to performing the actual quantitative determination, also it can be used chemometric methods such as Principal Components Analysis (PCA) in order to observe data clusters and discriminate outliers[33]. PCA is commonly used for classification of LIBS data[34-37]. In LIBS analysis, the PCA method allows

[26] M.D. Dyar, M.L. Carmosino, E.A. Breves, M.V. Ozanne, S.M. Clegg, R.C. Wiens, Comparison of partial least squares and lasso regression techniques as applied to laser-induced breakdown spectroscopy of geological samples, Spectrochimica Acta B 70 (2012) 51–67.

[27] J.M. Andrade, G. Cristoforetti, S. Legnaioli, G. Lorenzetti, V. Palleschi, A.A. Shaltout, Classical univariate calibration and partial least squares for quantitative analysis of brass samples by laser-induced breakdown spectroscopy, Spectrochimica Acta B 65 (2010) 658–663.

[28] R.C. Wiens et al., Pre-flight calibration and initial data processing for the ChemCam laser-induced breakdown spectroscopy instrument on the Mars Science Laboratory rover, Spectrochimica Acta B 82 (2013) 1–27.

[29] J.M. Tucker, M.D. Dyar, M.W. Schaefer, S.M. Clegg, R.C. Wiens, Optimization of laser-induced breakdown spectroscopy for rapid geochemical analysis, Chemical Geology 277 (2010) 137–148.

[30] J. El Haddad, L. Canioni, B. Bousquet, Good practices in LIBS analysis: Review and advices, Spectrochimica Acta Part B 101 (2014) 171–182.

[31] G. S. Senesi, Laser-Induced Breakdown Spectroscopy (LIBS) applied to terrestrial and extraterrestrial analogue geomaterials with emphasis to minerals and rocks, Earth-Science Reviews 139 (2014) 231–267.

[32] J.B. Sirven, B. Bousquet, L. Canioni, L. Sarger, S. Tellier, M. Potin-Gautier, I. Le Hecho, Qualitative and quantitative investigation of chromium-polluted soils by laser-induced breakdown spectroscopy combined with neural networks analysis, Analytical and Bioanalytical Chemistry (2006) 385: 256–262.

[33] R. Gaudiuso, M. Dell'Aglio, O. De Pascale, G. S. Senesi, A. De Giacomo, Laser Induced Breakdown Spectroscopy for Elemental Analysis in Environmental, Cultural Heritage and Space Applications: A Review of Methods and Results, Sensors 10 (2010) 7434-7468.

[34] J.L. Gottfried, R.S. Harmon, F.C. DeLucia Jr., A.W. Miziolek, Multivariate analysis of laser-induced breakdown spectroscopy chemical signatures for geomaterial classification, Spectrochimica Acta B 64 (2009) 1009–1019.

[35] B. Bousquet, J.B. Sirven, L. Canioni, Towards quantitative laser-induced breakdown spectroscopy analysis of soil samples, Spectrochimica Acta B 62 (2007) 1582–1589.

[36] A.M. Ollila, J. Lasue, H.E. Newson, R.A. Multari, R.C.Wiens, S.M. Clegg, Comparison of two partial least squares-discriminant analysis algorithms for identifying geological samples with the ChemCam laser-induced breakdown spectroscopy instrument, Applied Optics 51 (2012) 130–142.

[37] P. Pořízka, A. Demidov , J. Kaiser , J. Keivanian , I. Gornushkin, U. Panne, J. Riedel ,Laser-induced breakdown spectroscopy for in situ qualitative and quantitative analysis of mineral ores, Spectrochimica Acta Part B 101 (2014) 155–163.

spectra to be extracted in the form of linear combinations of the principal components (PCs), and their coordinates along the PCs (scores) are used to evaluate similarities and/or differences between the spectra. Then, they can be grouped into appropriate classes by analyzing the scores and PCs together, with no previous information needed for grouping the spectra[31].

Before evaluating the method, it is required a preprocessing in order to obtain quality information from the LIBS spectra. The most important pretreatments are baseline correction, signal alignment and data normalization, among them: offset correction and signal derivatisation, which are used to eliminate baseline distortion; centering, scaling and smoothing, which are used so as to remove unnecessary data and emphasize the noteworthy information; Multiplicative Scatter Correction (MSC); Standard Normal Variate (SNV) and so on[38-39].

In addition, it is essential to know if the model selected will be able to work quantitatively in the future with new similar data sets. The most used methods applied for the validation of multivariate calibration models developed by PLS are leverage correction, cross-validation and test set validation. Leverage correction is only an approximate validation method, which is used in the first stages of the calibration to get an idea of how good the model is. Cross validation is the usual method used when there are not a lot of samples to build the model. It is a validation technique based in the calibration data only. It is a validation method where a number of samples are left out of the calibration and used for prediction. This is repeated until all samples have been left out once. The most common cross validation methods is "leave-one-out" cross validation, i.e. by excluding one sample from the calibration set by a series of consecutive permutations in order to use it *a posteriori* to test the model. However, a more robust approach than cross-validation is based on two separate subsets from the original dataset: the calibration set

[38] A. Gredilla, Metals and Metalloids in estuaries: development of analytical tools for pollution monitoring, PhD Thesis, 2011.
[39] R.B. Anderson, S.M. Clegg, T. Graff, R.V. Morris, J. Laura , Generation of a database of laboratory laser-induced breakdown spectroscopy (libs) spectra and associated analysis software, Second Planetary Data Workshop (2015) #7053.
[40] L. Xu, Y.P. Zhou, L.J. Tang, H.L. Wu, J.H. Jiang, G.L. Shen, R.Q. Yu, Ensemble preprocessing of near-infrared (NIR) spectra for multivariate calibration, Analytica Chimica Acta 616 (2008)138–143.
[41] A. Rinnan, F. van den Berg, S.Balling Engelsen, Review of the most common pre-processing techniques for near-infrared spectra, Trends in Analytical Chemistry 28 (2009) 1201-1222.

dedicated to the construction of the model and the validation set dedicated to its evaluation. This is known as test set validation[42,43].

The main aim of our work was to develop a fast, cheap, and effective methodology for the analysis of terrestrial-extraterrestrial samples using a portable equipment of laser induced breakdown spectroscopy. We intended to prepare a routine method with minimal sample preparation steps, maximal throughput of samples through laboratory processing and negligible influence of operators on analytical results.

1. RESULTS

LIBS analyses were carried out over high temperature products such as the impact glasses, terrestrial-extraterrestrial materials, and the steel slag samples, terrestrial material. This fact allowed us to evaluate this potable instrument and also to perform a quantitative analysis of the samples. We opted to create a calibration curve with several standards pellets of known elemental concentrations, in view of future missions to Mars where it will be used calibration targets to investigate the chemistry of the Martian surface.

First of all, it was prepared those pellets, after it was verified their homogeneity and then, they were analyzed by LIBS.

1.1 Powder pellets

In order to realize the calibration curve, it was made 19 pellets with different concentrations of SiO (Alfa Aesar (99.5%)), MgO (Sigma-Aldrich (>99%)), CaO (Sigma-Aldrich (99.9%)), Al_2O_3 (Sigma-Aldrich (99.99%)), BaO (Sigma-Aldrich (99.99%)), Na_2O + Na_2O_2 (Alfa Aesar) and Fe_2O_3 (Alfa Aesar (99.99%)) powders. The concentration ranges of each element varied according to the percentages that could be found in the analyzed materials (see Fig.5.2).

[42] J. El Haddad, L. Canioni, B. Bousquet, Good practices in LIBS analysis: Review and advices, Spectrochimica Acta Part B 101 (2014) 171–182.
[43] P. Pořízka, A. Demidov , J. Kaiser , J. Keivanian , I. Gornushkin, U. Panne, J. Riedel ,Laser-induced breakdown spectroscopy for in situ qualitative and quantitative analysis of mineral ores, Spectrochimica Acta Part B 101 (2014) 155–163.

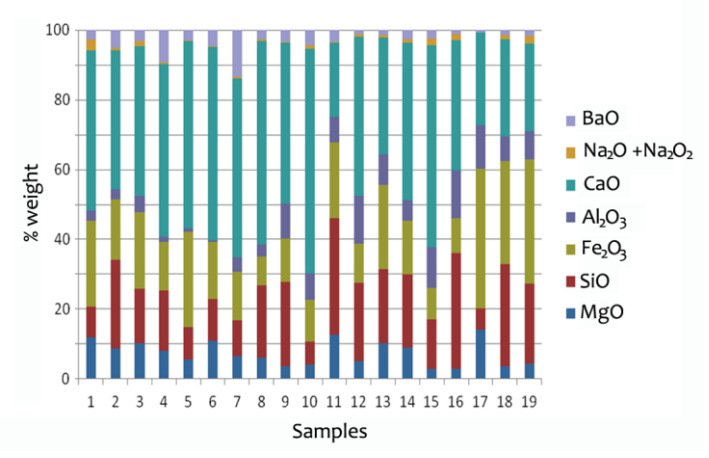

Fig.5.2. Concentrations of the elements (Ba, Na, Ca, Al, Fe, Si and Mg) present in the powder pellets belonging to the calibration curve (1-19). The concentrations are given in % weight.

The total weight of each powder mixture was 0.5 gr and it was not used any binder. The mixture of powders was milled in an agate mortar to ensure the homogeneity, and after, they were pressed at 9 tons of pressure (CrushIR, PIKE Technologies, Canada). The final pellets had a diameter of 12 mm and approximately 1 mm width. In the same way, a pellet for each standard (oxide powders) was prepared with the purpose to select the appropriate lines in the LIBS spectra for each element.

Afterward, these pellets were immediately stored in zip bags, without atmosphere contact, otherwise their volume could increase in a short time due to the presence of CaO and MgO, and they could be broken easily.

Moreover, it was made 6 pellets of the steelmaking slag Reference Material (RM) (NH 146, Brammer standard, Mittal Steel Oslava, Czech Republic), mixed with ethylcellulose to obtain different concentration of Si, Mg, Ca, Al and Fe, but within the range of concentration of the calibration pellets. Also, 3 pellets with only ethylcellulose and 6 measurements over Teflon were realized, considered as blanks.

1.2 Homogeneity of the powder pellets

The homogeneity is an important factor in the case of the calibration samples, since different signals of the same pellet would not be representative of that pellet. Therefore, Scanning Electron Microscopy coupled to Energy Dispersive X-ray

spectroscopy (SEM-EDX) was used to observe the elemental homogeneity, and Raman spectroscopy to examine the molecular composition of the calibration samples.

1.2.1 Scanning Electron Microscopy- Energy Dispersive X-ray Spectroscopy (SEM-EDX)

In the SEM images it could be observed that the size of the grain in the calibration samples was 1-5 μm (see Fig. 5.3).

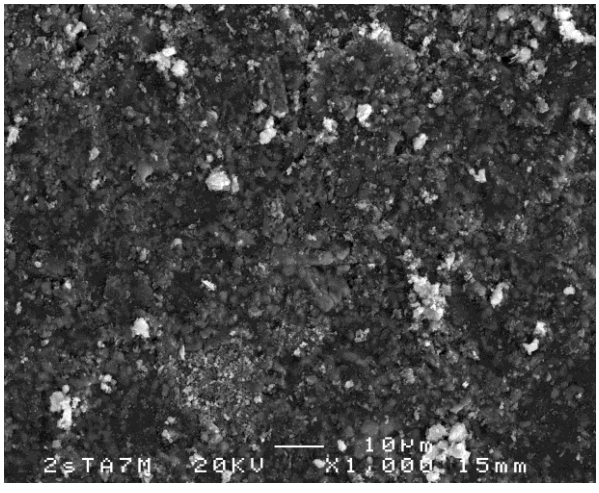

Fig. 5.3. SEM image of calibration sample 17.

Moreover, the analysis SEM-EDX allowed us to confirm the elemental homogeneity of the samples. For instance, in the Fig. 5.4, after knowing the elemental distribution by EDX mapping of that area of the sample 17, it could be performed a cameo image over the SEM image of that area and it could be observed homogeneous distribution of the elements.

It should be pointed out that the homogeneity could depend on the magnifications that you use in the analysis, i.e. images of higher number microns would seem more homogeneous than of less microns. The spot laser of our LIBS equipment is 193 μm, so the homogeneity of the samples was assured, since with images of 50 μm it was already observed the homogeneity in the elemental composition of the samples by SEM-EDX.

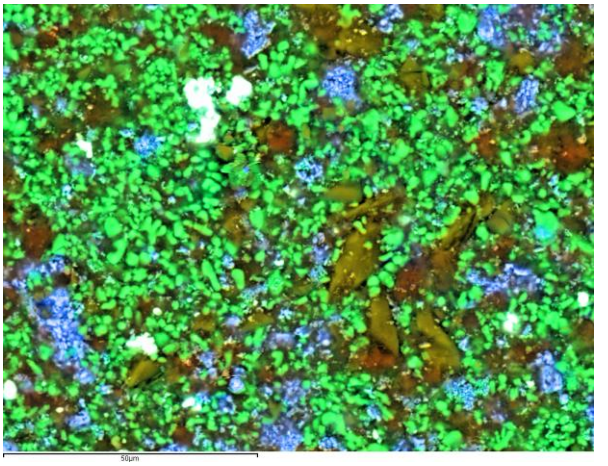

Fig.5.4. SEM mapping of the calibration sample 17. Green: Ca, blue: Fe, reddish: Mg, white: Ba, khaki: Si and brownish-reddish: Al. Na was not detected probably because this sample had the lowest sodium concentration.

1.2.2 Raman spectroscopy

It was accomplished Raman images over the calibration samples in order to observe the molecular homogeneity of the pellets before LIBS analysis. The measured area in each sample was of 70x70 µm.

During the analysis, it was observed that Al_2O_3 did not appeared in the samples, so perhaps it could be some polymorph of alumina which do not give Raman signal, as it has been mentioned in the Chapter 4. Likewise, CaO and MgO are also inactive in Raman spectroscopy, so it could not be identified. And BaO was not possible to detect either.

We were only able to identify Fe_2O_3, SiO and Na_2O +Na_2O_2. But, it could be observed a homogeneous distribution in all of them (see Fig.5.5).

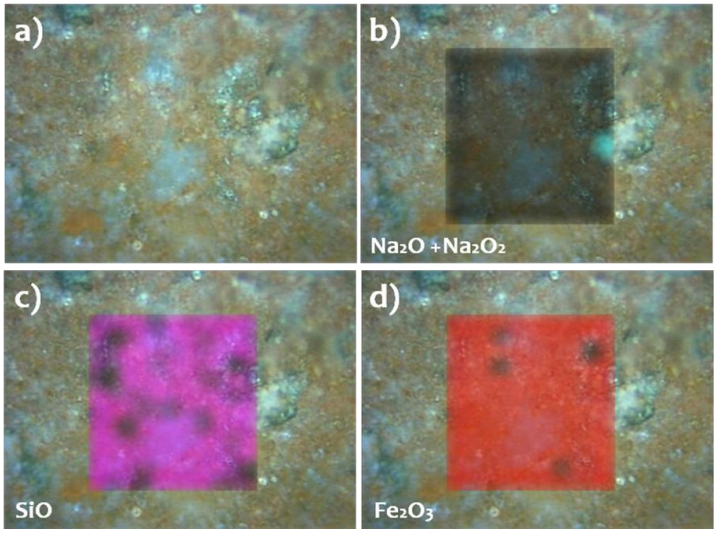

Fig. 5.5. Raman microscopic image (a) and presence of Na_2O +Na_2O_2 (b), SiO (c) and Fe_2O_3 (d) in a coloured area of 70x70 μm in the calibration sample 17.

On the other hand, by Raman spectroscopy it could be also recognized that after some hours in contact with the atmosphere, some new compounds were formed in the pellets, such as carbonates (like calcite ($CaCO_3$) and witherite ($BaCO_3$)) and hydroxides (like brucite ($Mg(OH)_2$) and portlandite ($Ca(OH)_2$). Besides, after one week it was also identified H_2O Raman bands in the pellets. Hence, it could be concluded that the contact with the atmosphere was an important factor to take into account in order to conserve the samples.

1.3 LIBS analysis of the powder pellets

The 19 calibration pellets were measured by LIBS in the UV (196-419 nm) and near IR (580-1000 nm) spectral range. It was realized three measured per sample in different position (aprox. each 4 mm). At each position, the experimental procedure consisted firstly in firing 10 cleaning shots, in order to avoid detecting contaminations at the surface of the pellets.

We assumed that all the oxide molecules are dissociated into the LIBS plasma due to the high temperatures (T> 10000 K), in order to be able to assimilate the atomic concentration as the initial oxide one.

1.3.1 Univariate and Multivariate calibration

The determination of peak areas of the LIBS spectra and the Principal component analysis (PCA) of the whole data was carried out using the PLS-Toolbox v.7.0.2 (Eigenvector Research, USA) implemented in MATLAB 2010 software (The Mathworks, MA, USA). PLS models, for elements quantification, were developed by means of OPUS program Version 7.2 from Bruker Gmbh (Bremen, Germany).

1.3.1.1 Identification of outliers

The identification of outliers between replicates of the calibration data set (19 calibration samples x 3 replicates, 57 total analyses) was realized applying principal components analysis (PCA) to the potential LIBS calibration set spectra (with mean and center as preprocessing spectral). Three PCs were used with a variance cumulative total of 92.35%, the addition of extra components did not increase the amount of explained data variance. There was high reproducibility in the measurement process of the calibration pellets. From the 57 measurements only six outliers were detected. The identification of these outliers was due to one of the replicate measurements for each pellet was away from the other replicates.

Also PCA was apply to the potential LIBS set spectra, which include the calibration set, the samples to analyze (LDG, DG and steel slag) and the test set (reference materials), with the aim to confirm if the future predicted dataset and the test set were in the same range of possible level of concentration that the calibration data set. As can be seen in the Fig. 5.6 in the scores plots over the PC1 and PC2 space, LDG and DG samples were a little away of the calibration samples, possibility because the level of Si concentration is higher in both types of samples, but the slag samples were in the same position in the scores of PC1/PC2 than the calibration set. The RM pellets were within the calibration data set.

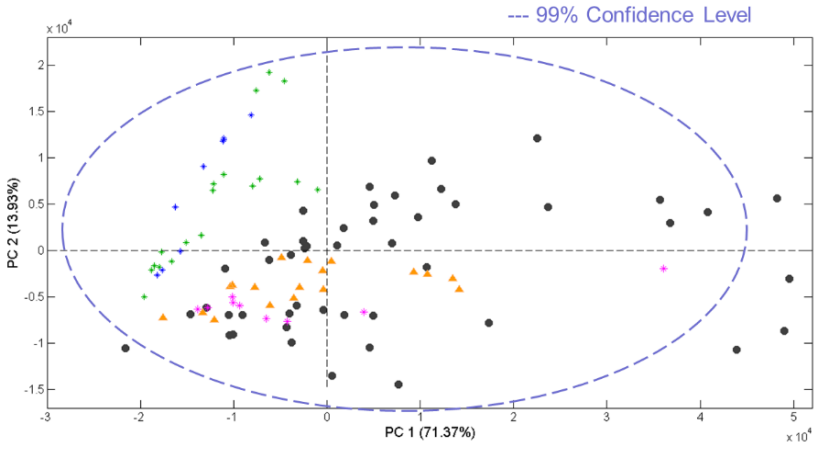

Fig. 5. 6. Projection of the scores on the space formed by the first and second PCs of LIBS data set spectra in the range of UV and IR. Orange: test set (RM), Black: calibration set, Pink: black steel slag, Green: DG and Blue: LDG.

Thus, PCA confirmed that we had a suitable dataset (representative and reflected the maximum variance shown by samples) to proceed to the quantification. We tried two kinds of calibration: univariate and multivariate.

1.3.1.2 Univariate calibration

Firstly it was carried out a univariate calibration. For that purpose, it was used the UV wavelength region.

The determination of the peak areas of the LIBS spectra were studied without normalization and using normalization. The normalization consisted in calculating the sum of all the lines intensity values, and the chosen lines were corrected with respect to that value. The results were similar, thus their peak areas without background level were considered for building the univariate models.

It was selected a spectral line for each element (neutral (I) or single ionized species (II)) without overlapping between the studied elements (see Fig. 5.7): Al(I) 308.21 nm, Ca(II) 396.87 nm, Fe(I) 373.74 nm, Mg(I) 285.16 nm and Si(I) 288.16 nm and Ba(II) 389.14 nm. Na was not taken into account because they did not present strong or relevant lines in the UV spectral range according to the intensities that gives our equipment.

Then, the areas of these lines were represented in front of the concentrations to found the univariate calibration curves obtained using the selected emission peaks.

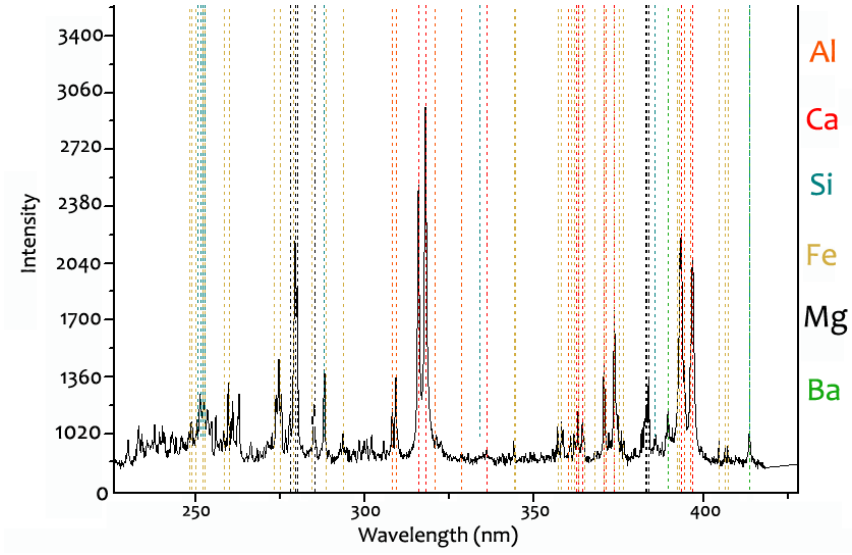

Fig. 5.7. A LIBS spectrum of the calibration sample with the overlapping characteristics emission lines of Al, Ca, Si, Fe and Mg.

In all cases, univariate calibration models presented low linearity and the correlation coefficient were too low with r_{cal}< 0.90 showing low robustness of the models (see Fig. 5.8). The poor linearity of the univariate calibration curves affects the accuracy and the precision of the prediction. Thus, the univariate calibration curves could be used only for rapid estimates of the element compositions in the samples. Therefore, it was tried the multivariate calibration.

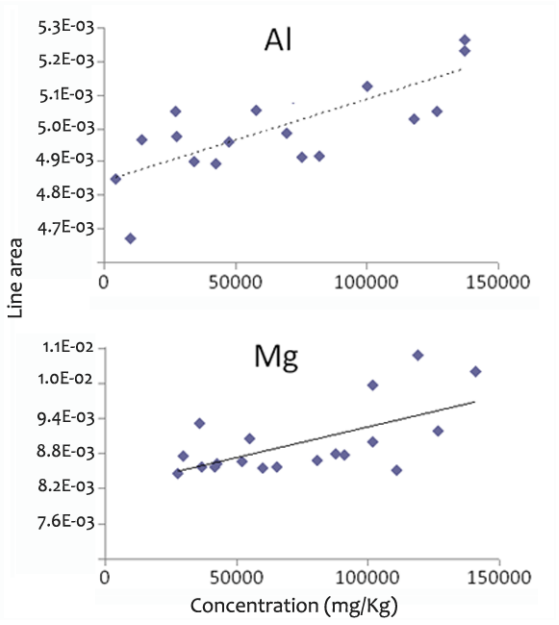

Fig. 5.8. Univariate calibration curves obtained using Al (r= 0.75) and Mg (r=0.63) selected emission line areas, versus the elemental concentration (mg·Kg-1) of the calibration pellets (all the calibration points are not represented to improve the visualization).

1.3.1.3 Multivariate calibration

PLS1 regression is a single response variable (elemental concentration) versus the observable variable (spectra, intensity at each spectrometer channels). In our case the data set was of 110 analysis (calibration set, test set and prediction set, i.e. the sample to analyze) and 4096 variables (wavelength, nm). The PLS multivariate models were created using the calibration data set, which predicted a limited number of output values (elemental concentrations) from a very large number of input variables (intensity at multiple wavelengths).

This calibration involved three phases, namely regression, validation and prediction. In the regression phase, 19 calibration pellets (3 replicates in different sites of each pellet) were used to make a calibration data set. This whole of data was used to construct the mathematical model per analyte. For the validation phase, it was employed a test set formed by the six steelmaking slag RM pellets (3 replicates in different sites of each pellet) of different concentrations, diluted with ethylcellulose. This dataset was used to test the model. The model estimates theoretical values for

each sample in the validation set, which are then compared to the experimental values whilst calculating the error.

The final phase of calibration was the prediction, where the robustness of the model was tested with another set of samples that was completely independent from the calibration and validation data set; this was the LIBS spectra of the impact glasses and steel slag samples.

(A) Combined UV + IR LIBS spectra

First, it was used the full spectra with the UV and IR spectral range. The obtained LIBS spectra of the oxide materials showed good signal-to-background ratio, a huge number of emission lines in the UV and IR region and revealed clear differences for samples of different composition, as it can be seen in the Fig. 5.9.

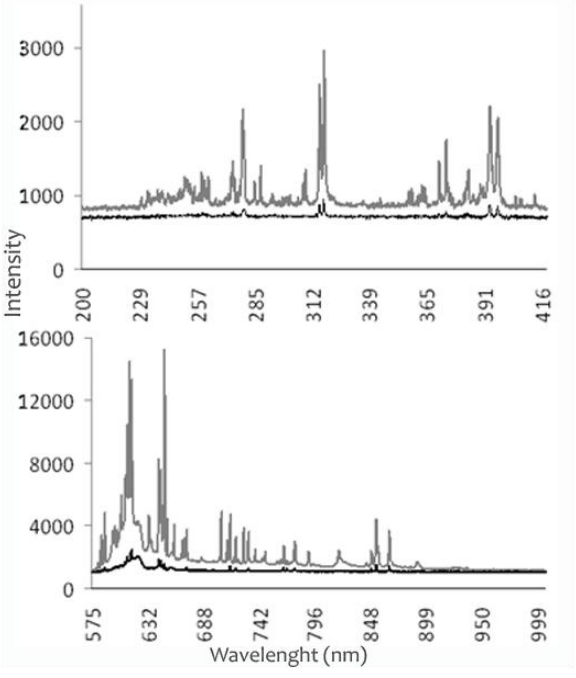

Fig. 5.9. Two representative LIBS spectra for 16 and 6 calibration pellet with significant difference in the content of Al_2O_3 oxide weight.

In particular, on the basis of spectral selectivity and sensitivity (see Fig. 5.10) of our portable instrument, besides the aforementioned lines of the univariate calibration, it was selected the following ones as the most significant emission lines for the

quantitative determination of each analyte: Al(I) 396.21 nm, Al(II) 704.40 nm, Ca(I) 616 nm, Fe(I) 275.01 nm, Fe(I) 667.15 nm, Mg(II) 279.63nm, Na(I) 589.16nm, Ba(I) 705.7 nm and Si(II) 634.88nm.

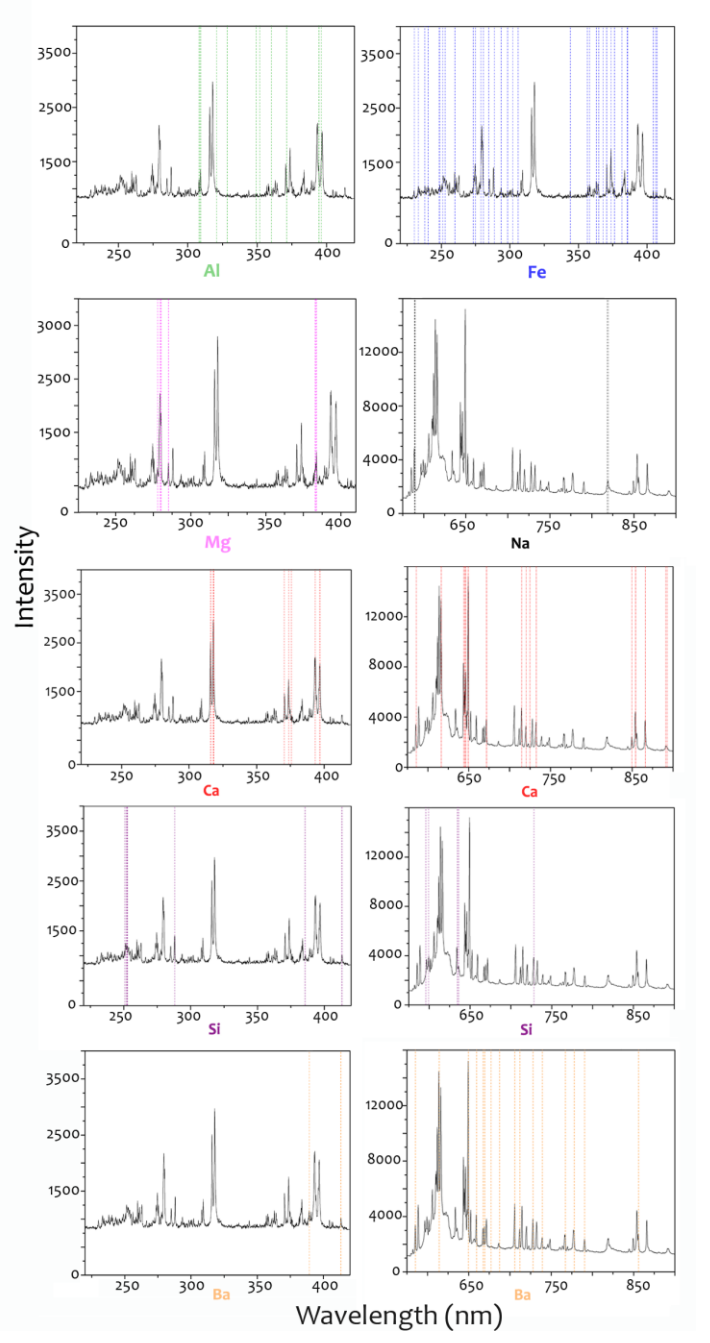

Fig. 5.10. Some representative LIBS spectra measurements made with our portatil instrument with the illustration of the characteristic emission lines of Al, Fe, Mg, Na, Ca, Si and Ba in the UV and IR region.

Predictive models were designed with 51 final calibration samples. Over the calibration set spectra it was tested several spectral ranges combined with different preprocessing algorithms and selected the optimum number of PLS factors with the minimum of the predicted residual error (RMSE). For that, the calibration set spectra was applied for the construction of around 450 preliminary Partial Least Squares (PLS) calibration models for each analyte (aprox. 3200 PLS models) using the full spectral range (UV-IR). The used equation to measure the error of the calibration model is as follows:

$$\mathrm{RMSEC} = \sqrt{\frac{\sum_{i=1}^{n}(x_i - y_i)^2}{n - f - 1}} \qquad (5.1)$$

Where x_i is the reference values of samples in the calibration population i; i=1, 2, ...n; y_i is the predicted sample values i; i=1, 2, ...n; n is the number of samples in the calibration data set and f is the number of latent variables (principal components) in the calibration regression model.

Ten preprocessing methods were employed:

(i) The Constant Offset Elimination (COE), which is commonly used to remove the baseline effect introduced by the spectrometer. It shifts the spectra in order to set the y-minimum to zero.

(ii) The Straight Line Subtraction (SLS), which fits a straight line to the spectrum and subtracts it. This is a good approach, especially when the entire spectrum or very broad regions are selected. In general, this method should only be used in situations where baseline aberrations are severe and a limited number of training sample spectra is available.

(iii) The Vector Normalization (SVN), which carries out a mean centering followed by a variance scaling.

(iv) The Multiplicative Scatter Correction (MSC), which performs a linear transformation of each spectrum for it to best match the average spectrum of the whole set.

(v) The differentiation by calculating the first derivative (FD) of the spectrum. Differentiation can be used to enhance spectral differences, being a very effective method for removing baseline offsets. The main disadvantages or

drawbacks of using derivative pre-processing are that the resulting spectra are very difficult to interpret and that it decreases the signal-to-noise ratio (SNR) by enhancing the noise.

(vi) Min-Max Normalization.

(vii) Second Derivate remove constant background signals.

(viii) First derivate (FD) + Straight line subtraction.

(ix) First derivate (FD) + Vector normalization (SNV).

(x) First derivative + MSC.

Also the mentioned spectral preprocessings were taken with only a spectral range of +/-5 nm of the characteristic line intensity of each specific element to build up PLS models that reflected the elemental concentration, but there were unsatisfactory results. Hence, they were not taken into account.

The preliminary PLS models were used for selecting the final PLS models (one for each analyte) based on adequate spectral range (including the characteristics and strong emission lines of each analyte), high regression coefficient (r), appropriate number of PLS factors (rank) and the lowest relative errors of cross validation (RMSECV). The RMSECV was calculated as follows:

$$\mathrm{RMSECV} = \sqrt{\frac{\sum_{i=1}^{n}\left(x_i - y_i\right)^2}{n-1}} \qquad (5.2)$$

Also, it was employed as quality indicators of prediction accuracy and predictive ability of the PLS models, the residual predictive deviation (RPD), defined as the ratio between the standard deviation of the population (SD) and the root mean square error of prediction (RMSEP) or of cross-validation (RMSECV); and the Bias value, which measures the average difference between reference and predicted values with the following equation:

$$bias = \sum_{i=1}^{n}\frac{\left(x_i - y_i\right)}{n} \qquad (5.3)$$

As a consequence of the high volume of results generated, it is impossible present all the results obtained for all preprocessing strategies in a table, it was only selected the best PLS models of each analyte, which are summarized in the Table 5.1.

Table 5.1. Modeling parameters and prediction capabilities of PLS-LIBS models in all UV-IR spectral range developed for the determination of Al, Ba, Ca, Fe, Na, Mg and Si.

Analyte	Spectral range (nm)	RPD	Rank	r	Bias (%)	RMSECV (%)	Preprocessing*
Al	682.48-601.3; 520.3-277	1.84	8	0.84	1.2	17	FD + SNV
Ba	925.7-763.5; 601.4-277	1.43	2	0.72	0.3	16	FD + MSC
Ca	925.72-844.54; 682.48-601.3; 520.32-439.14	2.04	6	0.87	0.3	10	MSC
Fe	1006.71-925.62; 763.56-682.38; 439.2-277	1.63	8	0.79	0.9	15	SNV
Mg	1006.7-520.2; 439.2-277	2.23	6	0.89	0.5	11	FD + SNV
Na	1006.7-844.5; 763.6-520.2; 358.15-276.97	1.19	10	0.55	0.9	18	Without preprocessing
Si	1006.7-601.3 ;520.3-358.1; 277.07-195.99	1.92	8	0.85	0.4	13	MSC

*Vector normalization (SNV); Multiplicative Scatter Correction (MSC) and First derivate (FD).

From none to different spectral preprocessing methods, such as SNV and MSC as well as a combination of them (FD + MSC), were required as optimal spectral pretreatment. The number of PLS factors (Rank) were low and ranged from 2 (for Ba) to a maximum one of 10 (for Na) as it can be seen in the Table 1. The RPD values were around 2 (except in the case of Na). The highest values of RDP suggest that the methods carried out a good prediction. Moreover, low values for bias were found in our PLS models (from 0.3 for Ba and Ca, and 1.2 for Al); the lower bias value, the better.

The Fig. 5.11 shows the comparison between the calibration and validation lines from the dataset in the case of Al, Fe, Mg and Si. As it can be observable, there are not significant differences between the calibration and validation line, with r values between 0.8 (for Fe) and 0.9 (for Mg).

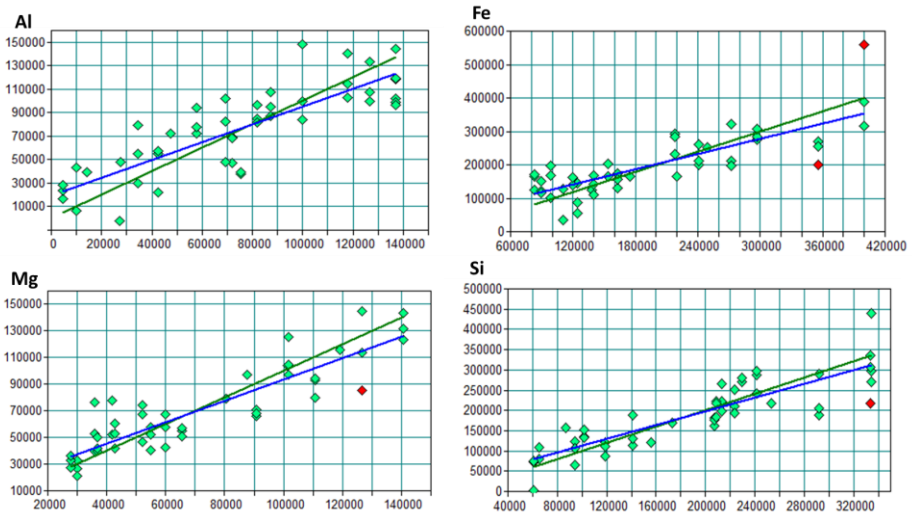

Fig 5.11. Model and validation plots produced with PLS1. It is displayed the known versus PLS predicted concentrations of Al, Fe, Mg and Si in mg·Kg^{-1}. The green circles and solid line represent the calibration curve, and the blue line represents the validation curve. The red circles are outliers.

(B) UV versus IR LIBS spectra

The same methodology of PLS calibration was applied separately to each spectral region. In the Table 2 and 3 can be seen details of spectral preprocessing, spectral range and parameters of quality of the final PLS models selected for each analyte.

In the case of PLS models of the LIBS spectra belong to the UV range, the RPD values were higher (2.63 for Mg) than in the case of PLS models of the LIBS spectra belong to the IR range. It was also better the regression coefficients (between 0.77 and 0.92), bias (low values, for instance 0.02 for Fe) and the RMSECV values (around 12%).

Table 5.2. Modeling parameters and prediction capabilities of PLS-LIBS models in the UV spectral range developed for the determination of Al, Ba, Ca, Fe, Mg and Si.

	RPD	Bias (%)	Rank	r	RMSECV (%)	Spectral range (nm)	Preprocessing*
Al	1.57	0.3	6	0.77	19	418.39-352.07;330.09-307.92; 285.84-197.55	Without preprocessing
Ba	1.64	0.9	5	0.78	5	418.39-396.22;374.24-352.07; 308.02-263.77 ; 241.79- 219.62	FD + SNV
Ca	1.66	0.1	4	0.80	12	418.39-352.07;330.09-285.84; 263.87-241.69	MMN
Fe	1.91	0.02	3	0.85	12	418.39-374.14;308.02-241.69; 219.72-197.55	FD + SNV
Mg	2.63	0.5	3	0.92	10	418.39-352.07; 330.1-219.7	SNV
Si	1.96	0.1	6	0.86	13	418.39-374.14;330.09-285.84 ; 263.87-241.70	SNV

*Mix-max normalization (MMN); Vector normalization (SNV) and First derivate (FD).

Table 5.3. Modeling parameters and prediction capabilities of PLS-LIBS models in the IR spectral range developed for the determination of Al, Ba, Ca, Fe, Na, Mg and Si.

	RPD	Bias (%)	Rank	r	RMSECV (%)	Spectral range (nm)	Preprocessing*
Ba	1.43	0.1	2	0.71	6	1006.71-963.94; 921.37-878.6 836.03-750.59; 708.02-622.60	MSC
Ca	1.25	0.2	2	0.60	16	1006.7-665.3; 622.68-579.92	MSC
Fe	1.14	0.6	3	0.48	21	1006.71-963.94; 921.4-793.3; 750.69-665.25; 622.68-579.92	SNV
Si	1.49	0.7	10	0.74	17	964-707.9; 665.35-579.93	MSC
Na	1.34	0.6	8	0.66	15	878.7-835.93 ;793.36-750.59 708.02-665.25;622.68-579.92	FD + SNV

*Vector normalization (SNV); Multiplicative Scatter Correction (MSC) and First derivate (FD).

Fig. 5.12 shows the correlation between the predicted by PLS models in the UV range spectral and the references values for Ca, Fe, Mg and Si.

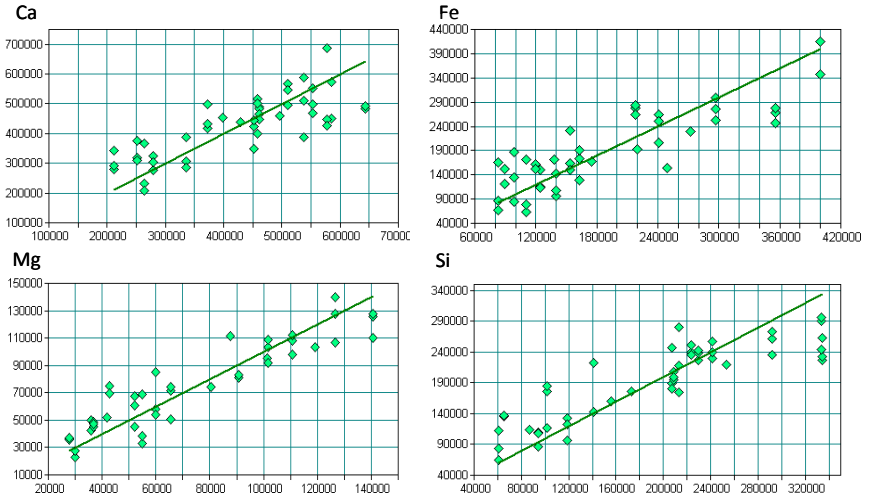

Fig 5.12. Model and validation plots produced with PLS1 using the UV spectral range. It is displayed the known versus PLS predicted concentrations of Ca, Fe, Mg and Si in mg·Kg^{-1}.The green circles and solid line represent the calibration curve.

An explication about the worst results with the IR spectral range could be due to distortion produced by self-absorption, which is when the plasma formed during the ablation absorbs its own emission, higher overlapping of the emission lines in that range, laser energy fluctuations, etc.

According to the results, it was considered to use the PLS models obtained when we combined UV and IR spectral range in next steps.

(C) Validation of PLS models using all the spectral range (UV-IR)

With the final PLS models of each analyte, two different types of validation were realized, cross-validation (LOO) and test set validation.

Cross-validation (LOO)

The constructed PLS calibration models for each analyte were validated using leave-one-out (LOO) cross validation, in which each sample in the calibration set is successively left out and treated as an unknown while the model is trained. In our case with 51 measurements, each new model was made on 50 measurements. The estimation of RMSE of cross-validation is RMSECV and the values obtained can be seen in the Table 5.1. The PLS models had low RMSECV (around 15%) taking into

consideration the high concentration values of each analyte used in the calibration data set.

Test set validation

Once we had the final models for the 7 analytes (Ca, Al, Fe, Si, Na, Mg and Ba) with UV and IR spectral region, they were validated using an external set of samples. As the testing test set must have the same measurement range that the calibration set (oxide pellets), we selected the steelmaking slag reference material, whose composition is a mixture of oxides.

The 6 pellets of this RM with different concentrations of the studied elements were measured in three positions (aprox. each 4 mm). The scores of PC1/PC2 confirmed that the selected validation set was in the same range that the calibration spectra set (see Fig. 5.13), as it can be mentioned before.

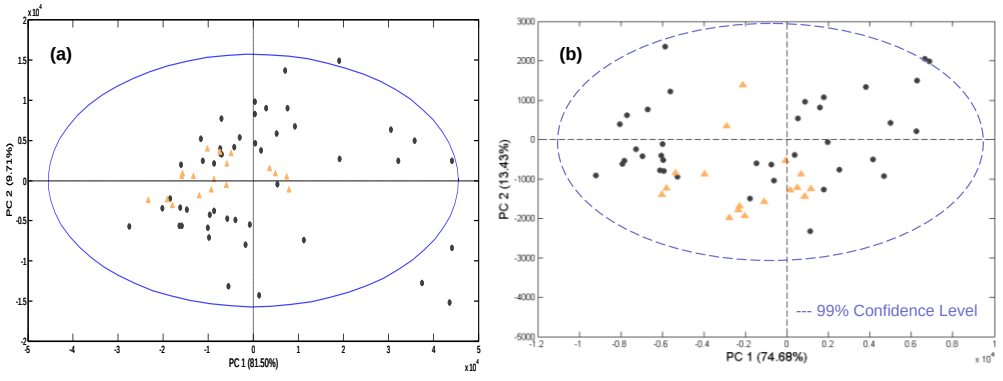

Fig.5.13. Projection of the scores on the space formed by the first and second PCs of calibration set in the spectral range of UV and IR (a) and in the UV range (b). Orange: validation set (Reference Material), Black: calibration set.

The test set validation gave excellent results mainly to Fe, Mg and Si, and satisfactory for Al and Ca, the RM has not certificated values for Ba and Na. The PLS approach provided better predictions that the univariate calibration.

1.4 Analysis of the samples

The predictive ability of the PLS models was evaluated on the impact glasses and black steel slag samples not used for calibration in PLS models.

Directly a total of 10 solid samples were measured in several positions (aprox. each 5 mm depend on the superficial irregularities) exposed to 3 laser shots to avoid erroneous assignation of an element in the first shot, due to possible impurities in the sample surface. Thus, it was obtained 18 measurements of 4 DGs, 13 measurements of 3 LDGs and 5 measurements of 3 black steel slag samples.

There is a statistics index, the Mahalanobis distance, which can advise about the applicability or not of one PLS model to a new sample. Thus, if the samples used in the calibration data set are similar to these new predicted samples, the value of this distance is low[44].

In the case of Al and Ca, in a few LDGs and DGs samples of the prediction set, the values of Mahalanobis distance were high; as consequence these predicted concentrations were considered as outliers by the selected PLS models. For Ba and Mg the concentrations found can be seen in the Fig. 5.14.

[44] R. De Maesschalck, D. Jouan-Rimbaud, D.L. Massart. The Mahalanobis distance, Chemometrics and Intelligent Laboratory Systems 50 (2000) 1–18.

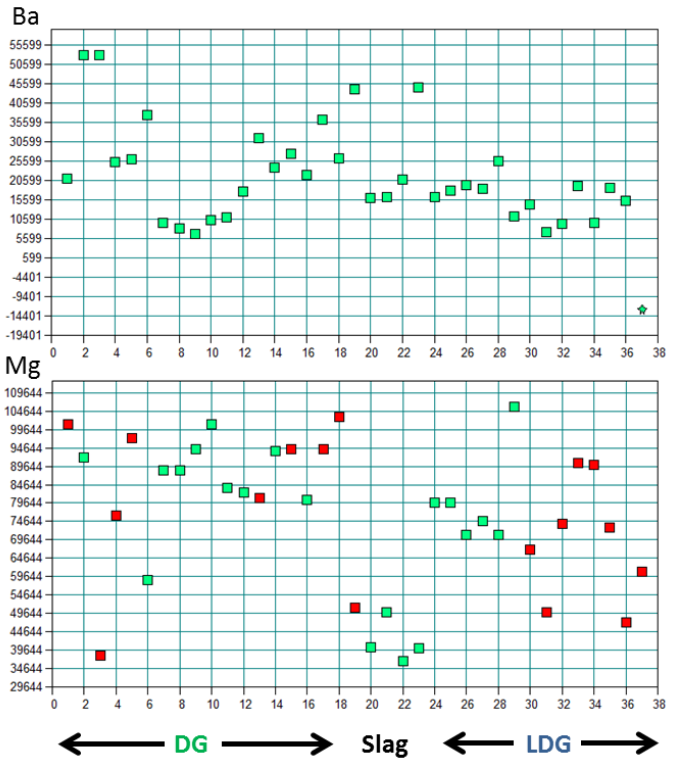

Fig. 5.14. Predicted concentration ($mg \cdot Kg^{-1}$) of Ba and Mg by the selected PLS models versus the number of measured samples (1-18: Darwin glass, 19-23: slag and 24-37: Libyan desert glass). Red squar: high value of MD; green squar: low value of MD; green star: possible outlier.

The predicted concentration values of Al, Ba, Ca, Fe, Mg and Na by each selected PLS models for the steel slag samples were in concordance with the composition tendency found with strong acid extraction and measured by ICP-MS in this PhD work (see next Chapter 6, nitric/hydrochloric acid extraction). The concentration values were between 18-21% for Al, 1.7-2% for Ba, 34-38% for Ca, 18-20% for Fe, 7-8% for Mg, 0.7-1% for Na and 13-15% for Si. On the other hand, the range of predicted concentrations of the impact glass samples was in accordance with the results of other authors in the bibliography[45-48]. In the LDG, the concentration values were

[45] A. Longinelli, G. Sighinolfi, V. de Michele, E. Selmo, d18O and chemical composition of Libyan Desert Glass, country rocks, and sands: New considerations on target material, Meteoritics and Planetary Science 46 (2011) 218–227.
[46] A. Greshake, C. Koeberl, J. Fritz, W. Reimold, Brownish inclusions and dark streaks in Libyan Desert Glass: evidence for high-temperature melting of the target rock. Meteoritics and Planetary Science 45 (2010) 973-989.
[47] G. Volksch, K. Heide, Structure and crystallization in natural glasses. Proceedings of International Congress on Glass, 18th, San Francisco, United States, 1998, 2124-2128.
[48] K.T. Howard,. Geochemistry of Darwin glass and target rocks from Darwin crater, Tasmania, Australia. Meteoritics and Planetary Science 43 (2008) 479-496.

between 81-85% for Si, 15-18% for Al, 0.3-1.4% for Ba, 0-2% for Ca, 0-5% for Fe, 1.8-2% for Mg and 0-0.7% for Na. In the case of DG, the concentration values varied around 80-85% for Si, 10-12% for Al, 1-4% for Ba, 0-5% for Ca, 0-8% for Fe, 0.8-8% for Mg and 0.3-2.4 for Na.

In order to evaluate the sensibility of the proposed PLS/LIBS models, the detection limit values[49] for the seven studied elements were established from the measurements of the Teflon and those from the 3 ethylcellulose pellets. The obtained LOD varied from 0.5% for Ba to 4.4 % for Mg, in all cases the LOD found were appropriate.

2. DISCUSSION

Traditional problems in PLS models for analytical techniques, such as spectroscopic noise, spectral distortion, baselines and complex backgrounds in the spectra were not found of relevant importance in our case, despite the portability of our LIBS equipment. The spectra were considered adequate. The calibration method (univariate or multivariate) depends on the degree of the uninformative variance in the spectra.

The experimental results obtained in this study showed that the univariate calibration approach traditionally used in LIBS did not provide satisfactory results for quantitative analysis of our samples; theirs calibration curves displayed no sufficiently linear trends.

A much more robust calibration approach was obtained by considering a multivariate model. The selected PLS models of the seven elements showed linearity in the calibration and validation curve with the selected dataset. The capability of this approach was checked using reference material slag pellets with excellent results in the case of Fe, Mg and Si.

[49] F. Allegrini, A. C. Olivieri , IUPAC-Consistent Approach to the Limit of Detection in Partial Least-Squares Calibration, Analytical Chemistry 86 (2014) 7858–7866.

The concentration values attained through PLS models to the steel slag samples was in accordance with the tendency of those obtained with the nitric/hydrochloric acid extraction, and the concentration values to the impact glasses was in line with the values shown in bibliography by other authors.

CHAPTER 6

WEATHERING OF THE STUDIED MATERIALS EXPOSED TO THE TERRESTRIAL ATMOSPHERE

Minerals can be susceptible to degradation when they are exposed to a variety of chemical (such as reaction with oxygen or water) and physical (mechanical: e.g. thermal stress or cryofracturing) processes acting at Earth's surface. The term weathering refers to the effects that these processes would have on surfaces exposed to the Earth environment[1].

[1] C.J. Bennett, C.Pirim, T.M. Orlando, Space-Weathering of Solar System Bodies: A Laboratory Perspective, Chemical Reviews 113 (2013) 9086–9150.

The presence of weathering products formed from slag is an indication of the reactivity of the material and may be a means of releasing trace elements, acidity, or alkalinity into the environment[2]. These secondary phases are the weathering products of primary phases after interaction with air or water[2].

In the case of meteorite weathering, this can be regarded as the alteration of original component phases of the meteorite to phases that are more stable at Earth's surface[3]. From the moment that a meteorite enters the Earth's atmosphere it is subject to interaction with the terrestrial environment[4]. It is important to ascertain whether their properties reflect processes that occurred prior to their fall on Earth or whether some of their characteristics have been modified by their extensive residence on our planet[5]. Prolonged weathering transforms many of its minerals, masks its original textures, redistributes elements, and eventually leads to its destruction[3]. Therefore, knowing the meteorites original composition can provide us evidences of the processes occurring during the formation and evolution of the Solar System[3]. Also, the processes of terrestrial weathering leave a "fingerprint" in meteorites that may be interesting to understanding those terrestrial weathering processes (rates of alteration, climatic influences on the type of weathering products formed, the temperatures at which they formed) and stability of surfaces[3].

As it happens in the meteorites, impact glasses are strongly and commonly affected by weathering processes in the moment that are in contact with the terrestrial atmosphere, due to the instability of glasses[6,7]. However, the study about their weathering has been practically overlooked.

We considered that the weathering processes of the meteorites could be extended to the impact glasses, in this case Libyan Desert Glasses (LDG) and Darwin Glasses

[2] N.M. Piatak, M.B. Parsons, R.R. Seal II, Characteristics and environmental aspects of slag: A review, Applied Geochemistry 57 (2015) 236-266.
[3] P. A. Bland, M. E. Zolensky, G. K. Benedix, M. A. Sephton, Weathering of Chondritic Meteorites, Meteorites and the early solar system II (2006) 853-867.
[4] P. A. Bland, A. W. R. Bevan, A. J. Tim Jull, Ancient Meteorite Finds and the Earth's Surface Environment, Quaternary Research 53 (2000) 131–142.
[5] G. Crozaz, M. Wadhwa, The terrestrial alteration of Saharan Shergottites Dar al Gani 476 and 489: A case study of weathering in a hot desert environment, Geochimica et Cosmochimica Acta 65 (2001) 971–978.
[6] C. Hamann, L. Hecht, M. Ebert, R.Wirth, Chemical projectile–target interaction and liquid immiscibility in impact glass from the Wabar craters, Saudi Arabia, Geochimica et Cosmochimica Acta 121 (2013) 291–310.
[7] S. Thackrey, G. Walkden, A. Indares, M. Horstwood, S. Kelley, R. Parrish, The use of heavy mineral correlation for determining the source of impact ejecta: A Manicouagan distal ejecta case study, Earth and Planetary Science Letters 285 (2009) 163–172.

(DG), since both materials have the same factors that explain the weathering in meteorites, such as the ample time since they landed, giving enough time for weathering in an oxidative environment, and the extreme shocking by the impact which make them peculiarly susceptible to weathering[8]. In addition, the weathering process depends on a similar group of factors that control the alteration of terrestrial rocks[9]. In the case of the rock interior, the micro environmental conditions that regulate the rates of chemical reactions are normally influenced by climate and include factors such as the pH and O_2 of pore and groundwater, temperature, drainage, microbial activity, the composition and crystal structure of the silicate or alloy, the nature of secondary oxidation products, the degree of porosity or fracturing, and the exposure time of the sample[8].

Nevertheless, how to distinguish a pre-terrestrial mineral from another mineral phase of terrestrial origin? When the meteorite is entering to the terrestrial atmosphere, the outer surface is heated, and some materials are vaporized[10]. Earth atmospheric entry is so rapid that all evidence of heating in the meteorite disappears within a few hundred micrometers, at the very most, beneath the surface. In meteorite interiors pre-terrestrial minerals are not modified by the brief and surface localized heating episode during atmospheric entry. On the contrary, if a secondary phase is superposed upon or crosscut fractures in the fusion crust, they are clearly terrestrial in origin[11]. In the case of impact glasses, to differentiate between terrestrial and pre-terrestrial origin of a mineral is more complicated, since it is a product formed in the Earth as well.

It is possible to study different weathering processes of meteorites due to their fall in different zones of the Earth, and therefore, in diverse environments, with different climate, range of exposure durations and histories[12]. The same study could be

[8] J.S. White, E.P. Henderson, B. Mason, Secondary minerals produced by weathering of the wolf creek meteorite, The American mineralogist 52 (1967) 1190-1197.
[9] P. A. Bland, M. E. Zolensky, G. K. Benedix, M. A. Sephton, Weathering of Chondritic Meteorites, Meteorites and the early solar system II (2006) 853-867.
[10] S.J. Wentworth, E.K. Gibson, M.A. Velbel, D.S. McKay, Antarctic Dry Valleys and indigenous weathering in Mars meteorites: Implications for water and life on Mars, Icarus 174 (2005) 383–395.
[11] P. A. Bland, M. E. Zolensky, G. K. Benedix, M. A. Sephton, Weathering of Chondritic Meteorites, Meteorites and the early solar system II (2006) 853-867.
[12] P. A. Bland, A. W. R. Bevan, A. J. Tim Jull, Ancient Meteorite Finds and the Earth's Surface Environment, Quaternary Research 53 (2000) 131–142.

performed with the impact glasses, found in different regions of the Earth[13]. In temperate or tropical areas, most meteorites, especially unrecovered ones, are destroyed by weathering on a short time scale compared to the rate of falling[14]. However, in arid regions (both "hot" deserts and the "cold" desert of Antarctica) weathering is slower, they can be preserved for thousands, tens of thousands, or, in Antarctica, millions of years after their fall[14,15]. Therefore, the conservation of meteorites depends mainly on climate[14]. In Antarctica, meteorites endure longer because the environmental conditions are relatively constant, besides they spend most of their long terrestrial time encased in ice and hence, the chemical weathering rate is lower[12,14]. Their compositions remain basically unchanged, they are largely preserved[12]. Weathering of Antarctic meteorites mainly occurs while they are exposed gradually to wind ablation on the surface of stranded ice fields[12,14]. In others arid areas such as the deserts of North Africa or Australia, where more than 3.8 million km^2 is arid or semiarid land, the weathering rate is also slow but not so low as in Antarctica[16]. This fact is owing to that in hot deserts, meteorites are exposed to an oxidizing atmosphere, diurnal temperatures that can exceed 35°C and to sporadic precipitation[16].

It should be noted that some of the Earth's deserts have been considered as analogs to Mars, such as the Atacama Desert[17,18]. Thus, weathering processes could be compared with conditions similar to Mars.

[13] A. Gucsik, C.Koeberl, F. Brandstätter, E. Libowitzky, M. Zhang, Infrared, Raman, and cathodoluminescence studies of impact glasses, Meteoritics & Planetary Science 39 (2004) 1273–1285.
[14] S.J. Wentworth, E.K. Gibson, M.A. Velbel, D.S. McKay, Antarctic Dry Valleys and indigenous weathering in Mars meteorites: Implications for water and life on Mars, Icarus 174 (2005) 383–395.
[15] G. Crozaz, M. Wadhwa, The terrestrial alteration of Saharan Shergottites Dar al Gani 476 and 489: A case study of weathering in a hot desert environment, Geochimica et Cosmochimica Acta 65 (2001) 971–978.
[16] P. A. Bland, A. W. R. Bevan, A. J. Tim Jull, Ancient Meteorite Finds and the Earth's Surface Environment, Quaternary Research 53 (2000) 131–142.
[17] R. Navarro-González, F. A. Rainey, P. Molina, D. R. Bagaley, B. J. Hollen, J. de la Rosa, A. M. Small, R. C. Quinn, F. J. Grunthaner, L. Cáceres, B. Gomez-Silva, C. P. McKay, Mars-Like Soils in the Atacama Desert, Chile, and the Dry Limit of Microbial Life, Science 302 (2003) 1018- 1021.
[18] M. L. Smith, M. W. Claire, D. C. Catling, K. J. Zahnle, The formation of sulfate, nitrate and perchlorate salts in the martian atmosphere, Icarus 231 (2014) 51–64.

Many meteorites were discovered in the deserts of North Africa and also in Australia[19-22], and their possible weathering processes should be similar to those suffered by LDG and DG respectively. Thus, the study of the weathering processes on these impact glasses could be considered as model methodologies to study in the future the weathering of meteorites.

Chapter 4 has presented the characterization of the inner and outer composition of the materials (steel slag, LDG and DG). In this chapter it is intended to determine those compounds probably formed by weathering processes. To help in the development of a methodology to ascertain the differentiation between original and weathered compounds, steel slag will be used as model materials. Various leaching tests will be tested over the steel slag collected from the factories, construction works and forest tracks.

Steel slag are materials formed at high temperatures that are in contact with the terrestrial environment, like the impact glasses, so it was thought that the same developed methodology could be used to clarify the weathering of materials formed from an extraterrestrial impact, like the LDG and DG ones. Moreover, we expected to obtain different alteration products as the studied materials were deposited in a Athlantic Climate (steel slag in Gipuzkoa, Europe), in a Desertic Climate (LDG in Libyan Desert, North-Africa) and in a Tropical Climate (DG in Tasmania, Australia).

The discussions of weathering products formed on the whole set of materials will be principally based on spectroscopic speciation (mineral phases identified through Raman micro spectroscopy results), and also on leached ions and compounds whose formation can be explained by thermodynamic speciation through chemical modeling simulations.

[19] S.J. Wentworth, E.K. Gibson, M.A. Velbel, D.S. McKay, Antarctic Dry Valleys and indigenous weathering in Mars meteorites: Implications for water and life on Mars, Icarus 174 (2005) 383–395.
[20] F. Wlotzka, Meteoritical Bulletin No. 68.(1989) Meteoritics 24, 57.
[21] A.J.T. Jull, F. Wlotzka, H. Palme, D.J. Donahue, Distribution of terrestrial age and petrologic type of meteorites from western Libya. Geochimica et Cosmochimica Acta 54 (1990) 2895–2898.
[22] P. A. Bland, M. E. Zolensky, G. K. Benedix, M. A. Sephton, Weathering of Chondritic Meteorites, Meteorites and the early solar system II (2006) 853-867.

A. ELECTRIC ARC FURNACE (EAF) STEEL SLAG

As it has been described in the Chapter 1, slag is a by-product which is used in numerous applications. However, slag use is partially restricted due to the fact that in the slag composition could be present potential toxic elements at a relative concentration, or the alteration thereof by external factors, such as water, acidic conditions, etc.

Carbonation is one of the most studied weathering process of steel slag[23-27], which happens when the slag is left outdoors because their oxides hydrate and their respective hydroxides react with the atmospheric CO_2[28] (as it can be seen in the Chapter 4: Part C). Many authors have studied its leaching behavior[29-31], proposing different accelerated leaching tests to simulate natural weathering of the slag exposed to the environment. Thereby, the release of potentially harmful trace

[23] R. Baciocchi, G. Costa, A. Polettini, R. Pomi, Effects of thin-film accelerated carbonation on steel slag leaching , Journal of Hazardous Materials 286 (2015) 369-378.
[24] N.T. Prasad, S. Sadhu, K.N.V.V. Murthy, S.R. Pilli, S. Ramesh, S.V.S.P. Kumar, G. Dharani, M.A. Atmanand, M.B.V. Rao, T.K. Dey, A. Syamsundar, Carbon-dioxide fixation by artificial reef development in marine environment using carbonated slag material from steel plant (2014) OCEANS'14 MTS/IEEE Conference, nº 6964442.
[25] H.P. Mattila, R. Zevenhoven, Chapter Ten - Production of Precipitated Calcium Carbonate from Steel Converter Slag and Other Calcium-Containing Industrial Wastes and Residues, Advances in Inorganic Chemistry 66 (2014) 347-384.
[26] D. Zingaretti, G. Costa, R. Baciocchi, Assessment of the energy requirements for CO2 storage by carbonation of industrial residues. Part 1: Definition of the process layout, Energy Procedia 37 (2013) 5850-5857.
[27] A. van Zomeren, S.R. van der Laan, H.B.A. Kobesen, W.J.J. Huijgen, R.N.J. Comans, Changes in mineralogical and leaching properties of converter steel slag resulting from accelerated carbonation at low CO 2 pressure, Waste Management 31 (2011) 2236-2244.
[28] M. Kianpour, M. Amin Sobati, S. Shahhosseini, Experimental and modeling of CO_2 capture by dry sodium hydroxide carbonation, Chem. Eng. Res. Des. 90 (2012) 2041–2050.
[29] M. Mäkelä, E. Heikinheimo, I. Välimäki, O. Dahl, Characterization of industrial secondary desulphurization slag by chemical fractionation with supportive X-ray diffraction and scanning electron microscopy, International Journal of Mineral Processing 134 (2015) 29-35.
[30] F. Engström, M.L. Larsson, C. Samuelsson, A. Sandström, R. Robinson, B. Björkman, Leaching behavior of aged steel slags Steel Research International 85 (2014) 607-615.
[31] N.M. Piatak, M.B. Parsons, R.R. Seal II, Characteristics and environmental aspects of slag: A review, Applied Geochemistry 57 (2015) 236-266.

elements from slag must be characterized and evaluated[32]. These tests are often considered to represent 'worst-case' leaching scenarios because of the crushing of the material and constant agitation throughout the test[32]. Single batch extraction tests are the most frequent type of leaching tests used on slag, in comparison with sequential chemical extraction tests, which are reported less commonly[32].

In order to go further away in the elemental quantification of EAF steel slag and its behaviour in the face of weathering some weeks after its generation, this part A of the chapter was performed to develop an innovative methodology. This consists mainly of fast lixiviation tests with different extractants (sequential extraction) over the slag samples, statistic analysis and thermodynamic speciation.

Lixiviation tests over the slag samples, characterized in Chapter 4, were carried out with Milli-Q water and acetic acid as extractants, in order to reproduce environmental conditions such as rain water and extreme situations respectively, which could suffer the reused slag along the time if it is left outdoors. Moreover, nitric/hydrochloric acid dissolution was employed to know the semi-total concentration of the elements present in the slag, i.e., the maximum extractable amount of the elements. The leachates were measured by means of Inductively Coupled Plasma-Mass Spectrometry (ICP-MS) and Ionic Chromatography (IC) techniques. Statistic analyses were then performed on the obtained results from the most adequate extraction protocol.

Finally the results of the most adequate extraction procedure will be used to carry out the chemical simulations to obtain a set of weathering reactions (thermodynamic speciation) that explains the formation of the weathered compounds detected through the spectroscopic analysis shown in part C of Chapter 4.

[32] N.M. Piatak, M.B. Parsons, R.R. Seal II, Characteristics and environmental aspects of slag: A review, Applied Geochemistry 57 (2015) 236-266.

1. SPECTROSCOPIC TECHNIQUES RESULTS

The presence of some mineral compounds found in our EAF steel slag (such as lepidocrocite (γ-FeOOH), goethite (α-FeOOH), limonite ($FeO(OH)\cdot nH_2O$), ilesite ($(Mn,Zn,Fe)SO_4\cdot_4H_2O$), gypsum ($CaSO_4\cdot 2H_2O$), bassanite ($CaSO_4\cdot 1/2H_2O$), natron ($Na_2CO_3\cdot 10\ H_2O$), nitratine ($NaNO_3$), brucite ($Mg(OH)_2$), calcite ($CaCO_3$), high magnesium calcite (HMC) ($Ca(Mg)CO_3$), aragonite ($CaCO_3$) and monohidrocalcite ($CaCO_3H_2O$), mainly identified by Raman spectroscopy) and the results of X-Ray Photoelectron Spectroscopy (XPS) analysis (Chapter 4: Part C) suggest the hydration of the original oxides and the further interaction with atmospheric acid gases (CO_2 and NO_x) as the main weathering process. The case of carbonation was the most notable weathering process, as it can be seen in Fig.6.1; where all the white zones are carbonated areas. When the slag samples were collected (2011), they were slightly carbonated, perhaps by the cooling outdoor and the irrigation with water or the atmospheric humidity. But four years later, in 2015, the carbonation is more appreciable, without many differences between the treated and the non treated steel slag.

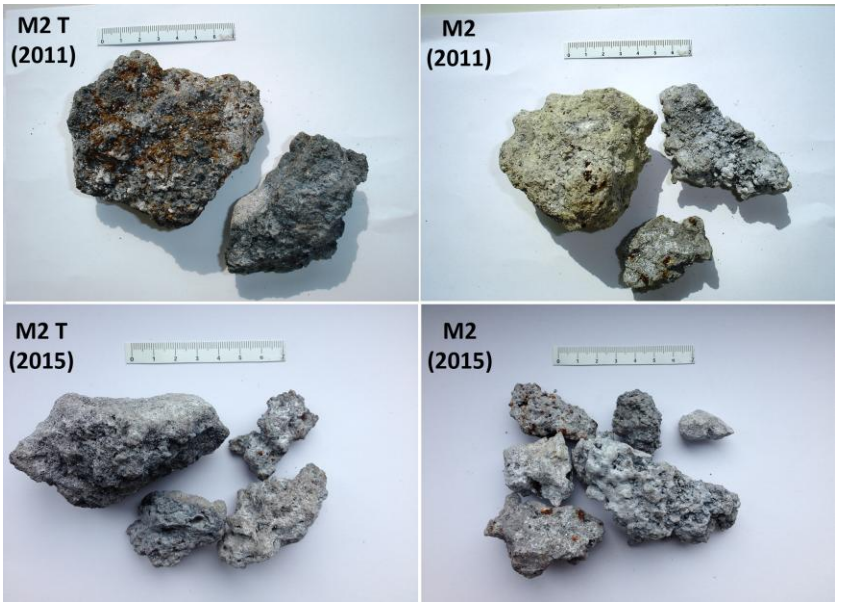

Fig. 6.1. Images of special steel slags, treated (M2 T) and without treatment (M2), collected in two different years: 2011 and 2015.

When the steel slag samples were broken, it was perceived that the slag samples appeared more carbonated outside, in the surface, but they were also being carbonated inside probably due to their porous structure[33].

The localization of the carbonation can be seen in Fig.6.2, where photographs of each slag were digitally processed by means of MATLAB software in order to provide major differences between color and image contrast of the slag samples. The software divided the slag sample surface according to colors. The calcium carbonate is the red color (confirmed by previous Raman measurements). It was noticeable that in the treated slag (see Fig. 6.2. b. and f), the carbonation was more uniform and went more inside than in the non-treated slag (see Fig. 6.2. d and. h). The most intense zones of carbonation were in the edge (a stronger red color) in all cases. On the contrary, in the case of stainless steel slag this carbonation was not observable. The surface was whitish as in the other cases, but there were only disperse grains of calcite. The other white areas promoted luminescence signals in the Raman spectra suggesting the presence of a highly vitreous matrix with small sized crystals.

Carbonation confers a high basicity to the steel slag under thermodynamically stable conditions. Besides, the carbonated product is more stable than the fresh slag, that's why the carbonation has been proposed as one of the adequate pretreatment of steel slag to decrease the risk of the metal leaching from the material[34].

[33] B. Pang, Z. Zhou, H. Xu, Utilization of carbonated and granulated steel slag aggregate in concrete, Construction and Building Materials, 84 (2015) 454-467.
[34] J. Yu, K. Wang, Study on Characteristics of Steel Slag for CO2 Capture, Energy & Fuels 25 (2011) 5483-5492.

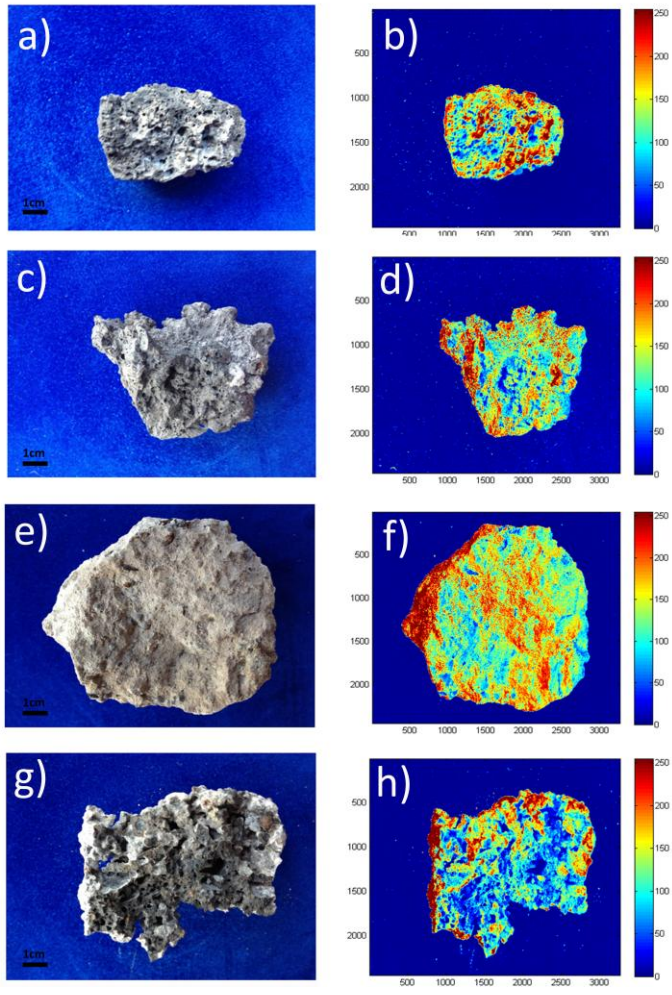

Fig. 6.2. Images of several broken slag: (a) M1 T, (c) M1, (e) M2 T and (g) M2, together with their respective processed images derived from MATLAB software. The color bar indicates the color intensities of the slag samples: from blue (darker zones) to red (lighter areas).

2. LEACHING TESTS RESULTS

The risk of hazardous contaminants released by secondary materials, like the steel slag, is usually accomplished by leaching experiments simulating different environmental conditions in the laboratory. The aim of those ageing experiments is to establish the mobility of the different elements, especially those hazardous and toxic elements. We selected three of ageing experiments (extraction with water, with acetic acid and with HCl/HNO_3 acids) to compare and propose the most

adequate methodology to simulate the weathering of steel slag materials in contact with the surrounding environment.

One of the leaching tests more commonly used to determine the release of trace elements from steel slag samples is the EN 12457-2 standard leaching test[35-38], which consists of the dissolution of a known amount of the slag with deionized water stirred by a rotary mixer during 24h (see Chapter 3)[39]. However, we adapted a previously developed extraction procedure using sonicated dissolutions of Milli-Q water with the steel slag, in order to simulate the leaching effect of water in a shorter time. To set the performance of the new procedure, the results of both methods have been compared.

In addition, given the good results in the comparison of the standard test with our focused ultrasound method, the leaching test with acetic acid was performed using sonication like in the procedure with the Milli-Q water. This extractant was selected to simulate the "worst-case" of leaching conditions for a steel slag exposed to the environment.

Finally, a mixture of nitric/hydrochloric acids was used as the extractant to be aware of whether slags with high level of metal concentrations (not metal-silicate) could have higher probability of mobilizing soluble metals from the slag towards the environment.

The concentration of the following elements: Ag, Al, As, B, Ba, Ca, Cd, Co, Cr, Cu, Fe, Hg, K, Li, Mg, Mn, Mo, Na, Ni, Pb, Se, Sb, Sn, Sr, Ti, V, W and Zn, was measured by ICP-MS. However, Ag, As and Hg were not taken into account, since their concentrations were under the detection limit (LOD) in all the cases ($LOD_{\text{Milli-Q water}}$; Ag: 11 µg/kg; As: 5.7 µg/kg; Hg: 22 µg/kg; Cd: 1 µg/kg; Co: 27 µg/kg; Se: 94 µg/kg; Mn: 227 µg/kg; Cu: 30

[35] S. Barella, A. Gruttadauria, F. Magni, C. Mapelli, D. Mombelli, Survey about Safe and Reliable Use of EAF Slag, ISIJ International 52 (2012) 2295–2302.
[36] S. Sorlini, A. Sanzeni, L. Rondi, Reuse of steel slag in bituminous paving mixtures Journal of Hazardous Materials 209-210 (2012) 84-91.
[37] F. Engström, M. L. Larsson, C. Samuelsson, Å. Sandström, R. Robinson, B. Björkman, Leaching Behavior of Aged Steel Slags, steel research int. 85 (2014) 607-615.
[38] D. Mombelli, C. Mapelli, S. Barella, A. Gruttadauria, G. Le Saout, E. Garcia-Diaz, The efficiency of quartz addition on electric arc furnace (EAF) carbon steel slag stability, Journal of Hazardous Materials 279 (2014) 586–596.
[39] EN 12457-2: Characterisation of waste –leaching – compliance test for leaching of granular waste materials and sludges – Part 2: one stage batch test at a liquid to solid ratio of 10 l/kg for materials with particle size below 4 mm (without or with size reduction), European Committee for Standarization, 2002.

µg/kg; Pb: 16 µg/kg; LOD $_{\text{Acetic acid}}$; Ag: 10 µg/kg; As: 0.30 µg/kg; Cd: 0.12 µg/kg; Co: 15 µg/kg; Hg: 25 µg/kg; Se: 150 µg/kg; LOD $_{\text{Nitric-hydrochloric acid}}$; Ag: 0.21 mg/kg; As: 0.73 mg/kg; Cd: 0.0040 mg/kg; Co: 0.47 mg/kg; Hg: 0.82 mg/kg; Se: 0.71 mg/kg).

2.1. Comparison of leaching tests

The Reference Material (RM) of steelmaking slag (NH 146, Brammer standard, Mittal Steel Oslava, Czech Republic) was used to compare the EN 12457-2 standard leaching test and our sonicated leaching text with Milli-Q water. Following the conditions of each test, the comparison was based on the same volumen of Milli-Q water (20ml) and particular size (<2mm) in both cases, but it was used 2 g of the RM slag in the European standard test and 0.5 g in our. The concentrations of Ca, Al, Fe, Mg, Cr, Mn and Ti, the main elements certified in the RM, were measured. Ti was under the detection limit in both cases (LOD_{Ti}: 19 µg/kg). The rest of the element concentrations were higher in our test than in the European standard test (see Table 6.1). So, even with lower quantity of sample in the same volume, the European standard test gave worse leaching results. This could be expected since Focused Ultrasound energy (FUS) is more effective in the extraction than merely rotary agitation.

Table 6.1. Concentrations (mg/kg) of extractable Ca, Al, Fe, Mg, Cr, Mn and Ti measured by the EN 12457-2 standard test, by our leaching test with Milli-Q water and the certified total concentrations in the slag RM.

	EN 12457-2	Our test	RM values
Ca	2140 ± 200	8200 ± 1200	289931 ± 429
Al	129 ± 18	1780 ± 360	22711 ± 476
Fe	156 ± 9	179 ± 10	203000 ± 3000
Mg	0.171 ± 0.023	1.41 ± 0.55	32991 ± 422
Cr	0.112 ± 0.016	0.103 ± 0.022	4722 ± 616
Mn	0.0478 ± 0.0084	0.232 ± 0.048	42756 ± 155
Ti	<LOD	<LOD	2338 ± 540

Therefore, given that our method required less operation time (6 min per sample versus 24h of the European standard), and consequently, less energy consumption, and also provided better leaching results; it was decided that the following leaching tests will be conducted irrespective of the nature of the extractant: to take 0.5 g of

the material (slag), add 20 mL of the extractant, insert the probe of the Ultrasound Focused device and work for 6 min.; then filtrate the extracted solution and measure the elements by ICP-MS.

2.2 Milli-Q water as extractant

As it has been mentioned previously, with this Milli-Q water leaching test we tried to simulate the effect of rain water and thus, to observe the soluble salts in the steel slag. Eight slag samples were tested and the results are plotted in Fig.6.3-6.5 for both dissolved anions and cations.

In the case of stainless steel slag (M6), it had the highest concentration of fluorides, sulphates and nitrates (see Fig. 6.3.a). By contrast, chlorides mainly appeared in the treated slag from common steel factory (M1T), which could be due to the larger proximity to the sea of that industry. The concentration of sulphate has to be taken into account if the steel slag is going to be used as filler, given that the soil is not able to filter them. So, this anion would pass directly to the groundwater[40].

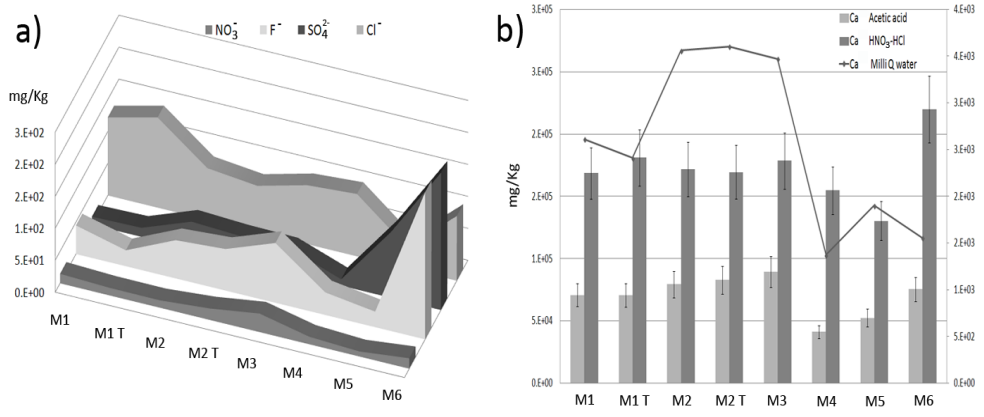

Fig.6.3. Ionic Chromatography results: a) average concentrations (mg/kg) of NO_3^-, F^-, SO_4^{2-} and Cl^- with Milli-Q water; and b) average calcium concentrations (mg/kg) found in slag with Milli-Q water (also with acetic acid and nitric-hydrochloric acid).

Calcium presented the highest concentration in the samples from special steel (M2 and M2T) (see Fig.6.3.b). This could due to the use of caustic lime (CaO) to a greater

[40] IHOBE, S. A. Libro Blanco para la minimización de residuos y emisiones, Servicio Central de Publicaciones del Gobierno Vasco, Vitoria-Gasteiz, Spain, 1999.

extent during the formation of the slag in the production of the special steel[39]. All samples were in the same range of Al concentration, except M4, M5 and M6 which had less concentration (see Fig. 6.4). Moreover, it should be noted that Al, B, Fe, Cu, K, Li, Mg, Mo, Na, Ni, Pb, Sb, V and Zn are toxic in high concentrations in soil and water[41-44].

With respect to Ba and Mg, the highest concentration values were in the unknown slag collected in Leioa (M4) (Fig. 6.4). The ingestion of Ba in soluble forms is highly toxic to animals, human beings and plants, and it was included in a list of elements that pose a risk to human health[45]. The slag from the stainless steel factory (M6) possessed the highest concentration of Fe and Na (Fig. 6.4).

[41] E. Álvarez, M. L. Fernández-Marcos, C. Monterroso, M. J. Fernández-Sanjurjo, Application of aluminium toxicity indices to soils under various forest species, Forest Ecology and Management 211 (2005) 227–239.
[42] E. Gusmão Pereira , M. A. Oliva , L. Rosado-Souza , G. Camargo Mendes ,D. Santos Colares, C. H. Stopato, A. Miyasaka Almeida, Iron excess affects rice photosynthesis through stomatal and non-stomatal limitations, Plant Science 201–202 (2013) 81– 92.
[43] M. Arienzo, E.W. Christen, N.S. Jayawardane, W.C. Quayle, The relative effects of sodium and potassium on soil hydraulic conductivity and implications for winery wastewater management, Geoderma 173-174 (2012) 303–310.
[44] F. Vyshpolsky, K. Mukhamedjanov, U. Bekbaev, S. Ibatullin , T. Yuldashev, A.D. Noble, A. Mirzabaev, A. Aw-Hassan, M. Qadir, Optimizing the rate and timing of phosphogypsum application to magnesium-affected soils for crop yield and water productivity enhancement, Agricultural Water Management 97 (2010) 1277–1286.
[45] T. A. Rodrigues Nogueira, W. J. deMelo, I. Machado Fonseca, M. Omir, Z. He, Barium uptake by maize plants as affected by sewage sludge in a long-term field study, Journal of Hazardous Materials 181 (2010) 1148–1157.

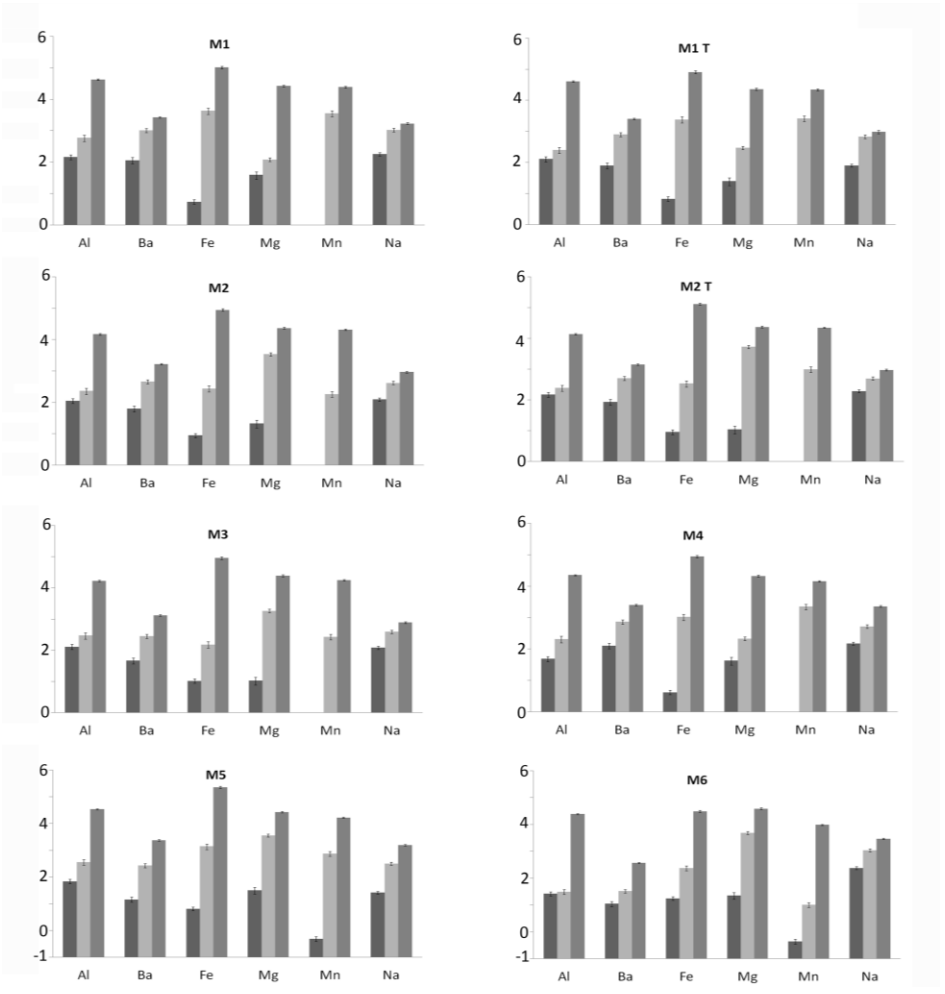

Fig. 6.4. Concentrations (log (mg/kg)) of the major elements (Al, Ba, Fe, Mg, Mn and Na) obtained with all the extractants: Milli-Q water (black colour), also, acetic acid (grey colour) and nitric-hydrochloric acid (dark grey colour), in the analyzed slag samples (M1, M1 T, M2, M2 T, M3, M4, M5 and M6). The short lines in each bar represent the standard deviation.

The highest concentrations of the rest of the measured elements appeared overall in stainless steel samples (B, Cr, K, Li, Ni, Pb and Ti) (see Fig. 6.5). Pb was under the detection limit in all the leachates except for one of the slag from a common steel factory (M5) and stainless steel slag (M6) (LOD_{Pb}: 17 µg/kg). On the other hand, without observing M6, the highest value of chromium was in the treated samples from special steel factory (M2T) (Fig. 6.5). If the chromium is in the hexavalent form, it would be directly correlated to carcinogenicity in humans and to toxicity of aquatic

organisms[46,47]. Also, Mo had the highest concentration value in M2, and Cu, Sr and V in M2T sample. It should be pointed out that strontium ion is slightly toxic[48]. In the case of Cu, M2T had the only value above the detection limit (LOD_{Cu}: 30 µg/kg); in M5 (common steel factory) and M6 (stainless steel factory) was not detected. Sb had the highest value in M1T (treated slag from common steel factory), W in M1 (slag without treatment from common steel factory) (Fig. 6.5) and Sn and Zn in M4 (unknown slag from Leioa) (Fig. 6.5). Zn was not detected in M5 (common steel factory) and M6 (stainless steel factory). Regarding tungsten, it is worth mentioning that the dissolution of metallic tungsten alloy particles can cause various environmental effects, such as soil acidification and toxic effects to plants, soil microorganisms and invertebrates[49]. On the other hand, the toxicity of metallic tin and inorganic tin compounds is low. However, organotin compounds are of high toxicological relevance[50].

[46] B. Dhal, H.N. Thatoi, N.N. Das, B.D. Pandey, Chemical and microbial remediation of hexavalent chromium from contaminated soil and mining/metallurgical solid waste: A review, Journal of Hazardous Materials 250– 251 (2013) 272– 291.
[47] J. Yaoa, L. Tiana, Y. Wanga, A. Djaha, F. Wanga, H. Chena, C. Sua, R. Zhuanga, Y. Zhoua, M.M.F. Choib, E. Bramantic, Microcalorimetric study the toxic effect of hexavalent chromium on microbial activity of Wuhan brown sandy soil: An in vitro approach, Ecotoxicology and Environmental Safety 69 (2008) 289–295.
[48] S. Chegrouche, A. Mellah, M. Barkat, Removal of strontium from aqueous solutions by adsorption onto activated carbon: kinetic and thermodynamic studies, Desalination 235 (2009) 306–318.
[49] N. Strigul, C. Galdun, L. Vaccari, T. Ryan, W. Braida, C. Christodoulatos, Influence of speciation on tungsten toxicity, Desalination 248 (2009) 869–879.
[50] H. Rüdel, Case study: bioavailability of tin and tin compounds, Ecotoxicology and Environmental Safety 56 (2003) 180–189.

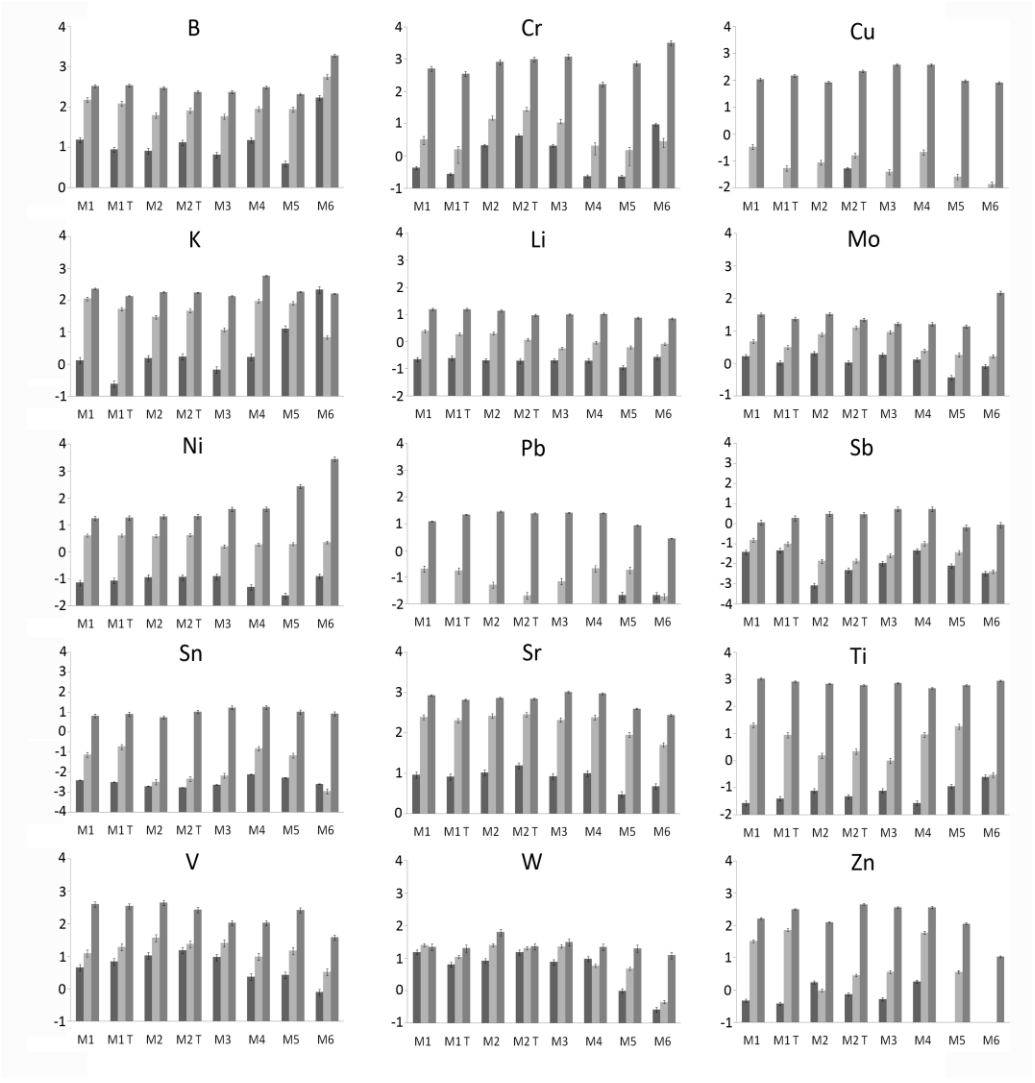

Fig. 6.5. Concentrations (log (mg/kg)) of some minor elements (B, Cr, Cu, K, Li, Mo, Ni, Pb, Sb, Sn, Sr, Ti, V, W and Zn) lixiviated with Milli-Q water (black colour), acetic acid (grey colour) and nitric-hydrochloric (dark grey colour) in the analyzed slag samples (M1, M1 T, M2, M2 T, M3, M4, M5 and M6). The short lines in each bar represent the standard deviation.

In view of these results about the soluble ions present in the slag materials, it seems that rain water is enough to mobilise them. Elements from special steel slag (above all, stainless steel slag) have more risk to be leached. They present the highest concentrations of the majority of the analyzed elements (F^-, NO_3^-, SO_4^{2-}, Ca^{2+}, Al, Fe, Na, B, Cr, K, Li, Ni, Pb, Ti, Cr, Cu, Sr and V) with Milli-Q water. Thus, if these black steel slags were to be used for instance as filler in soils or forest tracks, with time most of their elements would be available to the environment.

2.3 Acetic acid as extractant

Apart from reproducing extreme conditions, this leaching test allowed us to know the soluble salts plus the concentration of the elements bounded to the carbonates. With respect to the major elements using acetic acid, Ca had the highest value in M3 (unknown slag from Getxo) (Fig. 6.3.b), M1 (slag without treatment from common steel factory) had the biggest concentrations of Al, Ba, Fe and Mn (see Fig.6.4); M2T (treated slag from special steel factory) of Mg (see Fig. 6.4) and the Na continued having the highest value in the M6 (stainless steel factory) (see Fig.6.4). Big differences were seen comparing with the Milli-Q water results. For example, the Fe with Milli-Q water appeared above all in M6 slag, but with acetic acid had one of the lowest values, so maybe the iron in M6 samples would not be in carbonate form. The same happened with the M3 sample (unknown slag collected in Getxo).

In this acetic acid extraction, the high concentration of Ca (see Fig. 6.3.b) with respect to other elements could be explained by the frequent identification of calcite, HMC, HMC with aragonite and natron by Raman spectroscopy (see Chapter 4: Part C). Apart from this calcium with carbonates, calcium was identified in sulphates (gypsum ($CaSO_4 \cdot 2H_2O$), bassanite ($CaSO_4 \cdot 1/2H_2O$)) and silicates (larnite (β-Ca_2SiO_4), walstromite ($BaCa_2Si_3O_9$) (see Chapter 4: Part C).

The rest of the elements (Cu, K, Li, Sb, Ti and W) (see Fig.6.5) were mainly present in the M1 (slag without treatment from common steel factory) with acetic acid. The treated slag had the highest concentration values of Sn and Zn (Fig. 6.5). Zn was not detected in M6 (stainless steel factory). The B had again the highest value in the M6 slag, Pb in M4 (unknown slag collected in Leioa), V in M2 (slag without treatment from special steel factory) and the M2T (treated slag from special steel factory) had the highest concentrations of Cr, Mo, Ni and Sr (Fig. 6.5). Here, the Cr concentration in stainless steel slag was lower, but it could be due to the fact that the chromium would not be present as carbonate.

In these more extreme environmental conditions, M1 (slag without treatment from common steel factory) had more elements available (Fig. 6.5), but the slag from special steel (M2 and M2T) had the more harmful ones (Cr, Mo, Ni and V) (Fig. 6.5).

2.4 Nitric-hydrochloric acid as extractant

Regarding the nitric/hydrochloric solutions, these gave us the semi-total concentration (all except element bounded to silicates) of elements dissolved in them. M1 (slag without treatment from common steel factory) had the highest concentrations of almost all major elements: Al, Ba and Mn (see Fig. 6.3), together with M6 (stainless steel factory) which had the biggest value of Mg, Na and Ca (Fig. 6.3.b and 6.4). The iron had its highest value in M5 (common steel factory) (Fig. 6.4).

The rest of the elements, such as B, Cr, Mo and Ni (characteristic elements of special steel[51]) mainly appeared in M6 (Fig. 6.5). In this sample, it was found the highest concentrations of Cr and Ni in Milli-Q water and nitric/hydrochloric solutions. So, it means that M6 was the sample with the highest leaching of Cr and Ni and the highest presence of these elements.

M1 had the highest Li and Ti concentrations. The highest values of W, Pb and V were in M2 (slag without treatment from special steel factory) (Fig. 6.5). The highest value of Zn was in the M2T (treated slag from special steel factory) (Fig. 6.5). Cu and Sn specially appeared in the M4 (unknown slag from Leioa). K had the highest concentration in M4 slag. And the maximum values of Sb and Sr were in M3 (unknown slag from Getxo).

As it could be observed, characteristic elements related to special steel were present above in the special steel slag, including stainless steel slag (M2, M2T and M6). So, the differences between the slag compositions might be due to the manufacture of common, special or stainless steel, and to the productive process of each slag, according to each steelwork. In general, when looking at the same type of slag samples, they present a similar composition. The differences stem from the concentrations of the elements in them, which depend on the steel process (raw material, added compounds…).

[51] IHOBE, S. A. Libro Blanco para la minimización de residuos y emisiones, Servicio Central de Publicaciones del Gobierno Vasco, Vitoria-Gasteiz, Spain, 1999.

Apart from this, the last treatment realized to the slag when is stored, could have influenced on the slag composition as well. For example, in the M1T (treated slag from common steel factory), in which it has been carried out a magnetic separation of ironed materials, there was less iron concentration than in non treated slag (M1).

3. STATISTICAL ANALYSIS

3. 1 Correlation Analysis (CA)

Subsequently, with the whole concentration data set obtained from Milli-Q leaching test, correlation analysis was performed in order to know what elements were grouped for a common origin. For that purpose, a data matrix was prepared using the concentrations data of the measured elements (Al, B, Ba, Ca, Cr, Cu, Fe, K, Li, Mg, Mn, Mo, Na, Ni, Pb, Sb, Sn, Sr, Ti, V, W, Zn, F^-, Cl^-, NO_3^- and SO_4^{2-}) obtained in all slag samples (M1, M1T, M2, M2T, M3, M4, M5 and M6) for Milli-Q water extractant to know if those elements from the same source can be mobilized towards the environment simply with water, the most probable situation that can be given.

Observing the positive correlations between elements ($r > 0.82$ at a 95% confidence level) (see Table 6.2), it was noticed the high correlation value between Cr and Fe (0.94), which could be indicating the existence of chromite ($FeCr_2O_4$), compound identified in these samples in the previous Chapter 4: Part C. Chromite is a mineral with low solubility but there is an exception when manganese oxides are available, since they are the only known naturally occurring oxidants for chromite[52]. This could happen in these samples, where the manganese is one of their major elements (see Fig. 6.5). Sulphates also had a significant correlation with Fe and Mn (0.84 and 0.92 respectively), which would show the solubility of ilesite ((Mn^{2+}, Zn, Fe^{2+}) $SO_4.4H_2O$), also previously detected by Raman spectroscopy, in spite of Zn is negatively correlated with sulphates (-0.73). Moreover, it should be noted that Na exhibited a high correlation with F^- (at a 90% confidence level). This relationship could show the presence of NaF, compound that is used in the steel production with the purpose of

[52] M. Ivarsson, C. Broman, N. G. Holm, Chromite oxidation by manganese oxides in subseafloor basalts and the presence of putative fossilized microorganisms, Geochem. Trans. 12 (2011) 1-10.

regulating the grade of oxidation to the combustion of C to CO[53]. On the other hand, Cr and Mg were negatively correlated. This is remarkable, since contrarily this Cr-Mg connection was positive in the correlation matrix of acetic acid and nitric-hydrochloric solution. And moreover, magnesiochromite ($MgCr_2O_4$) was identified by Raman spectroscopy and through SEM-EDS (Scanning Electron Microscope coupled to Energy-Dispersive X-Ray) in some of these samples. So, the magnesiochromite was not soluble in Milli-Q water.

In the case of sulphates, they had a negative correlation with Ca. This might be related to gypsum ($CaSO_4.2H_2O$) or bassanite ($CaSO_4.1/2H_2O$) (identified by Raman spectroscopy), which dissolve slowly in water.

[53] J. L. Enríquez, E. Tremps, S. de Elío de Bengy, D. Fernández, Acería eléctrica. Monografías sobre Tecnología del Acero Parte I. Universidad Politécnica de Madrid, 2009.

Table 6.2. Correlation matrix obtained from Milli-Q water-soluble fraction data (rcrit = 0.82).

	Al	Ba	B	Cr	Cu	Fe	K	Li	Mg	Mn	Mo	Na	Ni	Pb	Sb	Sn	Sr	Ti	V	W	Zn	Ca	F^-	Cl^-	NO_3^-	SO_4^{2-}
Al	**1**																									
Ba	0.40	**1**																								
B	-0.63	-0.50	**1**																							
Cr	-0.40	-0.51	**0.90**	**1**																						
Cu	0.75	0.70	-0.54	-0.25	**1**																					
Fe	-0.35	-0.70	**0.85**	**0.94**	-0.4	**1**																				
K	-0.70	-0.60	**1**	**0.90**	-0.61	**0.90**	**1**																			
Li	0	0.15	0.60	0.50	0.13	0.50	0.50	**1**																		
Mg	-0.40	0.44	-0.07	-0.45	-0.31	-0.60	-0.09	-0.15	**1.00**																	
Mn	-0.80	-0.73	0.60	0.40	**-0.90**	0.41	0.64	-0.30	0.19	**1.00**																
Mo	0.50	0.43	-0.31	-0.20	0.51	-0.12	-0.36	0.30	-0.16	-0.80	**1.00**															
Na	-0.10	0.20	0.65	0.72	0.20	0.55	0.60	0.65	-0.13	-0.11	0.20	**1.00**														
Ni	0.30	-0.20	0.40	0.70	0.32	0.71	0.35	0.65	-0.80	-0.34	0.50	0.60	**1.00**													
Pb	-0.71	-0.81	0.61	0.50	**-0.90**	0.52	0.70	-0.25	0.08	**1.00**	-0.70	-0.08	-0.22	**1.00**												
Sb	0.09	0.72	-0.30	-0.60	0.20	-0.64	-0.35	0.24	0.65	-0.40	0.05	-0.13	-0.50	-0.48	**1.00**											
Sn	-0.50	0.40	-0.20	-0.50	-0.30	-0.60	-0.18	-0.40	**0.84**	0.25	-0.30	-0.30	**-0.84**	0.01	0.60	**1.00**										
Sr	0.62	0.65	-0.40	-0.06	**1**	-0.23	-0.45	0.16	-0.33	-0.80	0.50	0.40	0.40	-0.80	0.04	-0.30	**1.00**									
Ti	-0.70	-0.81	**0.90**	**0.83**	-0.74	**0.90**	**0.93**	0.23	-0.22	0.80	-0.40	0.33	0.31	**0.83**	-0.60	-0.25	-0.58	**1.00**								
V	0.80	0.18	-0.50	-0.05	0.81	-0.07	-0.50	-0.05	-0.72	-0.70	0.42	0.03	0.52	-0.60	-0.33	-0.65	0.80	-0.43	**1.00**							
W	0.73	0.81	-0.50	-0.32	**0.90**	-0.50	-0.60	0.08	0.01	-0.81	0.54	0.31	0.12	**-0.82**	0.30	-0.10	**0.85**	-0.75	0.58	**1.00**						
Zn	0.02	0.61	-0.40	-0.31	0.50	-0.41	-0.42	-0.03	0.20	-0.54	0.60	0.06	0.01	-0.60	0.17	0.26	0.55	-0.50	0.26	0.42	**1.00**					
Ca	**0.82**	0.06	-0.45	-0.07	0.70	0.04	-0.50	-0.04	-0.72	-0.64	0.60	0.00	0.57	-0.53	-0.41	-0.74	0.62	-0.35	**0.92**	0.52	0.17	**1.00**				
F^-	-0.50	-0.54	**0.94**	**0.95**	-0.41	**0.95**	**0.93**	0.55	-0.34	0.42	-0.01	0.70	0.62	0.50	-0.50	-0.40	-0.25	**0.90**	-0.25	-0.42	-0.34	-0.18	**1.00**			
Cl^-	0.23	0.50	0.14	-0.03	0.25	-0.02	0.06	**0.84**	0.15	-0.52	0.40	0.32	0.28	-0.52	0.70	-0.10	0.20	-0.21	-0.01	0.30	0.03	-0.07	0.08	**1.00**		
NO_3^-	0.34	-0.09	0.07	0.28	0.30	0.39	0.05	0.30	-0.64	-0.35	0.44	0.35	0.70	-0.30	-0.24	-0.50	0.25	0.05	0.40	0.21	-0.14	0.50	0.40	0.20	**1.00**	
SO_4^{2-}	-0.70	-0.80	**0.90**	0.81	-0.75	**0.84**	**0.92**	0.15	-0.16	**0.83**	-0.52	0.32	0.22	**0.90**	-0.60	-0.19	-0.60	**1.00**	-0.45	-0.73	-0.53	-0.40	**0.83**	-0.30	-0.03	**1.00**

3. 2 Principal Component Analysis (PCA)

The function of the Principal Component Analysis (PCA) is to decompose the original data matrix in new variables (Principal Components) that are linear combinations of the original ones. Besides, these variables are orthogonal to each other and explain the maximum sources of variance of the data[54].

Therefore, in order to observe the tendency of the whole quantitative data obtained from the analyzed steel slag samples, it was performed a PCA with the Milli-Q water dataset. The data set consisted on a matrix with the concentrations of the 26 measured elements in columns (Al, B, Ba, Ca, Cr, Cu, Fe, K, Li, Mg, Mn, Mo, Na, Ni, Pb, Sb, Sn, Sr, Ti, V, W, Zn, F^-, Cl^-, NO_3^- and SO_4^{2-}) and the 8 slag samples in rows (M1, M1 T, M2, M2 T, M3, M4, M5 and M6). The data were centered and scaled. PCA of the whole dataset was carried out using Leverage correction as validation method. As the results did not significantly change when the third PC was considered, the model with the two first principal components (46.92% and 26.49% of explained variance, respectively) with a total variance of 73.41% was finally selected.

The scores and loadings were projected bi-dimensionally defined by these two principal components, as it is shown in Fig. 6.6. In this PCA, it can be observed that the samples (objects) can be grouped according to the type of the steelwork that produce the slag (common, special and stainless steel), and four groups can be seen.

On the one hand, M1 and M1T form a group belonging to the factory that manufactures common steel. In this same group it was included the sample M4, with also negative values of PC1 and PC2. This association could be indicating that the sample M4, which comes from a civil building construction of the Campus of Bizkaia (Basque Country, Spain), is a slag from common steel production and perhaps, it could have been generated in the same industry or in other of similar characteristics of production.

[54] A. Gredilla, S. Fdez-Ortiz de Vallejuelo, J.M. Amigo, A. de Diego, J.M. Madariaga. Unsupervised pattern-recognition techniques to investigate metal pollution in estuaries, Trends Anal. Chem. 46 (2013) 59-69.

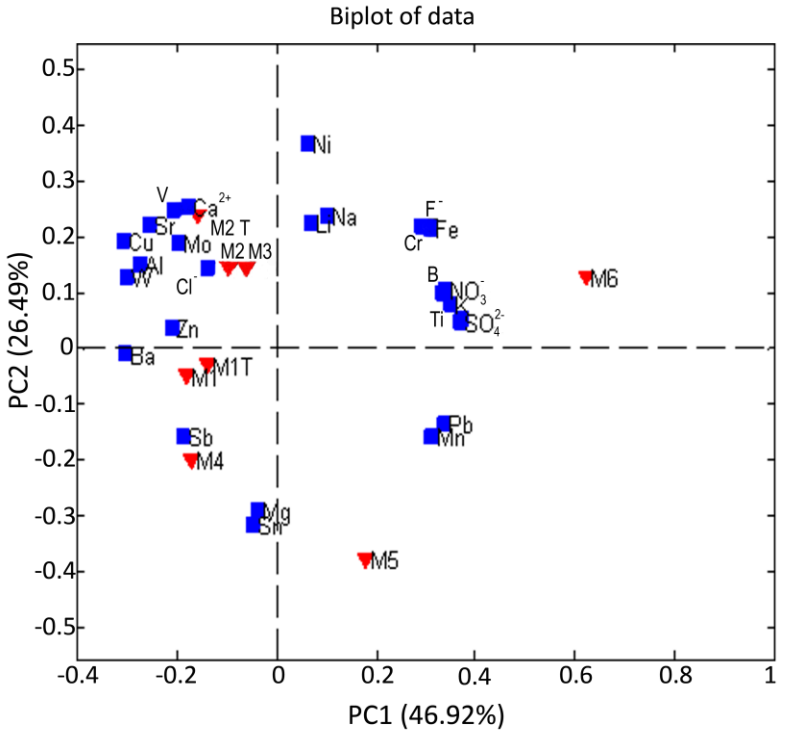

Fig. 6.6. Scores and loadings formed by PC1 and PC2. **M1**: slag without treatment from a factory manufacturing common steel, **M1T**: treated slag from the common steel industry, **M2**: slag without treatment from a factory manufacturing special steel, **M2T**: treated slag from the special steel industry, **M3**: slag from a civil building construction in Getxo, **M4**: slag from a civil building construction in the Campus of Leioa (Bizkaia), **M5**: slag from other factory manufacturing common steel, **M6**: slag from a factory manufacturing stainless steel of Belgium. The triangles represent the samples and the squares the analyzed elements.

On the other hand, with negative values of PC1 and positive of PC2, the second group is formed by the samples M2 and M2T, which belong to the factory that produces special steel. The M3 (unknown slag from Getxo) also is part of this group, so the explanation could be as in the previous group. This last sample could come from special steel or from a similar production. M6 and M5 samples with positive values of PC1 pertain to the same industry chain, but they were produced in different places and probably with different steel manufacture because M6 was produced in the stainless steel production and M5 in the common steel production. For these reasons, M5 is closer to the group of M1, M1T and M4. It should be noted that M5 sample was introduced later in the analysis to observe whether it was put into the

same group of common steel slag and if the other groups were remained with the introduction of a new sample.

PC1 is characterized by Al, Ba, Cr, Cu, Fe, Li, Mo, Na, Ni, Sr, V, W, Zn, Ca, Cl^- and NO_3^-. Whereas in the case of PC2 B, K, Mg, Mn, Pb, Sb, Sn,Ti, F^- and SO_4^{2-} play an important role.

The overlapping of the scores and loadings (Fig. 6.6) shows that the M6 sample is more influenced by SO_4^{2-}, NO_3^-, Ti, F^-, K, B, Fe, Cr, Na, Li and Ni, whereas the M5 sample by Mn and Pb. As for Cu, Cl^-, Ca, V, Mo, Sr, Al, W and Zn, they are the variables that explain most of the variance of the M2, M2T and M3 samples. The M1, M1T and M4 were characterised by Ba, Sb, Sn and Mg.

In summary, the results of the biplot PC1/PC2 indicated that in the positive values PC2 were the special steel slag (M2, M2T, M3 and M6) and in the negative ones the common steel slag (M1, M1T, M4 and M5). So, the PC2 could be connected with the type of steel produced. This model could help us to classify the origin (type of steel production) of the unknown slags that are being reused (in civil building construction, road construction, etc.) according to its respective elemental composition.

4. SIMULATION PROCESSES THROUGH CHEMICAL MODELLING

The quantification of cations and anions in the leachates obtained when Milli-Q water was used as extractant, gave always a higher amount (sum of the molar concentrations times the valence) of cations than anions. This was attributed initially to the soluble bicarbonate because this anion could not be measured by Ionic Chromatography, Therefore, its concentration was theoretically calculated by using the electroneutrality principle (sum of cations equal to sum of anions). All this chemical information was related to different experimental situations related to soluble salts, i.e., the chemical system must be compatible with the absence of precipitates. But when the pH and concentration values of all the cations and anions were introduced in the thermodynamic model, the calcium carbonate formation was

always predicted. As this does not represent the experimental observations, the initial assumption (presence of dissolved bicarbonate in the milli-Q extracts) must be rejected.

Thus, we needed to take into account the presence of another anion not measured, like the soluble silicate (SiO_4^{2-}). The existence of silicate was corroborated by the presence of some anhydrous calcium silicates, such as gehlenite ($Ca_2Al(AlSiO_7)$), merwinite ($Ca_3Mg(SiO_4)_2$), monticellite ($CaMgSiO_4$), walstromite ($BaCa_2Si_3O_9$) and larnite (β-Ca_2SiO_4), found in our steel slag samples by Raman spectroscopy and XRD analysis. Calcium silicates are reactive with water[55]. So, chemical modelling of Ca and Si were realized.

If we take into account an acid attack on calcium silicates phases, only the calcium cation is leached at the time of the SiO_2 formation (see reaction 5.1). Then the Ca can react with the bicarbonate anion obtained after the CO_2 (g) capture by the basic aqueous solution (see reaction 6.2) leading to the precipitation of calcite on the surface of the steel slag particles (see reaction 6.3)[56]:

$$CaSiO_3\,(s) + 2H^+\,(aq) \leftrightarrow Ca^{2+}\,(aq) + H_2O\,(l) + SiO_2\,(s) \qquad (6.1)$$

$$CO_2\,(g) + H_2O\,(l) \leftrightarrow H_2CO_3\,(aq) \rightarrow HCO_3^-\,(aq) + H^+\,(aq) \qquad (6.2)$$

$$Ca^{2+}\,(aq) + HCO_3^-\,(aq) \leftrightarrow CaCO_3\,(s) + H^+\,(aq) \qquad (6.3)$$

Thus, this acid attack does not promote the presence of any extra cation nor anion in the solution, other than the concentrations given by the saturation conditions of the different solid phases present in the slags. Apart from these calcium silicates, other metal silicates have been identified by means of Raman spectroscopy in these analysed steel slag materials, like tephroite (Mn_2SiO_4), which could give similar reactions to those reported in the (6.1-6.3) ones.

[55] E.Durgun, H.Manzano, R.J.M.Pellenq, J.C.Grossman, Understanding and Controlling the Reactivity of the Calcium Silicate phases from First Principles, Chem.Mater. 24 (2012) 1262 –1267.
[56] W.J.J. Huijgen, G.J. Witkampb, R.N.J. Comans, Mechanisms of aqueous wollastonite carbonation as a possible CO_2 sequestration process, Chem. Eng. Sci. 61 (2006) 4242 – 4251.

In order to understand better the mineral association and the chemical reactions given in several conditions, thermodynamic chemical modelling was carried out using the MEDUSA software with the chemical equilibrium database HYDRA. The data introduced in the models were the pH, redox potential and the concentration values (mmol/L) obtained through Milli-Q water extractions of the slag. The pH varied around 10 and 11, and the redox potential varied from 66 to 95 mV. Hence, an intermediate constant redox value (80 mV) was fixed to use it in the modelling because it did not influence in the diagrams. The temperature used was 25°C and the modelling was performed as a function of pH. Fig. 6.7 shows the variation of the molar fractions of Si and Ca species depending on the pH fluctuations.

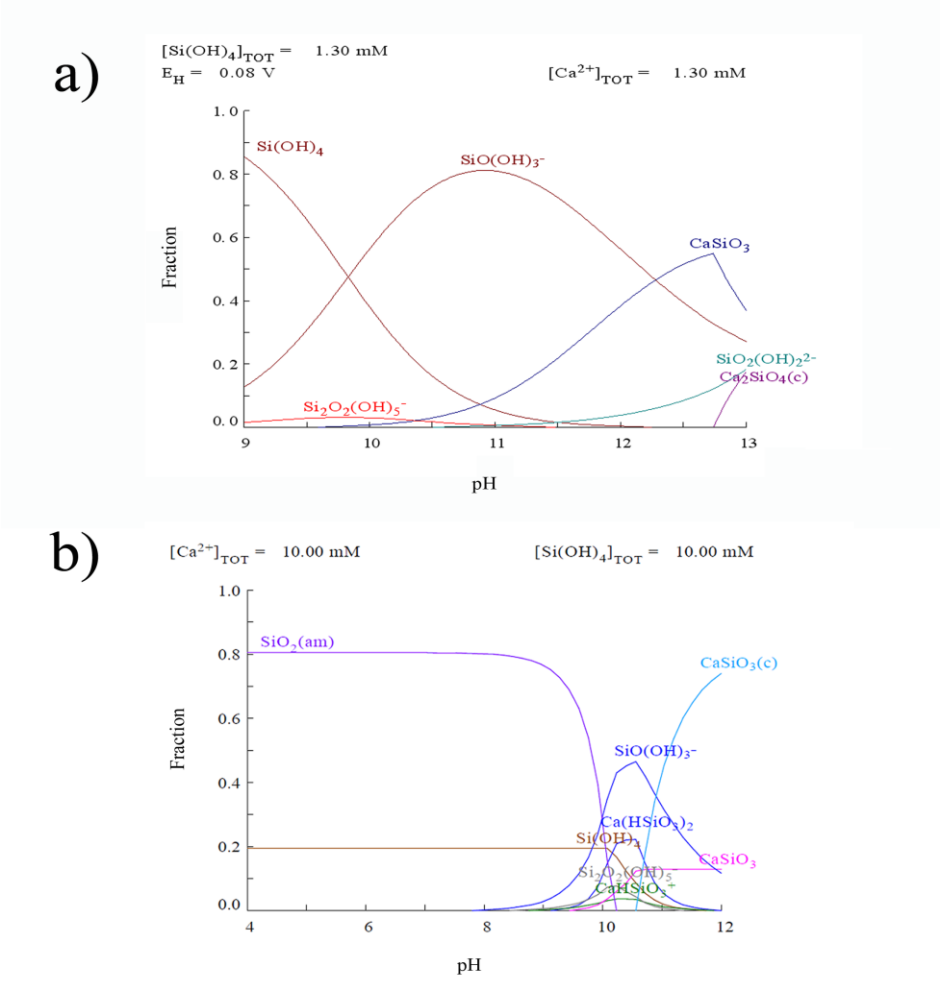

Fig. 6.7. Theoretical distribution of some species of calcium silicates when the solutions of Milli-Q water extract of the slag samples has: a) the real conditions analyzed, and b) higher values of Ca and Si.

On one hand, Fig. 6.7.a displays the profile obtained when the total concentrations of Ca and Si were the same and equal to some of the Ca values obtained from the lixiviation test with Milli-Q water (1.30 mmol/L). On the other hand, in order to observe what happened with higher Ca and Si concentrations and lower pH, it was performed a chemical modelling shown in the Fig. 6.7.b. Different chemical compounds were found in the chemical simulations. As it is said in the literature[57] , in acid to neutral solution of low concentrations, orthosilicic acid exists as the tetrahydroxy species ($Si(OH)_4$). According to the model, a decrease of pH would mean the formation of insoluble quartz (SiO_2) that is in equilibrium with two soluble species according to the following reactions:

$$Si(OH)_4\,(aq) \leftrightarrow SiO(OH)_3^- + H^+ \qquad (6.4)$$

$$SiO(OH)_3^- \leftrightarrow SiO_2(OH)_2^{2-} + H^+ \qquad (6.5)$$

The dominant species over the pH of the slag (10-11) in the experimental conditions with the mentioned concentration (1.30 mmol/L) is $SiO(OH)_3^-$ (see Fig. 6.7.a). It is the same found in the case of Fig. 6.7.b. After this point, the species that appear with Ca are $CaSiO_3$ and Ca_2SiO_4:

$$Ca^{2+} + SiO_3^{2-} \leftrightarrow CaSiO_3 \qquad (6.6)$$

These last species has been identified as compounds of steel slag, in our samples and in other works[58]. The overall weathering reaction of wollastonite ($CaSiO_3$) through solid-gas carbonation can be described in the following way[59]:

$$CaSiO_3(s) + CO_2\,(g) \rightarrow CaCO_3(s) + SiO_2(s) \qquad (6.7)$$

This last reaction (6.7) is the summation of the 6.1-6.3 reactions, can contribute to the CO_2 sequestration[59,60]; and besides, the presence carbonate formation guarantees

[57] R. Gout, G.S. Pokrovski, J. Schott, A. Zwick, Raman Spectroscopic Study of Aluminum Silicate Complexes at 20°C in Basic Solutions, Journal of Solution Chemistry 29 (2000) 1173-1186.
[58] H. Alanyali, M. Çöl, M. Yilmaz, S. Karagöz, Concrete Produced by Steel-Making Slag (Basic Oxygen Furnace) Addition in Portland Cement, International Journal of Applied Ceramic Technology 6 (2009) 736–748.
[59] W.J.J. Huijgen, G.J. Witkampb, R.N.J. Comans, Mechanisms of aqueous wollastonite carbonation as a possible CO_2 sequestration process, Chemical Engineering Science 61 (2006) 4242 – 4251.
[60] W. J.J. Huijgen, G.J. Witkamp, R.N.J. Comans, Mineral CO_2 Sequestration by Steel Slag Carbonation, Environmental Science and Technology 39 (2005) 9676 -9682.

the decrease of Cr leaching[61], element identified in our samples in risky species such as hashemite ($BaCrO_4$) and crocoites ($PbCrO_4$). Nonetheless, if the basic carbonates (like calcite) were acidified by atmospheric CO_2 or other acid, Cr (VI) specie would be released[61].

5. DISCUSSION

It was possible to know the weathering of fresh steel slag. On one hand, it was observed the weathering by hydration (lepidocrocite, goetite, limonite, ilesite, gypsum, bassanite, natron, brucite and monohidrocalcite) and interaction with atmospheric acid gases such as CO_2 and NO_x (natron, monohidrocalcite, calcite, high magnesium calcite (HMC), aragonite and nitratine). Carbonation gives basicity and stability to the slag, decreasing the metal leaching from it.

On the other hand, the leaching test with Milli-Q water performed to simulate weathering by rain water allowed us to know that the elements from special steel slag (above all, stainless steel slag) presented the highest concentrations of the majority of the analyzed elements (F^-, NO_3^-, SO_4^{2-}, Ca^{2+}, Al, Fe, Na, B, Cr, K, Li, Ni, Pb, Ti, Cr, Cu, Sr and V). The leaching test with acetic acid was the simulation of extreme acidic conditions when the slag wastes remain for many years in the environment. In this case, slag samples from common steel factory had the highest concentrations of most of the analyzed elements (Al, Ba, Cu, Fe, K, Li, Mn, Sb, Ti and W), but slags from special steel had the most harmful (Cr, Mo, Ni and V). With nitric/hydrochloric acid dissolution it could be observed that the differences between the slag compositions might be due to the manufacture of common, special or stainless steel, and to the productive process of each slag, according to each steelwork. In a same slag type, the differences stem from the concentration of the elements. Furthermore, it was remarkable that the highest concentrations of almost all the rest of the measured elements: B, Cr, K, Li, Ni, Pb, Ti and Cr, were in slag samples from stainless steel. So, care must be taken with the use of stainless steel slag, because this type had the highest concentrations and the highest leaching of elements.

[61] T. Van Gerven, E. Van Keer, S. Arickx, M. Jaspers, G. Wauters, C. Vandecasteele, Carbonation of MSWI-bottom ash to decrease heavy metal leaching, in view of recycling, Waste Management 25 (2005) 291–300.

In general, the higher concentrations found in the leachates were for Al, Ba, Ca, Fe, Mg, and Na with the three extractants. In the acetic acid and nitric/hydrochloric acid extraction, Mn is also one of the major elements.

In relation to the treatment performed by industries over the slag residues before reusing, it seems to have little influence on them. It could only increase the quantity of hydroxide compounds, when water is added to cool down, that are finally transformed to carbonate and decrease the iron materials in the case of slag from common steel, owing to the magnetic separation.

Considering that the most probable situation that can be given is the mobilization of the elements towards the environment with water, we focused on this extractant, and by means of PCA, we recognized and classified the unknown samples according to their elemental composition. The slag composition indicated if it had been manufactured in the production of common, special or stainless steel. Furthermore, because by Raman analysis had shown high presence of calcium silicates in the Electric Arc Furnace slag matrix (in these samples larnite and walstromite were identified), it was simulated the reactions between the calcium and silicates species (not measured by quantitative techniques) through chemical modeling. Thus, it was predicted the formation of different silicates in the slag.

Table 6.3. Localization of the highest concentration values of each measured element with each extractant in the steel slag samples. Blue: Milli-Q water; orange: acetic acid and yellow: nitric/hydrochloric acid.

	M1			M1T			M2			M2T			M3			M4			M5			M6		
Al		x	x							x														
Ba		x	x													x								
Mg											x					x								x
Fe		x																	x			x		
Mn		x	x																					
Na																						x	x	x
B																						x	x	x
Cr											x											x		x
K		x															x					x		
Li		x	x																			x		
Ni											x											x		x
Pb									x								x					x		
Ti		x	x																			x		
Cu		x								x							x							
Sr										x	x			x										
V								x	x	x														
Sb		x		x										x										
W	x	x							x															
Sn					x											x	x							
Zn					x							x				x								
Mo							x				x													x
Ca							x			x			x											x
F^-																						x		
SO_4^{2-}																						x		
Cl^-				x																				
NO_3^-																						x		

B. BLACK AND WHITE STEEL SLAG USED AS FILLER IN FOREST TRACKS ABOUT 18-34 YEARS AGO

In this part of the chapter, it was observed the weathering of the steel slags that had been exposed to the environment 18 and 34 years, to be used as filler in two forest tracks of Gipuzkoa (Basque Country, Northern Spain). Concretely, black steel slag (belonging to the short forest track (SFT)) and mixtures of black and white ones (from the long forest track (LFT)), since in this last case they leach together. Thus, it was known the slag weathering after a long period of time. In addition, it was measured the rain water of the area and the water collected on the LFT.

The area of the forest tracks belongs to temperate climate zone, so it does not have drastic changes in weather. Concretely, this zone presents a very high regular rainfall (1051-1734 mm total annual) due to the latitude of the territory and its proximity to the Bay of Biscay, and a mild temperature (11ºC on annual average)[62]. On the other hand, both tracks are closed to roads with high traffic intensity and urban centers with significant industrial history[62].

To study the weathering of the slag in that area, it was employed Raman spectroscopy results and the same leaching tests as for the fresh samples of the Part A: Milli-Q water, acetic acid and nitric/hydrochloric acid tests. The leached elements were also measured by means of Inductively Coupled Plasma/Mass Spectrometry (ICP-MS) and Ionic Chromatography (IC) techniques.

[62] El territorio histórico de Gipuzkoa, Gipuzkoako Batzar Nagusiak. 2006. Eusko Ikaskuntza.

1. SPECTROSCOPIC TECHNIQUES RESULTS

Weathering by hydration was observed in these steel slag samples with the presence of iron hydroxides such as goethite (α-FeOOH), lepidocrocite (γ-FeOOH), akaganeite (β-FeOOH), and also szomolnokite ($FeSO_4.H_2O$), brucite ($Mg(OH)_2$) and portlandite ($Ca(OH)_2$).

The presence of portlandite and brucite in the slag could be indicating the time evolution of CaO and MgO, compounds that are added to the furnace to generate the slag in the steel production[63] or come from the oxidation of the refractory bricks[64,65], by hydration processes[66]:

$$CaO+H_2O \rightarrow Ca(OH)_2 \quad (6.8)$$

$$MgO+H_2O \rightarrow Mg(OH)_2 \quad (6.9)$$

Both hydroxides could provoke an increase of volume in the slag[66] and to affect the structure of the forest track road, as it could be observed in some areas of our studied forest tracks where the surface of the road was broken and the slags could be seen easily (see Fig. 6.8). Besides, these fractures could cause that by rain water runoff, compounds leached from the slag could end up being deposited on surrounding land of the forest track.

[63] IHOBE, S. A. Libro Blanco para la minimización de residuos y emisiones, Servicio Central de Publicaciones del Gobierno Vasco, Vitoria-Gasteiz, Spain, 1999.
[64] H. Efendy, M. Safarudin, H. Sihombing, Molten metal-slag-refractory reactions during converting process, IJET-IJENS 10 (2010) 40-43.
[65] Z. Jin, T. Liu, Y. Yang, D. Jackson, Leaching of cadmium, chromium, copper, lead, and zinc from two slag dumps with different environmental exposure periods under dynamic acidic condition, Ecotoxicology and Environmental Safety 104 (2014) 43-50.
[66] I. Vîlciu, M. Nicolae, A. Nicolae, Minimization of the calcium oxide content in the steel slag, to be used in road construction, U.P.B. Scintific Bulletin Series B, 73 (2011) 205-220.

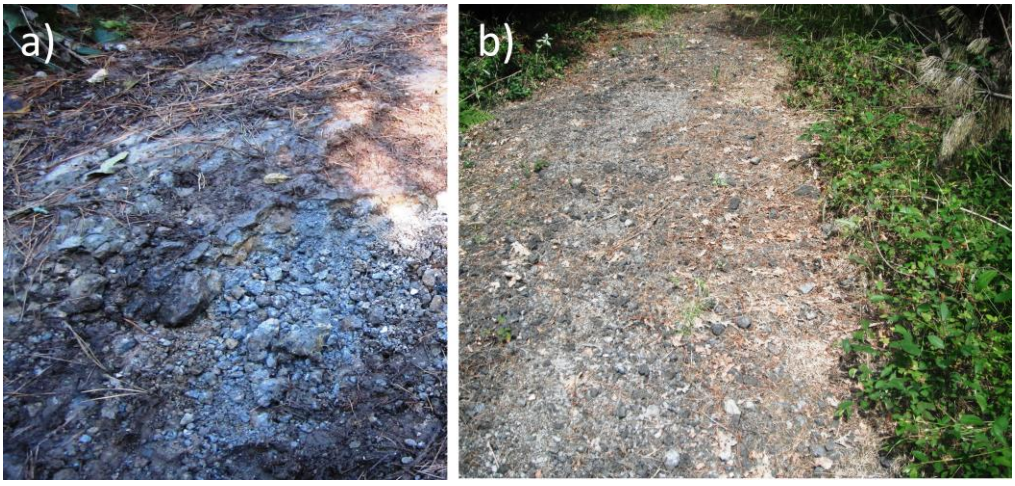

Fig.6.8. Images of steel slags in the LFT (a) and in the SFT (b).

Also, the existence of thaumasite ($Ca_3Si(CO_3)(SO_4)(OH)_6.12H_2O$)) is normally a sign of damage in materials like concrete and mortars[67], due to excessive sulfation. Generally, it generates a change of volume and besides, it can react with the calcium silicates present in the slag and disintegrate them completely[67-70].

Moreover, the interaction of the materials with atmospheric gases, like CO_2, was recognized with the often identification of carbonates such as calcite ($CaCO_3$), vaterite ($CaCO_3$) and HMC ($Ca(Mg)CO_3$) in the black steel slag. Although it was identified less compounds in the white slag composition, this had also compounds formed by weathering from environment CO_2 (carbonation), such as calcite ($CaCO_3$).

Hence, it was noted that the slag in contact with the atmosphere is changing its chemical composition, at least in this area situated near busy roads and industrialized urban areas and with plenty of rain.

[67] J. Aguilera, S. Martínez-Ramírez, I. Pajares-Colomo, M.T. Blanco-Varela, Formation of thaumasite in carbonated mortars, Cement and Concrete Composites 25 (2003) 991-996.
[68] S. Sahu, D.L. Exline , M.P. Nelson, Identification of thaumasite in concrete by Raman chemical imaging, Cement and Concrete Composites 24 (2002) 347-350.
[69] K.N. Jallad, M. Santhanam, M. D. Cohen, D. Ben-Amotz, Chemical mapping of thaumasite formed in sulfate-attacked cement mortar using near-infrared Raman imaging microscopy, Cement and Concrete Research 31 (2001) 953-958.
[70] N. Prieto Taboada, Desarrollo y aplicación de metodologías de análisis innovadoras para la evaluación del estado de conservación de materiales de construcción en edificios urbano industriales, PhD thesis. University of Basque Country, 2013.

2. LEACHING TESTS RESULTS

As it has been mentioned above, the purpose was to know the release of elements from steel slag after being used as filler during a long period of time. It was realized the same leaching tests as in the fresh slag (part A of this chapter), in order to know the weathering by rain water and extreme conditions, and also to extract most of the elements present in the slag, except those bound as silicates.

It was measured the following elements: Ag, Al, As, B, Ba, Ca, Cd, Co, Cr, Cu, Fe, Hg, K, Li, Mg, Mn, Mo, Na, Ni, Pb, Sb, Se, Sn, Sr, Ti, V, W and Zn. However, some of them were below the LOD in some slags (LOD $_{\text{Milli-Q water}}$; Ag: 7 µg/kg; Cd (in the SFT): 0.37 µg/kg; Sb (in the SFT): 0.10 µg/kg; Sn: 0.21 µg/kg (in the SFT slag); Ni (in the SFT slag): 7 µg/kg; Cu (in the SFT slag): 16 µg/kg; LOD $_{\text{Acetic acid}}$; Ag: 2 µg/kg; As (in the SFT slag): 2 µg/kg; Cr (in the SFT slag): 7 µg/kg; Cu (in the SFT slag): 82 µg/kg; LOD $_{\text{Nitric-hydrochloric acid}}$; Se (in the SFT slag): 6.85 mg/kg; As (in the SFT slag): 1.74 mg/kg.

2.1 Milli-Q water as extractant

It was simulated what elements would be lixiviated with rain water and therefore, available in the nearby soils to the slag.

In the Fig. 6.9 it can be observed the concentrations of the analyzed elements in the slag samples of both forest tracks using Milli-Q water.

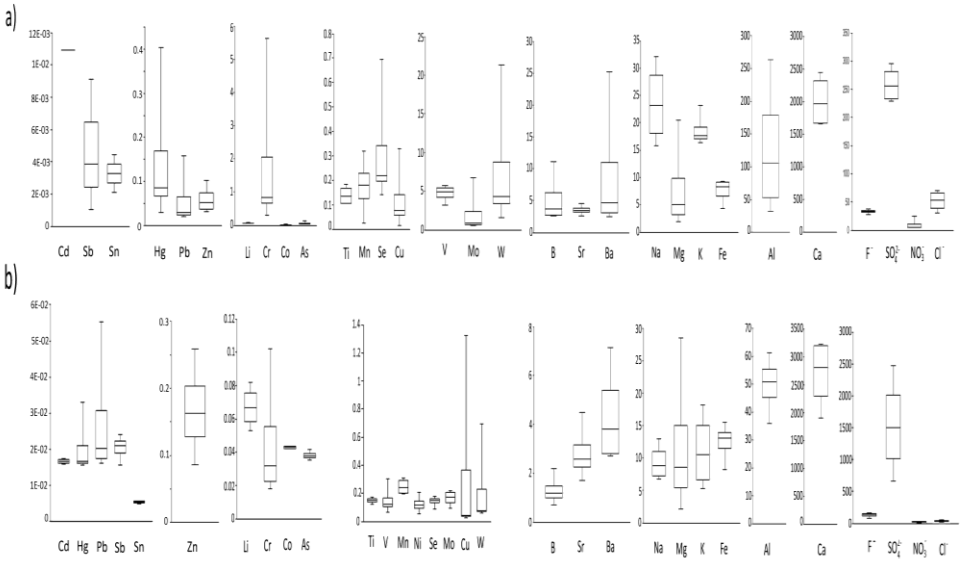

Fig.6.9. Graphical representation of the concentrations (mg/Kg) of the analyzed elements in the (a) SFT slag and (b) LFT slag, obtained from Milli-Q water dissolutions. Inside the box are the 95% of the values, the vertical line corresponds to the mean values and those of the opposite to the maximum and minimum values. The number of analyzed slag was 4 in each case (SFT and LFT).

The analyzed elements presented very similar ranges of concentration in the steel slag of each forest track, regardless of the point where they were collected. In general, the elements with the highest concentration values in both forest tracks were Ca, Al, Na, K, Mg and Fe. Nevertheless, comparing between slag samples of the two forest tracks, there were some exceptions. In some slag cases, several elements had more concentration in the SFT (short forest track) slag than in the LFT slag (long forest track), such as B, Ba, Na, Al, V, Cr, Se, Hg, Mo, Pb and W (see also Fig. 6.10.b and c). In contrast, in the LFT slag there was more concentration of Mg, Ca, Mn (a little difference), Fe, Co, Cu, Zn, Sb, Cd and Ni (see also Fig. 6.10.a and b). The rest of the element presented a similar range of concentration despite the forest track (Li, K, Ti, Sn and Sr).

With respect to the anions measured through IC, in the LFT there was more concentration of F^-, SO_4^{2-} and NO_3^- (see also Fig. 6.10.a). But in both forests tracks the highest concentrations were of SO_4^{2-}. Regarding Cl^- there was variation in all the sampling points of both forest tracks. This could be owing to the different exposure to the rain water.

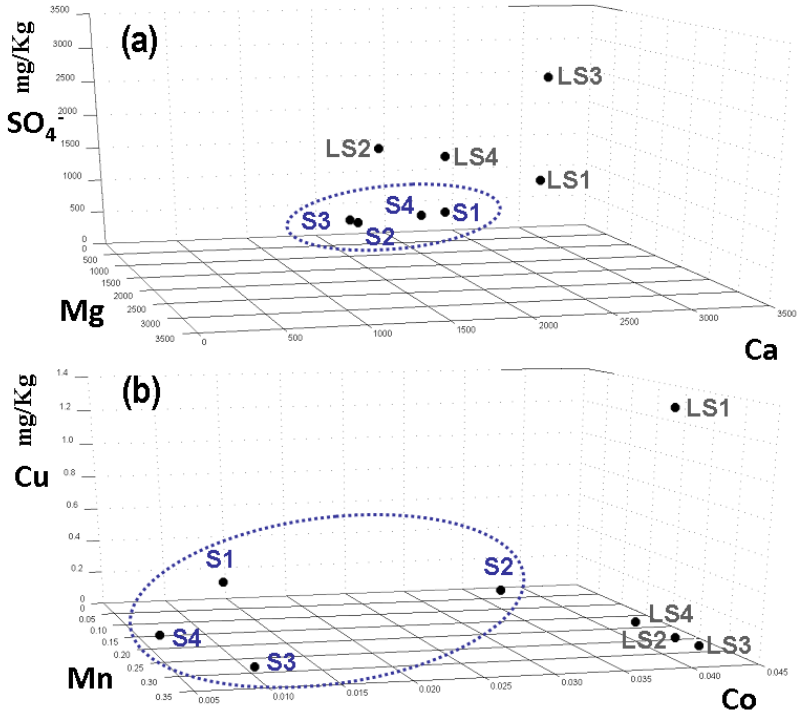

Fig.6.10. Spatial distribution of the concentrations (mg/Kg) of (a) SO_4^{2-}, Mg and Ca, (b) Cu, Mn and Co, using Milli-Q water as extractant in slag samples from the long forest track (LS1-LS4) and the short forest track (S1-S4)(blue color).

From the Fig. 6.10 it can be perceived that the slag samples are gathered according to if it is used only black steel slag (SFT) or mixture of black and white ones (LFT).

2.2 Acetic acid as extractant

The concentration data of acetic acid gave us an idea of which elements could be lixiviated from the slag with time in extreme conditions.

As in the leaching with Milli-Q water, the majority of the analyzed elements in the slag samples presented a very similar range of concentration comparing different sampling points in each forest track (see Fig.6.11). This could be due to the fact that the slag samples of each forest track come from the same steelwork.

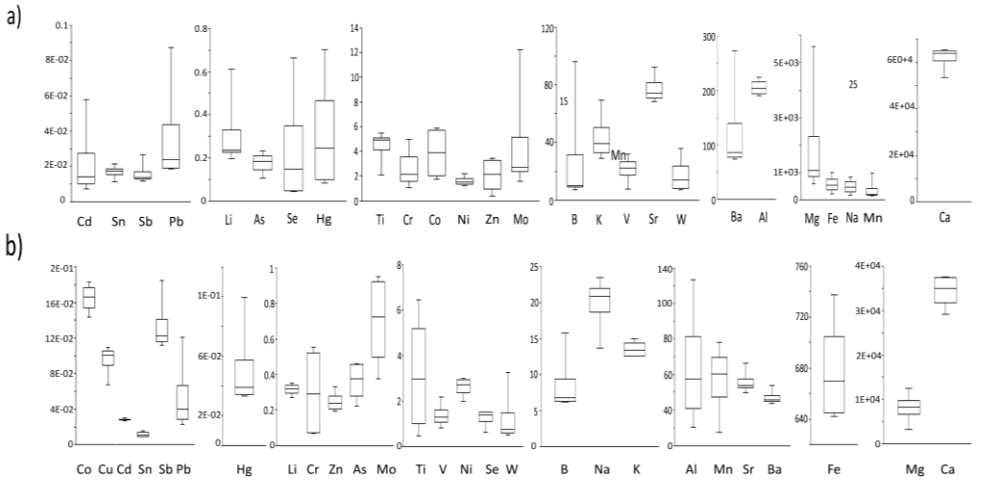

Fig.6.11. Graphical representation of the concentrations (mg/Kg) of the analyzed elements in the (a) SFT slag and (b) LFT slag, obtained from acetic acid dissolutions. Inside the box are the 95% of the values, the vertical line corresponds to the mean values and those of the opposite to the maximum and minimum values. The number of analyzed slag was 4.

In general, in both forest track the major concentration values were in Ca, Fe, Mg, Na, Mn and Al.

Nonetheless, there were also differences comparing some slag samples of the two forest tracks. In general, B, Na, Al, K, Ca, V, W, Cr, Mn, Co, Zn, Ba, Hg and Mo had more concentration values in the SFT slag than in the LFT slag (see also Fig.6.12.a and c). And Mg, Sb, Cu, Ni and Se in the LFT slag (see also Fig.6.12.a and b). The rest of the element presented a similar range of concentration regardless the forest track (Pb, Li,Ti, Fe, Sr, Cd and Sn).

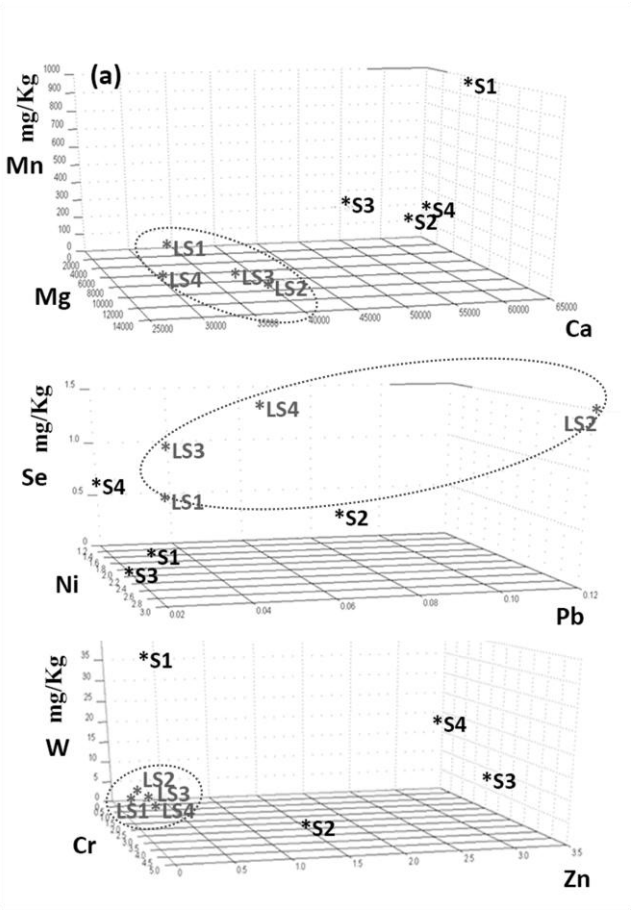

Fig.6.12. Spatial distribution of the concentrations (mg/Kg) of (a) Mg, Ca and Mn, (b) Ni, Pb and Se, and (c) Cr, Zn and W using acetic acid as extractant in slag samples from the long forest track (LS1-LS4) (grey color) and the short forest track (S1-S4).

It was once again observable the behaviour of the slag samples in the Fig. 6.12, where the samples come together depending on whether they are black steel slag or mixture of black and white.

2.3 Nitric-hydrochloric acid as extractant

The data obtained were the concentration of elements which were not as silicate forms. In the most of slag samples it was obtained a very similar range of concentration comparing both forest tracks (see Fig. 6.13), and besides, there were not significant differences of element concentrations between different points where it was collected the samples. The concentrations did not vary from the upper

to the lower points of each forest track as it happened in the leaching with Milli-Q water and acetic acid.

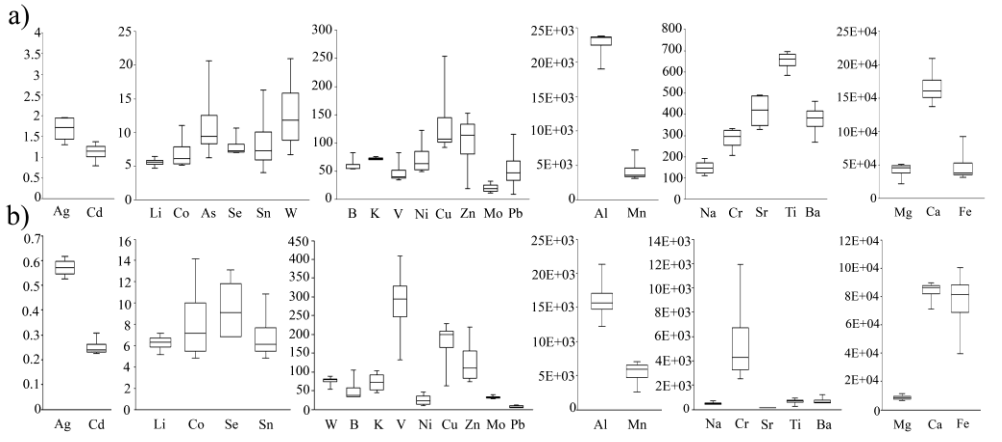

Fig.6.13. Graphical representation of the concentrations (mg/Kg) of the analyzed elements in the (a) LFT slag ,and (b) SFT slag, obtained from nitric-hydrochloric acid dissolutions. Inside the box are the 95% of the values, the vertical line corresponds to the mean values and those of the opposite to the maximum and minimum values.

Nevertheless, there were some elements with different concentrations, such as Al, Ag, Ca, Mg, Sr, Pb, Ni, Cd, Sb and As, with higher values in the track with mixture of slag (LFT) than in the other (see Fig.6.13). As was under the detection limit in the extractions of the samples belonged to the black slag forest track (SFT) (LOD_{As} = 1.74 mg/Kg). In contrast, in the SFT slag, there was more concentration of Na, V, Cr, Mo, Ba, Fe, Se, Hg and W (see Fig.6.13). These differences may be caused by the production methods of the steel, since both forest tracks have slags from different steelworks and by the presence of white steel slag in the long forest track.

In general, in the forest track filled with mixture of slag, the major elements were Ca, Fe, Al, Mg, and Mn, whereas in the forest track with only black slag were Ca, Fe, Al, Mg, Mn and Cr. In the Fig.6.14.a, where it is shown the tridimensional representation of some majority elements such as Fe, Mg and Ca, it can be distinguished two groups of samples according to the track (S1, S2, S3 and S4, and on the other hand, LS1, LS2, LS3 and LS4). With respect to some minor elements (W, Cr and Cd) (Fig. 6.14.b), it is again noticeable the formation of two groups according to the forest track. Finally, in the contour map (Fig.6.14.c), it can be seen simultaneously the maximum values of

some of the predominant elements in these slag samples (Na, Mg, Al, Ca and Fe) in both forest tracks:, where the highest values of Ca and Mg are in the long forest track (mixture of slags), and of Na in the short forest track (only black slag). Fe is a higher in SFT.

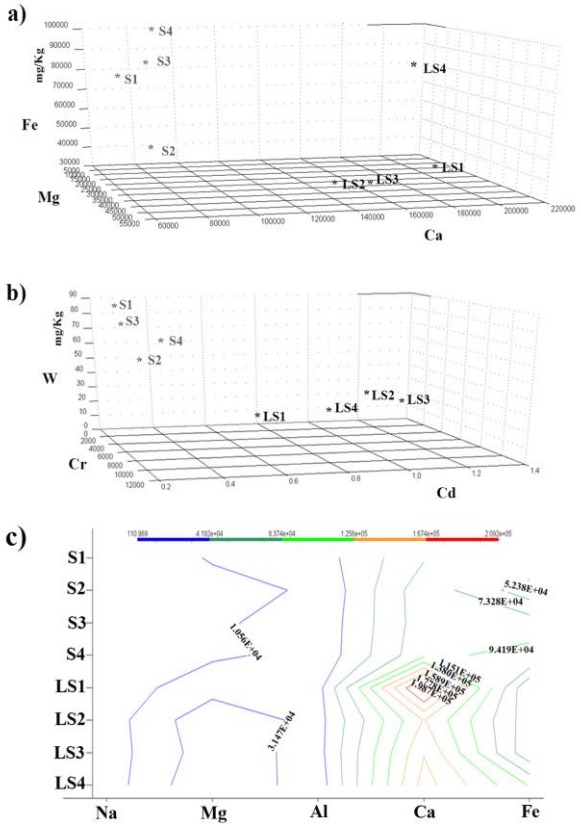

Fig. 6.14. Spatial distribution of the concentrations (mg/Kg) of (a) Fe, Mg, Ca, and (b) W, Cr and Cd; and (c) contour map of Na, Mg, Al, Ca and Fe concentrations (mg/Kg), in slag samples from the long forest track (mixture of slag; LS1-LS4) and the short forest track (only black slag; S1-S4). Color bar goes from low concentration (blue) to high concentration (red).

3. RAIN WATER SAMPLES RESULTS

The results obtained from rain water samples collected in the LFT are shown in the Fig. 6.15. It could be perceived that the rain water, which was in contact with the LFT, showed significantly higher levels of Mg, K, Fe, Mn, Li, B, Ti, V, Cr, Sr, Mo, Ag, Cd, Sb, Ba, W and Pb than the rain water sample taken directly from the atmosphere. This could be due to the fact that the forest track water sample was deposited in contact with the mixture of black and white slag during a certain period of time. It was known that the previous month to the sampling (December), it was very wet[71]. So, the weathering of the steel slags by water provoked that those elements were dissolved from the slag to the water.

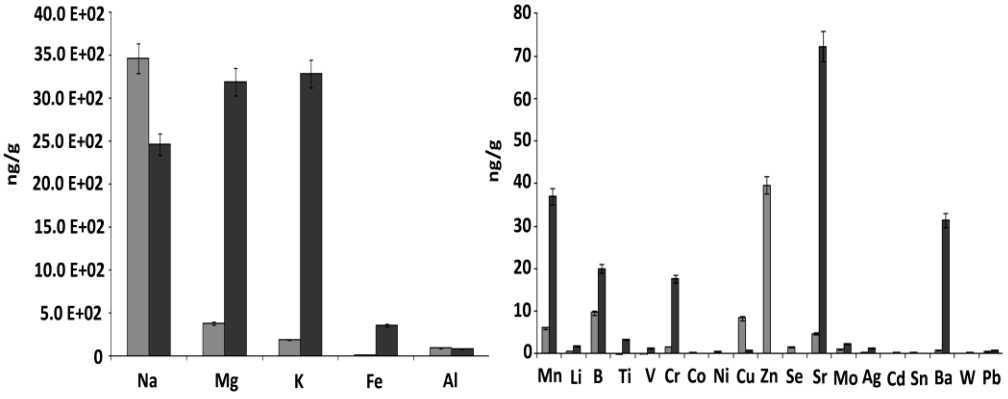

Fig.6.15. Concentrations (ng/g) of the elements found in rain water (grey) and in rain water deposited over the LFT (black).

4. STATISTICAL ANALYSIS

4. 1 Correlation Analysis (CA)

It was carried out a correlation analysis with the concentration values of Al, As, B, Ba, Cr, Cu, Fe, K, Li, Mg, Mn, Co, Mo, Na, Ni, Pb, Se, Sb, Sn, Sr, Ti, V, W, Zn, F^-, Cl^-, NO_3^-, SO_4^{2-} and Ca^{2+}, obtained from the Milli-Q water leaching tests of the LFT and SFT slag samples (see Table 6.4 and 6.5). It was made in order to distinguish possible relations

[71] Euskalmet. Meteorological Report November 2011. Meteorology and Climatology Management, Basque Government.

between the measured elements in water conditions, most probably situation that could be given.

The r critical value was 0.97 with a confidence level of 99%. In the case of the LFT slag data, the highest correlations were in Li-Co; Mg-V; Ba-K; Ca- Co; Fe-Se; Sn-F^-; W-Pb; NO_3^--Cl^- and above all, As-Ni, W-Hg and Hg-Pb. And among the negative correlations were in Mg-Se, Ni-Sb, As-Sb V-Fe, V-Se, and Cd-NO_3^-. On the other hand, in the SFT slag data, there were a great number of high positive correlations. With a Pearson coefficient of 1, it can be highlighted: Li-As, Cr-Pb, Cu-W, Cu-Hg, Mo-Ba, Mo-W, Cd-NO_3^-, Ba-W, Ba-Hg and Hg-W.

Table 6.4. Correlation matrix obtained from Milli-Q water-soluble fraction data of the LFT slag (rcrit = 0.97).

	Li	B	Na	Mg	Al	K	Ca	Ti	V	Cr	Mn	Fe	Co	Ni	Cu	Zn	As	Se	Sr	Mo	Cd	Sn	Sb	Ba	W	Hg	Pb	F^-	SO_4^{2-}	NO_3^-	Cl^-
Li	**1.00**																														
B	-0.41	**1.00**																													
Na	0.42	0.50	**1.00**																												
Mg	-0.89	0.78	-0.05	**1.00**																											
Al	0.79	-0.69	-0.21	-0.88	**1.00**																										
K	0.95	-0.10	0.60	-0.70	0.65	**1.00**																									
Ca	0.96	-0.56	0.16	-0.93	0.93	0.86	**1.00**																								
Ti	-0.81	-0.20	-0.80	0.46	-0.38	-0.95	-0.66	**1.00**																							
V	-0.83	0.83	-0.02	**0.99**	-0.81	-0.61	-0.87	0.37	**1.00**																						
Cr	0.61	0.15	0.93	-0.35	-0.01	0.67	0.36	-0.79	-0.35	**1.00**																					
Mn	0.18	0.63	0.97	0.18	-0.46	0.37	-0.10	-0.63	0.19	0.85	**1.00**																				
Fe	0.83	-0.78	0.14	-0.96	0.72	0.61	0.82	-0.41	**-0.99**	0.48	-0.06	**1.00**																			
Co	**0.98**	-0.38	0.33	-0.86	0.85	0.95	**0.98**	-0.80	-0.78	0.47	0.07	0.74	**1.00**																		
Ni	0.65	-0.56	-0.33	-0.72	0.96	0.56	0.84	-0.30	-0.63	-0.20	-0.55	0.50	0.77	**1.00**																	
Cu	0.30	-0.22	-0.46	-0.30	0.72	0.31	0.52	-0.13	-0.19	-0.49	-0.61	0.03	0.48	0.88	**1.00**																
Zn	-0.26	0.11	-0.62	0.25	0.25	-0.17	-0.03	0.26	0.34	-0.79	-0.63	-0.49	-0.06	0.49	0.84	**1.00**															
As	0.63	-0.55	-0.34	-0.70	0.96	0.54	0.82	-0.29	-0.61	-0.22	-0.56	0.48	0.76	**1.00**	0.89	0.52	**1.00**														
Se	0.91	-0.75	0.13	**-1.00**	0.84	0.72	0.92	-0.50	**-0.99**	0.43	-0.10	**0.98**	0.86	0.66	0.23	-0.32	0.64	**1.00**													
Sr	0.85	-0.42	0.58	-0.80	0.45	0.74	0.71	-0.68	-0.81	0.83	0.41	0.89	0.72	0.22	-0.24	-0.72	0.19	0.85	**1.00**												
Mo	0.27	0.74	0.92	0.18	-0.28	0.54	0.04	-0.77	0.25	0.73	0.91	-0.17	0.24	-0.29	-0.24	-0.29	-0.29	-0.13	0.28	**1.00**											
Cd	0.06	0.41	-0.08	0.17	0.27	0.28	0.17	-0.28	0.31	-0.33	-0.15	-0.42	0.25	0.49	0.80	0.83	0.51	-0.22	-0.44	0.26	**1.00**										
Sn	-0.61	0.25	-0.68	0.56	-0.11	-0.52	-0.41	0.54	0.61	-0.90	-0.60	-0.73	-0.44	0.15	0.57	0.92	0.17	-0.62	-0.93	-0.35	0.65	**1.00**									
Sb	-0.65	0.53	0.31	0.70	-0.96	-0.57	-0.83	0.32	0.61	0.20	0.54	-0.48	-0.77	**-1.00**	-0.89	-0.51	**-1.00**	-0.64	-0.21	0.26	-0.52	-0.16	**1.00**								
Ba	0.96	-0.19	0.65	-0.76	0.60	**0.97**	0.85	-0.92	-0.70	0.78	0.43	0.73	0.92	0.46	0.13	-0.38	0.44	0.79	0.88	0.50	0.05	-0.70	-0.46	**1.00**							
W	-0.70	0.94	0.24	0.95	-0.85	-0.44	-0.80	0.16	0.97	-0.10	0.44	-0.92	-0.67	-0.71	-0.31	0.16	-0.69	-0.93	-0.64	0.48	0.27	0.41	0.68	-0.51	**1.00**						
Hg	-0.68	0.95	0.27	0.94	-0.85	-0.41	-0.79	0.12	0.96	-0.06	0.47	-0.91	-0.65	-0.71	-0.32	0.14	-0.69	-0.91	-0.61	0.52	0.28	0.38	0.68	-0.48	**1.00**	**1.00**					
Pb	-0.67	0.95	0.20	0.93	-0.78	-0.39	-0.75	0.13	0.97	-0.15	0.39	-0.94	-0.62	-0.61	-0.19	0.27	-0.59	-0.92	-0.68	0.48	0.39	0.48	0.58	-0.50	**0.99**	**0.99**	**1.00**				
F^-	-0.52	0.02	-0.82	0.38	0.06	-0.51	-0.28	0.60	0.42	-0.96	-0.76	-0.56	-0.35	0.29	0.65	0.93	0.32	-0.46	-0.86	-0.53	0.58	**0.97**	-0.30	-0.67	0.20	0.17	0.28	**1.00**			
SO_4^{2-}	0.23	0.44	0.94	0.05	-0.42	0.35	-0.06	-0.57	0.03	0.91	0.97	0.12	0.08	-0.57	-0.73	-0.81	-0.59	0.04	0.56	0.79	-0.38	-0.76	0.57	0.46	0.28	0.31	0.20	-0.89	**1.00**		
NO_3^-	-0.19	-0.26	0.13	-0.02	-0.43	-0.36	-0.32	0.32	-0.16	0.32	0.24	0.28	-0.38	-0.63	-0.88	-0.83	-0.64	0.07	0.34	-0.19	**-0.99**	-0.60	0.65	-0.14	-0.11	-0.11	-0.23	-0.57	0.45	**1.00**	
Cl^-	-0.30	-0.30	-0.04	0.04	-0.44	-0.50	-0.39	0.48	-0.10	0.15	0.09	0.21	-0.48	-0.61	-0.83	-0.73	-0.63	0.00	0.21	-0.33	-0.97	-0.47	0.64	-0.28	-0.10	-0.11	-0.22	-0.42	0.30	**0.99**	**1.00**

Table 6.5. Correlation matrix obtained from Milli-Q water-soluble fraction data of the SFT slag (rcrit = 0.97).

	Li	B	Na	Mg	Al	K	Ca	Ti	V	Cr	Mn	Fe	Co	Cu	Zn	As	Se	Sr	Mo	Cd	Sn	Sb	Ba	W	Hg	Pb	F^-	SO_4^{2-}	NO_3^-	Cl^-
Li	**1.00**																													
B	**0.98**	**1.00**																												
Na	0.79	0.88	**1.00**																											
Mg	0.95	0.91	0.60	**1.00**																										
Al	-0.44	-0.60	-0.90	-0.22	**1.00**																									
K	-0.20	-0.07	0.41	-0.48	-0.71	**1.00**																								
Ca	0.54	0.61	0.40	0.68	-0.28	-0.41	**1.00**																							
Ti	-0.64	-0.76	**-0.98**	-0.41	0.96	-0.60	-0.27	**1.00**																						
V	-0.17	0.04	0.44	-0.33	-0.78	0.78	0.17	-0.58	**1.00**																					
Cr	-0.31	-0.21	0.25	-0.58	-0.54	0.97	-0.62	-0.45	0.62	**1.00**																				
Mn	-0.13	-0.30	-0.72	0.13	0.94	-0.91	0.02	0.85	-0.87	-0.79	**1.00**																			
Fe	-0.18	-0.28	-0.68	0.13	0.82	-0.92	0.31	0.81	-0.62	-0.88	0.92	**1.00**																		
Co	-0.07	0.01	0.44	-0.37	-0.63	0.94	-0.57	-0.60	0.54	0.97	-0.82	-0.96	**1.00**																	
Cu	0.93	0.91	0.62	**0.99**	-0.27	-0.46	0.78	-0.43	-0.21	-0.60	0.08	0.14	-0.40	**1.00**																
Zn	0.89	0.79	0.41	0.97	0.02	-0.63	0.55	-0.21	-0.55	-0.67	0.34	0.27	-0.46	0.93	**1.00**															
As	**1.00**	**0.99**	0.81	0.95	-0.49	-0.18	0.61	-0.67	-0.09	-0.31	-0.18	-0.18	-0.08	0.94	0.87	**1.00**														
Se	0.96	**0.98**	0.82	0.94	-0.54	-0.18	0.74	-0.68	0.03	-0.35	-0.22	-0.14	-0.14	0.96	0.82	**0.98**	**1.00**													
Sr	0.81	0.92	0.90	0.75	-0.77	0.10	0.76	-0.82	0.39	-0.11	-0.50	-0.34	0.04	0.81	0.56	0.87	0.93	**1.00**												
Mo	0.96	0.96	0.73	**0.98**	-0.41	-0.32	0.74	-0.57	-0.12	-0.46	-0.07	-0.02	-0.26	**0.99**	0.89	**0.98**	**0.99**	0.87	**1.00**											
Cd	**0.98**	**0.97**	0.75	**0.98**	-0.42	-0.29	0.71	-0.59	-0.12	-0.43	-0.09	-0.06	-0.21	**0.98**	0.89	**0.99**	**0.99**	0.87	**1.00**	**1.00**										
Sn	-0.67	-0.66	-0.76	-0.43	0.58	-0.42	0.19	0.76	-0.02	-0.43	0.51	0.74	-0.64	-0.34	-0.38	-0.63	-0.51	-0.45	-0.46	-0.51	**1.00**									
Sb	0.82	0.84	0.57	0.91	-0.30	-0.46	0.92	-0.39	-0.06	-0.64	0.05	0.22	-0.49	0.96	0.82	0.85	0.92	0.84	0.94	0.92	-0.14	**1.00**								
Ba	0.93	0.94	0.70	0.97	-0.39	-0.36	0.80	-0.53	-0.09	-0.51	-0.04	0.04	-0.32	**0.99**	0.88	0.96	**0.98**	0.88	**1.00**	**0.99**	-0.38	0.97	**1.00**							
W	0.95	0.93	0.66	**0.99**	-0.32	-0.41	0.77	-0.48	-0.18	-0.55	0.03	0.08	-0.35	**1.00**	0.92	0.96	0.97	0.83	**1.00**	**0.99**	-0.39	0.96	**1.00**	**1.00**						
Hg	0.94	0.93	0.65	**0.99**	-0.31	-0.42	0.77	-0.47	-0.19	-0.56	0.04	0.10	-0.36	**1.00**	0.92	0.96	0.97	0.83	**0.99**	**0.99**	-0.38	0.96	**1.00**	**1.00**	**1.00**					
Pb	-0.21	-0.11	0.35	-0.49	-0.60	**0.98**	-0.58	-0.53	0.62	**1.00**	-0.83	-0.92	**0.99**	-0.51	-0.60	-0.21	-0.25	-0.03	-0.37	-0.33	-0.51	-0.57	-0.43	-0.46	-0.47	**1.00**				
F^-	0.59	0.49	0.02	0.80	0.36	-0.90	0.64	0.20	-0.65	-0.94	0.66	0.69	-0.83	0.80	0.88	0.58	0.58	0.32	0.69	0.67	0.11	0.77	0.72	0.76	0.77	-0.91	**1.00**			
SO_4^{2-}	0.17	0.28	0.18	0.32	-0.23	-0.28	0.92	-0.11	0.38	-0.49	-0.03	0.35	-0.55	0.47	0.18	0.26	0.44	0.56	0.42	0.37	0.48	0.69	0.50	0.44	0.45	-0.48	0.40	**1.00**		
NO_3^-	**0.98**	**0.98**	0.77	**0.97**	-0.44	-0.27	0.71	-0.61	-0.10	-0.41	-0.11	-0.07	-0.20	**0.98**	0.88	**0.99**	**0.99**	0.88	**1.00**	**1.00**	-0.52	0.92	**0.99**	**0.99**	**0.99**	-0.32	0.66	0.37	**1.00**	
Cl^-	0.67	0.52	0.06	0.82	0.38	-0.83	0.38	0.15	-0.80	-0.80	0.65	0.53	-0.64	0.75	0.93	0.62	0.56	0.23	0.67	0.67	-0.16	0.63	0.67	0.73	0.73	-0.76	0.93	0.06	0.66	**1.00**

5. DISCUSSION

Weathering of the forest track steel slags in contact with the atmosphere was observed by means of Raman spectroscopy, with the presence of calcite, HMC, vaterite, goethite, lepidocrocite, akaganeite, szomolnokite, brucite, portlandite and thaumasite. These three later compounds could affect especially to the increase of slag volume. As it has been said, the latter two compounds could increase the slag volume, affecting to the road structure and increasing the possibilities of leaching from the slag by rain water.

Moreover, when it was performed leaching test over the forest track slags in the laboratory, it could be concluded that in each forest track, the variations of concentration in the slag samples of different sampling points are not very significant, so there is no a strong variation in their composition according to the area where they were collected. This could be due to the fact that the slag samples have been generated in the same type of furnace (EAF). Besides, comparing both forest tracks, the elements which appeared with higher concentrations were Ca, Fe, Mg, and Al, regardless of the extractant used and the point of collecting. Nevertheless, there were some differences between the slag compositions of both forest tracks, with respect to the concentration values.

In Table 6.6 are marked in which slag samples appeared the highest concentration values according to the extractant, and besides, those elements with similar concentrations to each extractant in both forest tracks (≈).

In addition, results from the analysis of the two rain water samples collected in the LFT showed that some elements go through from the slag to the environment in contact with rain water.

Table 6.6. Localization of the highest concentration values of some measured elements with each extractant in the steel slag samples. Blue: Milli-Q water; orange: acetic acid and yellow: nitric/hydrochloric acid. ≈ : similar concentration.

	LFT slag			SFT slag		
Al			x	x	x	
Li	≈	≈		≈	≈	
Ti	≈	≈		≈	≈	
Ba				x	x	x
Mg	x	x	x			
Fe	x	≈			≈	x
Mn	≈		≈	≈	x	≈
Na				x	x	x
B			≈	x	x	≈
Cr				x	x	x
K	≈		≈	≈	x	≈
Se		x		x		x
Ni	x	x	x			
Pb		≈	x	x	≈	
Cu	x	x	≈			≈
Sr	≈	≈	x	≈	≈	
Sn	≈	≈		≈	≈	
Cd	x	≈	x		≈	
V				x	x	x
Sb	x	x	x			
W				x	x	x
Zn	x		≈		x	≈
Mo				x	x	x
Co	x		≈		x	≈
As		x	x	x		
Hg				x	x	x
Ag	x	≈	x		≈	
Ca	x		x		x	
F^-	x					
SO_4^{2-}	x					
Cl^-				x		
NO_3^-	x					

C. LIBYAN DESERT GLASS (LDG)

Since the discovery of these intriguing melts, 74 scientist publications related to them have been spread (see Chapter 1, Part A). In all of them the authors suggested hypothesis that can explain the structure and the chemical characteristics of the glass and its origin in the Libyan Desert. However, the number of studies about weathering of Libyan Desert Glass is limited compared with the meteorites ones[72-77]. Nobody explains the weathering process of these materials formed in the Libyan Desert (Egypt). For instance, F. Fröhlich et al. (2013)[78] and A. Longinelli et al.[79] mentioned weathering, but that of the sandstones belonging to the zone where LDGs were discovered.

Because we did not find any works that research explicitly the weathering of LDG, and due to the importance of knowing its original and altered compounds, we characterized and compared the compounds identified in the surface with the compounds found inside our LDG samples, both matrix and inclusions (Chaper 4, part A).

[72] C. Burkhardt ,R.C. Hin, T. Kleine, B. Bourdon, Evidence for Mo isotope fractionation in the solar nebula and during planetary differentiation, Earth and Planetary Science Letters 391 (2014) 201–211.
[73] V. P. Semenenko, A. L. Girich, S. N. Shirinbekova, T. N. Gorovenko, N. V. Kichan, Genetic types of nanometer grains of minerals in meteorites, Nanosistemi, Nanomateriali, Nanotekhnologii 10 (2012) 1-10.
[74] , J. W. Ashley, M. P. Golombek, P. R. Christensen, S. W. Squyres, T. J. McCoy, C. Schroder, I. Fleischer, J. R. Johnson, K. E. Herkenhoff, T. J. Parker, Evidence for mechanical and chemical alteration of iron-nickel meteorites on Mars: process insights for Meridiani Planum, Journal of Geophysical Research: Planets 116 (2011) 1-22.
[75] A. Losiak, M. Velbel, A. Michael, Evaporite formation during weathering of Antarctic meteorites-a weathering census analysis based on the ANSMET database, Meteoritics & Planetary Science 46 (2011) 443-458.
[76] P.A. Bland, Terrestrial weathering rates defined by extraterrestrial materials, Journal of Geochemical Exploration 88 (2006) 257-261.
[77] A. Al-Kathiri, B.A. Hofmann, A. J. T. Jull, E. Gnos, Weathering of meteorites from Oman: Correlation of chemical and mineralogical weathering proxies with 14C terrestrial ages and the influence of soil chemistry, Meteoritics & Planetary Science 40 (2005) 1215-1239.
[78] F. Fröhlich, G. Poupeau, A. Badou, F. X. Le Bourdonnec, Y. Sacquin, S. Dubernet, J. M. Bardintzeff, M. Véran, D. C. Smith, E. Diemer, Libyan Desert Glass: New field and Fourier transform infrared data, Meteoritics & Planetary Science 48 (2013) 2517–2530.
[79] A. Longinelli, G. Sighinolfi, V. de Michele, E. Selmo, δ18O and chemical composition of Libyan Desert Glass, country rocks, and sands: New considerations on target material, Meteoritics & Planetary Science 46 (2011) 218–227.

LDG are exposed to the Libyan Desert, which is called the Western Desert in Egypt. This desert forms part of the eastern Sahara, and is the largest expanse of profound aridity on the face of the Earth[80]. In fact, it has been also used as an analogue for Mars[80].

The temperature of Libyan Desert is seldom below 4°C and frequently over 38°C[81]. Rain is spatially and temporally very variable, mainly in winter, with averages of 0–5 mm annually[82]. However, annual evaporation reaches over 2.5 mm and it may extent to 5.0 mm[82]. Moreover, there are persistent northerly trade winds, which provoke aeolian processes[81]. This whole of conditions could modify the mineralogical and chemical composition of the LDG with new terrestrial weathering products, within a few tens or millions of years[83]. So, the terrestrial weathering is significant in the composition of this material formed at high temperature and pressure with terrestrial environments.

In this part of the chapter, it was possible to report some mineral compounds produced by terrestrial weathering over LDG samples at micrometre-nanometre scale.

Moreover, it was realized the same sonicated leaching test with Milli-Q water used in steel slags, in order to know what elements were leached with water in this type of and samples, simulating rain. The leached elements were measured by means of Inductively Coupled Plasma-Mass Spectrometry (ICP-MS), Ionic Chromatography (IC) and Gas Chromatography-Mass Spectrometry (Solid Phase Micro Extraction (SPME)-GC-MS and Head Space (HS)-GC-MS) techniques. Moreover, simulation processes through chemical modelling complemented the results.

[80] A.J. Parsons, A.D. Abrahams, Geomorphology of Desert Environments, Springer, second edition. 2009.
[81] P. Malcolm, E.Losleben, Cultures of the world, Libya. 2004.
[82] I.A. Brookes, Aeolian erosional lineations in the Libyan Desert, Dakhla Region, Egypt. Geomorphology 39 (2001) 189–209.
[83] M. R. Lee, P.A. Bland. Mechanisms of weathering of meteorites recovered from hot and cold deserts and the formation of phyllosilicates. Geochimica et Cosmochimica Acta, 68 (2004) 893-916.

1. SPECTROSCOPIC TECHNIQUES RESULTS

In accordance with the mineral compounds identified in the LDG samples by Raman spectroscopy (see Chapter 4: Part A), it could be observed that limonite and possibly gypsum were weathering products formed by hydration. During weathering by hydration, hematite can be transformed into a mixture of hydrated iron oxide-hydroxide known as limonite. Indeed, iron-oxide/hydroxide weathering products can be formed within a few tens of years[84], and often fill cracks and mineral fractures, together with terrestrial quartz grains and carbonates, as it takes place in meteorites weathering[85].

In the case of gypsum, it could have been formed from the anhydrite hydration, given the long period of time from LDG formation. Moreover, as it has been explained in the Chapter 4, during this time, there were some periods with large quantity of water in the current Libyan Desert, so through cracks or fissures connected to the LDG surface it could have been explained the presence of water crystallization in the interior of the LDG, and therefore, hydrated mineral compounds such as gypsum could be present.

2. LEACHING TEST RESULTS: MILLI-Q WATER

Aqueous solutions that invade the impact glasses offer the possibility of leaching, or even terrestrial contamination as it has been mentioned in some meteorites[85].Therefore, in this section was sought the release of elements from our collected LDG samples. For that, it was employed the same method as in the steel slag, known the good results obtained with the focused ultrasound energy. It was realized the leaching test with Milli-Q water in order to simulate weathering by water. The measurements by ICP-MS and IC were realized in triplicate.

It was measured the following elements: Ag, Al, As, Ba, Ca, Cd, Co, Cr, Cu, Fe, Hg, K, Li, Mg, Mn, Mo, Na, Ni, Pb, Sb, Se, Sn, Sr, Ti, Tl, V, W and Zn. However, there was not

[84] PA Bland, F.J. Berry, C.T. Pilinger, Rapid weathering in Holbrook: An iron -57 Mossbauer spectroscopy study. Meteorit Planet Sci 35 (1998) 1387-1395.
[85] G.Crozaz, M. Wadhwa, The terrestrial alteration of saharan shergottites dar al gani 476 and 489: a case study of weathering in a hot desert environment, Geochimica et Cosmochimica Acta 65 (2001) 971-977.

Ag, and others were below the LOD (LOD_{Sb} : 0.36 µg/kg; LOD_{Hg}: 1.5 µg/kg; LOD_{Tl}: 0.010 µg/kg; LOD_{Pb}: 11 µg/kg; LOD_{As}: 0.31 µg/kg; LOD_{Se}: 0.31 µg/kg; LOD_{Cd}: 0.029 µg/kg; LOD_{V}: 0.37 µg/kg).

Moreover, given that some authors had found rare earth element (REE) content in LDG samples, as for example J.A. Barrat et al. (1997)[86] who dissolved the samples using HF-$HClO_4$ mixture, and C. Koeberl (1997)[87], who determined those elements by instrumental neutron activation analysis (INNA) and atomic absorption spectrometry, it was measured the following ones: La, Ce, Pr, Nd, Sm, Eu, Gd, Tb, Dy, Ho, Er, Tm, Yb, Lu, Th and U. There were not Tb, Ho and Er, and the following ones were below the LOD: Eu (0.0042 µg/kg), Dy (0.0038 µg/kg), Tm (0.0050 µg/kg), Yb (0.0010 µg/kg), Lu (0.0038 µg/kg) and U (0.0072 µg/kg). REE compositions provide additional evidence for terrestrial, are part of many rock-forming minerals[88], or extraterrestrial contributions[89].

Knowing if the sample has preserved meteoritic matter or it is terrestrial is extremely difficult. A limiting factor is that only a very small amount of the finely dispersed meteoritic melt or vapor is mixed with a much larger quantity of target rock vapor and melt, and this mixture later forms impact glass. In most cases, the contribution of extraterrestrial matter to this is very small, mostly much less than 1% by weight, leading to only slight chemical changes in the resulting glasses. Only elements that have high abundances in meteorites, but low abundances in terrestrial crustal rocks (in particular, the siderophile elements: Au, Co, Fe, Ir, Mn, Mo, Ni, Os, Pd, Pt, Re, Rh and Ru) can be used reliably[90]. In addition, the study of isotope compositions of

[86] J.A. Barrat, B.M. Jahn, J. Amossé, R. Rocchia, F. Keller, G.R. Poupeau, E. Diemer, Geochemistry and origin of Libyan Desert glasses, Geochimica et Cosmochimica Acta 61 (1997) 1953-1959.
[87] C. Koeberl, Libyan Desert Glass: geochemical composition and origin, Proceedings Silica 96 Meeting on Libyan Desert Glass and related desert events, Italy (1997)121–131.
[88] V.G. Papangelakis, G. Moldoveanu, Recovery of rare earth elements from clay minerals, ERES2014: 1st European Rare Earth Resources Conference Milos 04-07/09/2014.
[89] F. Martinez-Ruiz, M. Ortega-Huertas, P. Rivas, Rare earth element composition as evidence of the precursor material of Cretaceous –Tertiary boundary sediments at distal sections, Chemical Geology 232 (2006) 1-11.
[90] C. Koeberl, A. Shukolyukov, G. W. Lugmair, Chromium isotopic studies of terrestrial impact craters: Identification of meteoritic components at Bosumtwi, Clearwater East, Lappajärvi, and Rochechouart, Earth and Planetary Science Letters 256 (2007) 534-546.

elements such as Cr, O or REE ratios also allows distinguishing between extraterrestrial components from the continental crust[91,92].

With respect to anions it was measured F^-, Cl^-, NO_3^-, SO_4^{2-}, Br^- and $C_2O_4^{2-}$. The latter was measured to corroborate the presence of oxalates identified by Raman spectroscopy in our LDG samples.

The most leached element was Ca, and after K, Mg and Na. Then, there was another group of elements with lower concentration: Al, Cu, Ba, Fe, Mn, Ti, Sr and Zn. Finally, Ni, Cr, Co, Li, Mo, W and S presented the lowest concentration values (see Fig. 6.16).

[91] C. Koeberl, V.L Sharpton, B. C. Schuraytz, S. B. Shirey, J.D Blum, L. E. Marin, Evidence for a meteoritic component in impact melt rock from the chicxulub structure, Geochimica et Cosmochimica Acta 58 (1994) 1679-1684.

[92] F. Martinez-Ruiz, M. Ortega-Huertas, P. Rivas, Rare earth element composition as evidence of the precursor material of Cretaceous –Tertiary boundary sediments at distal sections, Chemical Geology 232 (2006) 1-11.

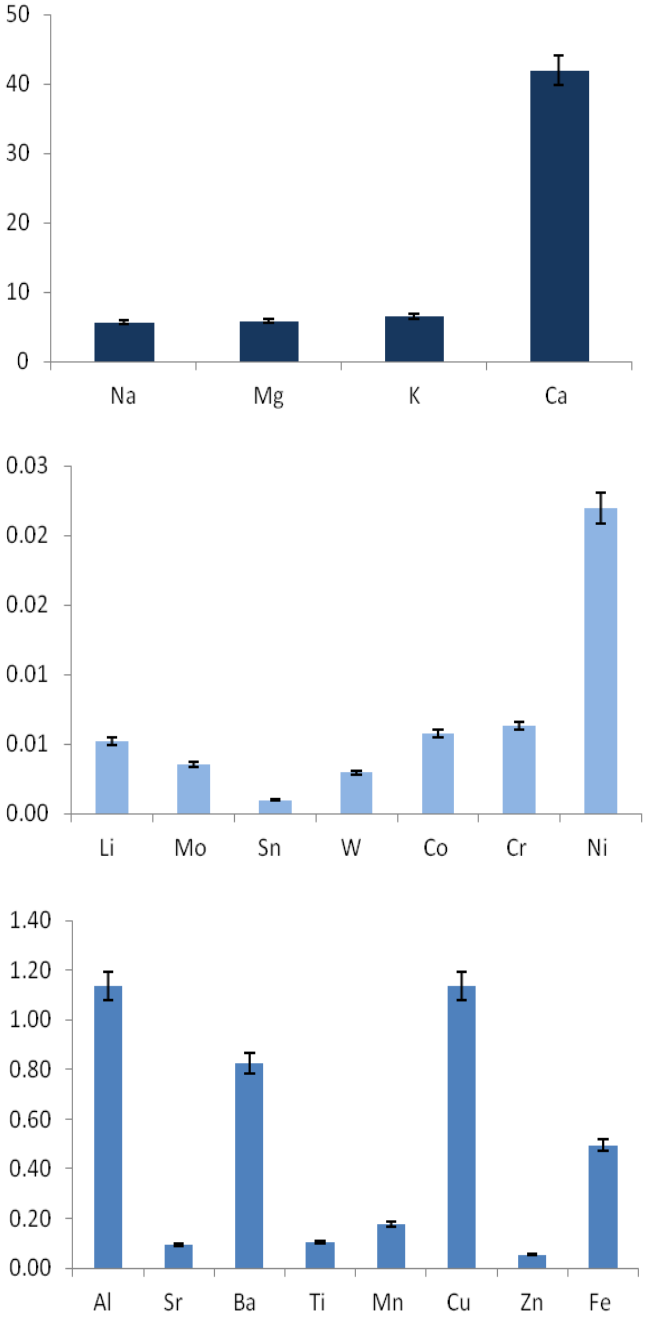

Fig. 6.16. Concentrations (mg/Kg) of several elements leached with Milli-Q water in LDG.

The REE concentrations in this samples were really low (see Fig. 6.17); so, perhaps they were not sufficiently leached with Milli-Q water, because they need aggressive

conditions to dissolve them, such as concentrated H_2SO_4 or HCl[93]. Or other possibility could be that there are not high concentrations of REE in these LDG samples.

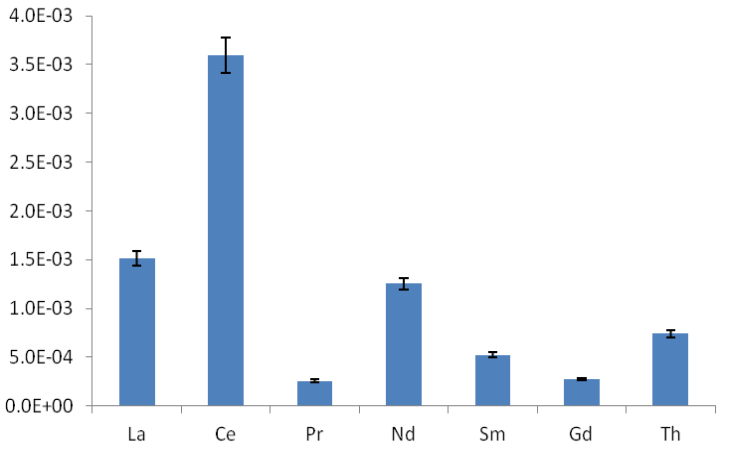

Fig. 6.17. Concentrations (mg/Kg) of several REE leached with Milli-Q water in LDG.

Among the measured anions, it was observed the high leaching of Cl^-, but also SO_4^{2-} and Br^- had an important presence in the leaching with Milli-Q water (see Fig. 6.18). The detection of $C_2O_4^{2-}$ and its quantification definitively verified the presence of oxalate in the sample, previously detected by Raman spectroscopy. This oxalate identification is remarkable because in no other research work about LDG has been mentioned. Moreover, this extractable oxalate must be with an alkaline metal because alkalinearth oxalates are highly insoluble.

[93] V.G. Papangelakis, G. Moldoveanu, Recovery of rare earth elements from clay minerals, ERES2014: 1st European Rare Earth Resources Conference Milos 04-07/09/2014.

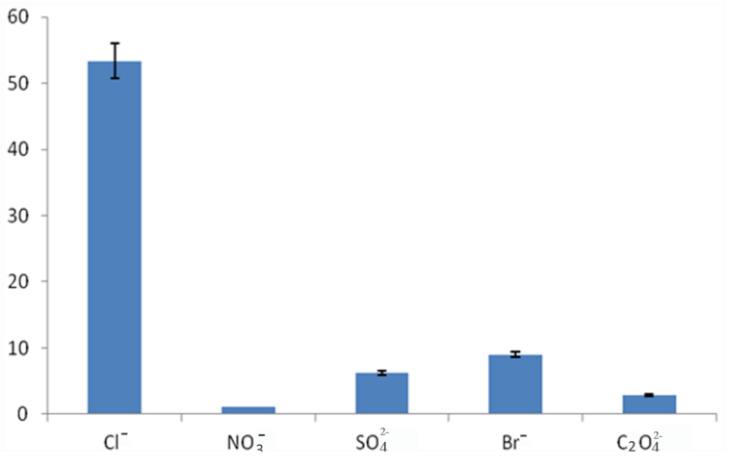

Fig. 6.18. Concentrations (mg/Kg) of the measured anions leached with Milli-Q water in the studied LDG.

F^- was not possible to identify because its peak in the chromatogram appeared split, with more than one peak inside it (see Fig.6.19). According to its position, it could be due to the presence of organic acids of short chain such as formic, acetic, propionic, butyric or benzoic acid. Moreover, apart from that peak, there was another unknown one in a position (t = 5.2 min) that could indicate the presence of another organic acid as well. However, by IC with conductimetric detection it was not possible to identify it.

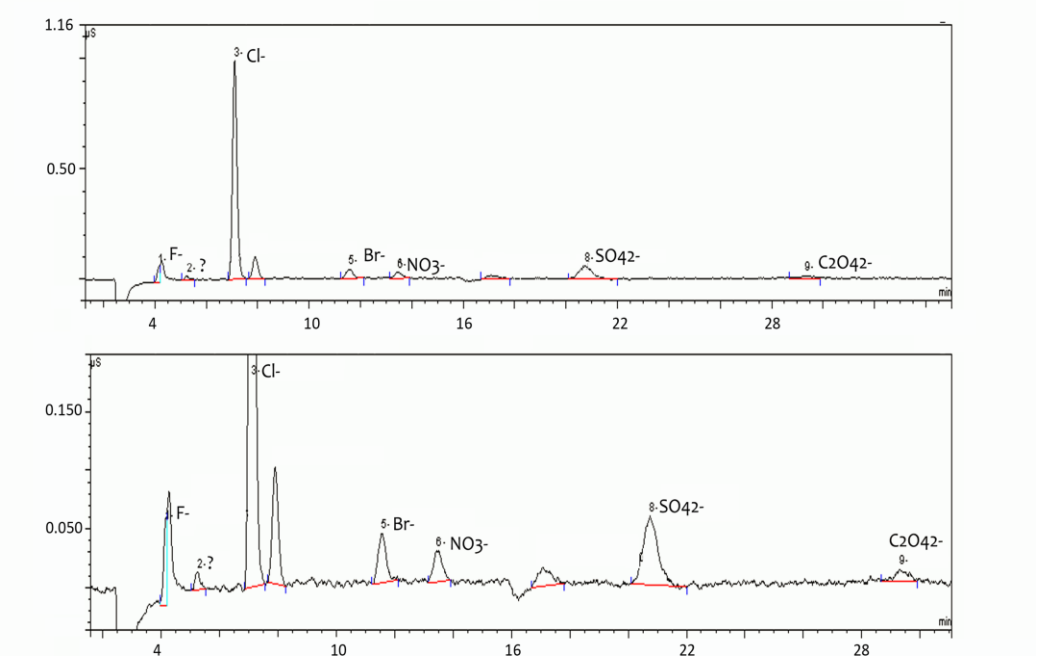

Fig.6.19. LDG sample ionic chromatogram (conductivity (µs/cm) versus detection time (min)) with: F^-, Cl^-, NO_3^-, SO_4^{2-}, Br^- and $C_2O_4^{2-}$, and the unknown peak at 5.2 min (the rest are impurities). The figure below is the upper one but enlarged.

3. GAS CHROMATOGRAPHY MASS SPECTROMETRY (SPME-GC-MS AND HS-GC-MS)

Because of the detection of organic compounds by Raman spectroscopy and possibly by IC in the LDG samples, it was employed GC- MS in order to know what organic compounds were exactly.

By means of HS-GS-MS it was identified n-hexadecanoic acid or palmitic acid (C_{16}-H_{32}-O_2). This compound is a common saturated fatty acid found in fats and waxes including olive oil, palm oil, and body lipids[94].

Their presence is an indication of an active interaction of the LDG with the surrounding environment for thousands or millions of years.

[94] ChemID*plus* A TOXNET DATABASE (http://chem.sis.nlm.nih.gov/chemidplus/).

4. SIMULATION PROCESSES THROUGH CHEMICAL MODELLING

The concentration of anions and metals, obtained in the leaching test with Milli-Q water over a LDG sample, allowed us to simulate the formation of anhydrite and calcite in a same brownish inclusion, at different conditions. These compounds were formerly identified by Raman spectroscopy.

Thermodynamic chemical modelling was carried out using the MEDUSA software with the chemical equilibrium database HYDRA. To perform the simulations we tried to found the chemical conditions to have the simultaneous presence of anhydrite and calcite with the soluble concentration values of Ca^{2+} (0.022 mmol/L), SO_4^{2-} (0.0015 mmol/L) at the dissolution pH (6.57) found in the leaching experiment. We took into account the permanent presence of atmospheric CO_2 (its current concentration value is 1.26 mmol/L) in contact with the LDGs. This can be simulated increasing the H_2CO_3 concentration from the minimum 1.26 mmol/L to a value where the previous chemical conditions are fulfilled. Such situation is presented in Fig. 6.20 where the molar fraction of Ca, SO_4^{2-} and CO_3^{2-} are displayed as a function of pH variations. For an initial anhydrite ($CaSO_4$) concentration of 50.0 mmol/l, we need to increase the H_2CO_3 concentration till 51.2 mmol/L to find at pH=6.57 an equilibrium situation where anhydrite, calcite, soluble calcium and soluble sulfate are simultaneously present.

It is noted that firstly, anhydrite (present at low pH values), in contact with water dissolves partially to Ca^{2+} and $CaSO_4$ species. With the unlimited CO_3^{2-} input, in the point of our pH dissolution (6.57) anhydrite and calcite coexist, which are in accordance with the Raman spectroscopic results. With more time and the unlimited CO_3^{2-} input, the dominant species would be calcite.

$$CO_2\,(g) + H_2O\,(l) \leftrightarrow H_2CO_3\,(aq) \rightarrow HCO_3^-\,(aq) + H^+\,(aq) \qquad (6.10)$$

$$Ca^{2+}\,(aq) + HCO_3^-\,(aq) \leftrightarrow CaCO_3\,(s) + H^+\,(aq) \qquad (6.11)$$

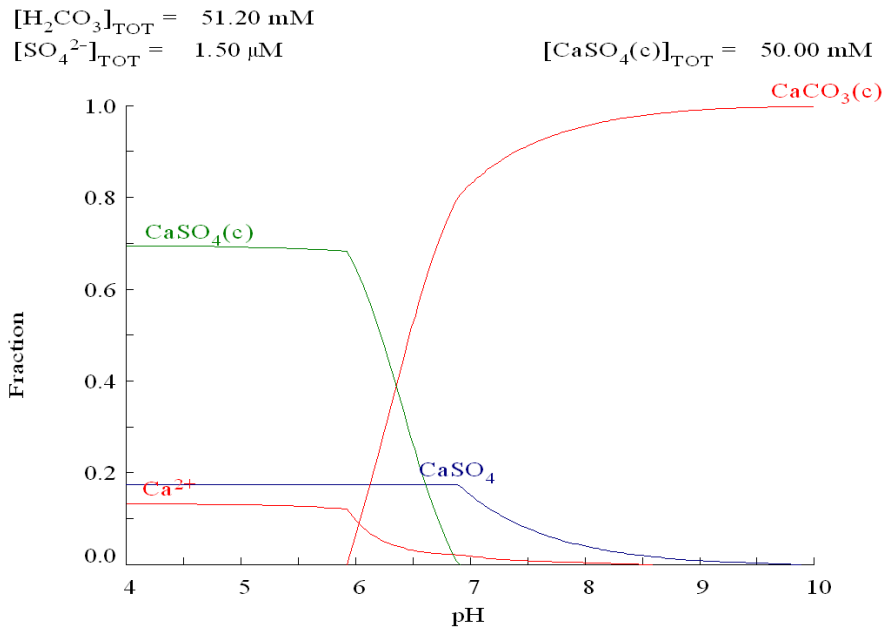

Fig. 6.20. Chemical modeling of $CaSO_4$ and $CaCO_3$ molar fraction facing pH variations.

5. DISCUSSION

LDG are estimated to be 28.5 million years old, so it can be supposed a pronounced weathering process. In this work, weathering processes by water were observed with the identification of limonite and gypsum by Raman spectroscopy. These compounds would have been formed from the hydration of an iron oxide and of a calcium sulphate respectively.

Moreover, organic compound could be observed in the dissolutions of Milli-Q water by means of CI and GS-MS, corroborating the Raman spectroscopy results (see Chapter 4, Part A). It was identified oxalates and n-hexadecanoic acid or palmitic acid (C_{16}-H_{32}-O_2), which could corroborate an active interaction of the LDG with the environment over time. There could be several possibilities. One of them could be that in the moment of LDG formation, the organic matter would be volatilized and decomposed due to the extreme conditions. Therefore, the organic compounds found in these LDG samples would be definitively posterior formations to the impact. However, with the temperature and pressure gradient during the impact glass

formation, there could have been an opportunity to the presence of organic compounds at low temperatures and pressures[95].

On the other hand, by means of chemical modelling it could be seen that with time all the calcium sulphates present in the LDG would pass to calcium carbonate in a constant contact with the terrestrial atmosphere.

In conclusion, the LDG composition could depend on the time factor, because passed a long period of time, the mineral compounds could be transformed by weathering in secondary minerals.

[95] K. T. Howard, M. J. Bailey,D. Berhanu, P. A. Bland, G. Cressey, L. E. Howard, C. Jeynes, R.Matthewman, Z. Martins, M. A. Sephton, V. Stolojan, S. Verchovsky, Biomass preservation in impact melt ejecta, Nature Geoscience 6 (2013) 1018-1022.

D. DARWIN GLASSES (DG)

There are 41 scientific publications related to Darwin Glasses (DG), however, as in the Libyan Desert Glass (LDG), it was not found works centered on the weathering of DG by the contact with terrestrial atmosphere. Hence, here it has been considered studying their weathering, having been in contact with the terrestrial atmosphere a long period, 816 thousand years, which could have provoked the formation of new compounds over the DG.

Tasmania's climate is classified as temperate[96]. The area where DG were collected has an average annual temperatures range between 5–7 °C in winter and 14 -16°C in summer, with 3500 mm rain annually in the uplands and 1200 mm near the coast[97]. Moreover, the temperate forests of Tasmania are really complex and contain species from the time when the island was part of the super-continent Gondwana[98]. Therefore, these conditions could favor the weathering of the DG.

In this part of the chapter, we based on Raman spectroscopy results to describe the mineral compounds produced by terrestrial weathering. Furthermore, we also employed the same sonicated leaching test with Milli-Q water, as in the LDG, to know the leached elements simulating rain. These extractions were measured with Inductively Coupled Plasma-Mass Spectrometry (ICP-MS), Ionic Chromatography (IC) and Gas Chromatography-Mass Spectrometry (Solid Phase Micro Extraction (SPME)-GC-MS and Head Space (HS)-GC-MS) techniques techniques as well. Moreover, simulation processes through chemical modelling complemented the results.

[96] H. Stern, G. De Hoedt, J. & Ernst, Objective classification of Australian climates. Australian Meteorological Magazine 4 (2000) 87-96.
[97] M. S. Fletcher, I. Thomas, Holocene vegetation and climate change from near Lake Pedder, south-west Tasmania, Australia, Journal of Biogeography 34 (2007) 665–677.
[98] Australian Government, Department of the Environment:
http://www.environment.gov.au/land/nrs/science/ibra/australias-ecoregions

1. SPECTROSCOPIC TECHNIQUES RESULTS

The blue-turquoise crystal observed in a α-cristobalite inclusions inside DW3 specimen, it was identified in the Chapter 4: Part B, as a mixture of copper compounds: malachite ($Cu_2CO_3(OH)_2$) and ponsjankite ($Cu_4SO_4(OH)_6{\cdot}H_2O$). They are unusual in these melt products but their presence could be explain by weathering of the samples. Literature confirms that Darwin Glasses were spread 400 km^2 away from the crater[99]; near this area, there is a copper mine (Mt. Lyell copper mine)[100] (see Fig. 6.21). The detected copper compounds were found inside the Darwin specimen, thus, it is proposed that in the impact of the extraterrestrial material the cristobalite was formed and then, when the Darwin Glass fell to the ground after the impact, arrived to a copper enriched soil incorporating new materials while cooling. Alternatively, the copper compounds could have been dissolved in infiltration water and incorporated through the fracture planes, crystallizing inside the glass matrix. Thus, they would not belong to the impact glasses.

Precipitation of copper minerals is considered a common pathway in natural waters with high concentration of copper. Cu precipitates are usually different depending on the surrounding conditions, for example, malachite is the major precipitate in natural waters and copper sulphides in anaerobic or biologically active sediments[101]. Precipitation or dissolution of Cu minerals is determined by the concentrations of the ions involved (Cu^{2+} and the correspondent anion)[100], so in presence of copper enriched waters, the precipitation of these found minerals is very likely.

[99] L. Neil, K.T. Howard, Rareinclusions in darwin glass:partial melts, 45th Lunar and Planetary Science Conference. 2014; 1932.
[100] D.L. Huston, Geochemical dispersion about the Western Tharsis Cu–Au deposit, Mt Lyell, Tasmania, Journal of Geochemical Exploration 72 (2001) 23.
[101] C. A. Flemming, J. T. Trevors, Copper toxicity and chemistry in the environment: a review, Water, Air *and* Soil Pollution 44 (1989) 143-158.

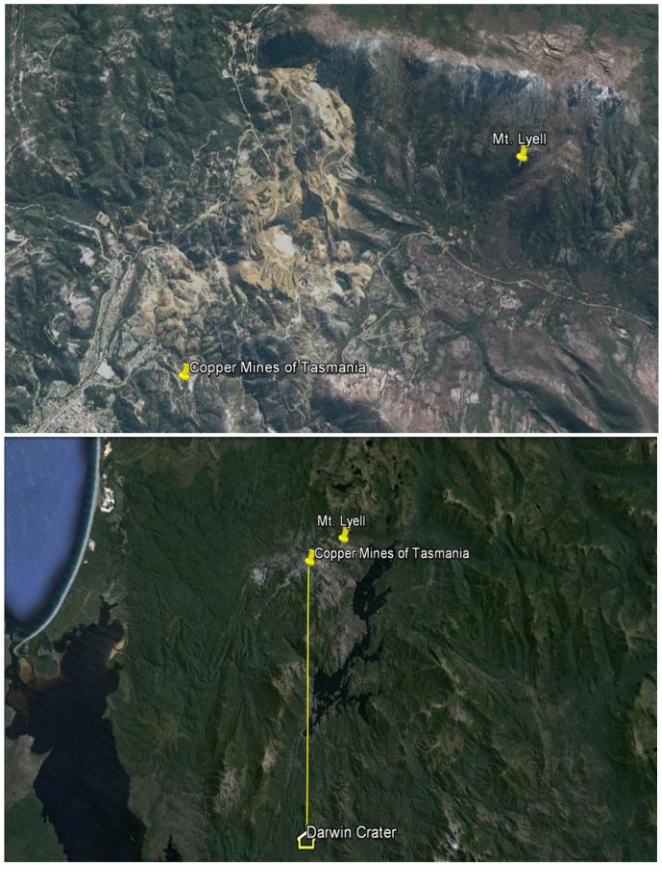

Fig.6.21. Maps of: copper mines of Tasmania (Mt. Lyell) (upper imagen) and approximate distance between Darwin Crater and Copper Mines (26 Km) (below image). Images collected from Google Earth.

2. LEACHING TEST RESULTS: MILLI-Q WATER

It was realized the same sonicated leaching test with Milli-Q water as in the steel slag and LDG samples. Thus, it was simulated what elements would leach due to the weathering provoked by with only water. It was analyzed DW3 and DW4 (see Chapter 4, Part b, Fig. 4.28) due to the fact that they are DG of different type. The measurements by ICP-MS and IC were realized in triplicate.

Ag, Al, As, Ba, Ca, Cd, Co, Cr, Cu, Fe, Hg, K, Li, Mg, Mn, Mo, Na, Ni, Pb, Sb, Se, Sn, Sr, Ti, Tl, V, W and Zn were measured. However, there was not Ag, and the following ones were below the detection limit in both samples: Sb(LOD_{Sb} : 0.36 µg/kg), Hg (LOD_{Hg}: 1.5 µg/kg), Tl (LOD_{Tl}: 0.010 µg/kg), Pb (LOD_{Pb}: 11 µg/kg), As (LOD_{As}: 0.31 µg/kg), Se

(LOD_{Se}: 0.31 µg/kg), Cd (LOD_{Cd}: 0.029 µg/kg) and V (LOD_{V}: 0.37 µg/kg). In the case of DW4, Na was under LOD (LOD_{Na}: 120 µg/kg), and in DW3, Fe (LOD_{Fe}: 8.2 µg/kg). Moreover, as in the LDG samples, it was measured the following REE: La, Ce, Pr, Nd, Sm, Eu, Gd, Tb, Dy, Ho, Er, Tm, Yb, Lu, Th and U. But, there were not Tb, Ho and Er. The following ones were below the LOD in both samples: Dy (0.0038 µg/kg), Tm (0.0050 µg/kg), Yb (0.0010 µg/kg), Lu (0.0038 µg/kg), Sm (0.0042 µg/kg) and U (0.0072 µg/kg); and La (0.0087 µg/kg), Ce (0.0.11 µg/kg), Pr (0.0036 µg/kg), Nd (0.0038 µg/kg), Gd (0.0018 µg/kg) and Th (0.0026 µg/kg) in DW3. In addition, F^-, Cl^-, NO_3^-, SO_4^{2-}, Br^- and $C_2O_4^{2-}$ were measured. Br^- and $C_2O_4^{2-}$ did not appear in DW4.

The most leached element in both samples was Ca, but DW3 had a much higher value than DW4. Then, Mg>Ba>K>Na presented the highest concentration values in DW3, and Mg>K>Ba in DW4. After, in the DW3 appeared Cu>Sr>Al>Mn>Zn concentration values, and in the DW4 Al>Fe>Zn>Sr>Cu>Mn. The elements with the lowest concentration values were Ni>Mo>Ti>Co>Li>Cr>W>Sn in DW3, and Ti>Ni>Li>Mo>Cr>Co>W>Sn in DW4 (see Fig. 6.22).

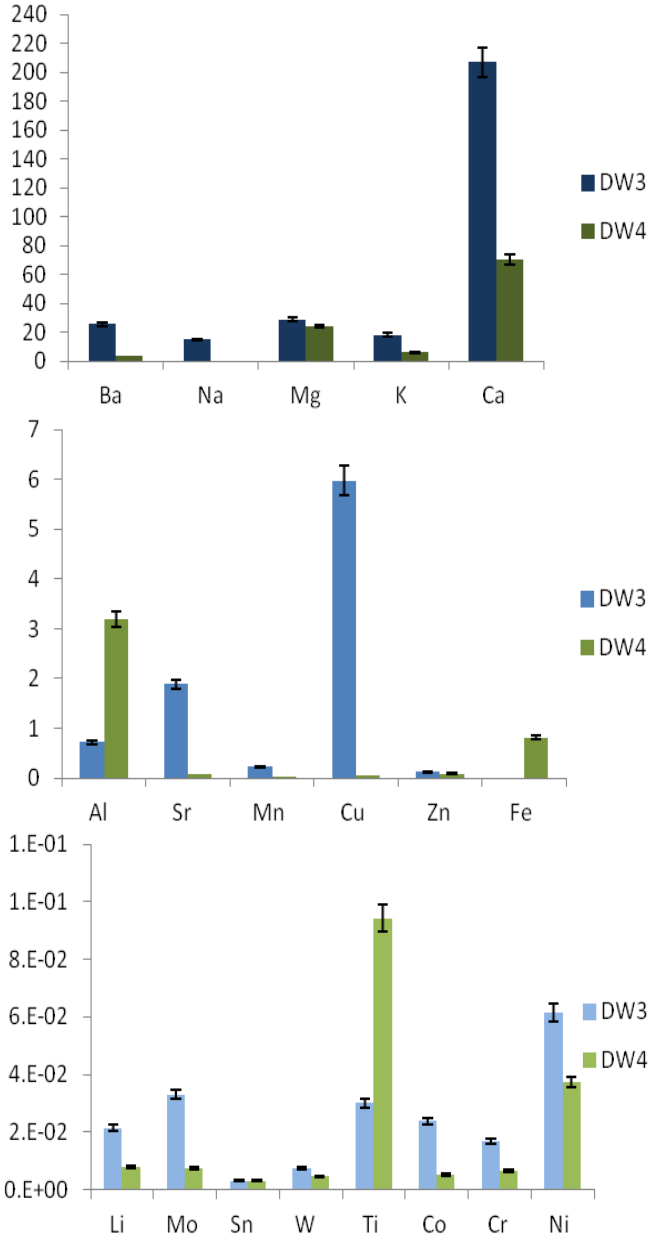

Fig. 6.22. Concentrations (mg/Kg) of several elements leached with Milli-Q water in a DG samples.

It could be observed that the cooper was more leached in the DW3 sample, which was the sample where it was identified the copper sulphate and carbonate by Raman spectroscopy.

Regarding REE, their concentration were really low (see Fig. 6.23), above all in the DW3 which had the majority of the REE below the LOD, with the exception of Eu that

had the highest value. Therefore, the quantity of REE leached with Milli-Q water is insignificant in these Darwin Glasses.

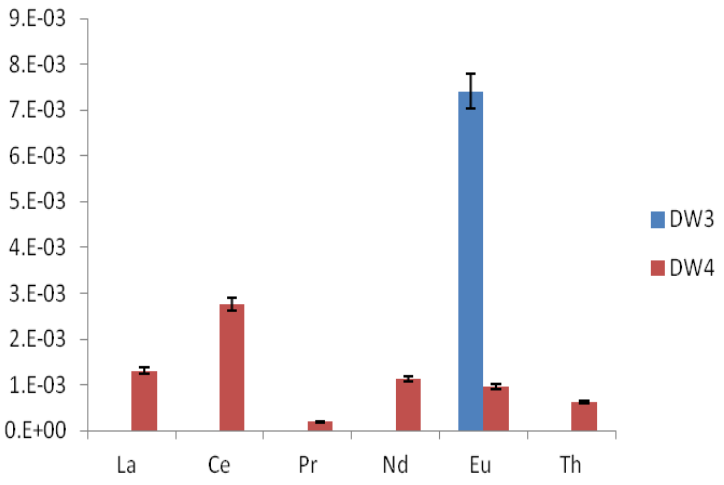

Fig. 6.23. Concentrations (mg/Kg) of several REE leached with Milli-Q water in a Darwin Glass sample.

K. T. Howard (2008)[102] measured also REE in DG through Laser Ablation Inductively Coupled Plasma Mass Spectrometry (LA-ICPMS). It was compared their La, Ce, Pr, Eu and Th concentrations, and their samples presented higher concentrations (35, 79, 8, 13 and 14 mg/Kg respectively). Perhaps, the methodology used in that work was more advantageous to measure those elements.

Among the measured anions, it was observed the high leaching of Cl^-, as in the case of LDG, but also of SO_4^{2-} and NO_3^-. The high concentration of Cl^- in LDG and DG could have its origin in the proximity to the sea (Mediterranean Sea or Red sea in the case of LDG and the Indian Ocean in the DG). Br^- and $C_2O_4^{2-}$ had lower concentration values and they were only detected in the DW3 sample (see Fig. 6.24). The detection of $C_2O_4^{2-}$ could be indicating the presence of possible oxalates.

[102] K. T. Howard, Geochemistry of Darwin glass and target rocks from Darwin crater, Tasmania, Australia, *Meteoritics & Planetary Science* 43 (2008) 479–496.

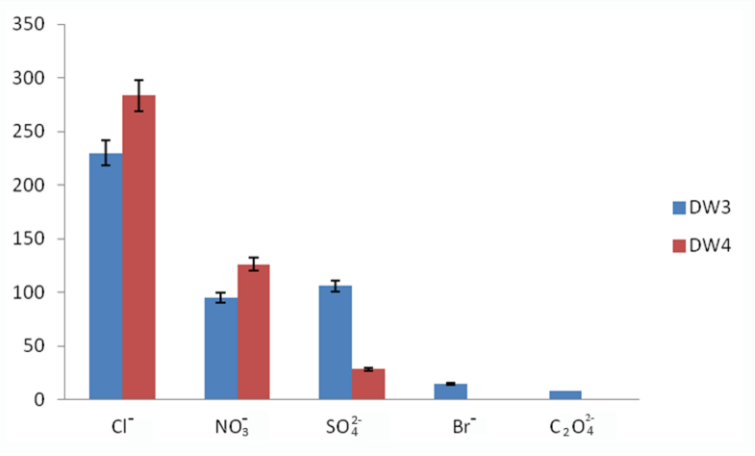

Fig. 6.24. Concentrations (mg/Kg) of the measured anions leached with Milli-Q water in a DG.

F^- was not possible to identify because its peak in the chromatogram appeared split, with more than one peak inside it (see Fig.6.25), just as in the LDG IC analysis. So, it could be due to some organic acids of short chain. Moreover, as in LDG chromatograms, it appeared the same unknown peak that could show the presence of another organic acid.

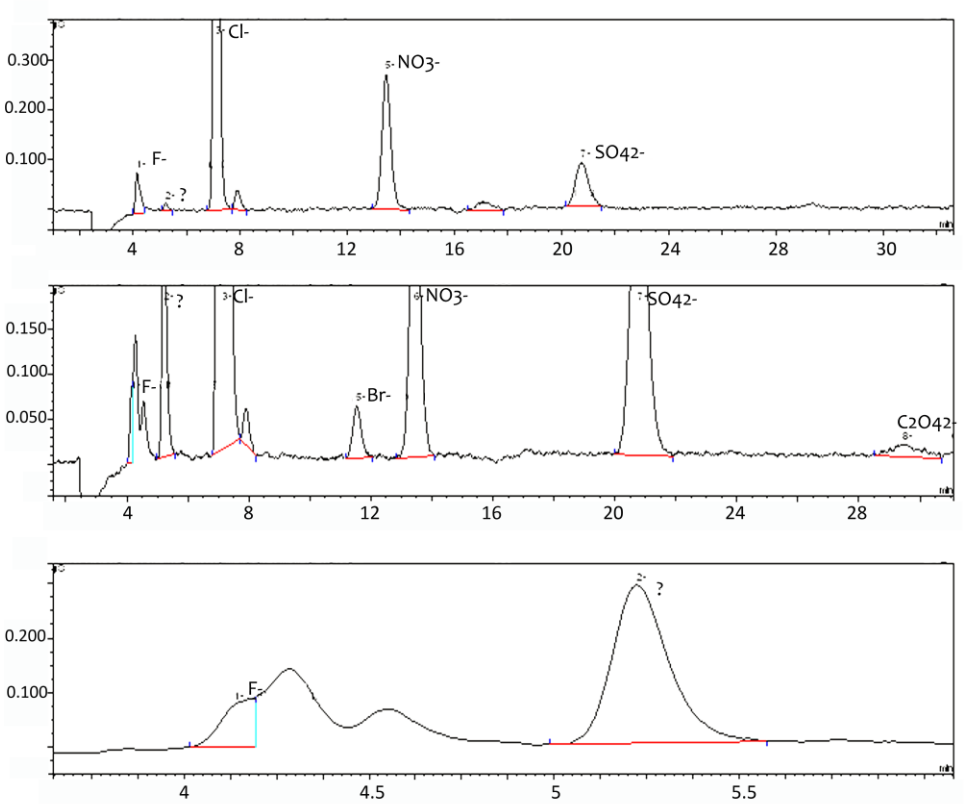

Fig.6.25. DW3 and DW4 ionic chromatograms (conductivity (μs/cm) versus detection time (min)) of: F^-, Cl^-, NO_3^-, SO_4^{2-}, Br^- and $C_2O_4^{2-}$, and the unknown peak at 5.2 min (the rest are impurities). The third figure is the second one but enlarged.

3. GAS CHROMATOGRAPHY MASS SPECTROMETRY (SPME-GC-MS AND HS-GC-MS,)

As a consequence of the detection of possible organic compounds by Raman spectroscopy and possibly by IC, it was employed Gas Chromatography- Mass Spectrometry (GS-MS) in order to identify what organic compounds were present in the DG samples. It should be noted that it was only found a publication with respect to organic compounds in Darwin Glasses (K. T. Howard et al. (2013))[103].

[103] K. T. Howard, M. J. Bailey,D. Berhanu, P. A. Bland, G. Cressey, L. E. Howard, C. Jeynes, R.Matthewman, Z. Martins, M. A. Sephton, V. Stolojan, S. Verchovsky, Biomass preservation in impact melt ejecta, Nature Geoscience 6 (2013) 1018-1022.

In this work, in the DW3 by SPME-GS-MS it was identified cyclohexanol,5-methyl-2-(1-methylethyl)-, (1.alpha.,2.beta.,5.alpha.); 4-Chlorobenzalacetone ($C_{10}H_9ClO$) and 1-Naphthalenecarbodithioic acid, ethyl ester ($C_{13}H_{12}S_2$). Instead, in the DW4 by the same injection it was differentiated 1,2-Benzenedicarboxylic acid, bis(2-methylpropyl) ester or Phthalic acid ($C_{16}H_{22}O_4$).

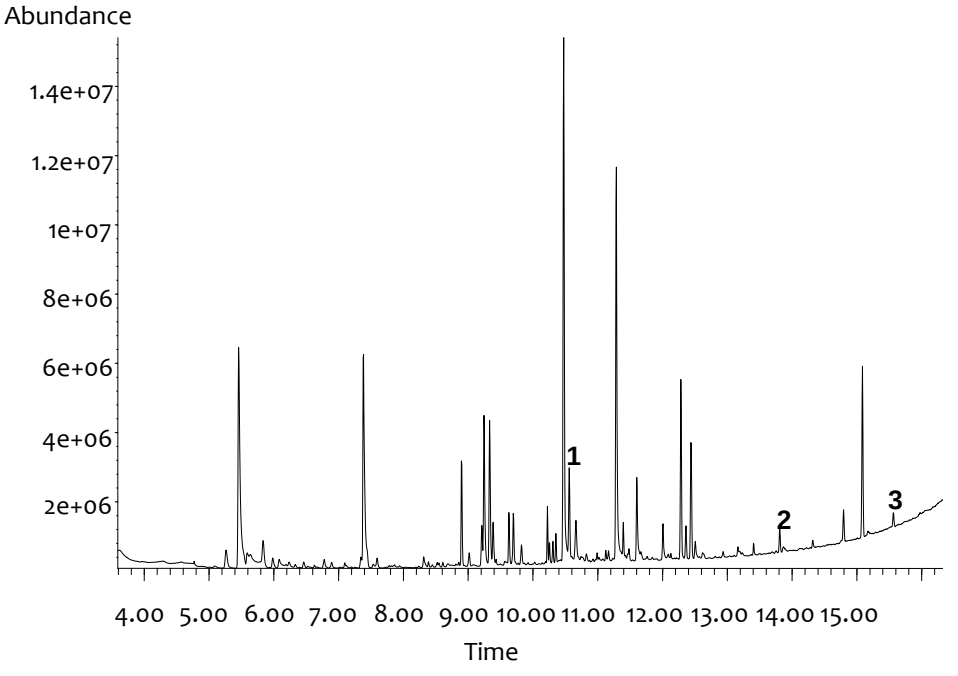

Fig. 6.26. DW3 gaseous chromatogram of 1: cyclohexanol,5-methyl-2-(1-methylethyl)-, (1.alpha.,2.beta.,5.alpha.), 2: 4-Chlorobenzalacetone and 3: 1-Naphthalenecarbodithioic acid, ethyl ester. The rest of the signals belong to the equipment column, others were also in the blanks and others were not possible to identify due to the low levels of coincidence with other compounds.

4. SIMULATION *PROCESSES THROUGH CHEMICAL MODELLING*

With the data obtained from ICP-MS in the leaching test with Milli-Q it was simulated the formation of compounds formed by weathering in the Darwin Glasses such as covellite (CuS), malachite ($Cu_2CO_3(OH)_2$) and ponsjankite ($Cu_4SO_4(OH)_6{\cdot}H_2O$), identified by Raman spectroscopy in the same sample (DW3).

The thermodynamic chemical modelling was performed with the same software and database as in the LDG samples. Our best chemical model assumed the initial presence of CuS (we have chosen a total concentration of 4 mmol/L) in equilibrium with soluble sulphate SO_4^{2-} at 0.82 mmol/L and considering the current H_2CO_3 concentration (1.26 mmol/L), the dissolution pH (6.52) and a potential redox around 0.10V. The temperature used was 25°C and the modelling was performed as a function of pH. In the Fig. 6.27 it can be seen the molar fraction of CuS, SO_4^{2-} and CO_3^{2-} depending on the pH variations. The CO_3^{2-} concentration value was that of normal atmospheric conditions (Fig. 6.27.a), but finally it was duplicated to simulate conditions of permanent contact with carbonic acid (accumulation of this component) from the atmosphere (Fig. 6.27.b).

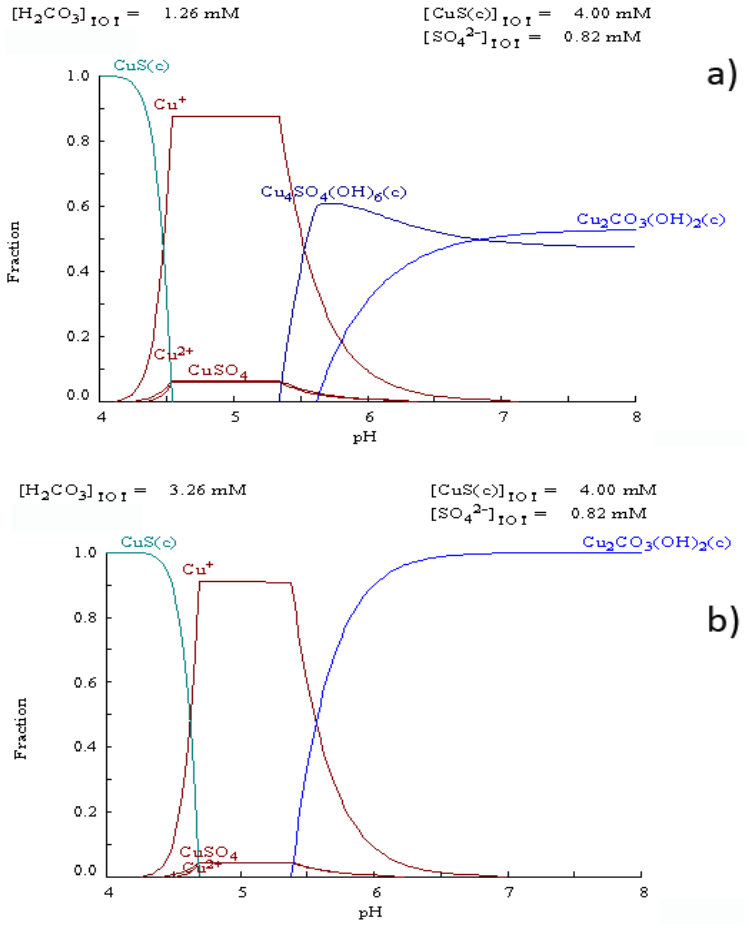

Fig. 6.27. Chemical modeling of malachite ($Cu_2CO_3(OH)_2$) and ponsjankite ($Cu_4SO_4(OH)6{\cdot}H_2O$) molar fraction facing pH variations, with normal carbonic conditions (a) and higher concentrations of its value (b).

The original compound would be CuS at low pH, but under the oxidizing conditions of the terrestrial atmosphere would pass to sulphates. In this case ponsjankite ($Cu_4SO_4(OH)_6{\cdot}H2O$) was identified by Raman spectroscopy IN THE DW3 sample. Moreover, at our pH dissolution (6.52) would have ponsjankite ($Cu_4SO_4(OH)6{\cdot}H_2O$) and malachite ($Cu_2CO_3(OH)_2$), in accordance with the Raman results. With time and and with the consequent unlimited CO_3^{2-} input, it would be only the carbonate, malachite ($Cu_2CO_3(OH)_2$).

5. DISCUSSION

Terrestrial weathering processes by exposition to the Earth atmosphere for a long time (816 thousand years) were evident in the Darwin Glasses, because it could be observable their transformation into mineral compounds such as malachite ($Cu_2CO_3(OH)_2$) and ponsjankite ($Cu_4SO_4(OH)_6{\cdot}H_2O$) with the support of chemical modeling and Raman spectroscopy. Efflorescences of this type have been described above all in Antartic meteorites[104]. According to literature those efflorencences are not detectable with the unaided eye (less than a 5%). However, the DW3 study is really interesting, since its efflorescences are larger, covering more or less 40% of the specimen matrix, as it can be seen in the Fig.4.27.d of the Darwin Glasses in the Chapter 4, Part B.

Ca, Mg, Ba, Na and K were the most leached elements simulating rain water in both samples. Afterwards, Al, Sr, Mn, Cu, Zn and Fe were the following elements which presented higher concentration values.

Given the results of the impact glasses leaching tests, they could be applicable to other extraterrestrial materials.

The organic compounds identified in the aqueous solutions, such as cyclohexanol,5-methyl-2-(1-methylethyl)-, (1.alpha.,2.beta.,5.alpha.); -Chlorobenzalacetone ($C_{10}H_9ClO$), 1-Naphthalenecarbodithioic acid, ethyl ester ($C_{13}H_{12}S_2$) and 1,2-Benzenedicarboxylic acid, bis(2-methylpropyl) ester or Phthalic acid ($C_{16}H_{22}O_4$),

[104] M. A. Velbel, D. T. Long, J. M. Gooding, Terrestrial weathering of Antarctic stone meteorites: Formation of Mg-carbonates on ordinary chondrites. Geochimica et Cosmochimica Acta 55 (1991) 67-76.

confirmed the interaction of the Darwin Glass with the environment. In addition, it is stated that the temperature at the moment of the impact and the Darwin Glass formation should be high enough to convert organic molecules to gas phases, removing the life at the impact site and vaporizing organic biomass. Nevertheless, there is always a gradient of temperatures and pressures, so there could be a chance of survival at relatively low temperatures and pressures, after modifications of organic compounds. The presence of CO, CO_2 and hydrocarbon gases could be a clue to organic precursors in high-velocity impact glasses. Moreover, the presence of nitrogen compounds could be indicative of protein remnants. The oxygen would have to be restricted during the impact and after, since oxidation break organic materials. Therefore, they could be trapped inside the Darwin Glass in a low-oxygen environment[105].

Unlike LDG samples, DG did not present so many mineral compounds. However, their weathering was more evident, maybe because of the vicinity of the area where they were collected, with the copper mines, or the higher influence of other factors such as more rain or more vegetation.

[105] K. T. Howard, M. J. Bailey,D. Berhanu, P. A. Bland, G. Cressey, L. E. Howard, C. Jeynes, R.Matthewman, Z. Martins, M. A. Sephton, V. Stolojan, S. Verchovsky, Biomass preservation in impact melt ejecta, Nature Geoscience 6 (2013) 1018-1022.

CHAPTER 7

INTEGRATED DISCUSSION AND CONCLUSIONS

In this concluding chapter an integrated discussion of the results shown in this PhD manuscript is presented, highlighting the most significant conclusions.

According to NASA requirements about Mars study, which must go beyond the mapping and center on detailed analysis at the regional to outcrop level, it was considered crucial to optimize the choice of instruments and their operating parameters by means of testing and interpretation of their data in terrestrial analogs to Mars, such as rock and minerals analogs, as well as Mars meteorites and environments on Earth.

Following the previous proposal, the main objectives of this work were to develop methodologies to the characterization of Libyan Desert Glasses (LDGs) and Darwin Glasses (DGs) (terrestrial-extraterrestrial materials), and steel slag samples (terrestrial analogs to meteorites), which allowed us to test the analytical instruments that we had at our disposal as well; and the study of the terrestrial weathering over this type of materials.

For that purpose, techniques such as Scanning Electron Microscopy with Energy Dispersive X-ray spectroscopy (SEM-EDX), Raman spectroscopy and Laser-Induced Breakdown Spectroscopy (LIBS), included in the recommended instruments, were employed to test over our samples (LDG, DG and steel slag). Moreover, other analytical techniques such as cathodoluminiscence, Micro-Energy Dispersive X-Ray Fluorescence Spectroscopy (μ-EDXRF), Electron Microprobe Analysis (EPMA) and (d) X-Ray Photoelectron Spectroscopy (XPS), Structural and Chemical analyser (SCA), X-Ray Diffraction (XRD), Inductively Coupled Plasma-Mass Spectroscopy (ICP-MS), Ionic Chromatography (IC) and Gas Chromatography-Mass Spectroscopy (GC-MS) were also used in different extent to complete the characterization of the materials.

The use of those analytical techniques permitted us to acquire knowledge about the response to them over these type of samples, and therefore, to facilitate future analysis of samples with similar formations and composition.

By means of Raman spectroscopy, it was possible to determine the effect of the pressure, temperature and water presence over the samples. Thus, it was known the temperatures and pressures at which samples were subjected, and their weathering compounds.

A wide range of mineral phases were found in all the studied samples. In the LDGs and DG, some of these phases are related to high and low temperatures and pressures, such as α-quartz, the low-temperature stable polymorph of SiO_2, which is converted by heating into β-cristobalite at 1470 °C; α-cristobalite, which is normally created on cooling process by transformation of its internal crystal structure from original higher temperature β-cristobalite. Therefore, the presence of α-cristobalite indicated the former presence of β-cristobalite and hence a temperature greater than 1470 °C and the following cooling process. Moreover, the effect of high temperature on the LDGs was also supported by the presence of a fullerene-type compound in a black inclusion reinforces this hypothesis because this high ordered compound can be formed at high temperatures (> 1800K) or at low temperature and medium pressure (15 GPa and 670K), rutile, which could be formed thermically from anatase to high temperatures. On the other hand, the high pressure conditions were corroborated by the presence of coesite (high-pressure polymorphs of quartz,

>30GPa, a strong indicator of formation from extraterrestrial impact) and aragonite. And the low pressure in LDG, settled state, was confirmed by calcite.

In comparison with DG, the origin of LDG might be not so clear because of the lack of impact crater associated. However, those mineral phases identified would be indicating the LDG formation by an extraterrestrial body impact due to the high pressure and temperature required to form some of the mineral phases, not reached by natural processes in the Earth, such as volcanic, tectonic processes or static load pressures produced by the weight of overlying rocks, and the subsequent cooling, with the corresponding low pressure and temperature mineral phases.

At first we thought that the distribution of the LDG compounds was: high pressure and temperature ones inside the samples, trapped during the impact; and the low pressure and temperature ones, in the superficial part, in contact with atmospheric conditions. Nevertheless, some compounds such as coesite, corundum (stable at 1200ºC) and anatase were found in inclusions of both inner and outer part of the LDG. Hence, we did not find a logical distribution of these compounds unless the LDGs suffered more than one impact when cooling but still in a melt form. Besides, depending on the time of fly, the areas of the LDG could not be cooled in the same way. Thus, the cooling could have been inhomogeneous and this is translated to the nature of the mineral phases trapped in the inclusions of the different LDGs that arrived to us.

Furthermore, bubbles were observed in the LDGs. They contained oxygen gas, nitrogen gas, liquid nitrogen and a compound attributable to carbon-nitrogen bonds. Fluid inclusions could have been trapped during boiling of geothermal/hydrothermal fluids. And gaseous vesicles could have been formed in the melt with a decrease of the solubility of dissolved gases, due to changes of the physical conditions (temperature, pressure, oxygen fugacity). Therefore, the formation of bubbles should have occurred during the impact moment.

The atmosphere, deposits, sands of the Libyan Desert and sandstones of the Tasmania region could be responsible for some compounds identified in the LDG and DG, incorporated in the moment of the impact(s) such as silicon oxides, cinnabar, carbonates (magnesite and calcite), anhydrite, gypsum, and pyroxenes (fosterite and

enstatite) in the LDGs, and silicon oxide, malachite, ponsjankite and covellite in the DGs. But, we cannot assign these compounds exclusively to a terrestrial contribution.

In addition, Raman bands that could imply the presence of oxalate in LDG were detected. The presence of oxalates is widespread in nature and they are formed by reaction of metals and oxalic acid excreted from fungi, lichens and plants. Therefore, LDG samples could have been colonized by microorganisms, something that it has not been reported so far in this type of samples.

The presence of organic molecules in both, LDGs and DGs, must be highlighted. In the LDGs the Raman spectra identified among the different organic molecules the presence of hydrocarbons. In the DG, it was also recognized Raman bands related to organic compounds, which could belong to aromatic hydrocarbons and Polycyclic Aromatic Hydrocarbon (PAHs). The origin of these hydrocarbons would be by any organic material that has been transformed at high temperature. PAHs can be formed by incompletely carbonized or combusted of organic matter at high temperature (500–700°C) over very short time periods. The occurrence of PAHs in non-common materials has been reported in the literature, like in amorphous superheated glassy mineraloid, asteroid, comet and meteorites.

With respect to the analysis of the steel slag materials from Electric Arc Furnace (EAF) production, considered as a terrestrial analogue to meteorites and connected to glassy materials because their composition is expected to be similar due to the fact that they have silicate matrixes and are produced at high temperatures, it allowed us to develop an innovative analytical procedure, based on the combination of Raman spectroscopy, μ-EDXRF and SCA (SEM-EDX+Raman). Thus, it was possible to perform a complete mineralogical and elemental characterization of any material subject of high temperatures during their formation.

The mineralogical composition of the black steel slag produced in Electric Arc Furnace included above all oxides (and sometimes hydroxides) of iron, silicates, carbonates, sulfates and amorphous carbon.

The treatment suffered by the slag, prior to its reuse as a secondary inert material, did not cause a significant change in the slag composition, only in the relative

presence of some compounds. The main difference between "treated slag" (principally washed with water for three months) and "original slag" was the presence of hydroxides (as lepidocrocite, goethite and limonite for iron), formed from the hydration of oxides (hematite mainly for iron) during the addition of water in the treatment carried out in each factory. In spite of this, in some occasions, it could be appreciated hydroxides in the slag without treatment, possibly owing to their interaction with the environmental atmospheric humidity. Besides, these hydroxides could transform to carbonate, and also it can decrease the iron materials in the case of slag from common steel, owing to the magnetic separation.

Moreover, nitrates (nitratine), sulfates (ilesite, bassanite and gypsum) and a great amount of carbonates (natron, vaterite and calcite) were observed mainly in the treated slags. Those products that originally are not in the slag and probably they would have appeared with the cooling process outdoors, due to the interaction of the original mineral phases with atmospheric acid gases and water.

Regarding calcite, in some cases its Raman bands were shifted, mostly due to the substitution of Ca atoms by Mg, with the subsequent formation of high magnesium calcite. In their Raman spectra, wavenumbers increased when the magnesium percentage augmented. Apart from this, aragonite was also present, mixed with high magnesium calcite. In these cases, it was not possible to calculate the magnesium percentage because their bands did not follow the same trend that the high magnesium calcite alone.

The analytical approach used in this work was of great usefulness. Major compounds can be easily identified by portable equipments while minor compounds require the use of Raman microscopy. The possibility to analyze the same point with Raman spectroscopy and SEM-EDS (SCA) facilitated the identification of trace compounds. XRD and XRF complemented and corroborated the Raman and SCA analysis.

XPS analysis together with Raman image permitted to show the widespread carbonation produced either by the water treatment in the steel slag surfaces or by the long term simple interaction with atmospheric CO_2 and humidity.

Apart from the slags collected from the furnace, old steel black and white steel slag materials deposited outside for years brought us a situation closer to that experienced by the LDG and DG.

There were differences in the mineralogical composition of these black and white steel slag samples. The chemical composition of black steel slag is more complex, in terms of the different compounds detected (hematite, magnetite, goethite, lepidocrocite, akaganeite, wüstite, magnesioferrite, calcite, vaterite, HMC, portlandite, brucite, quartz, larnite, tephroite, merwinite, thaumasite, szomolnokite, hashemite and crocoites), than the white one (magnesioferrite, calcite, quartz, cristobalite and mullite), according to Raman spectroscopy, XRD analysis and SEM-EDX.

It is remarkable, the identification of α-cristobalite in the white slag samples. In all of the compounds identified in the black slag samples, whenever its provenance, nothing related to molecular species formed at high temperature was confirmed. However, the only family of samples related to white slag materials revealed the presence of α-cristobalite, the stable form of quartz at high temperature (>1470^{o}C). This fact showed a clear indication of the different temperatures reached in the formation of black slag (<1300-1600ºC) during the primary metallurgy and white slag (>1700ºC) in the refined phase of the steel production.

In addition hashemite and crocoite were identified in the slag. They should be controlled in order to avoid, or at least minimize, the possible leaching of Cr(VI) and/or Cr(III) in the soil and their corresponding environmental consequences.

Beyond the identification of organic compounds by Raman spectroscopy, it was feasible to detect them in the solid samples through Pyrolysis- Gas Chromatography-Mass Spectroscopy (Py-GC-MS) with three temperatures (280ºC, 600ºC and 750ºC). In LDG and DG, most of the compounds appeared at 600ºC. Thus, this technique, in the LDG samples allowed us to identify hydrocarbons related to components of plants such as 1-nonanol, decanal, styrene and p-cresol, and on the other hand, others representative of bacterial life like also p-cresol and indole. In the DG samples it was determined also hydrocarbons related to components of plants such as 1-nonanol, decanal, styrene, p-cresol, β-d-mannofuranoside, O-geranyl and 1,4:3,6-Dianhydro-

.alpha.-d-glucopyranose. And moreover, compounds associated with bacterial life and animals were detected, such as p-cresol, indole and cholesta-3,5-diene.

The resistance of those compounds at the temperatures used in the analysis is surprising. Therefore, it is unclear whether their origin is before or after the impact of the extraterrestrial body on the Libyan Desert. Their resistance at those temperatures could mean that the compounds may predate the impact.

In the case of steel slag, both that collected directly from the factories and that from the forest tracks, organic compounds were not present to a large extent. It was only identified some long-chain hydrocarbon and aromatic hydrocarbons in the former, and an aliphatic and aromatic hydrocarbons in the latter. These compounds would be subsequent to the slag formation due to the high temperatures in the steel production.

Moreover, by means of portable LIBS equipment it was possible to quantify several elements in the samples by calibration approach without realizing any type of pre-treatment. Firstly, the homogeneity of the powder pellets used to make the calibration curve was corroborated through SEM-EDX and Raman image. Then, it was tried an univariate calibration, but the calibration models presented low linearity and correlation coefficient. Hence, multivariate calibration was used to quantify Fe, Mg, Si, Al, Ba, Na and Ca using UV and NIR spectral ranges, after a comparison between these spectral ranges together and separately. The validation of PLS models performed using a sample not belonging to the calibration data set, a slag reference material, gave excellent results to Fe, Mg and Si, and satisfactory for Al and Ca. The Rreference material has not certificated values for Ba and Na. We concluded that the PLS approach provided better predictions that the univariate calibration.

Concerning the weathering, it was observed mainly by Raman spectroscopy. In the fresh steel slag from the factories, the weathering by hydration was obserded as some compounds with hydration water molecules and hydroxides were clearly identified: lepidocrocite, goetite, limonite, ilesite, gypsum, bassanite, natron, brucite and monohidrocalcite. Moreover, other compounds that can only be formed by the interaction with atmospheric acid gases (CO_2 and NO_x) (natron, monohidrocalcite, calcite, high magnesium calcite (HMC), aragonite and nitratine) were also identified.

Weathering of the forest track steel slags, located at the temperate climate zone, was observed with the presence of goethite, lepidocrocite, akaganeite, calcite, vaterite, HMC, szomolnokite, brucite, portlandite and thaumasite in the black steel slag, formed by the reactivity of the slags in contact with the atmosphere of this area (humidity, atmospheric CO_2 and SO_X acid gasses), no originals from the steel production. In the white steel slag is also observable this reactivity through the presence of calcite (carbonation).It should be noted that the presence of brucite, portlandite and thaumasite in the black slag is indicating a high physical stress due to the volume increase promoted by these compounds and therefore, the corresponding damage to the forest track road structure because of its disintegration. In fact, the road breakage is visible right now, and it should be repaired. Moreover, the fractures can provoke that water can access the inner parts of the slags and more compounds can be leached from the slag to the surrounding areas by rain water runoff.

LDG are estimated to be 28.5 million years old, so it can be supposed a pronounced weathering process. Limonite and gypsum were weathering products formed by hydration in the Libyan Desert. During weathering by hydration, hematite can be transformed into limonite, which can be formed within a few tens of years and often fill cracks and mineral fractures, together with terrestrial quartz grains and carbonates. In the case of gypsum, it could have been formed from the anhydrite hydration, given the long period of time from LDG formation. During this time, there were some periods with large quantity of water in the current Libyan Desert, so through cracks or fissures connected to the LDG surface it could have been explained the presence of water crystallization in the interior of the LDG, and therefore, hydrated mineral compounds could be present.

Terrestrial weathering processes by exposition to the Earth atmosphere for a long time (816 thousand years) were evident also in the Darwin Glasses, because it could be observable their transformation into mineral compounds such as malachite ($Cu_2CO_3(OH)_2$) and ponsjankite ($Cu_4SO_4(OH)_6{\cdot}H_2O$), due to the presence of a copper mine near the area where DGs were found (Tasmania).

On the other hand, the leaching test with Milli-Q water performed to simulate weathering by rain water allowed us to know that the elements from special steel slag (above all, stainless steel slag) presented the highest concentrations of the majority of the analyzed elements (F^-, NO_3^-, SO_4^{2-}, Ca^{2+}, Al, Fe, Na, B, Cr, K, Li, Ni, Pb, Ti, Cr, Cu, Sr and V). The leaching test with acetic acid was the simulation of extreme acidic conditions when the slag wastes remain for many years in the environment, like the de-carbonation process by the atmospheric acid CO_2 or other acids of organic nature. And in this case, slag samples from common steel factory had the highest concentrations of most of the analyzed elements (Al, Ba, Cu, Fe, K, Li, Mn, Sb, Ti and W), but slags from special steel had the most harmful (Cr, Mo, Ni and V). With nitric/hydrochloric acid dissolution it could be observed that the differences between the slag compositions might be due to the manufacture of common, special or stainless steel, and to the productive process of each slag, according to each steelwork. The differences stem from the concentration of the elements in each slag type. Furthermore, it was remarkable that the highest concentrations of almost all the rest of the measured elements: B, Cr, K, Li, Ni, Pb, Ti and Cr, were in slag samples from stainless steel. So, care must be taken with the use of stainless steel slag, because this type had the highest concentrations and the highest leaching of elements.

In general, with the three extractants, the major elements found in the leachates were Al, Ba, Ca, Fe, Mg, Mn and Na. Although, in the case of Milli-Q extraction, Mn obtained was under the detection limit.

Considering that the most probable situation is the mobilization of the elements towards the environment with water, we focused on this extractant, and by means of PCA, we recognized and classified the unknown samples according to their ions released to the water extracts. The slag soluble composition indicated if it had been manufactured in the production of common, special or stainless steel. Furthermore, because by Raman analysis had shown high presence of calcium silicates in the Electric Arc Furnace slag matrix (in these samples larnite and walstromite were identified), it was simulated the reactions between the calcium and silicates species (not measured by quantitative techniques) through chemical modeling. Thus, it was predicted the formation of different silicates in the slag.

Moreover, when the leaching test were performed over the forest track slags in the laboratory, it could be concluded that in each forest track, the variations of concentration in the slag samples of different sampling points are not very significant, so there is no a strong variation in their composition according to the area where they were collected. This could be due to the fact that the slag samples have been generated in the same type of furnace (EAF). Besides, comparing both forest tracks, the elements which appeared with higher concentrations were Ca, Fe, Mg, and Al, regardless of the extractant used and the point of collecting. Nevertheless, there were some differences between the slag compositions of both forest tracks, with respect to the concentration values.

In addition, results from the analysis of the two rain water samples collected in the forest track with mixture of white and black steel slag showed that some elements go through from the slag to the environment in contact with rain water.

In the impact glasses it was employed the same method as in the steel slag, known the good results obtained with the focused ultrasound energy. The leaching test with Milli-Q water in order to simulate weathering by water was performed. In the LDG, the most leached element was Ca, and after K, Mg and Na. Then, there was another group of elements with lower concentration: Al, Cu, Ba, Fe, Mn, Ti, Sr and Zn. Finally, Ni, Cr, Co, Li, Mo, W and S presented the lowest concentration values. On the other hand, by means of chemical modelling it could be seen that with time all the calcium sulphates present in the LDG would pass to calcium carbonate in a constant contact with the terrestrial atmosphere.

In the DG samples, Ca, Mg, Ba, Na and K were the most leached elements simulating rain water. Afterwards, Al, Sr, Mn, Cu, Zn and Fe were the following elements which presented higher concentration values. Through chemical modelling, it was determined that with time and with the consequent unlimited CO_3^{2-} input, it would be only the carbonate, malachite ($Cu_2CO_3(OH)_2$).

The LDG and DG composition could depend on the time factor, because passed a long period of time; the mineral compounds could be transformed by weathering in secondary minerals.

Furthermore, in the Milli-Q dissolution of the impact glasses it was identified the presence of oxalates and, in the case of LDG n-hexadecanoic acid or palmitic acid, and in the DG, cyclohexanol,5-methyl-2-(1-methylethyl)-, (1.alpha.,2.beta.,5.alpha.); -Chlorobenzalacetone, 1-Naphthalenecarbodithioic acid, ethyl ester and 1,2-Benzenedicarboxylic acid, bis(2-methylpropyl) ester or Phthalic acid. These organic compounds show the interaction of the LDG and DG with the environment over time.

It is stated that the temperature at the moment of the impact and the DG and LDG formation should be high enough to convert organic molecules to gas phases, removing the life at the impact site and vaporizing organic biomass. Therefore, the organic compounds found in these LDG and DG samples would be definitively posterior formations to the impact. Nevertheless, there is always a gradient of temperatures and pressures, so there could be a chance of survival at relatively low temperatures and pressures, after modifications of organic compounds. The presence of CO, CO_2 and hydrocarbon gases could be a clue to organic precursors in high-velocity impact glasses. Moreover, the presence of nitrogen compounds could be indicative of protein remnants. The oxygen would have to be restricted during the impact and after, since oxidation break organic materials. Therefore, they could be trapped inside the DG or LDG in a low-oxygen environment. On the other hand, it could be possible that the organic compound would come with the extraterrestrial body.

Given the results of the impact glasses leaching tests, they could be applicable to other extraterrestrial materials.

Comparing both impact glasses, LDG presented more mineral phases than DG, but the DG weathering was more evident with the efflorescences of the cupper compounds. Besides, DG had higher concentrations of all the measured elements (Li, Al, Sr, Mo, Ag, Sn, Sb, Ba, W, Na, Mg, K, Ca, Ti,Mn , Co, Cu, Zn, Cr, Fe AND Ni) and anions (Cl^-, SO_4^{2-}, NO_3^-, Br^- and $C_2O_4^{2-}$) than LDG. The REE concentrations were very low in both samples. The number of organic compounds was higher in the DG as well. This differences could be due to the climate factor (more rain in Tasmania than in the Libyan Desert, and consequently more infiltration water from anywhere) and the abundant vegetation and fauna of the area where the DGs were discovered.

We concluded that impact glasses are very good markers about what happened around them, since they are able to keep compounds, both inorganic and organics, in their inclusions without the influence of high pressures and temperatures.

CHAPTER 8

APPENDICES

APPENDIX I. Future works

APPENDIX II. Glossary and list of abbreviations

APPENDIX III. Tables with the concentration values obtained from the leaching tests

APPENDIX IV. Scientific publications

APPENDIX I. FUTURE WORKS

Based on the knowledge acquired during the completion of this PhD thesis, new challenges in this line of research have been opened, which should be worked in the forthcoming future.

The characterization of meteorite's fragments, especially of those meteorites coming from Mars, should be tested to approach us to the study of that planet. The same analytical techniques employed in this thesis could be used on them to obtain a complete characterization, differentiating the inner compounds (not affected by the entry in the Earth atmosphere) from the new compounds formed in the fusion crust of the meteorites.

The calibration approach by LIBS with the elaboration of powder pellets will be improved in order to obtain better results, with the purpose to be used in the calibration plan for the next generation of Mars rovers. In particular, the use of an internal calibration element will be checked. Moreover, the next acquisition of the visible spectral range will be used to enhance the multivariate calibration approach.

The study of organic compounds should be expanded to the analysis of other type of impact glasses collected in other zones of the Earth, in order to perform a comparative study and to corroborate their capability to keep those types of compounds after an impact. Moreover, the identification of organic compounds in meteorites could help in the interpretation of some alterations suffered by such materials after years of interaction with the Earth atmosphere. This is especially interesting nowadays for Martian meteorites.

The accelerated weathering studies should be also extended to meteorites, in particular to those certified Martian meteorites. We should expect a better definition of the alteration processes suffered by such materials, distinguishing probably the alterations in the Earth from the extraterrestrial alterations.

APPENDIX II. GLOSSARY AND LIST OF ABBREVIATIONS

GLOSSARY

The following section summarizes the meaning of the specific terms used throughout the PhD work.

Asteroid: smaller rocky bodies, carbonaceous or metallic, larger than meteoroids and smaller than planets, orbiting the Sun.

Calibration curve: graphical relationship between the known values, such as concentrations, of a series of calibration standards and their instrument response.

Clast: a rock fragment or grain resulting from the breakdown of larger rocks

Coke: solid fuel consists of 90 to 95% carbon. Nitrogen, oxygen, sulfur and hydrogen are present in minor amounts.

Comet: a celestial body moving about the sun, usually in a highly eccentric orbit, consisting of ice, rocks, dust and gas.

Crystallization water: water of hydration that is necessary for the maintenance of a particular crystalline structure but capable of being removed by sufficient heat.

Degree of *crystallinity*: rocks composed entirely of crystals are called *holocrystalline*; those composed entirely of glass are *holohyaline* and rocks that contain both crystals and glass are *hypocrystalline.*

Efflorescences: deposits formed on a matrix when water containing salts is evaporated and the salts precipitate.

Euhedral crystallites: crystals having a defined form and easily recognizable faces. Many come from cooling magma.

Fusion crust: a thin, glassy coating, usually black and rarely more than 1 millimeter thick, which is formed by ablation on the surface of a meteorite.

Impact crater: a bowl-shaped depression with a raised rim, formed by the impact of a meteoroid (on the surface of the earth, moon, etc.).

Impact glass: natural rich silica-melts produced by impact events of a meteorite, asteroid or comet on any geographic area on the Earth.

Lacustrine sediments: sediments formed at the bottom or along the shore of lakes, as geological strata.

Leaching: extraction of removing soluble or other constituents from a matrix by the action of a percolating liquid.

Meteorite: meteoroid that reach the Earth's surface because it does not completely disintegrate in the atmosphere. Each day a lot of meteoroids enter the Earth's atmosphere. But only the largest ones reach the surface to become meteorites.

Meteoroid: particles of dust and ice or rocks up to tens of meters that are in the space, product of the passage of a comet or a broken up asteroid.

Nubian Sandstones: a variety of sedimentary rocks deposited on the Precambrian Basement in the eastern Sahara, north-east Africa and Arabia. It consists of continental sandstones with thin beds of marine limestones, and marls. Nubian sandstone was deposited between the Lower Paleozoic and Upper Cretaceous, with marine beds dating from the Carboniferous to Lower Cretaceous.

Porphyritic: an adjective used specifically for igneous rocks, for a rock that has a distinct difference in the size of the crystals, with at least one group of crystals obviously larger than another group.

Pig iron: product obtained from the first fusion iron in blast furnaces containing more carbon than steel or iron and breaks more easily.

Porphyritic: rock that has a distinct difference in the size of the crystals, with at least one group of crystals obviously larger than another group.

Shattering: mechanical process that occurs in the bedrock beneath meteorite impact craters or underground nuclear explosions. It evidences that the rock has been subjected to a shock with pressures in the range of 2-30 GPa.

Schlieren structures: irregular streaks or masses in igneous rock that differ from the surrounding rock in texture or composition.

Sedimentary rocks: types of rock that are formed by the deposition of material at the Earth's surface and within bodies of water.

Sediments: naturally material that is broken down by processes of weathering and erosion, and is subsequently transported by the action of wind, water, or ice, and/or by the force of gravity acting on the particle itself.

Siluro-Devonian Eldon Group Sandstones: sandstones from the Silurian and Devonian geologic periods recorded in Tasmania. They include Austral Creek Siltstone, Keel Quartzite, Amber, Bell and Crotty Formations and Florence Quartzite.

Target rock: surface rock.

Temperate climate: temperate latitudes of the globe lie between the tropics and the Polar Regions. The North Temperate Zone extends from the Tropic of Cancer (approximately 23.5° north latitude) to the Arctic Circle (approximately 66.5° north latitude). The South Temperate Zone extends from the Tropic of Capricorn (approximately 23.5° south latitude) to the Antarctic Circle (at approximately 66.5° south latitude). Temperate climates are those without extremes of temperature and precipitation. In this zone, the four seasons have clear demarcations.

Texture: degree of crystallinity, grain size, and fabric (geometrical relationships) among the constituents of a rock.

Thermal decomposition: a chemical phase transformation caused by the heat of the laser in Raman spectroscopy.

Weathering: effects that suffer minerals on surfaces exposed to the Earth atmosphere due to processes such as degradation by the exposition to a variety of

chemical (for example: reaction with oxygen or water) and physical processes (mechanical: e.g. thermal stress or cryofracturing).

LIST OF ABBREVIATIONS

DG: Darwin Glasses

μ-EDXRF: Micro-Energy Dispersive X-Ray Fluorescence Spectroscopy

EAF: Electric Arc Furnace

FUS: Focused Ultrasound

GC-MS: Gas Chromatography-Mass Spectrometry

HMC: High Magnesium Calcite

IC: Ionic Chromatography

ICP-MS: Inductively Coupled Plasma-Mass Spectrometry

IR: Infra red

LDG: Libyan Desert Glass

LF: Ladle Furnace

LFT: Long Forest Track

LIBS: Elemental quantification by Laser-Induced Breakdown Spectroscopy

LS: slag from long forest track

PCA: Principal Component Analysis

PLS regression: Partial Least Squares regression

REE: Rare Earth Element

S: slag from short forest track

SCA: Structural and Chemical Analyser

SEM-EDX: Scanning Electron Microscope-Energy Dispersive X-Ray Spectroscopy

SFT: Short Forest Trach

UV: ultraviolet

VFA: Volatile Organic Compounds

APPENDIX III. TABLES WITH THE CONCENTRATION VALUES OBTAINED FROM THE LEACHING TESTS

AIII.1. Concentration values (mg/Kg) of M1, M1T,M2, M2T, M3, M4, M5 and M6 obtained from the Milli-Q water leaching test (LOD: Limit of detection; n.a.: not appear).

		Al	Ba	B	Ca	Cr	Cu	Fe	K	Li	Mg	Mn	Mo	Na	Ni	Pb	Sb	Sn	Sr	Ti	V	W	Zn	F^-	Cl^-	NO_3^-	SO_4^{2-}
M1 Q	Mean	146	115	15.3	2612	0.427	<LOD	5.50	1.35	0.223	39	<LOD	1.64	180	0.072	<LOD	0.039	0.00390	9.1	0.0276	4.6	15.5	0.465	44.8	122	14.9	12.6
	Desv	27	25	2.3	460	0.044		0.89	0.30	0.042	11		0.24	20	0.017		0.010	0.00020	2.1	0.0052	1.0	2.6	0.052	9.4	20	1.6	1.4
M1 T Q	Mean	129	79	8.8	2410	0.274	<LOD	6.7	0.248	0.252	25.1	<LOD	1.05	79.6	0.086	<LOD	0.047	0.00307	8.2	0.0401	7.0	6.4	0.376	24.9	141	11.9	14.3
	Desv	24	17	1.4	430	0.028		1.1	0.055	0.047	6.8		0.15	9.2	0.020		0.012	0.00014	1.3	0.0074	1.6	1.1	0.042	5.3	23	1.3	1.6
M2 Q	Mean	113	63	8.2	3560	2.12	<LOD	8.9	1.56	0.206	21.1	<LOD	2.03	125	0.115	<LOD	0.00085	0.001933	10.0	0.078	10.7	8.5	1.74	60	81	11.6	43.0
	Desv	20	13	1.2	640	0.21		2.0	0.35	0.038	5.8		0.30	15	0.030		0.00022	0.000091	1.7	0.014	2.4	1.5	0.20	13	13	1.2	4.9
M2 T Q	Mean	151	86	13.3	3600	4.28	0.0534	9.2	1.77	0.197	11.1	<LOD	1.06	194	0.117	<LOD	0.0049	0.001676	15.6	0.0479	15.4	15.2	0.741	65	72	17.9	39.0
	Desv	27	19	1.9	640	0.44	0.0066	2.0	0.40	0.036	3.1		0.15	23	0.030		0.0013	0.000070	2.6	0.0088	3.4	2.6	0.087	14	12	1.8	4.5
M3 Q	Mean	130	46	6.6	3470	2.07	<LOD	10.5	0.69	0.207	10.7	<LOD	1.83	122	0.124	<LOD	0.0107	0.00233	8.5	0.078	9.5	7.7	0.517	94	92	29.03	37.8
	Desv	24	10	1.1	610	0.22		1.7	0.16	0.037	2.9		0.30	14	0.031		0.0030	0.00010	1.4	0.014	2.1	1.3	0.061	20	15	3.02	4.4
M4 Q	Mean	49.1	129	15.1	1370	0.236	<LOD	4.21	1.71	0.200	43	<LOD	1.31	150	0.049	<LOD	0.046	0.00761	9.9	0.0274	2.38	9.6	1.83	35.3	98	11.8	10.0
	Desv	8.8	27	2.4	240	0.025		0.70	0.39	0.038	12		0.20	17	0.012		0.012	0.00033	1.6	0.0051	0.52	1.7	0.21	7.5	16	1.2	1.1
M5 Q	Mean	69	14.5	3.97	1900	0.231	n.a.	6.5	13.1	0.112	32.1	0.49	0.400	26.3	0.0240	0.0214	0.0080	0.00528	3.00	0.114	2.71	0.93	n.a.	24.3	33.6	7.90	103
	Desv	13	3.2	0.62	340	0.024		1.1	3.0	0.020	8.9	0.11	0.055	2.8	0.0062	0.0060	0.0022	0.00021	0.50	0.021	0.59	0.17		5.2	5.4	0.81	12
M6 Q	Mean	26.4	11.2	168	1550	9.37	n.a.	17.7	216	0.271	22.6	0.434	0.82	240	0.126	0.0210	0.0034	0.00252	4.78	0.252	0.80	0.263	n.a.	230.2	101	16.4	215
	Desv	4.9	2.4	24	270	0.83		2.8	50	0.053	6.1	0.088	0.11	29	0.030	0.0060	0.0010	0.00012	0.77	0.048	0.17	0.045		48.4	16	1.8	23

AIII.2. Concentration values (mg/Kg) of M1, M1T,M2, M2T, M3, M4, M5 and M6 obtained from the acetic acid leaching test (n.a.: not appear).

		Al	Ba	B	Ca	Cr	Cu	Fe	K	Li	Mg	Mn	Mo	Na	Ni	Pb	Sb	Sn	Sr	Ti	V	W	Zn
M1 Q	Mean	590	1030	150	70800	3.25	0.342	4280	113	2.48	121	3550	4.84	1060	4.08	0.209	0.155	0.076	247	20.9	12.5	25.2	32.6
	Desv	130	160	22	9200	0.79	0.073	950	15	0.28	16	710	0.63	130	0.50	0.054	0.037	0.021	32	4.4	3.0	2.9	3.0
M1 T Q	Mean	252	790	121	70700	1.60	0.055	2420	53.7	1.91	294	2584	3.15	679	4.11	0.179	0.102	0.189	203	8.9	19.6	11.0	72.4
	Desv	56	120	17	9300	0.39	0.012	540	7.1	0.21	40	520	0.39	90	0.50	0.047	0.024	0.052	30	1.9	4.7	1.2	6.7
M2 Q	Mean	231	457	62.6	79300	14.2	0.091	278	30.4	2.04	3440	183	7.81	418	3.82	0.052	0.0138	0.00325	267	1.55	37.6	25.1	0.973
	Desv	52	70	9.2	9600	3.5	0.020	63	4.1	0.22	440	40	0.98	51	0.47	0.014	0.0032	0.00090	36	0.33	9.3	2.8	0.091
M2 T Q	Mean	247	511	82	83000	25.9	0.165	343	47.2	1.19	5350	990	12.6	502	4.18	0.0210	0.0143	0.0046	286	2.21	23.8	20.4	2.86
	Desv	56	75	12	11000	6.4	0.035	80	6.3	0.13	670	200	1.6	61	0.52	0.0054	0.0033	0.0013	40	0.48	5.9	2.3	0.27
M3 Q	Mean	300	284	58.7	90000	11.0	0.0402	153	12.1	0.570	1850	272	9.1	391	1.62	0.071	0.0266	0.0068	211	0.99	25.7	23.1	3.66
	Desv	70	41	8.5	12000	2.7	0.0086	35	1.6	0.061	240	55	1.1	50	0.20	0.019	0.0061	0.0019	30	0.22	6.4	2.7	0.35
M4 Q	Mean	208	740	89	41100	2.09	0.217	1040	95	0.93	216	2230	2.46	526	1.87	0.214	0.103	0.155	245	9.3	9.9	5.87	59.6
	Desv	50	110	13	5400	0.51	0.047	230	13	0.10	30	450	0.30	65	0.23	0.057	0.024	0.042	34	1.9	2.4	0.69	5.8
M5 Q	Mean	360	269	87	52300	1.51	0.0266	1400	81	0.631	3630	750	1.84	321	1.95	0.187	0.0372	0.070	89	18.5	15.0	4.83	3.67
	Desv	84	43	13	7300	0.38	0.0059	320	11	0.079	450	160	0.25	41	0.25	0.050	0.0090	0.020	12	4.1	3.8	0.58	0.37
M6 Q	Mean	31.3	33.1	555	75300	2.85	0.0142	238	7.03	0.824	4850	10.3	1.66	1080	2.25	0.0196	0.00419	0.00113	50.3	0.301	3.35	0.449	n.a.
	Desv	6.8	4.8	77	9600	0.67	0.0029	51	0.80	0.087	600	2.0	0.20	140	0.26	0.0050	0.00095	0.00030	6.4	0.062	0.80	0.046	

AIII.3. Concentration values (mg/Kg) of M1, M1T, M2, M2T, M3, M4, M5 and M6 obtained from the nitric-hydrochloric acid leaching test.

		Al	Ba	B	Ca	Cr	Cu	Fe	K	Li	Mg	Mn	Mo	Na	Ni	Pb	Sb	Sn	Sr	Ti	V	W	Zn
M1 Q	Mean	42400	2650	330	169000	517	108	102200	228	15.8	26500	24300	31.9	1690	17.7	12.17	1.16	6.6	855	1056	402	22.1	165
	Desv	2200	150	25	21000	90	11	9800	11	1.3	1900	1400	3.8	110	3.2	0.50	0.32	1.5	40	65	75	5.2	11
M1 T Q	Mean	41000	2540	339	181000	351	149	80900	135.2	15.9	22800	22000	23.5	962	18.5	21.57	1.92	8.1	654	816	350	20.4	314
	Desv	2200	150	25	23000	61	15	7600	6.1	1.3	1700	1300	2.8	63	3.4	0.99	0.53	1.8	31	53	64	4.9	22
M2 Q	Mean	14800	1665	297	172000	820	84.6	88300	180.6	14.0	23400	20800	32.8	929	20.7	28.5	3.08	5.4	741	681	445	63	125.4
	Desv	810	90	23	22000	140	8.8	8100	7.8	1.1	1700	1100	3.7	62	3.8	1.3	0.83	1.1	30	46	84	14	7.8
M2 T Q	Mean	13810	1436	236	169000	1010	217	132000	173.8	9.52	23700	22500	22.1	949	21.2	24.2	2.92	10.5	705	603	270	23.2	453
	Desv	750	73	20	22000	180	23	12000	7.1	0.78	1700	1100	2.5	65	3.9	1.1	0.78	2.1	30	40	51	5.2	30
M3 Q	Mean	17000	1332	235	178000	1200	379	91600	134.7	10.24	24700	17800	16.3	784	38.6	25.4	5.5	17.1	1034	728	108	31.5	361
	Desv	900	70	20	22000	210	40	8500	5.7	0.85	1800	940	1.8	54	7.2	1.1	1.4	3.6	43	50	20	7.3	23
M4 Q	Mean	22400	2540	306	154000	167	384	87300	578	10.59	20900	14390	16.2	2280	39.7	24.3	5.4	18.0	939	466	108	22.4	363
	Desv	1100	150	23	19000	30	40	8300	27	0.91	1500	830	1.9	150	7.3	1.1	1.5	4.1	50	30	20	5.4	26
M5 Q	Mean	34200	2360	206	130000	740	96	226000	184.3	7.56	26800	16880	13.6	1550	272	8.67	0.66	10.3	397	607	261	20.3	113.9
	Desv	1800	130	15	16000	130	10	22000	8.1	0.66	1900	960	1.6	100	50	0.39	0.18	2.5	20	42	50	4.8	8.1
M6 Q	Mean	24300	363	1860	220000	3220	80.9	31000	160.4	7.13	38600	9670	148	2930	2820	2.80	0.89	8.5	275	886	38.5	12.5	10.72
	Desv	1400	21	130	27000	580	8.8	3000	7.4	0.58	2900	490	18	200	530	0.11	0.25	1.8	14	60	7.0	3.0	0.68

AIII.4. Concentration values (mg/Kg) of S1, S2, S3 and S4 obtained from the Milli-Q water leaching test (LOD: Limit of detection).

		Ag	Al	As	Ba	B	Ca	Cd	Co	Cr	Cu	Fe	Hg	K	Li	Mg	Mn	Mo	Na	Ni	Pb	Sb	Se	Sn	Sr	Ti	V	W	Zn	F^-	Cl^-	NO_3^-	SO_4^{2-}
S1	Mean	<LOD	61	0.124	25.2	11.16	2440	0.0109	0.01145	0.297	0.328	7.29	0.404	17.4	0.0882	20.4	0.159	6.71	32.1	<LOD	0.03412	0.00909	0.69	<LOD	4.55	0.104	4.50	21.3	0.1017	36.9	277.3	25.0	70.4
	Desv		11	0.047	1.7	0.56	140	0.0010	0.00076	0.053	0.012	0.80	0.046	8.1	0.0013	5.2	0.038	0.87	8.7		0.00045	0.00080	0.18		0.83	0.022	0.57	1.9	0.0067	1.9	5.9	5.2	5.1
S2	Mean	<LOD	32.4	0.055	2.430	4.64	1652	<LOD	0.03646	5.618	<LOD	4.261	0.029753	23.2	0.0646	1.85	0.025	0.6063	27.55	<LOD	0.157	<LOD	0.22	<LOD	3.510	0.108	5.75	1.545	0.0308	28.1	235.5	4.92	29.8
	Desv		2.3	0.017	0.061	0.14	46		0.00065	0.091		0.089	0.000039	5.4	0.0068	0.10	0.010	0.0035	0.95		0.036		0.11		0.046	0.010	0.10	0.018	0.0017	2.8	4.8	0.94	3.2
S3	Mean	<LOD	264	0.048	3.28	2.63	1662	<LOD	0.0097	0.798	0.070	9.2	0.079	16.3	0.0639	6.37	0.319	0.737	15.8	<LOD	0.02060	0.00106	0.140	0.0021	2.67	0.183	3.20	3.97	0.065	34.6	228.15	4.46	64
	Desv		41	0.011	0.13	0.23	140		0.0014	0.061	0.023	1.4	0.010	1.1	0.0049	0.68	0.083	0.044	1.2		0.00057	0.00030	0.062	0.0012	0.11	0.035	0.33	0.55	0.018	2.4	6.02	0.38	11
S4	Mean	<LOD	151	0.0408	6.19	2.73	2270	<LOD	0.00588	0.880	0.080	9.16	0.092	17.9	0.0582	3.72	0.198	0.991	18.9	<LOD	0.0239	0.00384	0.214	0.0044	3.43	0.162	5.34	4.55	0.040	33.1	296	4.68	41.3
	Desv		35	0.0052	0.52	0.46	170		0.00084	0.086	0.011	0.60	0.011	3.9	0.0042	0.46	0.040	0.080	2.3		0.0054	0.00092	0.054	0.0011	0.32	0.011	0.14	0.70	0.014	2.5	59	0.81	8.8

AIII.5. Concentration values (mg/Kg) of S1, S2, S3 and S4 obtained from the acetic acid leaching test (LOD: Limit of detection).

		Ag	Al	As	Ba	B	Ca	Cd	Co	Cr	Cu	Fe	Hg	K	Li	Mg	Mn	Mo	Na	Ni	Pb	Sb	Se	Sn	Sr	Ti	V	W	Zn
S1	Mean	<LOD	213	<LOD	274	96.0	65300	0.0577	5.64	<LOD	<LOD	670	0.703	44.42	0.611	5600	978	12.246	600	1.692	0.0291	0.0267	0.049	0.0178	92.3	2.06	7.8	35.61	0.401
	Desv		35		11	3.1	1800	0.0016	0.47			440	0.059	0.48	0.023	180	81	0.083	11	0.086	0.0048	0.0014	0.019	0.0049	3.0	0.72	1.3	0.72	0.037
S2	Mean	<LOD	194.7	0.1847	74.0	7.2	63000	0.0174	5.88	4.97	<LOD	228	0.085	34.3	0.234	935	152.4	2.63	185.6	1.249	0.0875	0.0134	0.245	0.01137	71.3	5.47	32.0	7.08	1.13
	Desv		6.9	0.0059	3.1	1.1	1900	0.0031	0.37	0.66		22	0.036	1.6	0.014	30	7.5	0.14	4.1	0.081	0.0092	0.0013	0.053	0.00059	1.7	0.67	3.0	0.29	0.21
S3	Mean	<LOD	225	0.234	78.7	10.1	53400	0.0107	2.140	2.15	<LOD	1013	0.106	29.0	0.2349	1230	233	1.60	830	2.18	0.0188	0.0117	0.044	0.0166	68.5	4.99	20.3	8.23	3.46
	Desv		27	0.013	3.4	2.3	724	0.0015	0.059	0.50		92	0.019	1.3	0.0036	34	11	0.10	1000	0.16	0.0029	0.0038	0.016	0.0047	1.3	0.96	3.6	0.76	0.30
S4	Mean	<LOD	191	0.106	95	10.1	65000	0.0073	1.75	1.04	<LOD	430	0.385	69.3	0.1977	585	192	2.75	327	1.38	0.0187	0.0136	0.66	0.0214	77.6	4.8	24.6	20.0	3.2
	Desv		27	0.037	15	4.0	7300	0.0020	0.41	0.33		220	0.045	5.7	0.0078	92	52	0.18	41	0.39	0.0015	0.0013	0.15	0.0060	8.8	1.8	3.2	2.4	1.3

AIII.6. Concentration values (mg/Kg) of S1, S2, S3 and S4 obtained from the nitric-hydrochloric acid leaching test (LOD: Limit of detection).

		Ag	Al	As	Ba	B	Ca	Cd	Co	Cr	Cu	Fe	Hg	K	Li	Mg	Mn	Mo	Na	Ni	Pb	Sb	Se	Sn	Sr	Ti	V	W	Zn
S4	Mean	0.616	16000	<LOD	592	34.7	90000	0.231	4.84	12000	201	100000	2.74	54	6.1	7800	6418	30.3	518	32.2	8.7	0.602	<LOD	10.87	131	908	409	79.83	220.0
	Desv	0.027	1000		31	6.6	8700	0.061	0.38	6300	16	2000	0.34	10	2.0	200	51	1.8	12	4.9	1.0	0.046		0.82	11	41	31	0.68	2.5
S3	Mean	0.551	16000	<LOD	572	40.7	85300	0.226	5.7	5000	199	84000	2.79	43.9	6.54	8800	5400	28.8	405	46.0	5.01	0.51	<LOD	6.58	134.4	735	284	79.8	85.9
	Desv	0.013	260		19	1.8	9600	0.021	1.6	640	28	8100	0.14	5.8	0.22	300	200	3.4	15	2.8	0.34	0.10		0.44	3.7	17	9	7.1	5.4
S2	Mean	0.525	12100	<LOD	516	34.2	87200	0.308	8.61	3510	63	40000	1.822	88.5	5.13	6700	2600	39.4	429	10.5	11.2	0.239	11.37	4.81	145	725	302	54.4	73
	Desv	0.054	1100		51	2.8	6300	0.039	0.63	120	3	3500	0.096	8.1	0.16	640	230	2.8	32	2.1	1.7	0.031	4.00	0.41	12	78	29	5.4	17
S1	Mean	0.59	21300	<LOD	1241	105	71000	0.247	14.133	2510	228	79000	2.93	103.73	7.2	11600	7000	32.8	700	15.1	4.8	0.408	13.1	5.7	141	281	133	88	133.4
	Desv	0.16	5300		319	32	17000	0.012	0.090	170	61	8000	0.91	0.93	1.3	3200	2100	8.4	200	4.1	1.2	0.084	4.4	1.5	38	66	40	26	2.5

AIII.7. Concentration values (mg/Kg) of LS1, LS2, LS3 and LS4 obtained from the Milli-Q water leaching test (LOD: Limit of detection).

		Ag	Al	As	Ba	B	Ca	Cd	Co	Cr	Cu	Fe	Hg	K	Li	Mg	Mn	Mo	Na	Ni	Pb	Sb	Se	Sn	Sr	Ti	V	W	Zn	F^-	Cl^-	NO_3^-	SO_4^{2-}
LS1	Mean	<LOD	61.4	0.042	4.82	1.096	3200	0.0176	0.0435	0.0181	1.3	12.64	0.0165	14.0	0.0730	6.56	0.196	0.1455	7.4	0.21	0.0225	0.0156	0.15	0.00571	2.43	0.145	0.1201	0.0775	0.26	167.7	664	7.5	20.0
	Desv		4.3	0.010	0.32	0.076	200	0.0020	0.0032	0.0071	2.4	0.59	0.0015	7.8	0.0059	0.77	0.021	0.0048	1.1	0.20	0.0090	0.0028	0.10	0.00060	0.16	0.028	0.0031	0.0054	0.13	3.6	16	2.7	2.3
LS2	Mean	<LOD	36.0	0.0353	2.71	2.17	1900	0.0170	0.0418	0.0397	0.04932	8.2	0.0330	6.98	0.0527	28.5	0.28	0.205	10.3	0.054	0.055	0.0241	0.089	0.00564	1.68	0.155	0.301	0.695	0.18	142	1856	19.1	36.70
	Desv		8.2	0.0059	0.42	0.26	330	0.0018	0.0041	0.0083	0.00071	1.9	0.0046	0.74	0.0052	5.6	0.15	0.018	6.8	0.013	0.069	0.0019	0.022	0.00086	0.28	0.062	0.019	0.074	0.18	17	311	1.6	0.83
LS3	Mean	<LOD	53.3	0.0381	7.13	1.255	3200	0.01641	0.0437	0.1021	0.0275	15.5	0.01693	18.15	0.0821	2.1	0.31	0.217	12.9	0.123	0.0180	0.0203	0.177	0.00501	4.49	0.124	0.0647	0.076	0.086	76	2475	24.33	40.79
	Desv		8.0	0.0040	0.47	0.016	300	0.00076	0.0019	0.0091	0.0063	1.5	0.00065	0.86	0.0047	1.4	0.22	0.019	1.4	0.020	0.0016	0.0016	0.023	0.00021	0.44	0.096	0.0084	0.016	0.036	8	152	0.65	0.95
LS4	Mean	<LOD	48.4	0.0374	2.83	0.71	2400	0.0160	0.0422	0.0239	0.0400	13.5	0.0157	5.3	0.0598	10.5	0.202	0.0955	6.7	0.1048	0.0162	0.0216	0.145	0.00543	2.72	0.173	0.118	0.0588	0.142	136	1135	30.6	56.2
	Desv		6.3	0.0064	0.48	0.13	430	0.0014	0.0047	0.0076	0.0060	2.1	0.0021	1.3	0.0079	2.9	0.058	0.0079	1.4	0.0063	0.0027	0.0037	0.088	0.00092	0.50	0.040	0.016	0.0060	0.070	15	104	1.2	3.1

AIII.8. Concentration values (mg/Kg) of LS1, LS2, LS3 and LS4 obtained from the acetic acid leaching test (LOD: Limit of detection).

		Ag	Al	As	Ba	B	Ca	Cd	Co	Cr	Cu	Fe	Hg	K	Li	Mg	Mn	Mo	Na	Ni	Pb	Sb	Se	Sn	Sr	Ti	V	W	Zn
LS1	Mean	<LOD	186.87	0.296	68.0	6.37	32730	0.0269	0.143	0.068	0.110	646	0.0343	15.06	0.351	3200	93.5	0.3757	23.50	1.99	0.03069	0.118	0.6500	0.00924	59.59	1.20	0.817	0.625	0.211
	Desv		0.36	0.046	3.3	0.28	900	0.0022	0.013	0.026	0.010	21	0.0011	0.33	0.036	120	8.5	0.0028	0.45	0.16	0.00032	0.013	0.0068	0.00036	0.80	0.56	0.079	0.028	0.011
LS2	Mean	<LOD	101.10	0.4585	52.0	15.8	37500	0.02834	0.1828	0.554	0.068	642	0.0995	14.22	0.336	12420	116.2	0.950	21.53	3.0067	0.121	0.1266	1.51	0.01579	66.9	4.76	2.190	3.25	0.1921
	Desv		0.22	0.0026	2.1	1.1	1200	0.00082	0.0024	0.066	0.021	19	0.0055	0.68	0.014	220	9.3	0.060	0.20	0.0042	0.022	0.0049	0.12	0.00086	7.3	0.28	0.025	0.21	0.0045
LS3	Mean	<LOD	20.534	0.223	50.9	6.24	37300	0.0302	0.1743	0.0736	0.09638	737.2	0.0435	12.68	0.30122	7860	15.007	0.913	20.4	2.90	0.0225	0.112	1.268	0.00899	93.1	0.464	1.43115	0.888	0.332
	Desv		0.078	0.016	3.7	0.16	1500	0.0013	0.0058	0.0054	0.00030	5.7	0.0027	0.28	0.00025	130	0.079	0.045	1.0	0.22	0.0013	0.010	0.074	0.00034	2.7	0.035	0.00052	0.049	0.082
LS4	Mean	<LOD	49	0.456	47.0	7.29	29074	0.0279	0.1581	0.51	0.1044	693.6	0.0333	12.59	0.271	8800	67	0.535	13.67	2.509	0.049	0.184	1.50	0.0130	68.6	6.5	1.159	0.519	0.261
	Desv		62	0.067	3.8	0.74	49	0.0031	0.0059	0.20	0.0070	9.0	0.0019	0.60	0.010	420	17	0.013	0.32	0.031	0.015	0.021	0.11	0.0035	3.6	2.5	0.060	0.033	0.031

AIII.9. Concentration values (mg/Kg) of LS1, LS2, LS3 and LS4 obtained from the nitric-hydrochloric acid leaching test.

		Ag	Al	As	Ba	B	Ca	Cd	Co	Cr	Cu	Fe	Hg	K	Li	Mg	Mn	Mo	Na	Ni	Pb	Sb	Se	Sn	Sr	Ti	V	W	Zn
LS1	Mean	1.95	24000	6.28	368	54.3	210000	0.798	5.18	207.6	92.4	32000	0.751	70.2	6.45	22120	3450	10.94	165	53.8	8.61	1.64	10.6	4.06	490	733	34.6	6.73	19.15
	Desv	0.13	700	0.64	16	1.1	3000	0.030	0.32	9.1	4.3	1500	0.024	5.7	0.43	120	270	0.96	21	3.6	0.46	0.10	1.4	0.16	23	31	3.8	0.59	0.67
LS2	Mean	1.302	23600	9.85	400	83.1	140000	1.223	5.44	323	104.8	40000	1.2094	73.2	5.47	50000	7220	15.4	192	49.2	42.7	1.33	7.44	6.57	330	588	82.5	21.0	100.9
	Desv	0.052	1700	0.51	33	5.2	5400	0.058	0.46	20	5.9	3500	0.0062	7.3	0.63	3200	740	1.2	17	1.5	2.8	0.12	0.25	0.68	13	18	5.5	1.8	7.3
LS3	Mean	1.475	24000	9.05	463	54.8	155500	1.369	6.8	270	109	36000	1.04	76.1	5.69	43300	4000	22.9	128.3	72.2	115.3	1.58	7.04	7.98	500	722	38.5	14.1	153
	Desv	0.066	5500	0.91	136	2.8	8200	0.077	1.1	14	23	7000	0.12	3.1	0.13	4200	740	3.9	3.5	7.8	5.6	0.13	0.63	0.11	200	94	2.3	1.3	10
LS4	Mean	1.95	19000	20.6	268	55.2	170000	1.0756	11.1	334	254	92500	0.88	70.3	4.7	51000	3100	32	111	123	52.0	3.5	7.147	16	354	643	41.21	9.6	127
	Desv	0.35	3000	9.1	25	3.1	820	0.0048	5.7	71	162	9100	0.18	4.8	1.1	6000	280	20	10	70	1.2	2.2	0.029	12	36	68	0.91	3.4	24

AIII.10. Concentration values (mg/Kg) of DW4, DW3 and LDG obtained from the Milli-Q water leaching test (LOD: Limit of detection).

		Al	Ba	Ca	Co	Cr	Cu	Fe	K	Li	Mg	Mn	Mo	Na	Ni	Sn	Sr	Ti	W	Zn
DW4	Mean	3.19	3.64	70.5	0.00513	0.00642	0.0482	0.819	6.09	0.00796	24.1	0.0192	0.00738	<LOD	0.0373	0.00310	0.0740	0.0942	0.00451	0.0918
	Desv	0.16	0.18	3.5	0.00026	0.00032	0.0024	0.041	0.30	0.00040	1.2	0.0010	0.00037		0.0019	0.00015	0.0037	0.0047	0.00023	0.0046
DW3	Mean	0.719	25.7	207	0.0238	0.01693	5.98	<LOD	18.32	0.0213	28.7	0.225	0.0330	14.79	0.0614	0.00305	1.888	0.0300	0.00741	0.1206
	Desv	0.036	1.3	10	0.0012	0.00085	0.30		0.92	0.0011	1.4	0.011	0.0016	0.74	0.0031	0.00015	0.094	0.0015	0.00037	0.0060
LDG	Mean	1.139	0.826	41.9	0.00575	0.00630	1.135	0.495	6.46	0.00520	5.85	0.1762	0.00350	5.60	0.0220	0.000974	0.0954	0.1061	0.00294	0.0529
	Desv	0.057	0.041	2.1	0.00029	0.00032	0.057	0.025	0.32	0.00026	0.29	0.0088	0.00017	0.28	0.0011	0.000049	0.0048	0.0053	0.00015	0.0026

AIII.11. Concentration values (mg/Kg) of DW4, DW3 and LDG obtained from the Milli-Q water leaching test (n.a.: not appear).

		Cl^-	NO_3^-	SO_4^{2-}	Br^-	$C_2O_4^{2-}$
DW3	Mean	230	94.7	106.0	14.87	8.17
	Desv	12	4.7	5.3	0.74	0.41
DW4	Mean	283	126.3	28.4	n.a.	n.a.
	Desv	14	6.3	1.4		
LDG	Mean	53.3	1.108	6.28	9.01	2.81
	Desv	2.7	0.055	0.31	0.45	0.14

AIII.12. Concentration values (mg/Kg) of DW4, DW3 and LDG obtained from the Milli-Q water leaching test (LOD: Limit of detection).

		La	Ce	Pr	Nd	Sm	Eu	Gd	Th
DW4	Mean	0.001303	0.00276	0.0001875	0.001138	<LOD	0.000962	<LOD	0.000621
	Desv	0.000065	0.00014	0.0000094	0.000057		0.000048		0.000031
DW3	Mean	<LOD	<LOD	<LOD	<LOD	<LOD	0.00741	<LOD	<LOD
	Desv						0.00037		
LDG	Mean	0.001516	0.00359	0.000258	0.001253	0.000526	<LOD	0.000277	0.000741
	Desv	0.000076	0.00018	0.000013	0.000063	0.000026		0.000014	0.000037

APPENDIX IV. SCIENTIFIC PUBLICATIONS

Part of the results covered in this PhD Memory has been published as scientific papers in research journals. Others have been previously published in National and International Congresses. The list of such scientific contributions includes:

Scientific Papers in Research Journals:

1.- J. Aramendia, L. Gómez-Nubla, S. Fdez-Ortiz de Vallejuelo, K. Castro, X. Murelaga and J.M. Madariaga, New findings by Raman Micro-spectroscopy in the bulk and inclusions trapped in Libyan Desert Glass, Spectroscopy Letters, **44**, 521-525, 2011

2.- L. Gómez-Nubla, J. Aramendia, S. Fdez-Ortiz de Vallejuelo, K. Castro, A. Alonso, M.C. Zuloaga, L.A. Ortega, X. Murelaga and J.M. Madariaga, Spectroscopic integrated method in the way towards the search of the origin of Lybian Desert Glass, Macla, **16**, 70-71, 2012

3.- L. Gómez-Nubla, J. Aramendia, S. Fdez-Ortiz de Vallejuelo, K. Castro and J.M. Madariaga, Portable till SCA Raman devices to characterize harmful compounds contained in reused black slag from electric arc furnace, Journal of Raman Spectroscopy, **44**, 1163-1171, 2013

4.- L. Gomez-Nubla, J. Aramendia, A. Alonso-Olazabal, S. Fdez-Ortiz de Vallejuelo, K. Castro, L.A. Ortega, M.C. Zuloaga, X. Murelaga and J.M. Madariaga, Darwin impact glass study by Raman spectroscopy in combination with other spectroscopic techniques, Journal of Raman Spectroscopy, On-line, DOI: 10.1002/jrs.4700, 2015

Communications dedicated to Congresses:

1.- L. Gómez-Nubla, N. Goienaga, M. Maguregui, J. Aramendia, S. Fdez-Ortiz de Vallejuelo, K. Castro, I. Martinez-Arkarazo and J.M. Madariaga, Raman Spectroscopy applied to electric arc furnace black slags as a tool to determinate a possible environmental impact, GeoRaman IX, 9th International Conference on Raman spectroscopy Applied to the Earth Sciences, Sydney (Australia), 2010

2.- L. Gómez-Nubla, J. Aramendia, A. de Diego, K. Castro, S. Fdez-Ortiz de Vallejuelo and J. M. Madariaga, Chromium speciation by Raman Spectroscopy of black slags wastes deposited in forest tracks since 20 years ago, 13th Workshop on Progress in Trace Metal Speciation for Environmental Analytical Chemistry (TraceSpec2011), Pau (France), 2011

3.- L.Gomez-Nubla, J. Aramendia, S. Fdez-Ortiz de Vallejuelo and J.M. Madariaga, Relations between leachated compounds and Raman spectrum of Black Slag from E.A.F. to characterize them, Conference on Micro-Raman and Luminiscence studies in the Earth and Planetary Sciences (CORALS II), Lunar and Planetary Institute, Madrid (Spain), 2011

4.- J. Aramendia, L.Gomez-Nubla, S. Fdez-Ortiz de Vallejuelo, K. Castro, X. Murelaga and J.M. Madariaga, New findings by Raman micro-spectroscopy of Inclusions inside a Lybian Dessert Glass , Conference on Micro-Raman and Luminiscence studies in the Earth and Planetary Sciences (CORALS II), Lunar and Planetary Institute, Madrid (Spain), 2011

5.- L. Gómez-Nubla, J. Aramendia, S. Fdez-Ortiz de Vallejuelo and J.M. Madariaga, Leaching of some elements from slags used in Basque Country forest tracks, EMEC12, 12th European Meeting on Environmental Chemistry, Clermont-Ferrand (France), 2011

6.- L. Gurtubay, L. Batiz, A. Elias, A. Barona, G. Gallastegi, N. Rojo, L. Gomez-Nubla, S. Fdez-Ortiz de Vallejuelo and J. M. Madariaga, Carbonation ageing of EAF slag: implications for leaching behaviour, EUROSOIL2012, European Conference on Polluted Soils, Bari (Italy), 2012

7.- L. Gomez- Nubla, J. Aramendia, M. Villa-Amilibia, S. Fdz-Ortiz de Vallejuelo, I. Martinez-Arkarazo, K. Castro and J.M.Madariaga, Raman spectroscopy and SEM-EDS as tools for the diagnosis of the risk associated to use slag in forest track as filler material, GeoRaman X, 10th International Conference on Raman spectroscopy Applied to the Earth Sciences, Nancy (France), 2012

8.- L. Gómez-Nubla, J. Aramendia, S. Fdez-Ortiz de Vallejuelo, K. Castro, A. AIonso-Olazabal, M.C. Zuloaga, L.A. Ortega, X. Murelaga and J. M. Madariaga, Spectroscopic Integrated method in the way towards the search of the origin of Libyan Desert Glass, SEM-SEA 2012, Bilbao (España), 2012 (Oral)

9.- L. Gómez-Nubla, J. Aramendia, S. Fdez-Ortiz de Vallejuelo, K. Castro, A. AIonso-Olazabal, M.C. Zuloaga, L.A. Ortega, X. Murelaga and J. M. Madariaga, Raman analysis for the research of Impact Glasses: Searching for traces that could elucidate their formation, GeoRaman XI, 11th International Conference on Raman Spectroscopy and its applications to Geological, Planetary and Archaeological Sciences, St. Louis - Missouri (USA), 2014 (Oral)

10.- L. Gomez-Nubla, J. Aramendia, S. Fdez.-Ortiz de Vallejuelo and J. M. Madariaga, Identification of harmful compounds present in steel slag used in forest tracks through spectroscopic techniques, XXIV Reunión Nacional y VIII Congreso Ibérico de Espectroscopia, Logroño (España), 2014

11.- K. Castro, J. Aramendia, L. Gómez-Nubla, S. Fdez-Ortiz de Vallejuelo, A. AIonso-Olazabal, M.C. Zuluaga, L.A. Ortega, X. Murelaga and J. M. Madariaga, Spectroscopy analysis of different types of impact melts: Libyan desert glass and Darwin glass, XXIV Reunión Nacional y VIII Congreso Ibérico de Espectroscopia, Logroño (España), 2014

Spectroscopy Letters, 44:521–525, 2011

ISSN: 0038-7010 print/1532-2289 online
DOI: 10.1080/00387010.2011.610414

Taylor & Francis
Taylor & Francis Group

New Findings by Raman Microspectroscopy in the Bulk and Inclusions Trapped in Libyan Desert Glass

Julene Aramendia[1], Leticia Gomez-Nubla[1], Silvia Fdez-Ortiz de Vallejuelo[1], Kepa Castro[1], Xabier Murelaga[2], and Juan Manuel Madariaga[1]

[1]Department of Analytical Chemistry, University of the Basque Country, Bilbao, Spain
[2]Department of Stratigraphy and Palaeontology, University of the Basque Country, Bilbao, Spain

ABSTRACT Two specimens of Libyan Desert glass (LDG), the controversial glass fragments found in Great Sand Sea of Libyan Desert (Egypt), were analyzed by Raman microspectroscopy assisted by X-ray microfluorescence. Quartz, cristobalite, and anatasa were identified, together with other LDG compounds like corundum and feldspars, found in previous works. However, in our LDG inclusions, other uncommon compounds for high-temperature glasses were determined, such as, sodium carbonate, calcite, gypsum, anhydrite, and even cinnabar, indicating a trapping process just before the end of the cooling process conducive to the formation of the current glass phases of the LDG objects.

KEYWORDS inclusions, Libyan Desert glass, Raman spectroscopy, X-ray microfluorescence

INTRODUCTION

Libyan Desert glass (LDG) has been a mystery to scientists since its discovery in 1933. LDG is a natural glass that is scattered to a depth of ~2 m in the Great Sand Sea[1] (near the Libyan border), and it is estimated to be 28.5 million years old. LDG fragments are distributed in a vast region of the Western Desert of Egypt in the soils' surfaces lying in interdune channels, and it can be found as pieces of silica glass up to several kilograms in weight.[2] These glasses are commonly small irregular pieces with yellow to whitish translucent color together with brownish inclusions.

The first LDG was described by Clayton in 1933.[2] However, there is abundant evidence that it was used in prehistoric times. Various hypotheses about the origin of these glasses have been established, which prompted a controversy around their genesis. On one hand, some studies concluded that LDG originated through a high-temperature impact of an extraterrestrial body into sand or sandstone.[3] However, the lack of a crater[3] has caused the proposal of other hypotheses, such as an airburst of a meteoroid.[3,4] In this last theory, a low-altitude airburst explosion of an impacting extraterrestrial body would create deposits of glass through a high-temperature fusion process.[5] Nevertheless, the large volume of the glass and its very

This submission was presented during the CORALS-2 Meeting on Micro-Raman Spectroscopy and Luminescence Studies in the Earth and Planetary Sciences, which was held between May 19 and 21, 2011, in Madrid, Spain. This is an invited paper for a special CORALS-2 GEO-SPECTROSCOPY issue of *Spectroscopy Letters*.

Received 23 June 2011; accepted 1 August 2011.

Address correspondence to Julene Aramendia, Department of Analytical Chemistry, University of the Basque Country, P.O. Box 644, 48080 Bilbao, Spain. E-mail: jaramendia002@ehu.es

high silica content (approximately 98 wt% of SiO_2) led to the assumption that it was formed by shock-melting of quartz sand and/or sandstone during a meteorite impact.[6,7] The presence of schlieren and partly digested mineral phases, such as lechatelierite and baddeleyite, supports the theory of the impact origin.[1–2,8] Thus, it is important to determine the composition of different LDGs in order to know the real origin of the glass, as some authors claim.[9]

Several works have researched the composition of LDG, but only a few of them have used Raman spectroscopy.[5,6,9–11] Nonetheless, much more work has to be done because the origin of this glassy material is still uncertain. This is the why a new study on LDG pieces was done by using Raman microspectroscopy assisted by X-ray microfluorescence.

OBJECTIVE

The main aim of this work was to find new compounds, in the matrix as well as in the dark inclusions, by means of Raman microspectroscopy to help in the understanding of LDG origin.

MATERIALS AND METHODS

Samples

Two samples of Libyan Desert glass (LDG) that belong to the Collection of Meteorites of the University of the Basque Country were selected to perform this work. These samples have dimensions of 5×2 cm and 4×4 cm approximately, and theirs weights are 18.64 g and 23.38 g respectively. The smaller one (LIB-1) presents less brown inclusions than the bigger one (LIB-2), whose matrix is almost completely covered by brownish streaks.

Equipment

X-Ray Microfluorescence (μ-EDXRF)

Elemental analysis of the samples was carried out with portable ArtTax μ-EDXRF equipment, by Brucker AXS (Berlin, Germany), which incorporates an X-ray tube with molybdenum anode working at a maximum voltage of 50 kV/700 μA and a special Xflash detector (5 mm^2). The X-rays are collimated by a Tantalum collimator with a diameter of 0.65 mm. The measuring head of the equipment implements a CCD camera that allows focusing the sample by a motorized XYZ positioning unit controlled by the computer. After calibrating with a bronze reference standard, the measurements were done with an exposition time of 600 s. Light elements were measured under a helium flow.

Raman Spectroscopy

1. A hand-held InnoRam spectrometer by BWTE-$K_{INC.}$ (Newark, NJ, USA) provided with a 785 nm excitation laser and a microprobe (20× and 50× long-range objectives, with a lateral resolution of 10 and 2 μm respectively) was used. Laser power lower than 50 mW was used to avoid the thermodecomposition of the samples. Acquisition times as well as the number of scans were set to optimum values in order to obtain a good signal-to-noise ratio for all the measurements.

2. A Renishaw InVia Raman micro spectrometer, coupled to a DMLM Leica microscope (UK) with 5× (N PLAN, 0.12 aperture, visualization and focusing), 20× (0.40 aperture), 50× (lateral resolution of 2 μm), and 100× (lateral resolution of 1 μm) long-range objectives, was used with the 514 laser. For the 325 laser, a 40× objective was used. The microscope implements a Prior Scientific motorized stage (XYZ) with a joystick. The power applied was set at the source at a maximum of 50 mW, while on the sample it was always less than 20 mW.

The spectrometers were calibrated according to a procedure described elsewhere.[12] Spectral interpretation was done by comparison with pure standard compounds contained in the e-VISNICH spectral database,[13] which is an online Raman Spectra Database of Natural, Industrial and Cultural Heritage compounds (available at http://158.227.5.164/RamanDB/), and with the Rruff online database.[14]

RESULTS AND DISCUSSION

Raman Spectroscopy

The Raman analysis of the matrix of the LDG samples was done in areas without inclusions, obtaining three different spectra. One of them presented three intense and broad bands at 1374, 1554, and 1636 cm^{-1}. A second spectrum was obtained close to that reported in Fig. 3 of reference 5, showing five Raman bands at 1277 very strong (vs), 1382 (vs), 1517 strong (s), 1662 broad (br), and 1842 medium (m) cm^{-1}; these two spectra belong to silicate compounds

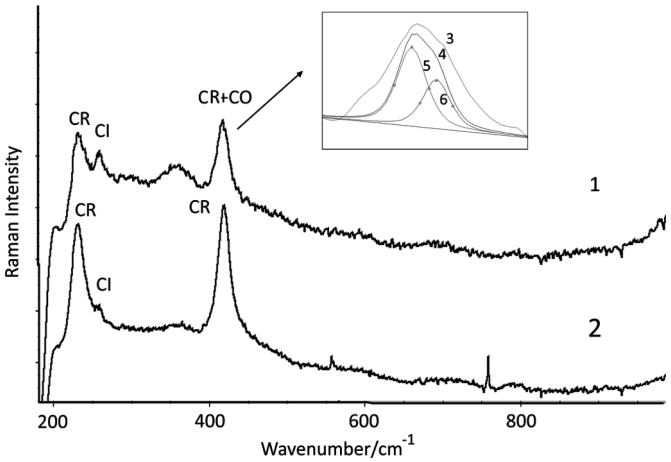

FIGURE 1 Raman spectra of (1) cristobalite (CR), cinnabar (CI), and corundum (CO). (2) cristobalite (CR) and cinnabar (CI). The overlapped Raman spectrum (3) is similar to the theoretical one (4), obtained from corundum ((5), 415 cm^{-1}) and cristobalite ((6), 418 cm^{-1}).

formed probably by melting oxide compounds. The glassy matrix reported as having broad Raman bands around 480 cm^{-1} and 820 cm^{-1}[5] presented in our case three bands at 447 (br), 810 (br), and 1049 (br) cm^{-1}.

The analysis of the brownish inclusions showed quartz (SiO_2, Raman bands at 204 (m), 263 weak (w), 354 (w), 401 very weak (vw), 463 (vs), 806 (w), and 1158 (vw) cm^{-1}), α-cristobalite (SiO_2, Raman bands at 230 (vs) and 418 (vs) cm^{-1}; see Fig. 1), and microcline feldspar ($KAlSi_3O_8$, Raman bands at 513 (m) and 529 (m) cm^{-1}). Quartz and cristobalite are typically found in LDG samples.[1,5,7,15] In this work, quartz was identified more frequently, in spite of being α-cristobalite, the silica form most often mentioned as LDG inclusion;[5] its presence proves that the temperature of glass formation was above 1470°C.[16]

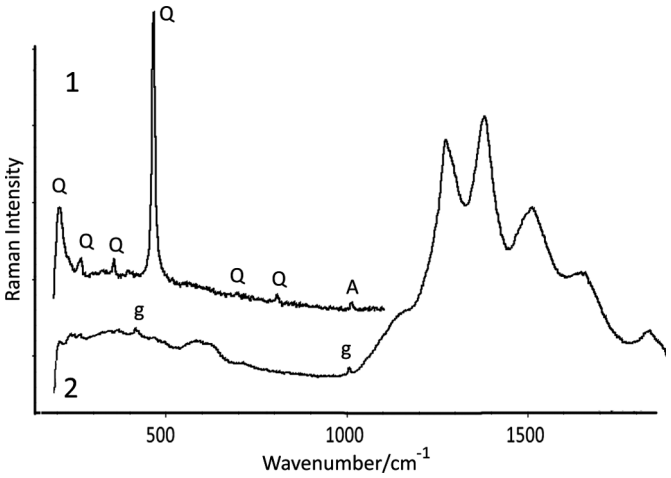

FIGURE 2 Raman spectra of (1) quartz (Q) and anhydrite (A); (2) gypsum (g) and silicate matrix.

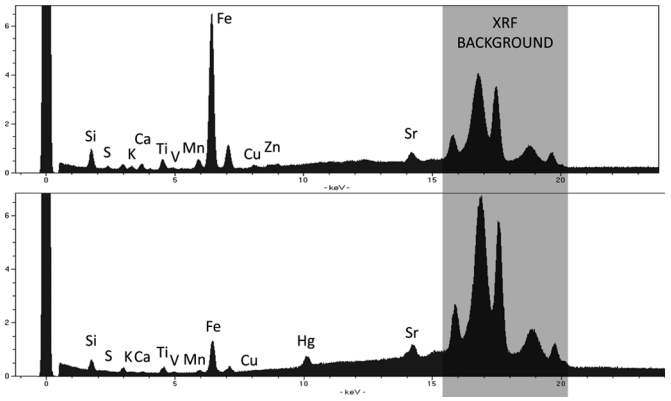

FIGURE 3 μ-EDXRF spectra of two inclusions of LDG sample.

Besides, anatasa (TiO_2, main Raman band at 143 (s) cm^{-1}) that reverts to rutile (TiO_2) at low temperatures,[5] anhydrite ($CaSO_4$, main Raman band at 1018 (w) cm^{-1}, see Fig. 2), amorphous carbon (C, Raman bands at ≈1300 (br) and ≈1600 (br) cm^{-1}), and corundum (Al_2O_3, Raman band at 416 (m) cm^{-1}; see the deconvolution in Fig. 1) were identified in the inclusions.

On the other hand, new compounds not determined in other studies, such as calcite ($CaCO_3$; Raman bands at 153 (w), 279 (m), 710 (w), and 1085 (vs) cm^{-1}), gypsum ($CaSO_4 \cdot 2H_2O$; Raman bands at 413 (w) and 1007 (w) cm^{-1}; see Fig. 2), sodium carbonate (Na_2CO_3; Raman bands at 695 (vw) and 1081(w) cm^{-1}), and cinnabar (HgS; main Raman band at 252 (m) cm^{-1};[17] see Fig. 1) were found in the inclusions of our LDG samples. Cinnabar was detected in a unique orangish inclusion but in several measurements; this inclusion was analyzed by μ-EDXRF to confirm the presence of Hg (see Fig. 3). All compounds with their Raman bands are summarized in Table 1.

X-Ray Microfluorescence (μ-EDXRF)

The elemental analysis revealed the presence of Si, K, Ca, Ti, V, Mn, Fe, and Sr, together with other elements like Al, Cl, Se, Cu, and S at trace levels (see Fig. 3). Hg was detected only in the orangish inclusion where cinnabar was identified by Raman spectroscopy. Some of these elements corroborated the presence of quartz, α-cristobalite, microcline

TABLE 1 Raman Bands of Mineral Compounds Found in the Matrix and Inclusions of LDG Samples

Compound	This study (wave number/cm^{-1})	Other LDG studies (wave number/cm^{-1})
LDG matrix	447 (br), 810 (br) and 1049 (br)	Glassy matrix: 480 (br) 820 (br)[5]
	1374 (vs), 1554 (vs) and 1636 (vs)	Not found
	1277 (vs), 1382 (vs), 1517 (s),	Figure 3 of reference[5]
	1662 (br), 842 (m)	
INCLUSIONS		
Quartz (SiO_2)	204 (m) 263 (w) 354 (w) 401(vw),	208 (w) 465 (m)[5]
	463 (vs) 806 (w) 1158 (vw)	
Cristobalite (SiO_2)	230 (vs) 418 (vs)	230 (s) 418 (s) 780 (w) 1076 (w)[6]
Rutile (TiO_2)	Not found	445 (m), 607 (s)[5]
Anatasa (TiO_2)	143 (vs)	142 (vs) 227 (vw) 395 (vw),
		515 (vw) 637 (w)[5]
Anhydrite ($CaSO_4$)	1018 (w)	418 (vw) 1018 (vs) 1130 (w)[5]
Zircon ($ZrSiO_4$)	Not found	1147 (s), 1201 (vs), 1223 (vs)[5]
Amorphous carbon	≈1300 (br) ≈1600 (br)	≈1300 (br) ≈1600 (br)[5]
Microcline feldspar	513 (m) 529 (m)	Not found
Gypsum ($CaSO_4 \cdot 2H_20$)	413 (w) 1007 (w)	Not found
Cinnabar (HgS)	255 (m)	Not found
Corundum (Al_2O_3)	416 (m)	Not found by Raman
Calcite ($CaCO_3$)	153 (w) 279 (m) 710 (w) 1085 (vs)	Not found
Sodium carbon (Na_2CO_3)	695 (vw) 1081 (w)	Not found

(br: Broad; v: Very; w: Weak; m: Medium; s: Strong).

feldspar, anatasa, anhydrite/gypsum, calcite, aluminum oxide, and cinnabar, previously identified by Raman measurements. Iron seems to be linked to the inclusions, according to the μ-EDXRF analysis (see Fig. 3), although any relevant Raman signal of iron oxides was detected by Raman microspectroscopy.

These new findings could be support the hypothesis of a high-temperature fusion process caused by an impact structure.[3,18] Besides, different carbonates present in the Gilf fluvial system could be trapped into the structure of LDG. Moreover, the age in which the LDG impacted the Earth coincided with Oligocene, the age when the drainage system was active. The carbonate sulphates could be formed by the reaction of the carbonates and the atmospheric SO_x.

CONCLUSIONS

According to the Raman results, in the LDG samples analyzed in this study, the dark brown inclusions contained mainly quartz, α-cristobalite, and calcite. Occasionally gypsum, sodium carbonate, microcline feldspar, anatasa, anhydrite, corundum, and cinnabar were identified. Previous studies had not found some of these compounds, such as gypsum, sodium carbonate, calcite, and cinnabar. Corundum has been determined in other works, but not by Raman spectroscopy. In addition, some Raman bands of the matrix were different from matrix Raman bands reported in other studies.[5] The presence of these new compounds could support the transport model of an impact structure.

ACKNOWLEDGMENTS

J. Aramendia and L. Gomez-Nubla are grateful to the Basque Government and to the University of the Basque Country (UPV-EHU) respectively, for their predoctoral fellowships. This work was financially supported by the Basque Government through the Environmental Analytical Chemistry Project 2007–2012 (Ref. IT-245-07). The authors are grateful for technical and human support provided by the Raman-LASPEA Laboratory of the SGIker (UPV/EHU, MICINN, GV/EJ, ERDF and ESF).

REFERENCES

1. Giuli, G.; Paris, E.; Pratesi, G.; Koeberl, C.; Cipriani, C. Iron oxidation state in the Fe-rich layer and silica matrix of Libyan Desert glass: A

high-resolution XANES study. *Meteoritics & Planetary Science* **2003**, *38*(8), 1181–1186.
2. Pratesi, G.; Viti, C.; Cipriani, C.; Mellini, M. Silicate-silicate liquid immiscibility and graphite ribbons in Libyan Desert glass. *Geochimica et Cosmochimica Acta* **2002**, *66*(5), 903–911.
3. Aboud, T. Libyan Desert glass: Has the enigma of its origin been resolved? *Physics Procedia* **2009**, *2*(3), 1425–1432.
4. Koeberl, C. Libyan Desert glass: Formation by meteorite impact or airburst? *CAG* **2011**, *23*, Abstract #7.
5. Swaenen, M.; Stefaniak, E. A.; Frost, R.; Worobiec, A.; Van Grieken, R. Investigation of inclusions trapped inside Libyan Desert glass by Raman microscopy. *Analytical and Bioanalytical Chemistry* **2010**, *397*(7), 2659–2665.
6. Greshake, A.; Koeberl, C.; Fritz, J.; Reimold, W. U. Brownish inclusions and dark streaks in Libyan Desert glass: Evidence for high-temperature melting of the target roch. *Meteoritics & Planetary Science* **2010**, *45*(6), 973–989.
7. Magna, T.; Deutsch, A.; Mezger, K.; Skála, R.; Seitz, H. M.; Mizera, J.; Řanda, Z.; Adolph, L. Lithium in tektites and impact glasses: Implications for sources, histories and large impacts. *Geochimica et Cosmochimica Acta* **2011**, *75*(8), 2137–2158.
8. Barrat, J. A.; Jahn, B. M.; Amossé, J.; Rocchia, R.; Keller, F.; Poupeau, G. R.; Diemer, E. Geochemistry and origin of Libyan Desert glasses. *Geochimica et Cosmochimica Acta* **1997**, *61*(9), 1953–1959.
9. Gucsik, A.; Koeberl, C.; Brandstätter, F.; Libowitzky, E.; Zhang, M. Infrared, Raman and cathodoluminescence studies of impact glasses. *Meteoritics and Planetary Science* **2004**, *39*(8), 1273–1285.
10. McHone, J. F.; Killgore, M.; Kudryavtsev, A. Cristobalite inclusions in Libyan Desert glass: Confirmation using Raman spectroscopy. *Abstracts of the Lunar and Planetary Science Conference* **2000**, *31*, 1877.
11. Halvorson, K.; McHone, J. F. Vredefort coesite confirmed with Raman spectroscopy. *Abstracts of the Lunar and Planetary Science Conference* **1992**, *23*, 477.
12. Castro, K.; Pérez-Alonso, M.; Rodríguez-Laso, M. D.; Madariaga, J. M. Pigment analysis of a wallpapers from the beginning of XIX century: Les monuments de Paris. *Journal of Raman Spectroscopy* **2004**, *35*, 704–709.
13. Maguregui, M.; Prieto-Taboada, N.; Trebolazabala, J.; Goienaga, N.; Arrieta, N.; Aramendia, J.; Gomez-Nubla, L.; Sarmiento, A.; Olivares, M.; Carrero, J.; Martinez-Arkarazo, I.; Castro, K.; Arana, G.; Olazabal, M. A.; Fernandez, L. A.; Madariaga, J. M. Dispersive Raman spectra database of original and decayed materials belonging to the natural, industrial and cultural heritage (e-VISNICH database). *ChemCH, 1st International Congress Chemistry for Cultural Heritage* **2010**, S6P2.
14. Downs, R. T. (2006) The RRUFF Project: An integrated study of the chemistry, crystallography, Raman and infrared spectroscopy of minerals. *Program and Abstracts of the 19th General Meeting of the International Mineralogical Association in Kobe, Japan,* O03-13.
15. Longinelli, A.; Sighinolfi, G.; Michele, V.; Selmo, E. δ^{18} O and chemical composition of Libyan Desert glass, country rocks, and sands: New considerations on target material. *Meteoritics & Planetary Science* **2011**, *46*(2), 218–227.
16. Smith, D. C.; Vernioles, J. D. The temperature of fusion of a Celtic vitrided fort: A feasibility study of the application of the Raman microprobe to the non-destructive characterization of unprepared archaeological objects. *Journal of Raman Spectroscopy* **1997**, *28*(2–3), 195–197.
17. Castro, K.; Pérez-Alonso, M.; Rodriguez-Laso, M. D.; Madariaga, J. M. Raman fibre optic approach to artwork dating. *Spectrochimica Acta, Part A* **2004**, *60*(12), 2919–2924.
18. Ramirez-Cardona, M.; El-Barkooky, A.; Hamdan, M.; Flores-Castro, K.; Jimenez-Martinez, N. I.; Mendoza-Espinosa, M. On the Libyan Desert Silica Glass (LDSG) transport model from a hypothetical impact structure. *International Geological Congress Oslo* **2008**; PIS-01.

Spectroscopic Integrated Method in the Way Towards the Search of the Origin of Libyan Desert Glass

/ LETICIA GOMEZ-NUBLA (1), JULENE ARAMENDIA (1), SILVIA FERNÁNDEZ-ORTIZ-DE-VALLEJUELO (1), KEPA CASTRO (1), AINHOA ALONSO-OLAZABAL (2), Mª CRUZ ZULUAGA (2), LUIS-ÁNGEL ORTEGA (2) XABIER MURELAGA (3) JUAN-MANUEL MADARIAGA (1).*

(1) Department of Analytical Chemistry, University of the Basque Country. Bº Sarriena s/n. 48940, Leioa (Spain)
(2) Department of Mineralogy and Petrology, University of the Basque Country. Bº Sarriena s/n. 48940, Leioa (Spain)
(3) Departament of Stratigraphy and Palaeontology , University of the Basque Country. Bº Sarriena s/n. 48940, Leioa (Spain)

INTRODUCTION

The Libyan Desert Glass (LDG) is a melt product whose origin is a controversy. Some authors mention that this material could be produced due to a high-temperature impact of a space material into the sand (impactite). Some others consider that the LDGs are the result of an airburst of a meteoroid, since there is a lack of crater (Swaenen, et al., 2010). However, the location of an impact crater is difficult to resolve because it would be covered by the Great Sand Sea desert or it would be destroyed by erosion (Barrat, et al., 1997). LDGs have been dated at 28, 5 millions of years in the Oligocene. These materials are spread along wide corridors between the dunes of the Great Sand Sea (South West of Egypt, near the Libyan border) (Ramirez-Cardona, et al., 2008). Aforetime, LDGs were used by prehistoric men to make various artifacts, as seen in several findings. It was also used in dynastic times on the scarab-shaped central motif of Tutankhamon's pectoral. (Pratesi, et al., 2002). LDGs are mainly composed by silica (SiO_2 ≈ 98%). Some compounds such as carbonates and sulphates were detected in previous studies (Aramendia, et al., 2011). These mineral phases could sustain the impact hypothesis, but it is not enough to elucidate the disagreement about the origin. The aim of this study is to carry out a deeper characterization of the inner part of Basque Country University collection specimens and to compare these results with data obtained from the surface of those materials. In this way, it has been avoided hypothetical crossed pollution present on the surface of the LDGs.

MATERIAL AND METHODS

In this work several specimens of Libyan Desert Glass was analyzed by Raman spectroscopy. For this purpose the samples were sliced making easier the measurements. Besides, in this way, inclusions trapped in the interior side of the LDG could be studied.

Raman spectroscopy is suitable for these prized materials. This is a non-destructive technique, therefore it is possible the identification of the molecular composition without the destruction of the sample. It was used several Raman equipments provided with two different laser wavelengths: 514 and 785 nm. Moreover, in order to improve the analysis of the inclusions, long range objectives of 5x, 20x, 50x and 100x were used. All the Raman measurements were done with laser power lower than 50 mW in order to avoid the thermodecomposition of the sample. Spectra were acquired between 5 and 15 seconds, and 10 to 15 accumulations.

In order to complement these results, an EVO 40 scanning electron microscope coupled to a X-Max energy-dispersive X-Ray spectroscopy equipment was used for electron image acquisitions and elemental composition determinations. SEM images were acquired at high vacuum employing an acceleration voltage of 20 KV. It was used a secondary electron detector. The elemental mapping analysis (EDS) was performed using an 8.5 mm working distance, a 35º take-off angle and an acceleration voltage of 20 KV.

RESULTS AND DISCUSSION

Macroscopically analyzed LDG are translucent glassy matrix with brownish spherical inclusions located all over the external surface before slicing. However, after the lamination of the samples, it could be observed that in the inner part the brownish inclusions were not discerned, whereas whitish inclusions could be easily perceived. Microscopically, it could be noticed little dark inclusions.

Raman spectroscopy allows determining the mineral phases of the inclusions. Comparing the results obtained from the inclusions of the surface and those obtained from the inner inclusions, it could be noticed important differences. Apart from the silica mineral phases such as cristobalite and quartz, other minerals were found in the inclusions distributed through the matrix of the LDG. In the inclusions located on the surface of the samples iron compounds were not detected, whereas they are the main component of the inner ones. In contrast, compound such as corundum is only present at the surface.

Besides, they were identified mineral characteristic phases of the LDG impact (high pressure) and of LDG settled state (low pressure). The presence of calcite suggests a possible transformation of high pressure aragonite to the low pressure calcite both detected in the present study.

Other couples of minerals similar in composition are also detected. In this way, sulphates as anhydrite and gypsum were detected. Anhydrite corresponds to the anhydrous phase of gypsum. During weathering, hematite can be transformed into a mixture of hydrated iron oxide-hydroxide known as *limonite*. The characteristic peaks and identified phases are summarized in Table 1. In the case of silicates, the identified cristobalite could be formed during high temperature, since it is a high-temperature mineral; in contrast quartz is the cristobalite low-temperature polymorph. High temperature mineral phases such as microcline and anatase

palabras clave: Vidrio, Desierto de Libia, Espectroscopia Raman, Inclusiones

key words: Desert Glass, Libya, Raman spectroscopy, Inclusions

* corresponding author: leticia.gomez@ehu.es

Compound	*This work (Wavenumber/cm^{-1})*	*Other LDG works (Wavenumber/cm^{-1})*
LDG matrix	Silicate: ≈1370(br), ≈1600(br)	Glassy matrix:
	Glassy matrix: 447 (br), 810 (br), 956 (br) and 1050 (br)	480(br) and 820(br)
Quartz	204(m), 263(w), 354(w), 401(vw), 463(vs), 806(w), 1158(vw)	208(w), 465(m)
Anatase	141 (vs), 394 (m), 512 (w), 636 (s)	142(vs), 227(vw), 395(vw), 515(vw), 637(w)
Calcite	153(w), 279(m), 710(w), 1085(vs)	Not Found
Anhydrite	1018(w)	418(vw), 1018(vs), 1130(w)
Gypsum	411 (m), 618 (vw), 668 (vw), 1006 (m)	Not Found
Amorphous carbon	≈1300(br), ≈1600(br)	≈1300(br), ≈1600(br)
Microcline feldspar	513(m), 529(m)	Not Found
Natrite	695(vw), 1081(w)	Not Found
Cristobalite	230 (vs), 418 (vs)	230 (s), 418 (s), 780 (w), 1076 (w)
Corundum	416 (m)	Not found by Raman
Aragonite	1083 (m)	283 (w), 714 (vw), 1087 (s)
Unidentified Silicate	239 (w), 263 (vw), 300 (br), 373 (br), 504 (w), 764 (s), 785 (vs), 968 (s)	Nout Found
Hematite	226 (w), 292 (m), 410 (w)	Not found
Limonite	171 (w), 208 (m), 243 (m), 300 (s), 399 (vs), 471 (br), 551 (s), 1282 (br)	Not found

Table 1*. Resume of Raman data summarizing characteristic Raman positions in cm $^{-1}$ of different compounds present in LDG, where the intensity of the bands are represented by v: very, s: strong, m: medium, w: weak and br: broad.*

were distinguished. By Raman spectroscopy respective low temperature polymorphs were not found. However, by optical microscopy of fine rutile microlites can be observed. This phase can correspond to the transition of the anatase with high temperature.

In order to complement the previous results it was carried out an element mapping using SEM-EDS. In this way it could be seen how the elements are distributed in the inclusions. In Fig. 1 the first image is corresponded with the SEM image of an inclusion of LDG. The other images are elemental maps done with EDS over the same inclusion. In those maps, the white colour represents the presence of an element and the black the absence.

It can be seen that the inclusions are not formed by only one compound. The inclusion analyzed in the image, around the big cavity, is composed mainly by silicon but some elements are concentrated in certain areas, such as: C, O, Mg, Al, K, Ca, Ti and Fe.

On the one hand, calcium and carbon maps are very similar. The place where the carbon and the calcium are more concentrated is the same. This fact supports the presence of calcite and/or aragonite, both determined by Raman. On the other hand, silicon, iron and aluminium compounds appear similarly place and are in concordance the mineralogy detected by Raman spectroscopy. This chemical and mineralogical heterogeneity was observed in all the analyzed samples.
This work is an approach to the knowledge of the origin of the Libyan Desert Glass. It can be concluded that the silica is the main component in LDG glassy matrix. Inclusions are composed by different compounds and therefore are chemically more heterogeneous. Besides, Raman spectroscopy result a useful tool for the analysis of LDGs although some other supporting techniques are required.

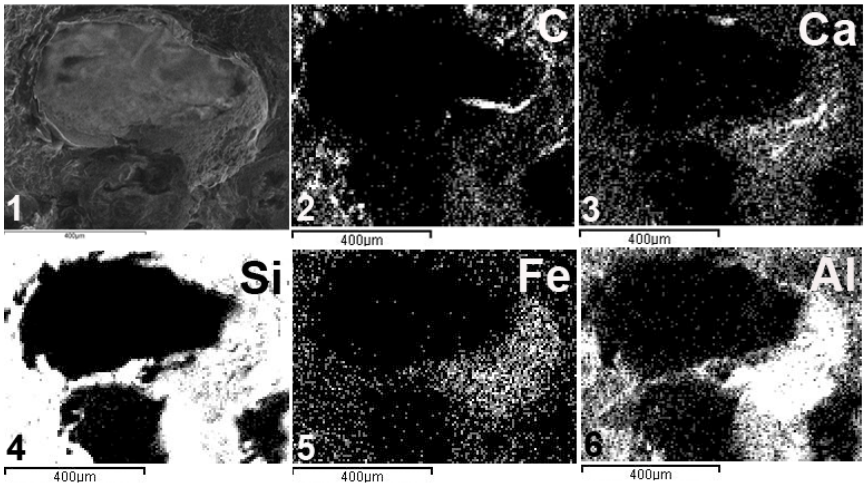

fig 1*. 1) SEM image of a LDG inclusion with a big cavity, 2) Carbon map, 3) Calcium map, 4) Silicon map, 5) Iron map and 6) aluminum map of that inclusion.*

ACKNOWLEDGMENTS

L. Gomez-Nubla and J. Aramendia are grateful to the University of the Basque Country (UPV/EHU) and to the Basque Government respectively, for their predoctoral fellowships. The authors are grateful for technical and human support provided by the Raman-LASPEA Laboratory of the SGIker (UPV/EHU, MICINN, GV/EJ, ERDF and ESF. Moreover, this work has been financially supported by the project "*Estudio de material asociado a impactos meteoriticos*" from the University of the Basque Country (UPV/EUH) (ref: AE11/26).

REFERENCES

*Aramendia, J., Gomez-Nubla, L., Fdez Ortiz de Vallejuelo, S., Castro, K., Murelaga, X., Madariaga, J.M. (2011): New findings by Raman micro spectroscopy in the bulk and inclusions trapped in Libyan Desert Glass. Spectrosc. Lett., **44**, 7-8, 521-525.*

*Barrat, J.A., Jahn, B.M., Amossé, J., Rocchia, R., Keller, F., Poupeau, G. R., Diemer, E. (1997): Geochemistry and origin of Libyan Desert glasses. Geochimic. Cosmochimic. Acta, **61**, 1953-1959.*

*Pratesi, G., Viti, C., Cipriani, C., Mellini, M. (2002): Silicate-silicate liquid inmmiscibility and graphite ribbons in Libyan Desert Glass. Geochimic. Cosmochimic. Acta, **66**, 903-911.*

Ramirez-Cardona, M., El-Barkooky, A., Hamdan, M., Flores-Castro, K., Jimenez-Martinez, NI., Mendoza-Espinosa M. (2008): On the Lybian Desert Silica Glass (LDSG) transport model from a hypothetical impact structure. International Gelogical Congress Oslo 2008. PIS-01.

*Swaenen, M., Stefaniak, E.A., Frost, R., Worobiec, A., Van Grieken, R. (2010): Investigation of inclusions trapped inside Libyan Desert Glass by Raman microscopy. Anal Bioanal. Chem.. **397**. 2659-2665.*

Research article

Journal of RAMAN SPECTROSCOPY

Received: 4 January 2013 Revised: 31 May 2013 Accepted: 3 June 2013 Published online in Wiley Online Library: 13 July 2013

(wileyonlinelibrary.com) DOI 10.1002/jrs.4342

From Portable to SCA Raman devices to characterize harmful compounds contained in used black slag produced in Electric Arc Furnace of steel industry

Leticia Gómez-Nubla,* Julene Aramendia, Silvia Fdez-Ortiz de Vallejuelo, Kepa Castro and Juan Manuel Madariaga

Black slag from steel production is an industrial waste used as secondary material for some applications (forest tracks, cement, etc.). When it disposed to the open air, little is known about possible side effects that could appear with time. To foresee those side effects, various Raman equipments were used. This analytical strategy has been applied to six different black slag. Four of them were obtained from two steel producers (two original and two with treatment of 'inerting'), and the other two sampled in civil construction works, which supposedly should be treated. Results showed the original mineral phases of the samples (iron and other metal oxides, silicates, ferrites…) and the new phases (calcite, natron, nitratine, goethite, limonite, ilesite, etc.) resulting from the superficial reaction with the atmospheric acid compounds. This fact indicates a strong reactivity between slag and surrounding environment where they have been deposited. Only with one of the three setups, all the compounds could not be detected: (1) the handheld spectrometer detected the major ones and few of the minor ones, (2) the laboratory Raman microprobe ascertained nearly all of the compounds, but cannot be translated to the field and (3) Structural and Chemical Analyser (SCA), which combines micro-Raman spectroscopy and Scanning Electron Microscopy/ Energy Dispersive X-Ray Spectroscopy (SEM-EDS) on the same spot, recognized the trace compounds, which were the most harmful ones. These results demonstrate the greater applicability of this new strategy in comparison with traditional methods for the chemical characterization of black slag and its alteration products.

All Supporting Information may be found in the online version of this article.

Keywords: black slag; handheld and micro-Raman spectroscopy; Raman Image; Structural and Chemical Analyser; alteration products

Introduction

In agreement with the current and increasing consumption of natural resources, the production of waste industrial products has grown enormously. In the particular case of steel industry, it generates worldwide almost 50 million tons of by-products per year, most of them, slag from the steel manufacture.[1,2] Specifically, in Basque Country (Spain), 835.000 tons of slag are generated each year from 14 steel manufacturers.[3]

This situation has prompted the search for solutions and alternatives to reuse these by-products in order to decrease the demand of others raw materials and contribute to the conservation of natural resources. In the last years, this slag, which is thoughtful inert[4], was being used for road construction[5–7], phosphate fertilizer[8,9], in ballast for railway tracks[10], hydraulic engineering[11], metal recovery[12], in cement production[2,13–17], in ports and harbours construction[18], as filler in the construction of forest tracks[19] and others applications that are under study.[20,21]

This kind of slag has low level of volumetric stability[22], and besides, it contains a great amount of heavy metals (As, Cd, Hg, etc.) in different structural forms (oxides, silicates, ferrites, etc.)[23] that could be released to earth, river or marine water and beaches, if it is simply deposited in seawater, sediments or lands[24], causing some environmental problems[24,25]. Both problems have been observed, for example, in commercial cement with slag as additive[13], in road construction[26], in agriculture with the slag as fillers [27] and in trace elements release from slag dumps.[28]

There are different slag types depending on the process of steel manufacturing: blast furnace slag, basic oxygen furnace slag, electric arc furnace slag and ladle furnace basic slag.[10] Thus, the final composition of these types of slag varies according to the furnace type, steel grades and process of generation.

The steel produced in Electric Arc Furnace is obtained from iron scrap and/or steel as raw material. As auxiliary elements, small quantities of iron mineral, caustic lime, spar-fluoride, coke, oxygen, prereduced (virgin charge to dilute undesirable metals that the used scrap could contain) and iron-alloys are added. According to the composition, the steels are divided in: (1) ordinary steels or to the carbon, (2) above all composed by iron and carbon and (3) alloyed steels or specials, with different metals

* *Correspondence to: Leticia Gómez-Nubla, Department of Analytical Chemistry, Faculty of Science and Technology, University of the Basque Country (UPV/EHU), P.O. Box 644, E-48080 Bilbao, Basque Country, Spain*
E-mail: leticia.gomez@ehu.es

Department of Analytical Chemistry, Faculty of Science and Technology, University of the Basque Country (UPV/EHU), P.O. Box 644E-48080 Bilbao, Basque Country, Spain

like Cr, Ni, Mo, V and W. These steels are manufactured in two steps: primary metallurgy, where black slag are produced, and secondary metallurgy, whose process involves the white slag generation. Initially, the scrap is melted through electric energy, and then, caustic lime and pure oxygen are added to the molten, in order to generate the slag by oxidizing the elemental iron, manganese and silicon. Finally the free FeO (wustite) is reduced with carbon dust. All mineral phases formed are integrated in the oxidized black slag that covers the molten liquid. It is a dark colour material with porous aspect and irregular morphology.[3,29]

This slag cannot be used directly and the administrative regulations impose to treat the originally produced slag to obtain a suitable 'treated slag' (it should be referred better as 'stabilized slag') for its use. In general, the need of treatment depends on the future use.[30]

In this work, several types of black slag, all of them coming from Electric Arc Furnace production of steel, have been studied. The main aims were to compare the compounds in black slag without and with treatment of 'inerting' (so-called 'treated slag') from two different steelworks, and to acquire knowledge about the presence of harmful compound in their mineral composition, in order to evaluate the possible reactivity with the environmental stressors. Several environmental conditions present in the treatment were selected to see if they had influence in the formation of new compounds in the original slag. Consequently, the possible impact that they could produce to medium–long term in soil and water, around the zone where the slag have been used, could be estimated.

To proceed with such research, it is necessary to establish previously an analytical procedure[31] to perform a detailed study of the composition and the characterization of major, minor and trace mineral phases present in the selected slag samples. To that purpose, Raman spectroscopy was selected as the analytical technique of choice, it is a non-destructive technique that it doesn't require sample preparation.[32]This work was performed with three different Raman spectrometers. First, it was used a handheld Raman spectrometer that allows field analysis *in situ* (thanks to the small size that makes easier the transport by only one person[33]) and can be used when the slag is utilized as secondary material for some applications. However, in our case, it was used in the laboratory to check its future use and to characterize major (and minor) mineral phases. To assist the handheld Raman analysis (spots around 100 microns), Energy Dispersive X-Ray Fluorescence (EDXRF, spots around 650 microns) was used. And then, a micro-Raman spectrometer plus Raman Image analysis were used in order to characterize minor and trace compounds, because it was possible to use magnification microscope objectives in order to focus the laser beam on the selected material layer. Finally, the Structural Chemical and Analyser (SCA) was used to identify compounds at trace level. SCA (Raman plus SEM/EDS) allowed us to merge the analytical advantages of several individual techniques in the same system (the EDS analysis helped to select what elements were present in the exact point of Raman measuring of the black slag) but at trace levels (spots of less than 5 microns). In spite of this, the analysis performed with this equipment is expensive, so it is not entirely suitable for the characterization of major and minor compounds. This can be more economically achieved with the handheld spectrometer (in the field) or with the Raman microprobe (in the laboratory). Therefore, this novel approach permits a characterization of the sample, from major till minor and trace compounds, based on its elemental and molecular composition.

Experimental procedure

Sample collection and pretreatment

In the present study, a total of six black slag samples (see Fig. S1 (Supporting Information)) from different locations in Bizkaia (Basque Country, Spain) were collected. Four of them came directly from two steel producers, and the other two were sampled in two civil construction works where slag were used as filling for vehicle roads.

- *M1*: black slag without treatment from factory manufacturing common steel. It has only been cooled outdoors.
- *M1 T*: treated black slag from the common steel industry. Its stabilization treatment in the factory consisted of outdoor cooling, irrigation with water, crushing, sifting and magnetic separation of ironed materials.
- *M2*: black slag without treatment from factory manufacturing special steel. It has only been cooled outdoors.
- *M2 T*: treated black slag from the special steel industry. Its stabilization treatment in the factory consisted of outdoor cooling and irrigation with water.
- *M3*: black slag (supposedly with treatment of 'inerting') from a civil building construction in Getxo (Bizkaia, Spain).
- *M4*: black slag (supposedly with treatment of 'inerting') from a civil building construction in the Campus of Bizkaia (Leioa, Bizkaia, Spain).

In the case of M3 and M4, the origin of the steel manufacturer was unknown as well as the treatment carried out. It was assumed that they were treated because the legislation of Basque Country requires using treated slag in any construction site.[30]

Respect to their colour, at first, the whole of the slag had a grey dark colour, but with time the slag went to a whitish colour.

In the laboratory, the six samples of black slag were divided in two portions. The first one was stored, and the second one was crushed, grinded, lyophilized, sieved and put in glass recipients until analysis by Raman, SCA and EDXRF. The grinding step was done first by hand and then mechanically by using a Fristch Pulverisette 6 (Indar- Orberstein, Germany) during 15 min, with two repetitions of 700 rpm. These conditions were changing according to the hardness of the slag. Later, grinded samples were lyophilized (Cryodos, Telstar) for 48 h to 150 mb and −52 °C approximately. Finally, the samples were sieved. Only the grains with less than 2 mm were used to measure by EDXRF. In the case of micro-Raman and SCA measurements, particle size between 2 mm and 250 μm were used.

Instrumentation

Raman spectroscopy, coupled to X-Ray elemental analysis, was used at different levels to identify major, minor and trace compounds in all the samples. Major and most of the minor compounds were identified by using portable (handheld) Raman and EDXRF spectrometers. Minor compounds and some trace mineral phases were identified using Raman microprobe and Raman Image analysis, assisted with Scanning Electron Microscopy/Energy Dispersive X-Ray Spectroscopy (SEM-EDS) measurements. Others trace and ultra-trace compounds were identified using the SCA (micro-Raman and SEM/EDS measurements together on the same spot) instrument.

Raman spectroscopy

Three different spectrometers were used to perform the analysis on the surface of the black slag, depending on the abundance (major, minor and trace) of the compounds under research. More than 60 measurements were performed per sample/spectrometer.

The search for major compounds was done using an InnoRam handheld spectrometer (B&WTEK$_{INC}$, Newark, USA) provided with a 785 nm excitation laser with a nominal laser power of 225 mW (20–100% of laser power was used) and a CCD detector (Peltier cooled). Data acquisition was done by BWSpec 3.26 software (B&WTEK$_{INC}$, Newark, USA), and the analysis, treatment and interpretation of the results was carried out by Omnic software (Thermo Fisher-Nicolet, Madison, Wisconsin, USA). Spectra were obtained with a resolution of 3–4 cm^{-1} in a spectral range of 200–2000 cm^{-1}. And in order to improve the relation signal-to-noise, the accumulations were modified too.

The analysis of minor (and trace) compounds was performed with a Raman microprobe device (a Renishaw RA 100 Raman Spectrometer, coupled to an Oxford fibre optic microprobe), equipped with 785 nm excitation laser and a CCD detector (Peltier cooled). The microprobe was joined to different long range lenses (4×, 20× and 50×) which allow us to focus the laser beam between 5 μm and 100 μm at the sample. The nominal power of the excitation source is 150 mW at 100% laser power; thermal decomposition in the black slag was never observed. The time of integration was between 10 s and 15 s, and the number of accumulation was varied in order to achieve the best signal-to-noise ratio. The data were acquired with WIRE 2.0 software (Renishaw, UK), and the analysis and treatment of these were realized with the previously mentioned Omnic software.

The Raman Image measurements were carried out by using a Renishaw InVia Raman spectrometer with a 514 nm excitation laser, coupled to a Leica DMLM microscope. The spectra were acquired with the Leica 50× N Plan (0.75 aperture) lens with 2 microns of spatial resolution. Additionally, for visualization and focusing, a Leica 5× N Plan (0.12 aperture) and a 20× N Plan EPI (0.40 aperture) lens were used. For focusing on and searching for points of interest, the microscope implements a Prior scientific motorized stage (XYZ) controlled by a joystick. The Stream Line option was used to obtain the Raman chemical images. Additionally, this device was also used for Raman microanalysis of selected points of interest. The spectral range chosen was 200–2000 cm^{-1}, and the acquisition time was 5 s with one accumulation per each spectrum, which ensured a suitable signal-to-noise ratio.

The spectrometers were calibrated daily with the 520 cm^{-1} silicon band. The quality of measurements was assessed by means of an internal calibration with the mentioned silicon chip.

The interpretation of the results was accomplished by comparison with standard Raman spectra from the e-Visart and e-Visnich databases [34,35] and spectra obtained from the on-line database RRUFF (http://rruff.info/).[36]

EDXRF analysis

All samples (grain sizes less than 2 mm) were measured to obtain the elemental composition by the portable ArtTax EDXRF equipment by Rontec (nowadays Brucker AXS Berlin, Germany) that incorporates a Mo X-ray tube working at a maximum voltage of 50 kV and a maximum current of 700 μA. The X-rays are collimated by a tantalum collimator with a diameter of 0.65 mm. The instrument contains a CCD camera to obtain images of the sample analysed (8 × 8 mm) and a computer-controlled motor-driven XYZ positioning unit to focus on the sample.

The samples were prepared as pressed powder pellets under 10 tons of pressure (CrushIR, PIKE Technologies, Canada): 0.5 g of each grinded, sifted and lyophilized slag and 0.1 g of methylcellulose. Methylcellulose was used as transparent binder in order to increase the mechanical stability of the black slag pellets. The final sample pellets had a diameter of 12 mm and 3 mm width. Several measurements were collected for the same pellet in order to assure more reliable results. The instrument was calibrated with a bronze standard. Exposition time of 1000 s at a voltage of 50 kV and a current of 700 μA were used. Spectra processing and manipulation were carried out using the ArtTAX program Version: 4.9.13.2 from Bruker AXS.

SEM-EDS and Structural and Chemical Analyser (SCA)

SEM-EDS and SCA measurements were performed on the same experimental platform. Grains sieved between 2 mm and 250 μm of each black slag were deposited on the surface of a special aluminium pin and glued to the surface by using a carbon adhesive tape. As the samples may contain carbon compounds, they were not covered with graphite to avoid interferences.

The experimental platform has three units. On the one hand, an EVO 40 Scanning Electron Microscope (Carl Zeiss NTS GmbH, Germany) coupled to an X-Max Energy-Dispersive X-Ray spectroscopy equipment (Oxford Instruments, Abingdon, Oxfordshire, United Kingdom) was used for electron image acquisitions and elemental composition determinations of the black slag. SEM images were acquired at high vacuum employing an acceleration voltage of 20 KV. Magnifications up to 10 000× were reached using a secondary electron (SE) detector. The second unit, EDS (Oxford Instruments, UK), was used for elemental mapping, and the analysis was performed using an 8.5 mm working distance, a 35° take-off angle and an acceleration voltage of 20 KV. The third unit is the SCA interface (Renishaw, UK), that uses in-SEM retractable collection optic to introduce the laser light and focus it into the sample as well as to collect the Raman signal through the in-Via micro-Raman spectrometer described earlier. The laser light and Raman signal are both transmitted between the Raman spectrometer and the SCA via 2 m fibre-optic cables.

For conventional SEM-EDS analysis (backscatter electron imaging plus x-ray mapping analysis), the retraction mechanism of the SCA was used to quickly move the optic away to a 'standby' position. This operation mode was used to set the positions of the trace elements in order to better focus with the SCA interface.

This SCA interface allows the user to perform Raman spectroscopy simultaneously with SE imaging inside the SEM, particularly on the spot areas selected previously (i.e. areas with high Cr density of this trace chromium element in the slag). Although the SCA used in this study is configured for use with 514 and 785 nm laser excitations, only the 785 nm laser was used to measure the slag samples. As previously, the Raman spectral interpretation was done by comparison with pure standard compounds contained in the spectral databases mentioned before.[34–36]

Results and discussion

The elemental characterization of slag at macro level (spots of 0.65 mm) was made through micro-EDXRF. The characteristic elements present in the analysed samples were: Ca, Ti, Cr, Mn, Fe, Cu, Zn, As, Rb, Sr, Ba, S, Sn, Si, V and Se. Whereas W, Sc, Nb

and Ni were occasionally observed. The slag samples from the factory near the sea border showed also the presence of K and Br. Ca, Cr, Mn and Fe had the most intense peaks in all the cases.

When the XRF spectra of non-treated and treated samples were compared, some important differences in the relative peak area of the elements were observed, indicating disparities in the composition of the samples. Probably, this is a consequence of the appearance of new mineral phases (many metallic oxides will be transformed in the corresponding hydroxides and/or carbonates) after the treatment suffered by these slag. Thus, a molecular analysis and comparison are required among treated and non-treated samples to confirm this observation.

The major mineral phases, summarized in Table 1, were identified by handheld Raman spectroscopy in the black slag samples. As it can be seen, all slag samples have the same major components. In this work, a major mineral phase is a compound that appears more than 20% in the whole set of spectra collected with the handheld Raman spectrometer.

Calcite ($CaCO_3$, Raman bands at 155 m, 281 s, 712 m, 1085vs, 1436w and 1749w cm^{-1}) was detected in all the samples. In fact, it was found in the non-treated slag samples, which they had only suffered from cooling (M1 and M2 samples), in the ones sampled after the stabilization treatment (M1T and M2T samples) and in those sampled at the civil works (M3 and M4 samples). Its presence is due to the use of caustic lime (CaO) in the formation of the slag during the production of the steel, in order to eliminate the phosphorous[3] from the raw materials. When cooling, the remaining caustic lime suffers a hydration process that transforms it into calcium hydroxide:

$$CaO(s) + H_2O \rightarrow Ca(OH)_2(s) \quad (1)$$

and then calcium hydroxide reacts with atmospheric CO_2 to give calcium carbonate (calcite):

$$Ca(OH)_2(s) + CO_2(g) \rightarrow CaCO_3(s) + H_2O. \quad (2)$$

The difference among samples is the relative abundance of calcite, as it can be observed in the Raman images shown in Fig. 1. Also, the intensity of the Raman bands of calcite in the normalized spectra is lower in the non-treated than in the treated ones. The abundance observed for the M2 and M2 T sample is similar to that shown in Fig. 1. Moreover, the abundances in M3 and M4 samples are similar to the obtained for the M1 T samples (and consequently to M2 T sample), confirming that M3 and M4 samples belong to treated slag material.

To sum up, the experimental evidence shown in Fig. 1 allows us to conclude that calcite is formed after cooling the slag, without any special treatment. When the slag is removed from the Electric Arc Furnace, the material is at a temperature of 800 °C

Table 1. Raman bands list of compounds found in original and degradation products from different black slag studied (M1: common steel industry; M1 T: treated from common steel industry; M2: special steel industry; M2 T: treated from special steel industry; M3: from Getxo town; M4: from Leioa town)

Compound		Formula	M1	M2	M1T	M2T	M3	M4	Wavenumbers/cm^{-1}
Calcite	*PR*	$CaCO_3$	X	X	X	X	X	X	155 m, 281 m, 712 m, 1085vs, 1433w, 1747w
HMC	*PR*	$Ca(Mg)CO_3$	X	X	X	X	X	X	154s, 281 m, 713 m, 1087vs
HMC + Aragonite	*PR*	$Ca(Mg)CO_3 + CaCO_3$	X	X	X	X	X	X	277 m, 709 m, 1090vs
Lepidocrocite	*PR*	γ- FeO(OH)	X	X	X	X	X	X	215 m, 248vs, 305 m, 346 m, 375s, 525 m, 646 m
Magnetite	*PR*	Fe_3O_4	X	X	X	X	X	X	314 m, 477 m, 558 m, 680vs
Magnesioferrite	*PR*	$MgFe_2O_4$	X	X	X	X	X	X	327 m, 435 m, 613vs
Larnite	*PR*	β-Ca_2SiO_4	X	X	X	X	X	X	846sh, 857vs, 976 m
Walstromite	*PR*	$BaCa_2Si_3O_9$	X	X	X	X	X	X	664s, 990 m
Hematite	*PR*	α-Fe_2O_3	X	X	X	X	X	X	223s, 288vs, 408 m, 497w, 608w
Goethite	*MR*	α-FeOOH		X	X	X	X	X	248 m, 300 m, 384vs, 475vw, 529w
Tephroite	*MR*	Mn_2SiO_4	X	X	X		X		810 m, 843 m
Limonite	*MR*	$FeO(OH) \cdot nH_2O$				X		X	296 m, 396vs, 470vw
Ilesite	*MR*	$(Mn, Zn, Fe)\ SO_4 \cdot 4H_2O$		X			X		427s, 488s, 622s, 1024vs
Amorph. Carbon	*PR*	C		X		X			1306br, 1608br
Gypsum	*MR*	$CaSO_4 \cdot 2H_2O$		X					414 m, 492 m, 619 m, 670 m, 1008s, 1135 m
Bassanite	*MR*	$CaSO_4 \cdot 1/2H_2O$		X					429 m, 487 m, 627 m, 668 m, 1015s
Rutile	*MR*	TiO_2	X						237 m, 448vs, 611s
Natron	*MR*	$Na_2CO_3 \cdot 10\ H_2O$				X			1070 m
Nitratine	*MR*	$NaNO_3$				X			190 m, 724 m, 1067vs
Brucite	*MR*	$Mg(OH)_2$		X					278 m, 443 m
Magnesiochromite	*SCA*	$MgCr_2O_4$			X				570w, 699s
Chromite	*SCA*	$FeCr_2O_4$		X					279 m, 680vs
Hashemite	*SCA*	$BaCrO_4$				X			351s, 859vs
Crocoite	*SCA*	$PbCrO_4$			X				843vs

* s: strong; m: medium; w: weak; v: very; br: broad; sh: shoulder
HMC: calcite with high content in magnesium
PR: Portable Raman spectroscopy
MR: micro-Raman spectroscopy
SCA: Structural Chemical Analyser (SEM/EDS + micro-Raman)

Journal of RAMAN SPECTROSCOPY

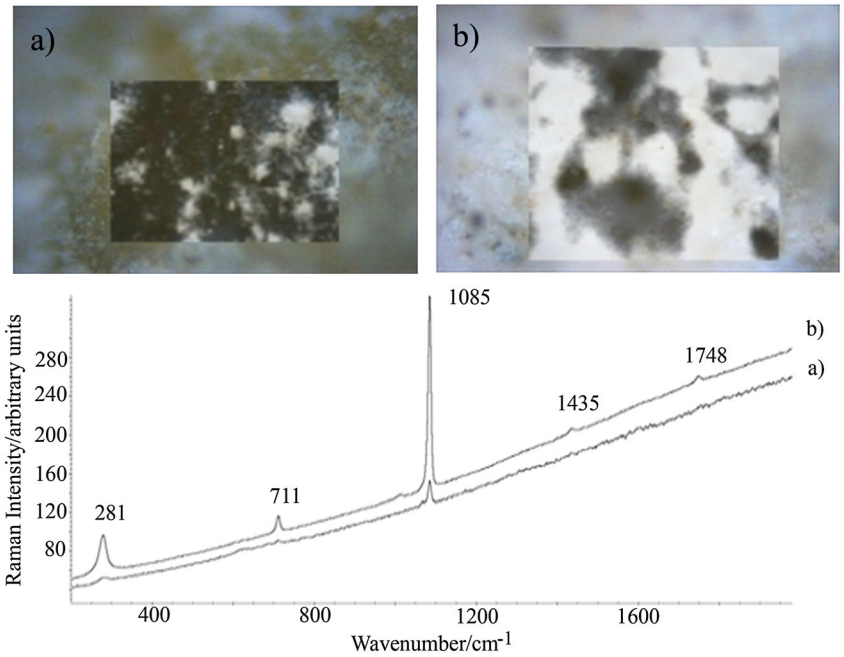

Figure 1. Raman images showing the relative abundance of calcite in Samples M1 (a) and M1 T (b). The indicated spectra belong to a pixel having half of the calcite Raman intensities for each image.

or above, thus no carbonate can be present. But as the cooling process proceeds in open air, the presence of atmospheric humidity and CO_2 is enough to transform part of the remaining CaO into $Ca(OH)_2$, according to reaction (1), and then to $CaCO_3$, following reaction (2). Thus, before starting the stabilization process of the slag, some calcite is always formed. After the stabilization treatment, all the CaO should be transformed to calcite ($CaCO_3$, reactions 1–2), like it is observed in the M1 T Raman image (Fig. 1.b), where calcite occupies practically all the Raman image.

However, calcite was not the only calcium carbonate observed. As a matter of fact, aragonite ($CaCO_3$, Raman bands at 206 m, 705 m and 1085vs cm^{-1}) was also detected. But, it was always found mixed with other compounds (its peaks never appeared alone), and it is not a major compound because it appears only in less than 5% of the collected spectra. Some authors report the formation of aragonite when the concentration of magnesium is relatively high with regard to calcium. This is the case of the black slag, which may contain magnesium coming from the refractory bricks of the furnace.[3,29]

In some cases, the Raman peaks of the calcite were found shifted few wavenumbers (see Fig. 2.a–d). This could be also due to the presence of magnesium, which replaces the calcium atoms of the calcite, forming calcite with high magnesium content (HMC) ($Ca(Mg)CO_3$, Raman bands at 154 s, 281 m, 713 m and 1087vs cm^{-1}). Depending on the magnesium percentage, the peaks are more or less shifted. The greater displacement of the peaks is observed when the magnesium percentage is higher.[37] Raman bands found for HMC can be seen in Table 2, concluding that the amount of magnesium is not constant for all the samples. The trend of the Raman bands as a function of the percentage of magnesium is shown in Figs. 2.e and 2.f based on data described elsewhere.[37] Those Raman shifts in HMC as a function of a mean magnesium percentage can be introduced

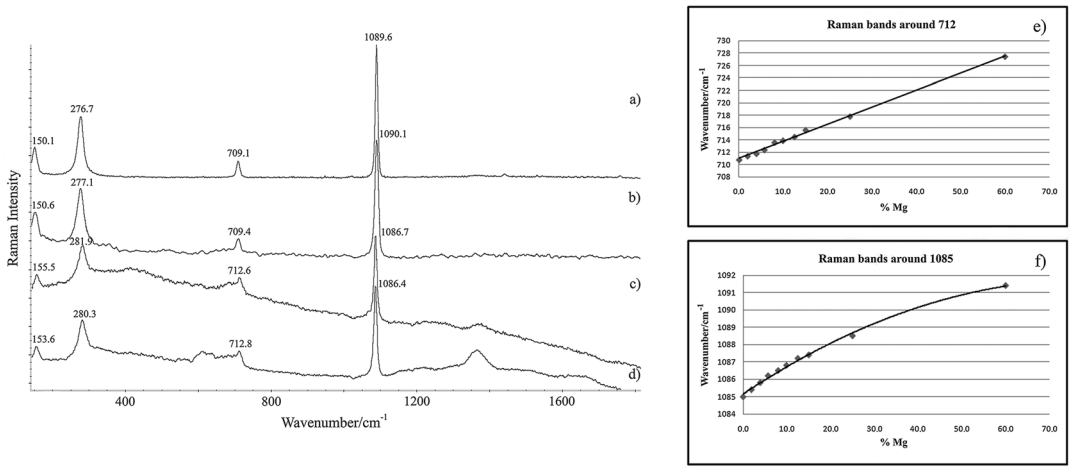

Figure 2. Raman spectra obtained with the portable device of high magnesium calcite with aragonite: a), b); and only high magnesium calcite c), d) with around 7% Mg. Tendency of Raman bands according to the percentage of magnesium in the calcite for the 712 and 1085 peaks (e, f).

Table 2. High magnesium calcite (HMC) Raman bands (T, L, υ_4 and υ_1) of several black slag samples (*M1, M2, M1 T* and *M2 T*) and their magnesium percentage calculated

	M1	*M2*	*M1T*	*M2T*
T	155.5	153.7	153.6	155.1
L	281.9	279.7	280.3	282.0
υ_4	712.6	712.1	712.8	712.8
υ_1	1086.7	1086.3	1086.4	1086.9
% **Mg**	7.7	5.6	7.0	8.6

(both fits are shown in both figures) in a polynomial function (derived from Figs. 2.e and 2.f) and can be used to calculate the magnesium percentage in HMC. Thus, our Raman bands were inserted in the mathematical functions obtaining a mean value of the magnesium content. According to the results of some samples, as it is summarized in Table 2, the estimated magnesium ranged between 5% and 10%. Apart from the slag sampled in the steelworks (treated and non-treated), HMC also appeared in those sampled in the civil construction sites, confirming its presence as major mineral phase (like in the case of calcite) of the slag materials.

Regarding the residual iron contained in black slag, it is worth mentioning that it was originated from the scrap used in the fabrication of the steel.[3] In this production, the reduction process of hematite ores in Electric Arc Furnace, due to mixtures of CO and CO_2, produces metallic iron by means of a series of intermediate oxides. At high temperatures (>570 °C), the reduction of iron oxides is realized in the following form:

$$Fe_2O_3(\text{hematite}) \rightarrow Fe_3O_4(\text{magnetite}) \rightarrow FeO\ (\text{wüstite}) \rightarrow Fe.$$

At lower temperatures (<570 °C), Fe is produced without FeO [38,39].The metallic iron can be oxidized in the cooling process of the slag and in contact with open atmosphere it turns into Fe^{+2} and Fe^{+3} forms. Some reactions of transformation are the following ones[29]:

$$Fe^{+2} + 2OH^- \rightarrow Fe\ (OH)_2$$
$$4Fe\ (OH)_2 + O_2 + 2H_2O \rightarrow 4Fe\ (OH)_3.$$

Consequently, the main iron oxides and hydroxides that could be observed in the analysed slag (Fig. 3 and Fig. S2 (Supporting Information)) were: lepidocrocite (γ-FeOOH, Raman bands at 213 m, 245vs, 303 m, 345 m, 373 s, 523 m and 645 m cm^{-1}), goethite (α-FeOOH, Raman bands at 200w, 245 m, 300 s, 387vs, 477w and 529 s cm^{-1}), limonite (FeO (OH).nH_2O, Raman bands at 240 m, 297 s, 394vs, 473w and 551 m cm^{-1}), hematite (α-Fe_2O_3, Raman bands at 223 s, 287vs, 409 s, 494w and 610w cm^{-1}) and magnetite (Fe_3O_4, Raman bands for this material at 314 m, 477 m, 558 m and 680vs cm^{-1}). In the last case, the main peak of magnetite should be at 667 cm^{-1}, but in the majority of the collected spectra, it is displaced due to be stoichiometric substitution of the iron for cobalt, nickel and traces of aluminium, present in its structure.[36] Also, this displacement could be attributed to differences in the average oxidation state of the iron.[40,41] The presence of hydroxides was higher in the treated slag than in the slag without treatment, due to the added water in the pretreatment.

The spectra taken with the micro-Raman system also revealed the presence of magnesioferrite ($MgFe_2O_4$, Raman bands at 167 m, 329 m, 436 m, 613vs and 662sh cm^{-1}) (see Fig. 3.b) and brucite ($Mg(OH)_2$, Raman bands at 278 m and 444 m cm^{-1}). These compounds can be formed because of the magnesium that comes from the decaying of ceramic bricks. These bricks belong to the furnaces of the oxidize phase of steel production and they are a material rich in MgO.[3,29]

Sodium carbonate decahydrated ($Na_2CO_3.10H_2O$, Raman band at 1067vs cm^{-1}), and nitratine ($NaNO_3$, Raman bands at 190 m, 724 m, 1068vs and 1385 m cm^{-1}) were also found in some treated samples. Their presence could be justified by the possible use of Na_2O as alkaline melting[42] to decrease the melting point and eliminate part of the slag of the own process. Na_2O can remain in the slag, and the combination with atmospheric CO_2 or NO_x gas attack (during the cooling process outdoors) and water (during treatment of 'inerting' that is performed in the steelworks) can form sodium carbonate decahydrated ($Na_2CO_3 \cdot 10\ H_2O$) and nitratine ($NaNO_3$).

In addition, several Raman spectra revealed the presence of silicates as tephroite (Mn_2SiO_4, Raman bands at 808 s and 840 s cm^{-1}) (see Fig. S2 (Supporting Information)), walstromite ($Ba_2Ca_2Si_3O_9$, Raman bands at 664 s and 990 m cm^{-1}) (see Fig. S3. b (Supporting Information)) and larnite (β-Ca_2SiO_4, Raman bands at 846sh, 857vs and 976 m cm^{-1}). Furthermore, it was identified a group of Raman peaks at ~1230 m and ~1370 s cm^{-1}, which appeared in many spectra alone as silicates or with hematite peaks (see Figs. 3.b and Fig. S2 (Supporting Information)). The peak at 1370 cm^{-1}, present in the spectrum of hematite and silicates, can be the sum of the characteristic second band of hematite at 1350 cm^{-1}, which above 800 °C upshifted compared to pure hematite, and the peak of silicates. [43,44] In general, the silicate compounds identified in this work must be mainly related to those

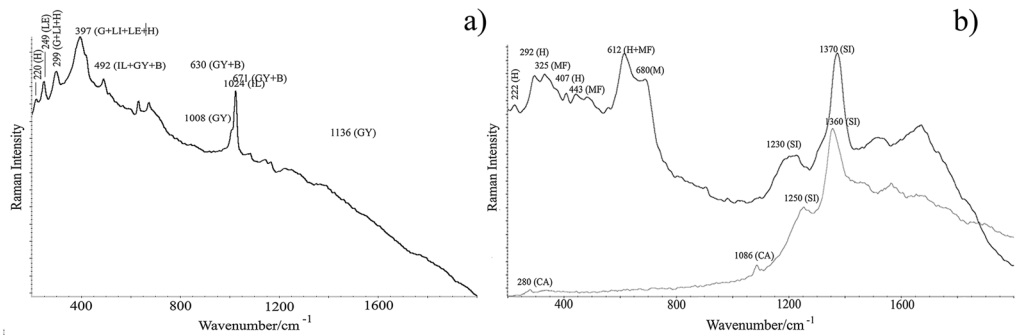

Figure 3. Micro-Raman spectrum of: a) sample M2: mixture of goethite (G), limonite (LI), lepidocrocite (LE), hematite (H), gypsum (GY), bassanite (B) and ilesite (IL); b) sample M1 T: hematite (H), magnesioferrite (MF), magnetite (M) and silicates (SI).

compounds formed during the formation of the black slag in the Electric Arc Furnace. On the other hand, amorphous carbon (C, Raman bands at ~1306 s and ~1608 s cm^{-1}) has also been identified at trace level in some slag.

Additionally, by micro-Raman analysis, several sulfates were detected, such as ilesite ((Mn^{2+}, Zn, Fe^{2+}) $SO_4.4H_2O$, Raman bands at 207 m, 263 m, 427 s, 488 s, 623 s and 1024vs cm^{-1}), gypsum ($CaSO_4.2H_2O$, Raman bands at 293w, 414 m, 493 m, 619 m, 670 m, 1008vs and 1135 m cm^{-1}) and bassanite ($CaSO_4.1/2H_2O$, Raman bands at 236 m, 430 m, 487 m, 628 m, 668 m, 1015vs and 1128w cm^{-1}). These two last compounds appeared always mixed; around 75% bassanite and 25% gypsum (see Fig. 3.a). The sulfur is present in the black slag because when the slag was formed, the desulfuration has not been carried out yet. This process happens in a subsequent phase where the black slag has already left the furnace.[3] Micro-Raman spectroscopy also provided information about the presence of rutile (TiO_2, Raman bands at 237 m, 447vs and 610 s cm^{-1}) in most of the analysed samples, but always as a minor compound.

The slag is very heterogeneous, and in many occasions apparent Raman displacements of some peaks can be seen, probably owing to the overlap of different compounds. This is mainly observed when micro-Raman spectroscopy was used to identify minor compounds. If those minor mineral forms are not perfectly focused, signals for major compounds will appear as the predominant ones, leading the Raman bands of minor compounds as shoulders or as overlapped peaks, which must be resolved applying mathematics to define individual bands where two or more peaks overlap in a broad signal.

The possibility to have other minor compounds not well identified came from the EDS maps, which revealed good correlations among elements not belonging to compounds clearly identified by the portable and micro-Raman devices. Therefore, we concluded on the presence of other compounds, probably at the trace level, which require further experimentation.

As these compounds were not identified with the conventional Raman systems, we performed new measurements using the SCA device (SEM-EDS plus Raman). This technique allowed us to search for trace minerals, since the SEM images helped us to select a given point (spot) for analysis and with EDS obtained elemental distribution maps of interest. We selected only areas where elements, which were not in the compounds defined till now, shown high correlations. Then, the Raman spectra were collected in only such areas.

As an example, Fig. S3 (Supporting Information) shows the results that can be attained: the SEM image of a micro-fraction of M1 T sample together with the image of its elemental composition, where the relative proportion of each element identified

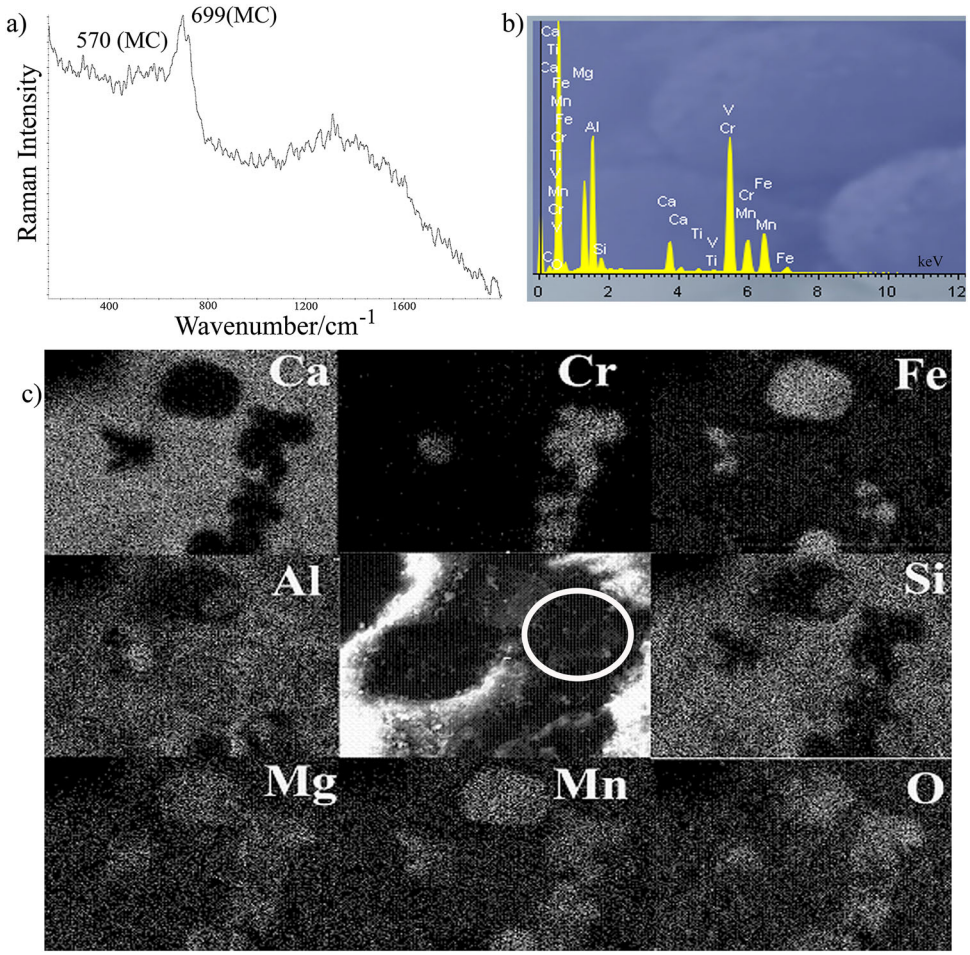

Figure 4. SCA results of magnesiochromite (MC) in M1 T sample: a) Raman spectrum, b) EDS analysis and c) SEM image (40 μm) plus EDS mapping for different elements.

increases the intensity of the white colour (Fig. S3.a (Supporting Information)), and one of the Raman spectra obtained on a spot of the whole area (Fig. S3.b (Supporting Information)).

The EDS images show the main grains (mainly composed by chromium and calcium), and over them a group of micro crystals that could have formed subsequently, i.e. minerals phases that would have been adhered to the surface of original grains of larger size. It could be said that silicon and calcium maps are quite similar; this suggests the formation of dicalcium silicate, tricalcium silicate or other intermediate silicates[3], but having the Si and Ca as remarkable elements. This has been corroborated with the larnite and walstromite (Fig. S3.b (Supporting Information)) identified by Raman analysis. Also, white zones of Al map and Mg map have great resemblance, although they were not so identical as the Si and Ca maps. It could be thought in the presence of some crystal of magnesium alumino-silicate or magnesium aluminate in order to explain the strong white colour in their maps. Besides, the SEM microphotography suggests that magnesium alumino-silicates or magnesium aluminates would be as crystals in the interior side of slag structure, not in the surface.

In relation to iron, it is the main compound in the raw materials, and its presence in the slag has been identified in different forms, as it has been seen by Raman spectroscopy. In this case, Fig. S3.a (Supporting Information) shows four zones very intense in the Fe map that can be associated with four crystals that appear in the SEM microphotograph. As no other element is present in the same zones of white intensity (it is observed four black holes in the Cr map), it is assumed that the Fe would be in the form of oxide (hematite and magnetite) or hydroxide (lepidocrocite and goethite). Hematite and magnetite (Fig. S3.b (Supporting Information)) were identified in their associated Raman spectra. Also, there was a small crystal of Fe situated in the top left part, whose profile coincides with the S and Mn. This corroborates the existence of ilesite crystal ($(Mn^{2+}, Zn, Fe^{2+})SO_4 4H_2O$) identified by Raman spectroscopy.

Finally, the grain that contained chromium was perfectly defined, occupying almost the 50% of the microphotograph, and its image matches mostly with that of manganese and something with magnesium (Fig. S3.a (Supporting Information)). This distribution suggested the presence of Cr and Mn oxides. It is known that iron, manganese and silicon oxides are integrated in the slag that covers the molten liquid after the beginning of the steel production process [3], but other compounds can be formed.

After that screening performed individually with the SEM-EDS and the confocal micro-Raman instruments, the SCA analysis was started. As an example, Fig. 4 shows the global results of a measurement performed on the M1 T sample, where the Raman spectrum reveals the presence of magnesiochromite ($MgCr_2O_4$, Raman bands at 570 s and 697vs cm^{-1}) (Fig. 4.a). This confirms the previous hypothesis from the chromium and magnesium images in the EDS analysis shown in Fig. S3.a (Supporting Information). Thus, with the information obtained from the grouping of the results of all these techniques, the presence of magnesiochromite could be unequivocally corroborated.

Following the same analytical strategy, other compounds not detected by conventional micro-Raman spectroscopy were identified. In particular, chromite ($FeCr_2O_4$, Raman bands at 217w, 280 m, 396w and 680vs cm^{-1})[45], crocoite ($PbCrO_4$, Raman bands at 134w, 337sh, 357 s, 374sh, 399w and 840vs cm^{-1})[46] and hashemite ($BaCrO_4$, Raman bands at 350 s, 402 m, 860vs and 896w cm^{-1}). The presence of these two last compounds, which contain chromium (VI), must be highlighted from the human health risk point of view.

Conclusions

In order to use black slag as by-product for some applications, it is necessary to know their composition and all changes that they could suffer in each process (formation, outdoor cooling, irrigation with water, etc.). For it, by means of a combination of Raman spectroscopy, SCA and μ-EDXRF, it had been established the mineralogical and elemental composition of some black slag samples produced in Electric Arc Furnace of steel industry. It included above all oxides (and sometimes hydroxides) of iron, silicates (tephroite, larnite and walstromite), ferrites and chromites, few carbonates, magnesium oxides, sulfates, rutile and amorphous carbon. The appearance of the peaks around 1240 m cm^{-1} and 1370 s cm^{-1}, assigned to silicates, can be considered typical feature in terms of the number of times appearing in the Raman spectra. Those would be the main matrix of the black slag.

The main difference between 'treated slag' (principally washed with water for three months) and 'original slag' was the presence of hydroxides (as lepidocrocite, goethite and limonite for iron), formed from the oxides (hematite mainly for iron). The first ones appeared in the slag after hydration with added water in the treatment of each factory. In spite of this, in some occasions, it could be appreciated hydroxides in the slag without treatment, possibly owing to their interaction with the environmental atmospheric humidity. Moreover, it was distinguished nitrates (nitratine), sulfates (ilesite, bassanite and gypsum) and a great amount of carbonates (natron and calcite), products that originally were not in the slag and probably they would have appeared with the cooling process outdoors, due to the interaction with atmospheric acid gases. With regard to calcite, in some cases, its Raman bands were shifted, possibly due to the substitution of Ca atoms for Mg, which would be calcite with high content in magnesium. In their Raman spectra, wavenumbers increased when the magnesium percentage augmented. Apart from this, aragonite was also present, mixed with high magnesium calcite. In these cases, it was not possible to calculate the magnesium percentage because their bands did not follow the same trend that the high magnesium calcite alone.

Aside from other toxic elements, the presence of chromium in the SCA results and EDXRF spectra was clear. It has been detected in the Raman spectra of crocoite, hashemite, chromite and magnesiochromite. The molecular forms of chromium (III) are not so toxic, but the two chromates (those of lead and barium) may suppose a risk for the health of the environment (soils, plants, animals and humans) where those slag materials are reused.

Finally, it should be noted that there was not a tendency in the appearance of the majority of identified compounds in the treated and original slag. The treatment suffered for the slag did not cause a significant change in the slag composition (only changes in the relative presence of some compounds). However, some compounds (nitrates and sulphates) are formed as a consequence of the reaction among basic compounds of the slag (carbonates) with the atmospheric acid gases. This fact will be shown in a forthcoming paper.

In conclusion, the analytical approach used in this work to determine the composition and characterization of different

black slag has been of great usefulness. Major compounds can be easily identified by portable equipments while minor and trace compounds require the use of Raman microscopy. The possibility to analyse the same point with Raman spectroscopy and SEM-EDS (SCA) facilitated the identification of trace compounds, something that with only one of the techniques had not been possible. So, in future works, this methodology would be the first step to characterize and compare different slag from different places and producers.

Acknowledgements

This work has been financially supported by UFI program of the UPV/EHU through the Global Change and Heritage project (Ref. UFI11/26). Technical and human support provided by the Raman-LASPEA Laboratory of the SGIker (UPV/EHU, MICINN, GV/EJ, ERDF and ESF) is gratefully acknowledged. Leticia Gomez-Nubla and Julene Aramendia are grateful to the University of the Basque Country (UPV/EHU) and Basque Government, respectively, for their pre-doctoral fellowship.

Supporting information

All Supporting Information may be found in the online version of this article.

References

[1] D. M. Proctor, K. A. Fehling, E. C. Shay, J. L. Wittenhom, J. J. Greens, C. Avent, R. D. Bigham, M. Connolly, B. Lee, T. D. Shepker, M. A. Zak, *Envirom. Sci. Technol.* **2000**, *34*, 8.
[2] P. E. Tsakiridis, G. D. Papadimitriu, C. Tsivilis Koroneos. *J. Hazard. Mater.* **2008**, *152*, 2.
[3] S. A. Ihobe, Libro Blanco para la minimización de residuos y emisiones, Servicio Central de Publicaciones del Gobierno Vasco, Vitoria-Gasteiz, **1999**.
[4] BOPV, Nº 239. DECRETO 423/1994 sobre gestión de residuos inertes e inertizados, **1994**. Anexo I (http://www.euskadi.net).
[5] Norma para el Dimensionamiento de Firmes de la Red de Carreteras del País Vasco. Servicio Central de Publicaciones del Gobierno Vasco, Vitoria-Gasteiz, **2006**.
[6] Y. Xue, S. Wu, H. Hou, J. Zha, *J. Hazard. Mater.* **2006**, *138*, 2.
[7] B. Das, S. Prakash, P. S. Rreddy, V. N. Misra, *Resour. Conserv. Recycl.* **2007**, *50*, 1.
[8] H. Motz, J. Geiseler, *Waste Manage.* **2001**, *21*, 3.
[9] A. N. Shilton, I. Elmetri, A. Drizo, S. Pratt, R. G. Haverkamp, S. C. Bilby, *Waste Res.* **2006**, *40*, 1.
[10] C. Navarro, M. Díaz, M. A. Villa-García, *Environ. Sci. Technol.* **2010**, *44*, 14.
[11] R. Dippenaar, *Ironmak. Steelmak.* **2005**, *32*, 1.
[12] H. Shen, E. Forssberg, *Waste Manage.* **2003**, *23*, 10.
[13] M. Frías, J. T. San-Jose, I. Vegas, *Mater. Construcc.* **2010**, *60*, 297.
[14] C. Shi, J. Qian, *Resour. Conserv. Recycl.* **2000**, *29*, 3.
[15] Catálogo de Residuos Utilizables en la construcción: Escorias de acería de horno de arco eléctrico, IHOBE, ficha 2.3, Bilbao, **2007**.
[16] P. Lana, V. Gomes da Silva, M. Gomes da Silva, *Global Slag Magazine.* **2006**, *4*, 14.
[17] G. Woltron, A. Tec, C. Potocan, R. Tessadri, *Global Slag Magazine.* **2006**, *4*, 18.
[18] S. Ozeki, International Iron and Steel Congress, Stockholm, Sweden, **1997**.
[19] J. Ansorena, F. Izco, D. Merino, P. Tamés, *Valorización de escorias de acería en la construcción de pistas forestales*, parte I, Sustrai, **2003**, *70*, 52.
[20] R. Zevenhoven, J. Fagerlund, A. Wiklund, E. Nduagu, A. M. Forsman, M. Fält, H. P. Mattila, S. Eloneva, A. Said, International Flame Research Foundation, **2009**.
[21] D. Bonenfant, L. Kharoune, S. Sauve, R. Hausler, P. Niquette, M. Mimeault, M. Kharoune, *Ind. Eng. Chem. Res.* **2008**, *47*, 20.
[22] M. Frías, M. I. Sánchez de Rojas, A. Uria, *Mater. Constr.* **2002**, *52*, 267.
[23] J. Waligora, D. Bulteel, P. Degrugilliers, D. Damidot, J. L. Potdevin, M. Measson, *Mater. Charact.* **2010**, *61*, 1.
[24] N. Arrieta, N. Goienaga, I. Martinez-Arkarazo, X. Murelaga, J. I. Baceta, A. Sarmiento, J. M. Madariaga, *Spectrochim. Acta Part A* **2011**, *80*, 55.
[25] E. García-Ramos, A. Romero-Serrano, B. Zeifert, P. Flores-Sánchez, M. Hallen-López, E. G. Palacios, *Steel Res. Int.* **2008**, *79*, 5.
[26] A. Dawson, *WATMOVE report* (COST Action 351), Univ. of Reading, UK, **2007**.
[27] J. H. Van der Waals, A. S. Claassens, 28th Annual Meeting on Mining and the environment Conference II. Sudbury, Ontario; **2003**.
[28] M. B. Parsons, D. K. Bird, M. T. Einaudi, C. N. Alpers, *Appl. Geochem.* **2001**, *16*, 6.
[29] J. Hernández Puy, Estudio de la estabilidad volumétrica, propiedades físicas y químicas de la escoria negra de acero de horno de arco eléctrico. MSc. Thesis, Universitat Politècnica de Catalunya, Barcelona, **2007**.
[30] BOPV Official Bulletin of the Basque Country, Nº 4. Decreto 34/2003 por el que se regula la valorización y posterior utilización de escorias procedentes de la fabricación de acero en hornos de arco eléctrico, en el ámbito de la Comunidad Autónoma del País Vasco, **2003**. (http://www.euskadi.net).
[31] K. Castro, A. Sarmiento, E. Princi, M. Pérez-Alonso, M. D. Rodríguez-Laso, S. Vicini, J. M. Madariaga, E. Pedemonte, *TRAC, Trends Anal. Chem.* **2007**, *26*, 347.
[32] P. Colomban, *J. Raman Spectrosc.* **2012**, *43*, 1529.
[33] I. Martínez-Arkarazo, D. C. Smith, O. Zuloaga, M. A. Olazabal, J. M. Madariaga, *J. Raman Spectrosc.* **2008**, *39*, 1018.
[34] K. Castro, M. Perez-Alonso, M. D. Rodriguez-Laso, L. A. Fernandez, J. M. Madariaga, *Anal. Bioanal. Chem.* **2005**, *382*, 248.
[35] M. Maguregui, N. Prieto-Taboada, J. Trebolazabala, N. Goienaga, N. Arrieta, J. Aramendia, L. Gomez-Nubla, A. Sarmiento, M. Olivares, J. A. Carrero, I. Martinez-Arkarazo, K. Castro, G. Arana, M. A. Olazabal, L. A. Fernandez, J. M. Madariaga, Chemch, First International Congress Chemistry for Cultural Heritage **2010**, *168*.
[36] R. T. Downs, The RRUFF Project: an integrated study of the chemistry, crystallography, Raman and infrared spectroscopy of minerals. Program and Abstracts of the 19th General Meeting of the International Mineralogical Association in Kobe, Japan. O03-13, **2006**.
[37] W. D. Bischoff, S. K. Sharma, F. T. Mackenzie, *Am. Mineralog.* **1985**, *70*, 581.
[38] R. Y. Chen, W. Y. D. Yuen, *Oxid. Met.* **2001**, *56*, 89.
[39] W. K. Jozwiak, E. Kaczmarek, T. P. Maniecki, W. Ignaczak, W. Maniukiewicz, *Appl. Catal. Gen.***2007**, *326*,17.
[40] V. S. F. Muralha, T. Rehren, R. J. H. Clark, *J. Raman Spectrosc.* **2011**, *42*, 2077.
[41] J. Van der Weerd, T. Rehren, S. Firth, R. J. H. Clark, *Mater. Charact.* **2004**, *53*, 63.
[42] S. Sarkar, V. V. V. Subrahmanyam, *J. Min. Mat. Characterizat. Engineer.* **2009**, *8*, 57.
[43] Y. Leon, C. Lofrumento, A. Zoppi, R. Carles, E. M. Castellucci, P. Sciau, *J. Raman Spectrosc.* **2010**, *41*, 1550.
[44] F. Froment, A. Tournié, P. Colomban, *J. Raman Spectrosc.* **2008**, *39*, 560.
[45] C. Ming, S. Jinfu, M. Ho-Kwang, *Chinese Sicience Bulletin.* **2008**, *53*, 3341.
[46] K. Castro, M. Pérez-Alonso, M. D. Rodríguez-Laso, J. M. Madariaga, *J. Raman Spectrosc.* **2004**, *35*, 704.

Research article

Journal of RAMAN SPECTROSCOPY

Received: 1 October 2014 Revised: 6 February 2015 Accepted: 13 February 2015 Published online in Wiley Online Library

(wileyonlinelibrary.com) DOI 10.1002/jrs.4700

Darwin impact glass study by Raman spectroscopy in combination with other spectroscopic techniques

L. Gomez-Nubla,[a]* J. Aramendia,[a] A. Alonso-Olazabal,[b] S. Fdez-Ortiz de Vallejuelo,[a] K. Castro,[a] L. A. Ortega,[b] M. C. Zuluaga,[b] X. Murelaga[c] and J. M. Madariaga[a]

Darwin impact glass appeared in Tasmania (Australia) around 800 000 years ago by meteorite impact. To further study the formation process, several specimens of Darwin glass from the meteorites collection of the University of the Basque Country were analysed. Raman spectroscopy was considered the most suitable technique to determine the differences in composition between the surface layer and the inner matrix. These analyses were complemented by other techniques such as Scanning Electron Microscopy Energy Dispersive X-Ray Spectroscopy, Electron Micro Probe Analysis and Energy Dispersive X-Ray Fluorescence. The major elements found were Si, Al, Fe, K and Ca, together with a range of minor elements Ti, Cl, Zr, Ba, S, Cr, Mn, Ni and Sr. On the micrometre scale, highly heterogeneous elemental composition was found in the glassy matrixes, in particular a gradient in the concentration of iron and aluminium. Raman spectroscopy identified the characteristic silica vitreous matrix of impacted glasses with small inclusions of α-cristobalite (a mineral phase that indicates high temperature formation) and vesicles with iron or iron and nickel oxides filling the pores. Finally, malachite [$Cu_2CO_3(OH)_2$], ponsjankite [$Cu_4SO_4(OH)_6 \cdot H_2O$] and covellite (CuS) were identified by Raman spectroscopy formed after impact as secondary minerals due to the weathering of copper ore deposits incorporated to the matrix. Copyright © 2015 John Wiley & Sons, Ltd.

Additional supporting information may be found in the online version of this article at the publisher's web site.

Keywords: tektite; Darwin glass; Raman spectroscopy; Scanning Electron Microscopy Energy Dispersive X-Ray Spectroscopy; formation temperature

Introduction

Impact glasses have been formed or modified by the hypervelocity of a single impact with an extraterrestrial rock, probably at pressures higher than 45 GPa during the initial stages of meteorite crater formation.[1]

One of these impact glasses, Darwin Glass, was discovered by aboriginal people in western Tasmania, Australia.[2] Despite the lack of conclusive evidence for an impact origin and a paucity of published information, the source of Darwin glass seems to be a buried structure located in a densely forested valley close to the Darwin crater (impact circular structure 1.2 km in diameter).[1,2] Glass fragments were recovered 20 km from the source crater and within a 400 km^2 strewn field. The impact hypothesis is supported by the distribution of glasses relative to the Darwin crater; that is, there is a decrease in glass abundance away from the crater. The proportion of white melt is greatest closest to the crater, and the proportion of the black melt and splash form increase with distance from the crater. The largest fragments of glass are found closest to the crater. This distribution and the high abundance are sign of the transport of melt products during the impact processes, and it has been explained because of the presence of swamps infiltrating water, at the time of impact.[3] The idea of a Darwin crater with lacustrine sediments that comprise quartzites and slates of Siluro–Devonian age is the only explanation for the spatial distribution.[3]

According to argon isotope data, these Darwin glasses were formed around 816 000 years ago.[1] Physically, they are often irregular fragments, twisted masses or chunks up to 10 cm in size. Moreover, Darwin glass is generally vesicular and shows flow/layering structures without strain in thin section marked by bands of elliptical bubbles or vesicles.[2] Basically, the glass population can be subdivided on the basis of shape [the majority (~94%) are irregular

* *Correspondence to: L. Gomez-Nubla, Department of Analytical Chemistry, Faculty of Science and Technology, University of the Basque Country (UPV/EHU), Barrio Sarriena s/n, 48940, Leioa, Spain.*
E-mail: leticia.gomez@ehu.es

a *Department of Analytical Chemistry, Faculty of Science and Technology, University of the Basque Country (UPV/EHU), Barrio Sarriena s/n, 48940, Leioa, Spain*

b *Department of Mineralogy and Petrology, Faculty of Science and Technology, University of the Basque Country (UPV/EHU), Barrio Sarriena s/n, 48940, Leioa, Spain*

c *Department of Stratigraphy and Palaeontology, Faculty of Science and Technology, University of the Basque Country (UPV/EHU), Barrio Sarriena s/n, 48940, Leioa, Spain*

and ropy, and the remainder have either a spheroid, droplet and elongate shape] and colour (53% dark green, 31% light green, 11% black and 5% white).[3]

The chemical composition and rare earth element (REE) patterns indicate that Darwin glass consists of a number of major and trace elements originating from upper crustal sediments, such as argillaceous sandstones.[4-6] There are two groups of glasses in line with geochemical analyses. The first group is composed of SiO_2 (85%), Al_2O_3 (7.3%), TiO_2 (0.05%), FeO (2.2%), MgO (0.9%) and K_2O (1.8%). The second group has lower average SiO_2 (81.1%) and higher average Al_2O_3 (8.2%), FeO (1.5%) and MgO (1.3%) abundances.[3]

Fragments of Darwin glass have been previously analysed using techniques such as X-ray emission Particle Induced X-Ray Emission (PIXE),[1] Elastic Backscattering Spectrometry (EBS),[1] $^{40}Ar/^{39}Ar$ single-grain laser fusion technique,[2] optical microscopy,[7] Scanning Electron Microscopy Energy Dispersive X-Ray Spectroscopy (SEM-EDS),[7] current plasma spectroscopy Direct Current Plasma (DCP),[8] Atomic Absorption Spectrometry (AAS),[8] Electron Probe Microanalysis (EPMA)[8] and Instrumental Neutron Activation Analysis (INAA).[8] In only one study[9] was Raman spectroscopy used for analysis, but it was not a Darwin glass-specific study.

Despite the literature found, there is not much information about the molecular composition of inclusions and matrix of Darwin glass. The purpose of this paper is to investigate these materials. Thus, in this work, a complete Raman spectroscopic study has been carried out with the aim of understanding more about the formation process of these glasses. In order to complete the study, complementary analyses were performed by using Energy Dispersive X-Ray Fluorescence (EDXRF), SEM-EDS and EPMA to provide elemental information.

Experimental procedure

Sample collection

Four specimens of Darwin glass from the impact melt and meteorite samples of the collection of the University of the Basque Country (UPV/EHU) were analysed for this work (Fig. 1). They present different hues and geometrical forms. The first one, labelled as DW1 (Fig. 1b), has a spheroid form and a green brownish dark colour. Its glassy matrix seems to be very homogeneous. The second one (DW2, Fig. 1c) is the most different specimen of the group. It is very light and translucent, with some bubbles inside the bulk. The third one, DW3 (Fig. 1d), is completely black, and it has many inclusions, mainly white and turquoise. Finally, the last one (DW4, Fig. 1a) is dark green with no inclusions, and it is the biggest specimen, at 4.5 × 3.7 cm, whereas the other samples are no bigger than 1 × 1 cm. Moreover, DW4 has two distinguished sides regarding the colour: a dark one (labelled DW4d) and a lighter one (labelled DW4l).

In order to avoid possible surface contamination, the samples were sliced, and in this way, it was possible to analyse the inner part of the glasses.

Instrumentation

EDXRF

A portable XRF spectrometer (X-MET5100 model, Oxford Instrument) equipped with an X-ray rhodium tube that provides a 40-kV voltage was used, and it includes a high-resolution silicon drift detector. The calibration was performed with the method of fundamental parameters; these are based upon the theoretical relationship between the measured X-ray intensities and the concentration of the elements in the reference material. This theoretical relationship is based upon X-ray physics and the measured values of fundamental atomic parameters in the X-ray region of the electromagnetic spectrum. The experimental conditions were as follows: 50 s and three replicates. Several measurements were performed in all the samples in order to obtain reliable results.

SEM-EDS and EPMA

Polished thin sections were employed for visual analysis by a NIKON optical polarising microscope, SEM and EPMA analysis. Backscattered electron images, mineralogical analysis and X-ray

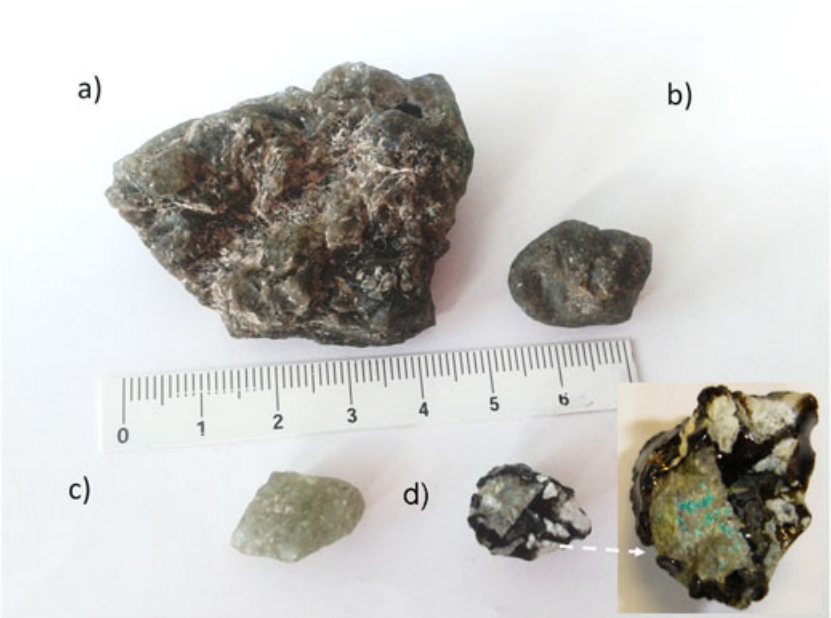

Figure 1. Image of several Darwin glasses: (a) DW4, (b) DW1, (c) DW2 and (d) DW3. This figure is available in colour online at wileyonlinelibrary.com/journal/jrs

Journal of RAMAN SPECTROSCOPY

elemental maps were obtained by a JEOL JSM-6400 SEM with an Oxford Pentafet photon energy instruments Link Isis X-ray (EDS) system. The microtexture observations and elemental analysis were performed on carbon-coated polished thin sections to eliminate charging effects. Qualitative analysis was performed in mapping modes. Quantitative microanalysis by EDS was carried out using the ZAF method, based on correction of the matrix effect in multi-elemental analysis that takes place in the simultaneous determination of the concentration of each element present in a multi-element material.

Some quantitative measures of glass and vesicle fillings were performed by CAMECA SX-100 electron microprobe (EPMA). The operating conditions for X-ray mapping were 15 kV accelerating potential, 15 nA beam current, 2 μm scan distance and 100 ms acquisition time of X-ray peak per point and a lower detection limit of 600 mg/kg for a mapped element.

Raman spectroscopy

A Renishaw InVia Raman micro spectrometer was used with a 514-nm laser, coupled to a Digital Microimaging Light Microscope (DMLM) Leica microscope with 5× N PLAN (0.12 aperture), 20× N PLAN EPI (0.40 aperture), 50× N PLAN (0.75 aperture) and 100× (lateral resolution of 1 μm) long-range objectives. The spectra were obtained in the range of 100–3000 cm^{-1}.

In addition, an InnoRaman handheld spectrometer (B&W Tek, Inc.) with a 785-nm diode laser, a Charge Coupled Device (CCD) detector (Peltier cooled) and a nominal laser power of 330 mW at the source were used. The laser power was reduced in order not to promote mineral phase transformation and/or photoburning. A 20× and 50× long-range focusing lens was used. All the spectra were obtained in the spectral range of 200–2000 cm^{-1}. The data acquisition was performed using BWSPEC 3.26 software (B&W Tek, Inc.).

In both cases, several scans were accumulated for each spectrum to improve the signal-to-noise ratio. Both spectrometers were calibrated daily to the 520.5 cm^{-1} silicon line, and the analysis, treatment and interpretation of their results were carried out using OMNIC software (Thermo Fisher-Nicolet). The results were interpreted by comparing the collected Raman spectra with Raman spectra of pure standard compounds of the e-VISARCH and e-VISART Raman spectra database and with RRUFF online database.[10,11]

Results and discussion

In this section, results obtained by EDXRF, SEM-EDS, EPMA and Raman spectroscopy will be discussed.

EDXRF

The EDXRF results revealed that the same major elements were found to be present in all of the samples. Differences in the relative amount of these elements were attributed to the variation in sample colour (Table 1). The major elements in all the studied samples found were as follows: Si, Al, Fe, K and Ca together with minor elements Ti, Cl, Zr, Ba, S, Cr, Mn, Ni and Sr. In all the studied cases, Si is the most concentrated element. The DW1 and DW4d samples presented the following decreasing order in concentration, Si > Al > Fe > K > Ca, whereas DW2 and DW4l, Si > Al > K > Fe > Ca. The darkest specimens are those with a lower relative silicon content and a higher iron and aluminium content. In the case of DW4, EDXRF confirmed that the colour differences were due to the different elemental compositions. The silicon concentration is higher on the light side, whereas aluminium and iron are low. This elemental composition is consistent with the geochemistry of the target rocks at Darwin crater.[3] Finally, DW3 represents a special case because of the presence of copper. The inner matrix of this specimen was found to contain calcium.

Table 1. Major elements (%) present in the samples and % of Cu and some minor elements that appeared only in some samples

%	Si	Al	Fe	K	Ca	Cu	Ti	Cl	Zr
DW1	77	10	7	4	<LOD	<LOD	0.8	0.9	0.1
DW2	84	9	2	3	0.09	0.01	0.8	1	0.2
DW3	67	8	3	1	15	3	1	1	0.06
DW4d	76	7	7	6	0.35	<LOD	1	3	0.2
DW4l	77	8	5	5	0.19	<LOD	1	3	0.2

There are other minor elements, such as Ba, S, Cr, Ni, Mn and Sr, that appeared in less than 0.1%.
LOD, Limit of detection

SEM-EDS

The SEM images (Fig. S1a, supporting information) of the thin sections revealed that Darwin glass is highly vesicular with a glassy groundmass. The glassy groundmass is holohyaline (>80% glass) ranging from colourless to brownish in colour defining Schlieren structures. Schlieren structures indicate different flow/layering zones of the silicate matrix as impact melts display. These structures are characterised by the presence of abundant elliptical vesicles. Moreover, some flow structures can adapt to vesicle distribution and vice versa.

In order to gain a better understanding of the colour variations of the glass and flow structures, the specimens were analysed by SEM-EDS. The results revealed variations in the matrix. SEM backscattered images and various mappings by EDS determined evident compositional differences (Fig. 2). The intensity of the white colour in the image determines the relative proportion of each major element. In the Si EDS map (Fig. 2), the white area corresponds to silica-rich inclusions or pure silica (a high temperature SiO_2 polymorph), and it is surrounded by gradient concentrations of other elements such as Al, Fe, K and Mg (Fig. 2). According to the results, the aluminium and iron maps are very similar, suggesting the formation of aluminium iron silicate, which is a very common compound of sediments.[12] It is proposed that the mineral phase was incorporated to the matrix during the impact.

EPMA

To confirm the elemental distribution found by SEM-EDS, semi-quantitative analysis by EPMA was carried out in different areas of the glassy matrix (Fig. 3). The ranges for the compositions of the main elements were the following: SiO_2 varies from 80 to 90 wt.% (excluding the SiO_2 pure inclusions), Al_2O_3 9.1 to 5.0 wt.%, FeO 4.0 to 2.0 wt.%, MgO 0.80 to 0.30 wt.%, K_2O 2.3 to 1.8 wt.%, CaO 0.030 to 0.010 wt.% and TiO_2 0.60 to 0.35 wt.%. The high heterogeneous composition, in a micrometre scale, reflects the melting heterogeneity process as well as mixing differences during the transport before the solidification.

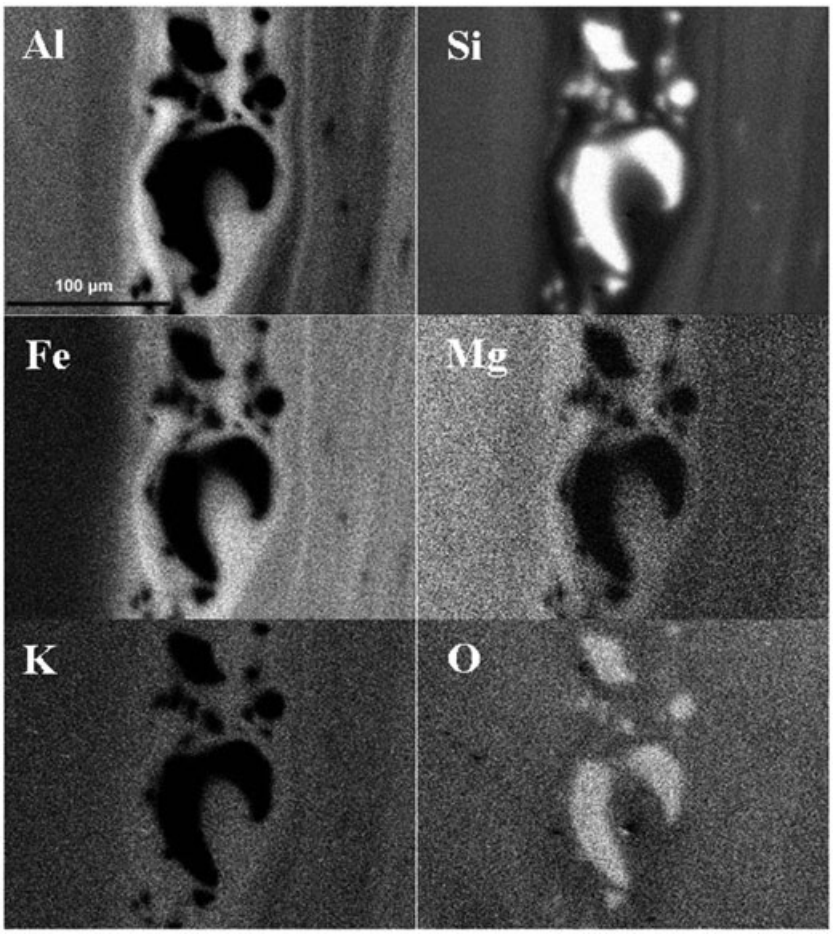

Figure 2. Energy dispersive X-ray spectroscopy mapping of a silica-rich inclusion and the distribution of major element around it.

Raman spectroscopy

By means of Raman spectroscopy, it was determined that the dark bulk of all Darwin glasses was a silica vitreous matrix with its main Raman bands at 110 (vw, very weak), 480 (s, strong), 810 (w, weak), 930 (sh, shoulder) and 1021 (s) cm^{-1}, very similar to those obtained in other silica-rich impact glasses (Fig. 4 and Table 2).[13,14] However, the relative intensities of the Raman bands of Darwin glass are really different to other impact glasses; in the case of Libyan desert glass (LDG), the 480-cm^{-1} band is the most intense one. In contrast, in Darwin glass, apart from the band at 480 cm^{-1}, there is also another major band at 1021 cm^{-1}, whilst in LDG, the band is very weak. This fact could be due to the presence of REE and heavy metal content, which are responsible of the luminescence. In addition, some large white crystals were seen in the margins of the bulk and in the centre within the glassy matrix with the naked eye. These white crystals were composed of α-cristobalite (SiO_2), identified by Raman peaks at 230 (s, Rigid Unit Modes (RUM)[15]), 417 (vs, lattice and O–Si–O bending modes), 783 (m, symmetric Si–O–Si stretch) and 1076 (m, antisymmetric Si–O–Si stretch) cm^{-1} (Fig. 5a). The α-quartz, which is the low-temperature stable polymorph of SiO_2, is converted into β-cristobalite at 1470 °C. And in the cooling process, β-cristobalite transforms into α-cristobalite. Therefore, the presence of α-cristobalite normally indicates the former presence of β-cristobalite and, hence, a temperature greater than 1470 °C.[16]

As shown in Fig. S1b supporting information, some areas of the thin sections are rich in vesicles and bubbles indicating disequilibrium and rapid quenching conditions, characteristics of impact glasses. Other vesicles are filled with angular mineral fragments that represent target sedimentary material.[5] They always appeared as perfect elliptical vesicles, as it can be observed in the microphotography of Fig. 6e. In some of these vesicles (Fig. 5b), nickel–iron or iron oxide was identified around the entire vesicle, with Raman bands at 210 (m), 270 (s), 382 (br) and 584 (br) cm^{-1}.[17] Taking into account the identified bands, this compound could be hematite or also an iron–nickel compound, which has been previously identified in meteorites, specifically in ordinary chondrites[16] where they appeared also filling pore spaces.

A blue-turquoise crystal was observed macroscopically in the centre of one of the biggest α-cristobalite inclusions inside DW3 specimen (Fig. 1d). The presence of this type of crystal is unusual in these melt products. The Raman spectroscopic analysis revealed the presence of a mixture of copper compounds, such as malachite [$Cu_2CO_3(OH)_2$] with spherical structure and ponsjankite [$Cu_4SO_4(OH)_6 \cdot H_2O$] (Fig. 6b and Table 2). In addition to the white crystals of α-cristobalite and not necessarily related to those blue crystals, covellite (CuS) was often found as evidenced by its characteristic Raman band at 471 cm^{-1} (Fig. 6c).

Raman spectroscopic analysis of the Darwin glass samples has revealed a number of mineral phases, which can be used to estimate the temperature of formation. SiO_2 is transformed into α-cristobalite at 1470 °C; thus, it had to be formed during the impact. In contrast, the malachite carbonate disappears at temperatures higher than 800 °C, which could mean that this compound was

Journal of RAMAN SPECTROSCOPY

adhered to the silica matrix after the impact. Literature confirms that Darwin glasses were spread 400 km^2 away from the crater;[7] near this area, there is a copper mine (Mt. Lyell copper mine).[18] The detected copper compounds were found inside the Darwin specimen; thus, it is proposed that in the impact of the meteorite, the cristobalite was formed and then, when the Darwin glass fell to the ground after the impact, arrived to a copper-enriched soil incorporating new materials whilst cooling. Alternatively, the copper compounds could have been dissolved in infiltration water and incorporated through the fracture planes, which can be seen in Fig. 4, crystallising inside the glass matrix. Thus, they would not belong to the impact glasses. Precipitation of copper minerals is considered a common pathway in natural waters with high concentration of copper. Cu precipitates are usually different depending on the surrounding conditions; for example, malachite is the major precipitate in natural waters, and copper sulphides in anaerobic or biologically active sediments.[19] Precipitation or dissolution of Cu minerals is determined by the concentrations of the ions involved (Cu^{2+} and the correspondent anion),[19] so in presence of copper-enriched waters (as those coming from Mt. Lyell copper mine), the precipitation of these found minerals is very likely. Terrestrial weathering processes are evidence of the preterrestrial history of the meteorites interferes, because weathering transforms the original minerals and redistributes chemical elements. Hence, they could be used as a tracer of the terrestrial geochemical processes, because they have been exposed in the Earth for million or thousand years. Nevertheless, the real interest in studying these weathering processes is to avoid misinterpretation with the real composition of fresh falls.[20] In this way, some efflorescences have been described above all in Antartic meteorites.[20] According to literature, those efflorescences are not detectable with the unaided eye (less than 5%). However, the DW3 study is really interesting, because the efflorescences are large, covering more or less 40% of the specimen matrix, as it can be seen in this case (Fig. 1).

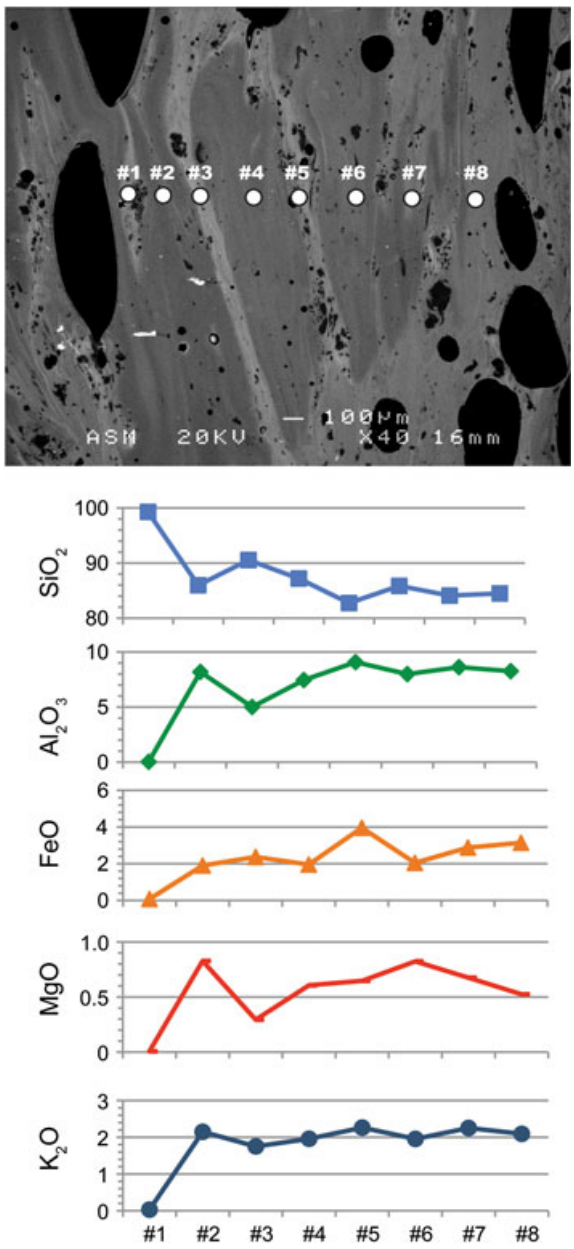

Figure 3. Cross section of the Darwin glass thin section on SEM image with the analysed points by electron microprobe. Below, scatter diagrams for the analysed major elements. Point #1 is a silica pure inclusion. This figure is available in colour online at wileyonlinelibrary.com/journal/jrs

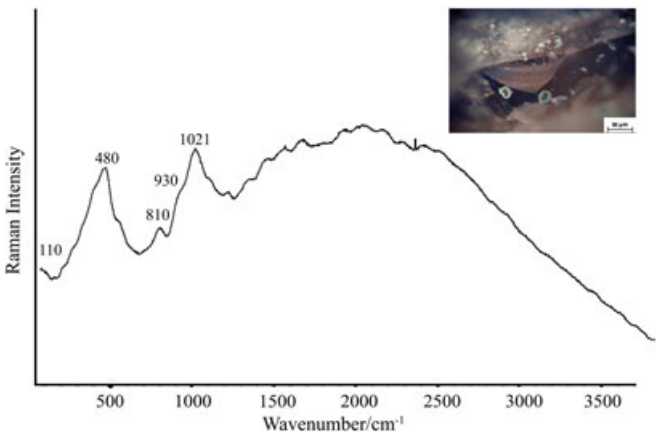

Figure 4. Microimage of DW3 with details of the crystals and Raman spectrum of the black matrix. This figure is available in colour online at wileyonlinelibrary.com/journal/jrs

Table 2. Raman bands of the compounds identified in the analysed Darwin glasses where v is very, w is weak, m is medium and s is strong

Compounds	Raman bands
Vitreous matrix	110 (vw), 480 (s), 810 (w), 930 (sh), 1021 (s)
Cristobalite (SiO_2)	230 (s), 417 (vs), 783 (m), 1076 (m)
Malachite [$Cu_2CO_3(OH)_2$]	152 (m), 179 (m), 220 (w), 270 (w), 355 (w), 432 (s), 486 (vw), 534 (vw), 720 (vw), 972 (vw), 1063 (vw), 1099 (vw), 1368 (vw), 1492 (s)
Ponsjankite [$Cu_4SO_4(OH)_6 H_2O$]	137 (m), 195 (m), 244 (vw), 319 (vw), 391 (m), 421 (m), 483 (m), 596 (m), 619 (m), 728 (vw), 909 (vw), 972 (vs), 1076 (w), 1097 (w), 1125 (vw), 3251 (vw), 3371 (vw), 3404 (vw), 3561 (vw), 3585 (vw)
Covellite (CuS)	162 (vw), 267 (w), 341 (vw), 471 (vs), 923 (vw)
Ni and Fe oxide	210 (m), 270 (s), 382 (m), 584 (w)

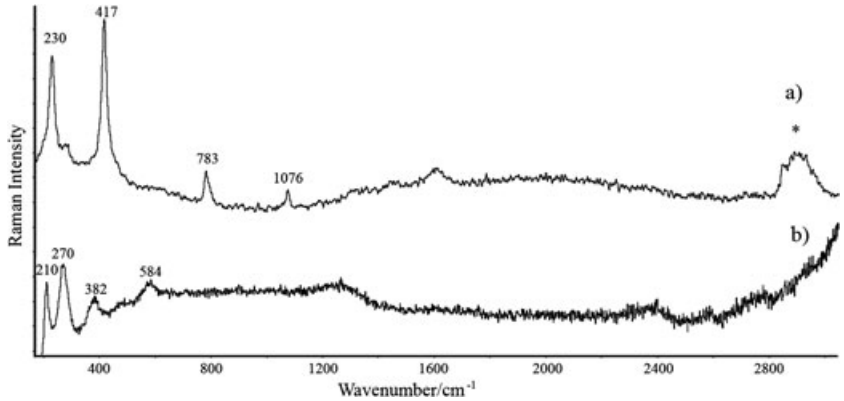

Figure 5. Raman spectra of (a) cristobalite and * typical vibration signal of –CH at around 2900 cm^{-1} and (b) iron or nickel and iron oxide. This figure is available in colour online at wileyonlinelibrary.com/journal/jrs

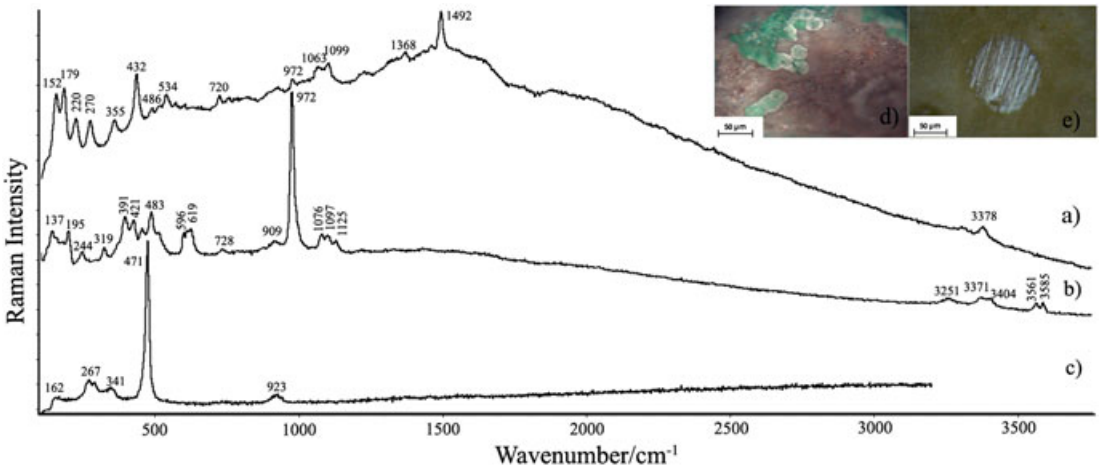

Figure 6. Raman spectrum of (a) malachite, (b) ponsjankite and (c) covellite. Microphotographs of (d) ponsjankite (intense turquoise colour) and malachite (spherical structure) and (e) covellite with its spherical structure. This figure is available in colour online at wileyonlinelibrary.com/journal/jrs

Conclusions

The findings using a number of spectroscopic techniques were used to propose some possible ideas about how the Darwin glass was formed by melting and mixing of local target rocks from Darwin crater.

The major elements found in the Darwin glass samples were Si, Al, Fe, K and Ca, and the minor elements Ti, Cl, Zr, Ba, S, Cr, Mn, Ni and Sr. SEM-EDS revealed variations in the matrix especially in the case of Fe and Al. Raman spectroscopy identified the characteristic silica vitreous matrix, together with α-cristobalite (SiO_2) inclusions in DW3 specimen, which indicated that the glasses were formed at high temperatures. The relative amount or concentration of Cu in DW3 sample was of major interest.

In contrast, the presence of malachite [$Cu_2CO_3(OH)_2$], ponsjankite [$Cu_4SO_4(OH)_6 \cdot H_2O$] and covellite (CuS) suggests the formation of new minerals as a consequence of the infiltration waters and copper mines present in the surroundings. These compounds were formed or incorporated to the matrix after the impact. In meteorites study, the terrestrial weathering is crucial because it modifies the mineralogical, chemical and isotopic composition,[21] so they must be taken into account.

Acknowledgements

This work has been funded by GRUPO CONSOLIDADO (Ref. IT-742-13) Project, UFI programme of the UPV/EHU through the Global Change and Heritage project (Ref. UFI11/26) and *Meteoritos y productos de impactos*: *Procesos comunes en el Sistema Solar* Project (Ref. AE13/18). Leticia Gomez-Nubla and Julene Aramendia are grateful to the UPV/EHU for their pre-doctoral and post-doctoral fellowships, respectively. Technical and human support provided by Singular Coupled Multispectroscopy Laboratory (LASPEA) from the SGIKER (UPV/EHU, MICINN, GV/EJ, ERDF and ESF) is gratefully acknowledged.

References

[1] M.J. Bailey, K.T. Howard, K.J. Kirkby, C. Jeynes, *Nucl. Instrum. Methods Phys. Res., Sect. B* **2009**; *267*, 2219.
[2] C.H. Lo, K.T. Howard, S.L. Chung, S. Meffre, *Metorit. Planet. Sci.* **2002**; *37*, 1555.
[3] K.T. Howard, *Metorit. Planet. Sci.* **2009**; *44*, 115.
[4] K.T. Howard, P.W. Haines, *Earth Planet. Sci. Lett.* **2007**; *260*, 328.
[5] K.T. Howard, *Metorit. Planet. Sci.* **2008**; *43*, 479.
[6] J. Matsuda, H. Yajima. Lunar and Planetary Science Conferences. **1989**; *20*, 628.

[7] L. Neil, K.T. Howard, 45th Lunar and Planetary Science Conference. **2014**; 1932.
[8] T. Meisei, C. Koeberl, J. Ford, *Geochim. Cosmochim. Ac.* **1990**; *54*, 1463.
[9] E. Faulques, E. Fritsch, M. Ostroumov, *J. Mineral. Petrol. Sci.* **2001**; *96*, 120.
[10] K. Castro, M. Perez-Alonso, M.D. Rodriguez-Laso, L.A. Fernandez, J. M. Madariaga, *Anal. Bioanal. Chem.* **2005**; *382*, 248.
[11] R.T. Downs, Program and Abstracts of the 19th General Meeting of the International Mineralogical Association **2006**; O03–13.
[12] J. Komlos, R.K. Kukkadapu, J.M. Zachara, P.R. Jaffé, *Water Res.* **2007**; *41*, 2996.
[13] J. Aramendia, L. Gomez-Nubla, S. Fdez-Ortiz de Vallejuelo, K. Castro, X. Murelaga, J.M. Madariaga, *Spectrosc. Lett.* **2011**; *44*, 521.
[14] M. Swaenen, E.A. Stefaniak, R. Frost, A. Worobie, R. Van Grieken, *Anal. Bioanal. Chem.* **2010**; *397*, 2659.
[15] I. P. Swainson, M. T. Dove, D. C. Palmer, *Phys. Chem. Miner.* **2003**; *30*, 353.
[16] D. C Smith, J. D. Vernioles, *J. Raman Spectrosc.* **1997**; *28*, 195.
[17] A. Weselucha-Birczynska, M. Zmudzka, *J. Mol. Struct.* **2008**; *887*, 253.
[18] D.L. Huston, *J. Geochem. Explor.* **2001**; *72*, 23.
[19] C. A. Flemming, J. T. Trevors, *Water Air Soil Poll.* **1989**; *44*, 143–158.
[20] M. A. Velbel, D. T. Long, J. M. Gooding, *Geochim. Cosmochim. Ac.* **1991**; *55*, 67.
[21] M. R. Lee, P. A. Bland, *Geochim. Cosmochim. Acta* **2004**; *68*, 893.

Supporting Information

Additional supporting information may be found in the online version of this article at the publisher's web site.

“Everything will be okey in the end. If it’s not okey, it’s not the end”
John Lennon

One of the important parts of the exploration of the Solar Systems is the study of Extraterrestrial Materials as well as of Terrestrial Analogs in a detailed way, being necessary process studies at analog sites, field workshops, instrument and operations tests, and laboratory measurements. Terrestrial analogs are defined as materials of environments on Earth that present one or more geological or environmental conditions similar to those found on an extraterrestrial body (Moon, Mars, etc.), either current or past.

This PhD thesis is our first attempt to mainly characterize terrestrial-extraterrestrial materials materials and terrestrial analogs to meteorites, and to test several analytical techniques (Raman spectroscopy, SEM/EDX, LIBS and GC-MS) over them, which will be used in space explorations. For this purpose, impact glass, that is, material formed by hypervelocity impact of meteorites, comets or asteroids on the Earth surface, has been studied. Concretely, Libyan Desert Glasses (LDG), found in Africa, and Darwin Glasses (DG), discovered in Australia. Also, steel slag (terrestrial analogs to meteorites) collected from factories and from forest tracks (they were used as filler decades ago) were considered.

The characterization of major, minor and trace compounds, the assignation to each compound as original or formed after weathering processes as well as the identification of mineral phases of high pressures and temperatures has been an important contribution to the study of these materials. New mineral phases, organic compounds and compounds related to biological activity have been identified, compounds not mentioned so far in samples such as LDG and DG. Moreover, accelerate weathering processes by interaction with water and acids have been tested, firstly with the steel slag materials, and then, the impact glasses were evaluated with the water methodology. On the other hand, it has been performed an elemental quantification through a portable LIBS instrument using a multivariate calibration procedure. All these results have been useful to develop a complete and innovative analytical methodology to characterize extraterrestrial and terrestrial analog materials.